
DNA Self-Assembled Filaments for Micro- and Nanoscale Propulsion

Alexander Mario Maier

Dissertation
durchgeführt an der Fakultät für Physik
der Ludwig-Maximilians-Universität
München

vorgelegt von
Alexander Mario Maier
aus Traunstein

2017

Erstgutachter: Prof. Dr. Tim Liedl

Zweitgutachter: Prof. Dr. Erwin Frey

Datum der Abgabe: 17.03.2017

Datum der mündlichen Prüfung: 18.05.2017

Content

1. INTRODUCTION	1
1.1 NATURE'S MICROSWIMMERS.....	2
<i>Life at low Reynolds numbers</i>	3
1.2. ARTIFICIAL MICRO- AND NANOSWIMMERS.....	4
1.3. STRUCTURAL DNA NANOTECHNOLOGY.....	7
<i>DNA tile assembly</i>	7
<i>DNA origami</i>	8
2. SELF-ASSEMBLED DNA TUBES FORMING HELICES OF CONTROLLED DIAMETER AND CHIRALITY	10
2.1 ARTIFICIAL MICRO- AND NANOHELICES.....	10
2.2 CONTROLLING THE NANOSCALE HELICAL SHAPE OF DNA TILE TUBES THROUGH BASE PAIR INSERTIONS AND/OR DELETIONS.....	12
2.3 CONTROLLING THE MICROSCALE HELICAL SHAPE AND CHIRALITY OF DNA TILE TUBES THROUGH <i>TILE SHIFTING</i>	18
2.4 COMBINING BASE PAIR INSERTIONS/DELETIONS, <i>TILE SHIFTING</i> AND CY3 MODIFICATIONS IN DNA TILE TUBES.....	22
2.5 CONCLUSIONS AND OUTLOOK.....	24
3. MAGNETIC PROPULSION OF MICROSWIMMER WITH DNA-BASED FLAGELLAR BUNDLES	26
3.1 MAGNETIC ACTUATION OF HELICAL ARTIFICIAL SWIMMERS.....	26
3.2 CONSTRUCTION AND PROPULSION OF MICROSWIMMERS WITH DNA-BASED FLAGELLAR BUNDLES.....	27
3.3 CONCLUSIONS AND OUTLOOK.....	30
4. DNA-BASED NANOSWIMMERS FOR ENHANCED DIFFUSIVE SWIMMING	31
4.1 ENHANCED DIFFUSION.....	31
4.2. CONSTRUCTION OF DNA-BASED NANOSWIMMERS.....	33
4.3 MAGNETICALLY ACTUATED ENHANCED DIFFUSION OF DNA-BASED NANOSWIMMERS.....	38
4.4 CONCLUSIONS AND OUTLOOK.....	43
5. ATPASE-FUNCTIONALIZED DNA NANOSTRUCTURES FOR THE PROPULSION OF AUTONOMOUS MICROSWIMMERS	44
5.1. THE F1FO-ATPASE ROTARY MOTOR COMPLEX.....	44
5.2. DNA FILAMENT – F1-ATPASE MOTOR PROTEIN HYBRIDS.....	45
5.3 F1-ATPASE – DNA FILAMENT HYBRIDS COUPLED TO A MICROPARTICLE: A PROTOTYPE FOR AUTONOMOUS MICROSWIMMERS.....	50
5.4. CONCLUSION AND OUTLOOK.....	53
6. ASSOCIATED PUBLICATIONS	55
6.1. ASSOCIATED PUBLICATION P1.....	55
6.2 ASSOCIATED PUBLICATION P2.....	62
APPENDIX A: SUPPORTING INFORMATION FOR ASSOCIATED PUBLICATION P1	68
APPENDIX B: SUPPORTING INFORMATION FOR ASSOCIATED PUBLICATION P2	78
APPENDIX C: MATERIALS AND METHODS FOR CHAPTER 2	101
APPENDIX D: MATERIALS AND METHODS FOR CHAPTER 4	102
APPENDIX E: MATERIALS AND METHODS FOR CHAPTER 5	109
BIBLIOGRAPHY:	113

List of Figures

1.1: Schematic of prokaryotic flagellum and eukaryotic cilium.....	2
1.2: Propulsion mechanisms at low Reynolds number.....	4
1.3: Artificial magnetic microswimmers.....	5
1.4: DNA tile assembly.....	7
1.5: DNA origami.....	9
2.1: Design of tile-assembled tubes.....	12
2.2: DNA tile tubes with nanoscale helical shape.....	13
2.3: Dependence of the position of base pair insertions and deletions on the tube's cross sectional geometry.....	15
2.4: Dependence of the position of base pair insertions and deletions on the tube's radius of curvature.....	15
2.5: Comparison of predicted and measured radius of curvature of tubes with position - dependent base pair insertions and deletions.....	16
2.6: 6-helix tile tubes with position-dependent base pair insertions and deletions.....	18
2.7: Schematic of tile shifting.....	19
2.8: DNA tile tubes with microscale helical diameter.....	20
2.9: Relation between tile-shifting and interhelical angle.....	21
2.10: Base pair insertion-induced switching of the chirality of tile-shifted tubes.....	22
2.11: Base pair deletion-induced increase of the helical diameter of Cy3-modified tubes.....	23
3.1: Propulsion mechanisms of magnetically actuated microswimmers with rigid helical filament and with flexible filament.....	27
3.2: Construction of magnetic microswimmers with artificial DNA flagella.....	28
3.3: Locomotion of a microswimmer driven by a DNA flagellar bundle.....	29
4.1: Comparison of enhanced and normal diffusion.....	33
4.2: Construction scheme for DNA origami - magnetic bead hybrids.....	34
4.3: Multimerization of DNA Origami monomers.....	35
4.4: Prevention of magnetic nanoparticle aggregation.....	35
4.5: Diversity of DNA origami - magnetic bead hybrids.....	36
4.6: Separation of single-tail from multi-tail hybrid structures.....	37
4.7: Determination of the diffusion coefficient of nanoparticles via 2D tracking.....	40
4.8: Diffusion of hybrid particles w/o magnetic actuation.....	41
4.9: Diffusion of hybrid particles along and perpendicular to the rotation axis of the external magnetic field.....	42

5.1: Schematic of the F1Fo ATPase rotary motor protein.....	45
5.2: ATPase at varying salt concentrations.....	46
5.3: Design scheme of DNA artificial flagella – F1-ATPase motor protein hybrids.....	47
5.4: Purification of neutravidin-modified DNA origami constructs.....	48
5.5: Attachment of ATPase to neutravidin-modified DNA constructs.....	49
5.6: Coupling efficiency between neutravidin-modified and biotin-modified DNA origami constructs.....	50
5.7: Construction scheme for autonomous microswimmers.....	51
5.8: Magnetic microparticle - ATPase - DNA origami hybrid.....	52
5.9: Detachment of hybrid flagella from magnetic particles upon addition of ATP.....	53

Zusammenfassung

Auf der Mikroebene nutzen viele prokaryotische Mikroorganismen die Rotation helikaler Filamente, sogenannter Flagellen, um sich fortzubewegen. Die Nachahmung dieser hoch entwickelten Strukturen eröffnet einen vielversprechender Ansatz für die Konstruktion künstlich angetriebener Mikro- und Nanoroboter. Die Realisierung künstlicher Flagellen bedarf einer Methode, welche die komplexe Proteinarchitektur dieser Filamente möglichst genau imitieren kann. Neben ihrer Hauptfunktion als Träger der Erbinformation hat sich die Desoxyribonukleinsäure (DNA) in den letzten Jahren als vielseitiger Baustein im Bereich der molekularen Selbstassemblierung etabliert. In vorliegender Dissertation werden auf DNA Selbstassemblierung beruhende Filamente vorgestellt, welche als künstliche Flagellen für den Antrieb von Mikro- und Nanoschwimmern sorgen.

Mikrometer lange, helikale DNA Nanotubes, welche in Form und Größe bakteriellen Flagellen gleichen, wurden unter Zuhilfenahme des „DNA tile assembly“ realisiert. Das Einfügen und/oder Entfernen von Basenpaaren ermöglichte es uns die helikale Struktur der Nanotubes auf der Nanoebene zu kontrollieren. Nanotubes mit Mikrometer großen helikalen Durchmessern und definierter Chiralität wurden anhand einer neuartigen Design Technik, dem *“tile shifting”*, konstruiert.

Durch das Anbinden der helikalen Strukturen an magnetische Mikropartikel konzipierten wir eine neue Klasse von biokompatiblen Mikroschwimmern. Diese hybriden Strukturen lassen sich durch ein externes Magnetfeld antreiben, steuern und bewegen sich mittels eines Flagellenbündels, ähnlich wie Bakterien, fort.

Mithilfe der DNA Origami Technik waren wir zudem in der Lage, DNA Nanoflagellen mit definierter Form zu konstruieren und an magnetische Nanopartikel anzubinden. Die daraus resultierenden Nanoschwimmer wurden magnetisch angeregt und zeigten eine leichte Erhöhung ihrer Diffusion gegenüber einer reinen Brownschen Molekularbewegung. Eine solch erhöhte Diffusion kann für die Fortbewegung von Nanorobotern von Vorteil sein, falls eine gerichtete Bewegung durch thermische Kräfte verhindert wird.

Abschließend konstruierten wir einen Prototyp eines sich autonom fortbewegenden DNA-basierten Mikroschwimmers, indem wir den molekularen Motor F – ATPase zwischen DNA Flagellum und Mikropartikel integrierten. Nach Bereitstellung des Motortreibstoffes ATP lösten sich jedoch die künstlichen Flagellen von den Partikeln, wodurch ein Antrieb der Schwimmer verhindert wurde. Die erfolgreiche Anbindung der DNA Flagellen und die Aktivität der integrierten ATPase stellen dennoch wichtige Schritte für die Realisierung autonomer Mikroschwimmer dar.

Die in dieser Dissertation gewonnen Erkenntnisse zeigen, dass DNA basierte molekulare Selbstassemblierung ein ausgezeichnetes Instrument für die Konstruktion von biokompatiblen künstlichen Filamenten ist, welche als Antriebsmechanismus künftiger Generationen von Mikro- und Nanorobotern Verwendung finden können.

Abstract

The rotation of helically shaped filaments, so-called flagella, is one major strategy used by many motile microorganisms to achieve propulsion. Mimicking these highly evolved structures can be a promising approach for the construction of artificially propelled micro- and nanorobots. Realizing artificial flagella, however, requires a technique, which can precisely copy the complex architecture of these protein filaments. Besides its fundamental function as carrier of the genetic information, DNA has proven to be a versatile building block in molecular self-assembly. In this dissertation, DNA-self assembled filaments are presented, which function as artificial flagella for the propulsion of micro- and nanoswimmers.

Micrometer-long helically shaped DNA nanotubes, which closely resemble bacterial flagella, were constructed by applying the DNA tile assembly technique. Through the insertion and/or deletion of base pairs, we generated bending and twisting in the DNA nanotubes, which allowed us to control the tubes' helical shape in the nanoscale regime. Nanotubes with microscale helical diameters and defined chirality were constructed by introducing a new design technique, the so-called *tile shifting*.

By coupling the helical filaments to magnetic microparticles, we constructed a new class of fully biocompatible artificial microswimmers. The hybrid structures were actuated and steered by an external magnetic field and propelled by means of a flagellar bundle similar to motile bacteria.

The DNA origami technique further allowed us to realize nanometer-sized artificial DNA flagella with defined shape and to attach them onto magnetic nanoparticles. The resulting nanoswimmers were actuated by a magnetic field and exhibited a slight enhancement of their diffusivity, in comparison to a mere Brownian motion. Such an enhanced diffusion can be of advantage for the locomotion of nanorobots if a directed motion is unfeasible due to strong thermal forces.

Finally, we constructed a prototype of an autonomously propelling DNA-based microswimmer by incorporating the molecular motor F-ATPase between DNA flagella and magnetic microparticle. Unfortunately, we observed a detachment of the artificial flagella upon addition of the "motor fuel" ATP, which inhibited the propulsion of the swimmer. The successful coupling of the artificial flagella and the activity of the incorporated ATPase, nevertheless, constitute important steps towards the realization of autonomous microswimmers.

The insights gained in this dissertation illustrate that DNA molecular self-assembly is an excellent tool for constructing fully biocompatible artificial flagella, which can provide future micro- and nanorobotic devices with an effective propulsion mechanism.

1. Introduction

A friend of mine (Albert R. Hibbs) suggests a very interesting possibility for relatively small machines. He says that, although it is a very wild idea, it would be interesting in surgery if you could swallow the surgeon. You put the mechanical surgeon inside the blood vessel and it goes into the heart and “looks” around (Of course the information has to be fed out.) It finds out which valve is the faulty one and takes a little knife and slices it out. Other small machines might be permanently incorporated in the body to assist some inadequately-functioning organ.

Richard Feynman (1959) [1]

In 1959, Richard Feynman gave a visionary talk that became a defining moment in the field of nanotechnology. In his talk entitled „ There’s plenty of room at the bottom“ [1], he, among other things, touched upon the idea of developing miniaturized machines that can travel inside the body and perform surgery or assist malfunctioning organs. Such micro- or nanorobots have since that day been inspiring to mankind even beyond scientific disciplines. A famous example is the 1966 movie "Fantastic Voyage", where a surgical team travels through the bloodstream of an injured person in a miniaturized submarine to destroy a life-threatening blood clot.

Half a century later, nanotechnology has become a well-established research field that attracts increasing research attention. Among many disciplines, it also includes nanorobotics, which aims at bridging the gap between robotics and nanotechnology [2]. In nanorobotics, a nanorobot is defined as an active structure, which consists of nanometer-sized components and can perform tasks such as actuation, sensing, manipulation, propulsion, signalling, information processing, intelligence, and swarm behaviour [3]. Although currently realized micro- and nanorobots are yet not able to perform all these tasks at the same time and are still far away from the “mechanical surgeons” envisioned by Albert R. Hibbs, the realization of such miniaturized machines is rapidly developing supported by the strong progress in nanofabrication and microelectronics [2, 4].

Of particular interest for such nanorobotic devices is a propulsion mechanism that works in a fluidic environment where most of the proposed applications are located. Unfortunately, traversing through micro- and nanofluidic environments is fundamentally different from what "macroscopic beings" experience when moving through fluid, and requires special strategies [5]. As is often the case, nature can serve as an inspiring source.

1.1 Nature's microswimmers

In diverse disciplines ranging from natural sciences over engineering to architecture, nature has served as a blueprint for constructing advanced materials and strategies [6]. In searching for an appropriate mode of locomotion for micro- and nanoscopic devices, drawing from those modes developed by nature's microorganisms is a logical choice.

At the microscale, many microorganisms need to be motile in order to perform a wide spectrum of activities, such as searching for food, orienting themselves toward light, spreading their offspring, and forming colonies [7]. They achieve these tasks by either crawling or gliding along surfaces [8], by polymerizing their protrusions [9] or by swimming [10, 11]. Within these different strategies, swimming is particularly promising as it brings the advantage of high velocity, efficiency, specificity, controllability, and simple propagation. In order to propel through the liquid environment, microorganisms, including many bacteria and eukaryotic cells, have grown one or many appendages that protrude from the surface of their cell bodies. Depending on their composition and beating pattern, these protrusions are usually subdivided into three categories: the prokaryotic flagellum, the eukaryotic flagellum and the cilium.

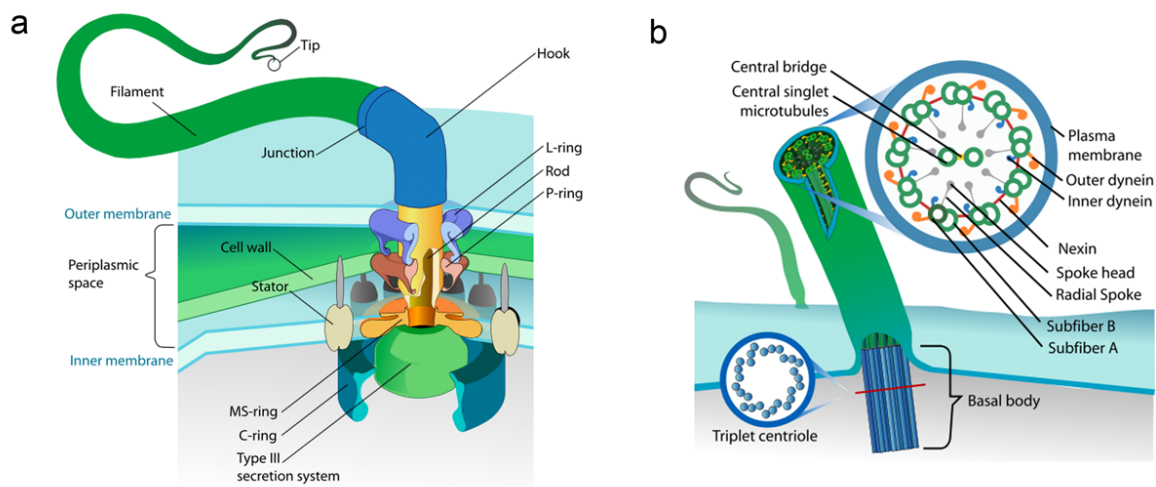


Figure 1.1: Schematic of prokaryotic flagellum and eukaryotic cilium. (a) Prokaryotic flagellum and (b) eukaryotic cilium as found in many motile prokaryotic and eukaryotic microorganisms. These images have been obtained from the Wikipedia websites <http://en.wikipedia.org/wiki/Flagellum> and <http://en.wikipedia.org/wiki/Cilium> respectively, where they are stated to have been released into the public domain by its author.

The prokaryotic flagellum assembles from the protein flagellin into a helical hollow cylinder [12]. It is several nanometres thick with a sharp curvature close to the outer membrane called the "hook" as illustrated in Figure 1.1a. The bacterial flagellar motor is located at the inner cell membrane [13] connecting the flagellum to the cell body, and consists of more than 20 proteins. It is driven by a flow of positively charged hydrogen ions through the cell membrane, which induces a conformational change that rotates the

bacterial flagellum. The rotary engine can achieve angular velocities of up to 1050 rps, resulting in a propulsion speed of around 60 cell lengths per second [14] and generates torques higher than 10^3 pN · nm [13]. A sudden change in the direction of rotation can be achieved by a conformational change in the rotor [15]. A prominent example can be found in *E. coli* bacteria, which swim by rotating a helical bundle consisting of several synchronized flagella in a corkscrew-like motion. Such multi-tailed bacteria can also change the swimming direction in a fascinating process called run-and-tumble as described by Howard Berg in 1973 [10].

In contrast, the eukaryotic flagellum consists of an arrangement of microtubule doublets, which is anchored via a basal body in the cell membrane of the microorganism. A prominent example is the sperm flagella [11]. Another difference can be found in the beating pattern of eukaryotic flagella. While the bacterial flagellum rotates, the eukaryotic flagellum performs a wave-like motion. This motion is driven by dynein motor proteins which cause sliding of the microtubules against one another resulting in a bending of the flagellum [16].

The cilium shown in Figure 1.1b is - neglecting length and function - according to the latest research believed to be structurally identical to the eukaryotic flagellum [17]. Distinctions are made between motile and non-motile cilia. While the non-motile or primary cilia serve as a sensory device, motile cilia beat jointly to move the surrounding liquid or achieve self-propulsion of the microscopic organism. Even though motile cilia and eukaryotic flagella are very similar in structure they differ significantly in their beating patterns. In contrast to the propeller-like or wave-like motion of the flagellum, the cilia beats forwards and backwards performing a power and recovery stroke [18].

These three motions performed by flagellated or ciliated microorganisms are fundamental swimming strategies of propulsion at the micron scale. To understand why swimming requires these special beating patterns, the hydrodynamics of viscous media must be taken into consideration.

Life at low Reynolds numbers

At the micro- and nanoscale, the physics behind motion are quite different from the one we are used to. For a human being, swimming in water relies on gaining a forward momentum by displacing the surrounding water and gliding for a moment. The motion is roughly reciprocal as after each glide the movement that led to the acceleration is reversed. For a microorganism, however, viscosity in the surrounding fluid becomes the dominant factor and the effect of inertia becomes negligible. As a consequence, there is no such thing as glide, leading to the effect that a periodic motion will undergo a loop in configuration space with no effective change of position, as first stated by E.M. Purcell in his Scallop Theorem [5]. In other words, a reciprocal motion will push the microorganism forward and backward by the same amount, which makes macroscopic swimming techniques ineffective. The Reynolds number (Re) is a quantity that describes whether the inertial forces or the viscous forces in a fluid dominate.

$$Re = \frac{U \cdot L}{\rho \cdot \eta} \quad (1.1)$$

Here, U and L are the velocity and characteristic length of the swimmer, ρ and η are the density and the viscosity of the fluid. At the scale of microorganisms, where viscous forces dominate over inertial forces, one therefore speaks of the low Reynolds number regime.

Bypassing the problem of reciprocal actuation at low Reynolds number requires breaking the time-reversibility of the propulsive motion. In order to produce a net displacement, biological propulsion mechanisms move in a non-reciprocal motion as described in the previous subchapter. The different propulsion mechanism can be categorized to be either oar- or corkscrew-like [5].

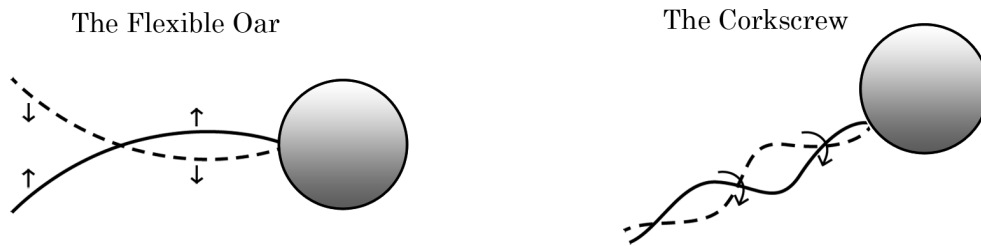


Figure 1.2: Propulsion mechanisms at Low Reynolds number. Schematic of two main strategies used by microorganisms to achieve propulsion at low Reynolds number: (a) the oar-like and (b) the corkscrew motion.

The oar-like motion is derived from the rowing of a boat, where a rigid oar is used to achieve propulsion. However, at low Reynolds number the rod has to be flexible in order to achieve propulsion. When a flexible rod is exposed to fluid drag, it will bend in different directions during the forward and backward stroke and thereby break the time-invariance of the motion [19] as illustrated in Figure 1.2a.

For the corkscrew-like motion the propulsion mechanisms requires either a rigid helical structure [20, 21] or a flexible rod that can bend into a helical shape during propulsion [22, 23]. The non-reciprocity of the motion is fulfilled when the helix rotates (Figure 1.2b), because the helix will never return to the same position in configuration space at any given time. A swimmer performing such a movement drives through its viscous environment like a corkscrew through the cork of a wine bottle.

1.2. Artificial micro- and nanoswimmers

Accompanying the advances in micro- and nanofabrication, many different synthetic strategies for the fabrication of micro- and nanoscale swimmers, which resemble the architecture and function of natural swimmers, have arisen over the last few decades. For example, glancing angle deposition [20, 24], rolled-up technique [25], direct laser

writing [21], template-assisted synthesis [26], as well as self-assembly [19, 27] have been used to construct artificial swimmers from different materials such as glass, metals and organic materials.

Swimmers constructed by these diverse methods have been proposed for potential applications in cargo transport [28-30], targeted drug delivery [31-33], biochemical sensing [34-36], cell trapping, manipulation and characterization [37, 38], as well as in minimally invasive procedures and biopsy [39].

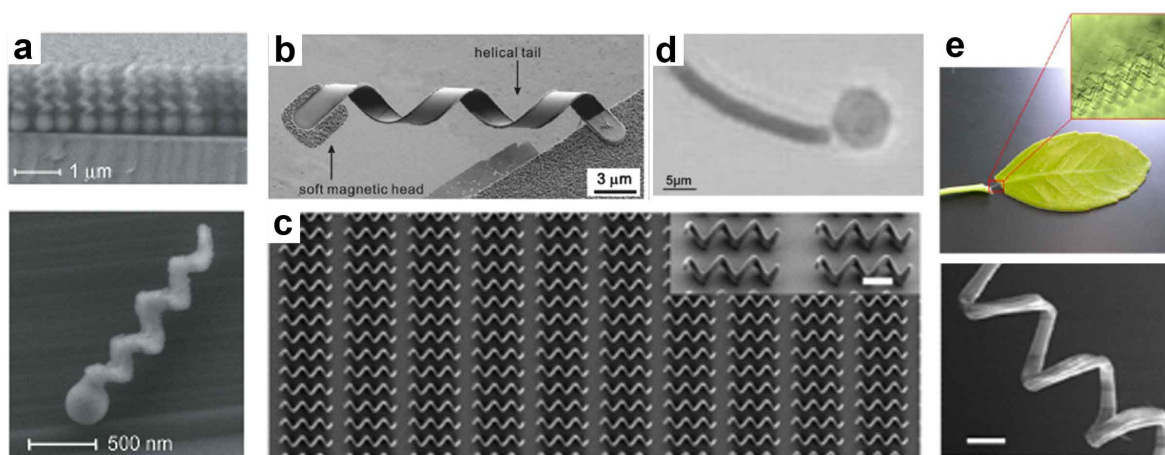


Figure 1.3: Artificial magnetic microswimmers. (a) Glass microswimmers formed by glancing angle deposition (GLAD). Reprinted by permission from ref. [20]. Copyright (2009) American Chemical Society. (b) Artificial bacterial flagella (ABF) fabricated by the rolled-up technique. Reprinted by permission from ref. [25]. Copyright (2009) American Chemical Society. (c) Helical swimmers constructed by 3-d direct laser writing. Scale bar: 10 μm . Reprinted by permission from John Wiley and Sons: *Advance Materials* ref. [21], copyright 2012. (d) Flexible oar-like swimmer self-assembled from magnetic microparticle. Reprinted by permission from Macmillan Publishers Ltd: *Nature* ref. [19], copyright 2005 (e) Assisted synthesis of helical swimmers using plant vessels as template. Scale bar: 50 μm . Reprinted by permission from ref. [26]. Copyright (2014) American Chemical Society.

For the actuation of the artificial swimmers diverse strategies were followed. Micro- and nanoscale structures driven by phoretic gradients [40-45], light [46], magnetic fields [19-21, 24, 25, 27] and even sound waves [47] were demonstrated. Within these approaches, however, two main mechanisms of actuation are standing out – phoretic swimmers, which swim by self-propulsion and exploit the phoretic properties of the surrounding fluid and magnetic swimmers which are driven by a deformation of their structure actuated by an external energy source.

Phoretic actuation requires an asymmetric decomposition of the swimmer's surface with a reactive chemical. The asymmetry then converts gradients of the reactant in the surrounding fluid into a hydrodynamic flow. The first phoretic swimmers was independently demonstrated in 2004 by Praxton et al. and Fournier-Bidoz et al., who were able to show that bimetallic micrometre-sized rods are propelled in hydrogen peroxide solutions [40, 41]. Since then, phoretic swimmers have been demonstrated to exploit electrophoretic [42], diffusiophoretic [43] and thermophoretic [44] gradients.

While this class of swimmer has shown impressive characteristics such as complex manoeuvres, payload capture and payload manipulation [45] their major disadvantage is that they greatly depend on the fuel supply in the surrounding fluid, which restricts their use to very unique environments.

In contrast, magnetically actuated swimmers are to a great extent independent of the medium they swim in, as their actuation is provided by an external energy source. They are usually constructed from magnetic materials or are functionalized with such. An external magnetic field provides the motion and spatial control over this class of swimmer. A prominent example of a magnetically actuated microswimmer was proposed by Dreyfus et al. in 2005 who used a self-assembled chain of magnetic beads to form a flexible magnetic flagella-like tail and demonstrated the first controlled swimming motion of magnetically actuated microswimmers [19]. In 2016, we demonstrated that similar to peritrichous bacteria, magnetic microswimmers can be propelled by a bundle of artificial flagella (see Associated Publication P2) [27]. Recently, magnetically driven swimmers have even been reduced in size down to the nanoscale [24]. In this regime, Brownian motion increasingly dominates the motion of such small particles and makes maintaining a directed motion difficult.

In technical and medical applications, micro- and nanoswimmers are envisioned to perform various tasks ranging from health care, lab-on-a-chip to environmental science [38, 48]. They are foreseen to move through body fluids delivering medicine to tumour sites, to drill open blocked arteries in order to prevent heart attacks or to remove toxic materials in water streams. For biomedical applications, magnetic microswimmers are especially suitable as they can be actuated from afar, which makes their propulsion mechanism biocompatible.

Another field, where artificial swimmers may contribute to, is the study of collective behaviour or “swarming”. This phenomenon has been observed in many biological systems, such as flocks of birds or fish swarms, where the entities move in high densities. Artificial swimmers could provide a well-controlled model system to study this behaviour at small scales providing insights into non-equilibrium physics at low Reynolds numbers [49].

For the manufacture of micro- and nanoswimmers two fundamental different strategies can be applied. So far, most swimmers have been built by the well-established top-down approach, where large technical equipment is used to cut larger materials into the desired micro- or nanoshape. Although, this approach is commonly used to construct micro- and nanoscale objects, it has disadvantages in terms of parallelization and usually requires expensive technical equipment.

The bottom-up approach, on the other hand, uses single atoms, larger molecules or nanoscale components as building blocks, which self-assemble into the desired nanostructure. This allows cost-effective and simultaneous construction of billions of structures in a simple one-pot reaction.

Within the different molecular self-assembly techniques, DNA has proven to be a reliable and versatile building block [50], with its synthesis becoming more and more cost efficient every year [51].

1.3. Structural DNA nanotechnology

Despite its important function as the carrier of genetic information, DNA nowadays also plays an important role in structural nanotechnology. The Watson-Crick base pairing [52], which allows hybridization between DNA strands to be highly selective and the ability to form connections between strands through holiday junctions have made DNA a promising nanoscale building block.

DNA tile assembly

In 1982, Nadrian Seeman proposed that DNA could be used to construct materials with nanometre-sized addressability and complex nanoscale shapes that could serve as frameworks for protein crystallization [53]. Since then his visionary idea started to arouse increasing interest in biophysicist and biochemists alike. In order to realize such structures, he used branched DNA architectures, which consisted of multiple DNA crossover junctions, commonly known as DX tiles [54, 55] (Figure 1.4a), which he later assembled into large crystal structures [56]. The DX (double crossover) tiles consist of two helical domains connected by two crossover junctions. Modifications in the DX design, such as hairpin loops and sticky ends later allowed assembling proteins and nanoparticles on large tile lattices [57, 58].

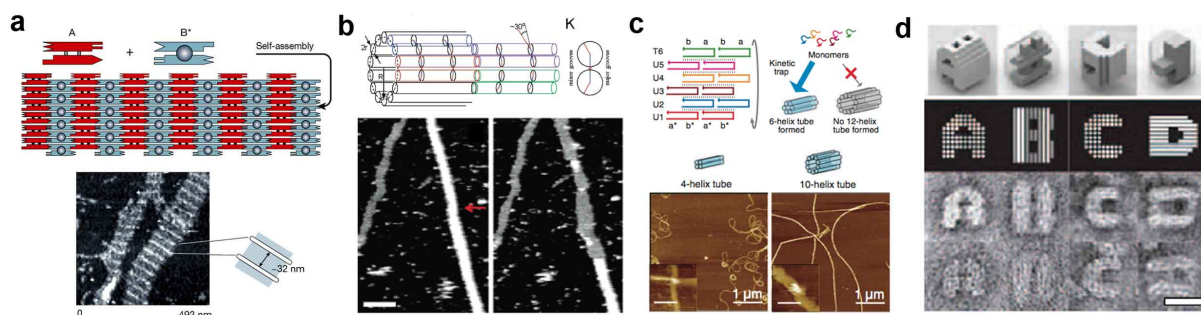


Figure 1.4: DNA tile assembly. (a) DX (double crossover) tiles and the slightly modified DX+J tiles forming 2D DNA lattices. Reprinted by permission from Macmillan Publishers Ltd: Nature ref. [63], copyright 2003. (b) DX tile-assembled tubes with varying diameters. Scale bar: 100 nm. Reprinted by permission from ref. [59]. Copyright (2004) American Chemical Society. (c) Tile-assembled tubes with controlled circumferences formed from half-crossover tiles. Reprinted by permission from AAAS: Science ref. [61], copyright 2009. (d) Complex 3D structures designed by half-crossover tiles. Scale bar: 20 nm. Reprinted by permission from AAAS: Science ref. [62], copyright 2012.

In 2004, Rothmund et al. presented the first tube structure assembled from such DX tiles [59] (Figure 1.4b). His tubes assembled in a simple one-pot reaction from only a handful of tiles and grew as long as 50 μm in length, however, they had the disadvantage that their circumference could not be controlled. Although, initiating the tube growth from a seed later solved this problem, the formation of tubes with defined circumference

still remained tedious [60]. In 2008, Yin et al. solved this problem by presenting a new design based on half crossover tiles, which allowed the construction of tubes with defined circumference [61] (Figure 1.4c). In 2012, the same group demonstrated that a similar tile-based “Lego brick” design allowed them to construct complex 3D shapes [62] (Figure 1.4d).

DNA origami

In 2006, Paul Rothemund published a novel DNA-based self-assembly technique, DNA Origami, that drastically increased the complexity in geometrical shape and size of DNA nanostructures [64]. In contrast to DNA tile assembly, DNA origami does not require a tight stoichiometric control over the DNA strands. It relies on the folding of a several thousands bases long DNA “scaffold” strand extracted from M13 bacteriophage genome by hundreds of short “staple” strands. Each staple is designed to be complementary to distinct parts in the scaffold and thereby staples the scaffold strand into the desired shape. While first DNA origami constructs were two-dimensional, by 2009 three-dimensional shapes were realized [65]. In the same year, Dietz et al. introduced discrete amounts of bending and twisting into the DNA constructs, which allowed constructing twisted and curved DNA origami [66]. The progress was strongly supported by the introduction of the computer program “caDNAno”, which helped to design new DNA origami structures with less errors and in less time [67].

Similar to the DNA tile assembly, hairpin loops can be introduced on the structure, allowing the creation of patterns on the DNA origami surface [64]. Furthermore, by chemically modifying staple strands in the origami design, functionalization of the structures with nanocomponents is possible, which is of great importance for DNA origami structures to be applied in practical applications. For example, chiral plasmonic nanostructures consisting of a DNA origami template and gold nanoparticles were shown to exhibit a designed optical response [68]. Such hybrid materials have also been demonstrated for proteins [69] and other metals, such as silver [70]. Of special interest for the work presented here is the attachment of magnetic particles to DNA nanostructures. Such constructs have been presented by Kauert et al., who demonstrated that magnetic microparticles can be attached to DNA origami constructs via a streptavidin-biotin connection [71].

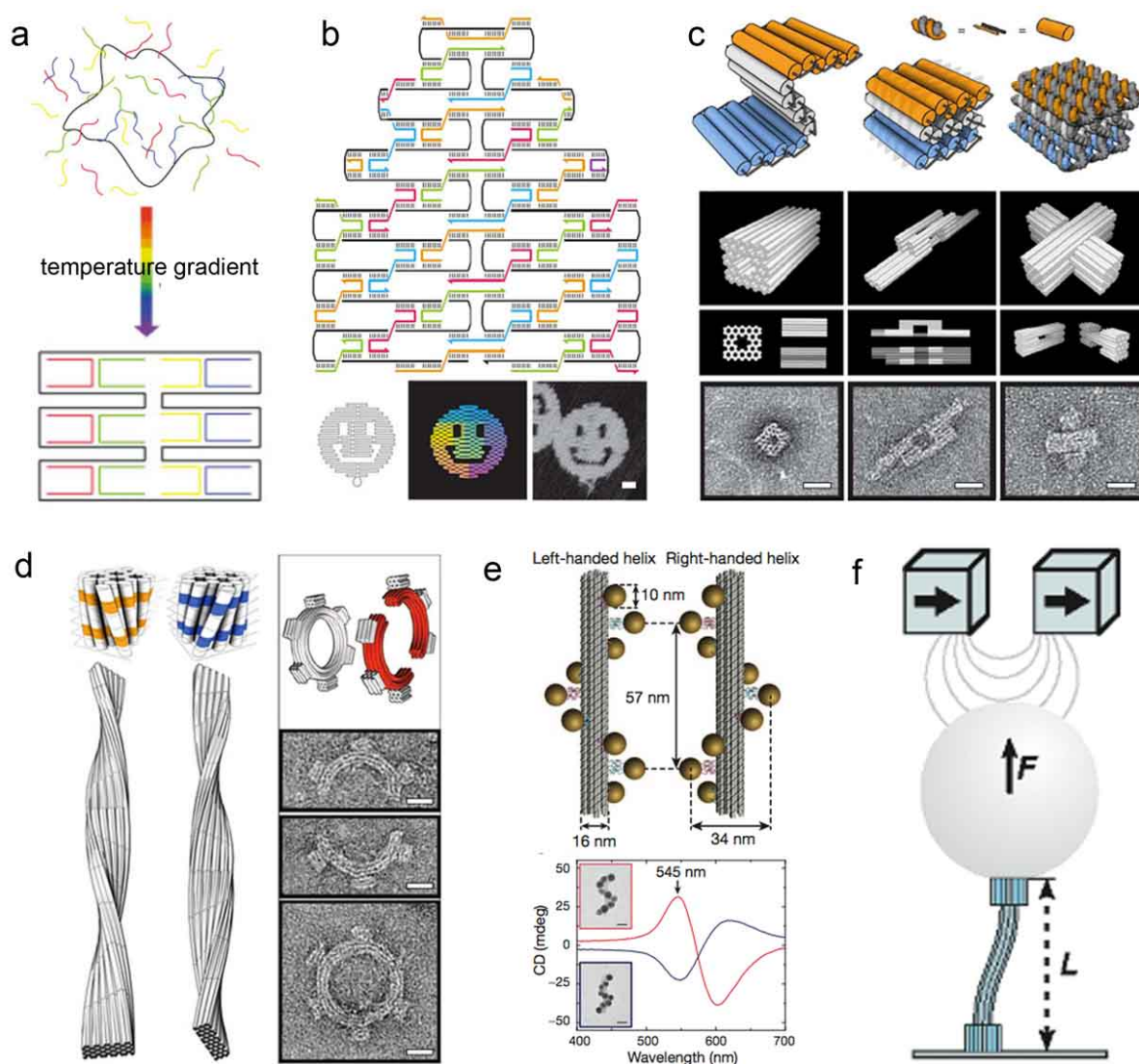


Figure 1.5: DNA origami. (a) DNA origami constructs are formed by a long DNA scaffold strand and by hundreds of short staple strands through thermal annealing. (b) One of the first origami structures resembling a smiley face. Reprinted by permission from Macmillan Publishers Ltd: Nature ref. [64], copyright 2006. (c) 3-dimensional origami constructs with arbitrary shape. Reprinted by permission from Macmillan Publishers Ltd: Nature ref. [65], copyright 2009. (d) DNA origami with curved and twisted shape. Reprinted by permission from AAAS: Science ref. [66], copyright 2009. (e) Gold nanoparticle functionalized DNA origami constructs as plasmonically active structures. Reprinted by permission from Macmillan Publishers Ltd: Nature ref. [68], copyright 2012. (f) Magnetic microsphere functionalized DNA origami for determining the rigidity of the DNA bundles. Reprinted by permission from ref. [71]. Copyright (2011) American Chemical Society. Scale bars: 20 nm.

Combining the properties of magnetic micro- and nanoparticles with the advantages of DNA self-assembly techniques has so far received little attention by the DNA nanotechnology community. In this dissertation we will illustrate how artificial filaments constructed solely from DNA can serve as biocompatible artificial flagella. When attached to magnetic micro- and nanoparticles, these structures yield a new class of biocompatible artificial micro- and nanoswimmer, which is strongly desired for future technical and biomedical applications.

2. Self-Assembled DNA Tubes forming Helices of Controlled Diameter and Chirality

Helical shapes can be found throughout all structural levels of biological materials. The most prominent example is DNA, which consists of two intertwined helical chains [52], but also many other structures like cellulose fibrils [72], the shell of holoplanktonic mollusks [73] or the filament of bacterial flagella [13] show helical assemblies. The helical shape of these structures results from an intrinsic chirality in the geometry of their building blocks [74], where a lack of mirror symmetry frustrates an otherwise straight 2D assembly. Examples of such chiral building blocks are nucleotide bases in DNA duplexes and filamentous proteins in bacterial flagella or rod-like viruses [75]. In higher-ordered biological materials, such as wood, bone, tendon, ligament, hoof and horn [76], helical structures are often incorporated in order to provide high mechanical stability and flexibility. For example, in wood and bones they serve as reinforcement elements, providing these materials with a high damage tolerance [77].

These outstanding properties have served mankind as a source of inspiration for the design and construction of macroscopic helical tools. For example, springs and screws have become integral components of classical mechanical engineering in the macroscopic world. Here, helical springs have been applied to store and release mechanical energy, thereby absorbing shocks or maintaining a force between two surfaces. Helical screws have been used to convert rotation into linear motion, making it possible to accurately position and fasten objects. Nevertheless, a fully exploitation of the outstanding properties of helical structures as found in its natural counterparts, requires miniaturization to the micro- and nanoscale.

2.1 Artificial micro- and nanohelices

In the last decades, many advances have been made in producing artificial micro- and nanohelices by top-down fabrication methods, in which larger material is shaped into the desired micro- or nanostructure. For example, induced self-scrolling [78-80], glancing angle deposition [20, 81-83] of evaporated or sputtered materials, and 3D direct laser writing [21, 84] in photoresists, have been applied. Within these approaches, micro- and nanohelices were produced from diverse materials, such as alloy, glass or plastic with lengths and diameters ranging from many micrometers down to the nanometre scale [24].

Within bottom-up approaches, vapour phase deposition has taken a leading role in the construction of micro- and nanohelices. Especially carbon nanotubes (CNTs) and carbon nanowires (CNWs) of helical shape were formed by this method. Typical diameters and lengths of these structures are 50–1000 nm and 0.3–3 μm , respectively [79, 85, 86].

Both, bottom-up and top-down fabricated artificial micro- and nanohelices were shown to possess extraordinary mechanical properties, which closely resemble their

natural counterparts. For example, helices with super-elasticity [80, 85, 87] and high mechanical strength [88] could be constructed. These properties make them promising candidates for the construction of shape memory materials [80, 87] and composites with improved mechanical integrity [89] as well as potential building blocks in mechanical micro- and nanosprings [79], biomedical sensor devices [90], and photoelectronic devices [76]. Furthermore, micro- and nanoscrews were recently shown to function as propulsion mechanisms for artificial micro- and nanoswimmers [20, 24, 26, 27, 33, 91]. Such devices are foreseen to deliver drugs or remove blood clots in future biomedical devices [2, 48, 92].

Although, many advances have been made over the last years, large-scale production of 3D micro- and nanostructures with controllable shape is still challenging for the above-described methods. Moreover, most of the employed materials are not biocompatible, which is a mandatory criterion for a potential realization in biomedical applications. In order to achieve all the requirements in one system, one would need an easy-to-adjust, biocompatible and chiral building block, which can be self-assembled into larger objects.

Bottom-up DNA self-assembly offers such subunits, which consist solely of biocompatible DNA and can be shaped into structures of designed curvature and twist. This was first demonstrated for DNA origami constructs by Dietz et al. in 2009 [66]. The closely related DNA tile tube assembly, however, shows a similar if not better suitability for the construction of artificial helices with defined micro- and nanoscale diameter as will be shown in the subsequent chapters.

Tile tubes assemble in a simple one-pot reaction from only a handful of oligonucleotides referred to as tiles by forming a short building block, which self-polymerizes into micrometre long structures. In the 2008 presented self-assembly scheme by Yin et al. [61], single-stranded DNA oligonucleotides formed short tube segments of ~ 7 nm in lengths, which self-polymerized into micrometre long tubes of controlled circumference. In the design, each oligonucleotide exhibits four sequence domains by which it can bind to adjacent tiles via the hybridization of complementary DNA strands (Figure 2.1). The circumference of the tubes can be adjusted via the number of tiles within a tube, with n tiles assembling into a n -helix tile tube. Depending on whether n is even or odd the tubes close with no (Figure 2.1a) or with a discrete amount of offset (Figure 2.1b). Therefore, tubes with odd number of helices exhibit a certain amount of twist along their longitudinal axis, while tubes with even number of helices are straight. The offset-based tube distortion is called *supertwist* and was previously studied in detail by Schiffels et al. [93].

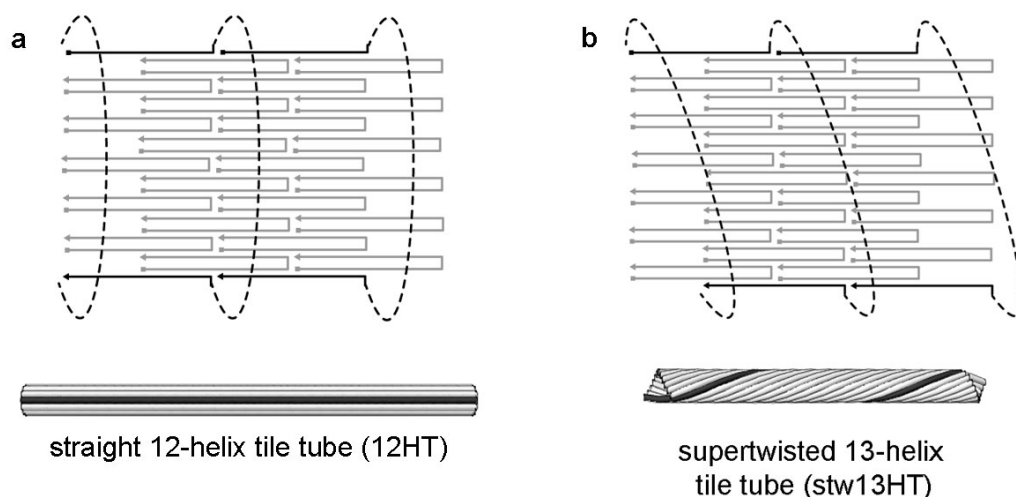


Figure 2.1: Design of tile-assembled tubes. (a) An even number of DNA tiles folds into straight tubes as exemplarily illustrated for the 12-helix tile tube. (b) In contrast, an odd number of tiles has to overcome an offset in order to close. This offset leads to a so-called supertwist in the tube's structure as illustrated for the 13-helix tile tube. Reprinted by permission from ref. [94]. Copyright (2017) American Chemical Society.

In Publication P1, we introduced new design rules that allowed us to construct helically shaped DNA tile tubes with defined helical diameters and chirality. We gained these design rules by systematically testing the relationship between the helical shape of the assembled tube and i) the number and relative position of inserted or deleted base pairs, ii) the relative position of tiles within the tube segment, and iii) the arrangement of Cy3 modifications on the tube. In what follows, we present a short summary of the published work accompanied by a detailed description of the follow-up research on helically shaped DNA tile tubes. Publication P1 is provided in chapter 6.1.

2.2 Controlling the nanoscale helical shape of DNA tile tubes through base pair insertions and/or deletions

From previous work on DNA origami, it is known that base pair insertions or deletions can generate nanoscale bending and twisting in DNA constructs [66]. The same idea has been recently used on DNA tile tubes to construct DNA nanorings [95]. For the realization of tile tubes with nanoscale helical shape, we build upon these studies and focused on tubes with even number of helices n . These tubes are naturally straight and therefore constitute a perfect platform to test the effect of base pair insertions and deletions on their shape. We systematically inserted and deleted base pairs in distinct helices of tile tubes with different sizes and analysed the helical shape as demonstrated for base pair insertions in Figure 2.2.

We found that formerly straight DNA tile tubes formed helical shapes after the insertion or deletion of base pairs within distinct positions of the tube's structure. Because the diameter of the structures was below the resolution limit of light

microscopy, we could not resolve the helical 3D shape in solution. We therefore applied transmission electron microscopy, which resolved the tubes structure with nanometre precision as illustrated for an 8-helix tile tube with one insertion in Figure 2.2a. The downside of this technique however was that prior to TEM imaging samples had to undergo a preparation process, which resulted in a 2D confinement of the tube structure. This confinement made it impossible to directly determine the helical diameter and pitch from the confined shape. In order to gain a measure of the impact of insertions and deletions on the helical shape of the tubes, we extracted and analysed the radius of curvature r_c in place of the diameter and pitch. R_c is related to the tube's diameter D and pitch P via

$$r_c = \frac{D}{2} + \frac{P^2}{2\pi^2 D} \quad (2.1)$$

According to a theoretical study on 2D confined filaments, the curvature of a confined helical structure stays virtually unaffected between two curvature inversion points along the tube's contour [96] and can therefore be reliably extracted from TEM images.

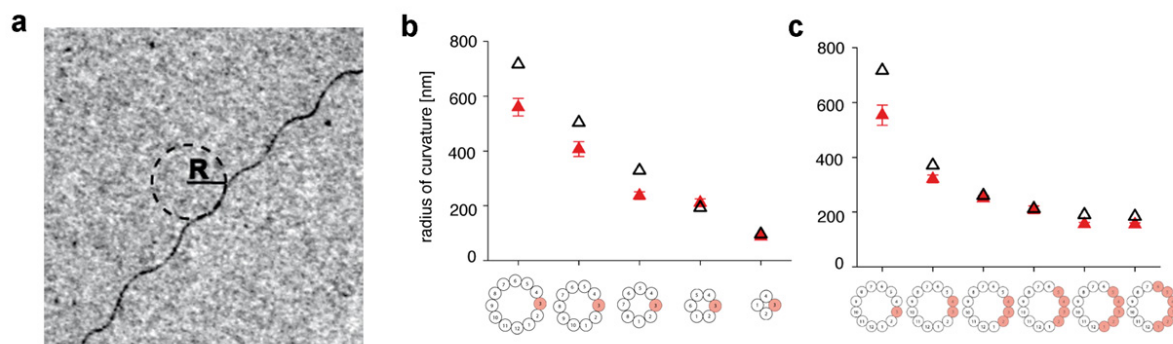


Figure 2.2: DNA tile tubes with nanoscale helical shape. (a) The insertion of an additional base pair into the repetitive segment of a tile tube resulted in a helical shape of the overall structure as exemplarily illustrated for an 8HT by TEM. From this shape, we extracted the radius of curvature r_c . (b) We observed a steady decrease of r_c in tubes with decreasing tube size. (c) In tubes of equal size, we observed a decrease of r_c with increasing number of insertions. Reprinted by permission from ref. [94]. Copyright (2017) American Chemical Society.

We found that r_c steadily decreased for decreasing tube sizes in tubes with one insertion or deletion per tube segment as exemplarily illustrated for 12- to 4-helix tubes with one insertion in Figure 2.2b. Within tubes of a given number of helices, several insertions or deletions resulted in decreasing values of r_c as exemplarily demonstrated for 12-helix tubes with 1 to 6 insertions in Figure 2.2c (see chapter 6.1 for additional analysis of tubes with only deletions and for tubes with both insertions and deletions). These observations suggest that the amount of bending exerted by base pair insertions and/or deletions is distributed over the whole DNA tube structure and increases stepwise. The presented approach therefore constitutes an excellent technique for the controlled

construction of helically shaped nanotubes.

We continued our study by comparing our measured values of r_c to theoretical predictions from a DNA toy model published by Dietz et al. [66]. We found that the model only slightly overestimated the measured data. The predicted values for each tube are illustrated as black triangles in Figure 2.2b and 2.2c. The biggest deviation between model and experiment was found for tubes with only one insertion (see first data point in Figure 2.2c) or one deletion (see chapter 6.1). We believe that nicks and crossovers in the tube's structure absorbed some of the bending induced by insertions or deletions. This "buffering" effect was most present in tubes with few insertions and deletions, because it had to be overcome only once. In the model, however, a perfect double stranded DNA was assumed which did not account for this effect.

In order to achieve even smaller r_c , we installed combinations of insertions and deletions within the same tube type. Surprisingly, we found that tubes with the same number of insertions and deletions on opposite sides of the tube's cross section mainly formed helical structures instead of rings, as one would expect for symmetry reasons (see chapter 6.1). These observations also contradicted with recently published material on DNA nanoring formation, where a similar arrangement of insertions and deletions led to the assembly of rings [95]. We believe that in our tile tube design the amount of twist exerted by insertions differed from that exerted by deletions.

In order to understand the origin of this discrepancy, we took a closer look at the relative position of insertions and deletions within the tile tube design. In a DNA tile tube, each double helix is connected to two neighbouring helices via DNA crossovers. In the absence of insertions or deletions, crossovers to the same neighbouring helix repeat every 21bp corresponding to two full helical turns of the DNA double helix. The distance between crossovers to different neighbouring helices however alternates between 10bp and 11bp as illustrated in Figure 2.3. Because an insertion or deletion of a base pair primarily exerts stress on the nearest crossover points, we believe that it makes a difference whether the modification is installed in the 10bp or the 11bp region. In the former case, an insertion should push the neighbouring helices via the cross over points towards a larger interhelical angle (Figure 2.3a), while a deletion should pull them towards a smaller angle (Figure 2.3b). For the latter case, the opposite situation should apply, with insertions pulling (Figure 2.3c) and deletions pushing (Figure 3d). Note that this behaviour is induced by the helicity of the DNA double strand and its cross over, which transfers the induced stress and strain to the neighbouring helices in opposite directions if produced in the 10bp or the 11bp region (see arrows in Figure 2.3).

We speculate that this pushing or pulling generates a deformation of the tube cross section from a circular into an elliptical shape as illustrated in Figure 2.3a to Figure 2.3d, respectively. This deformation then alters the distance between the insertion or deletion and the bending axis (dashed line in Figure 2.3) and thereby affects the amount of bending exerted by the insertion or deletion. Following this hypothesis, an insertion or deletion, which reduces the distance to the tube's bending axis, should give rise to a stronger bending and therefore smaller r_c and vice versa.

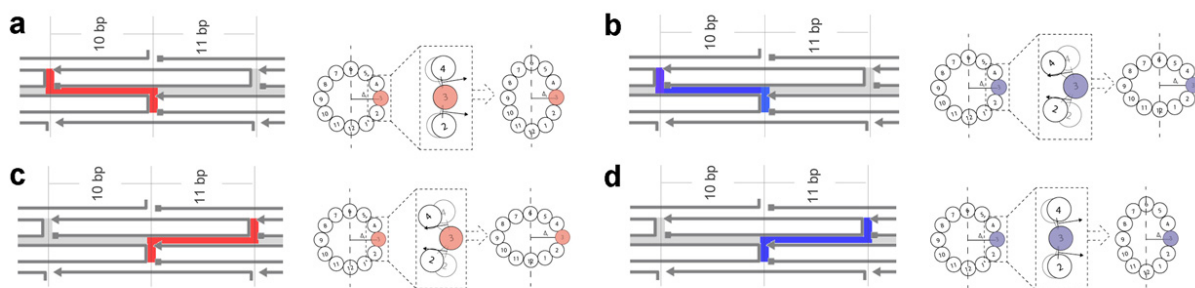


Figure 2.3: Dependence of the position of base pair insertions and deletions on the tube's cross sectional geometry. (a) Insertion (red) and (b) deletion (blue) installed in the 10bp region of a double helix segment within the tile tube's repetitive architecture. (c) Insertion (red) and (d) deletion (blue) installed in the 11bp region. Depending on the position, the insertion or deletion either pushes or pulls on its neighbouring helices via the nearby cross over points. We speculate that this pushing and pulling leads to a deformation of the tube's cross sectional shape, which again affects the amount of bending exerted by the respective insertion or deletion.

We tested this hypothesis by comparing r_c of 12- to 4-helix tile tubes with insertions in the 10bp region to 12- to 4-helix tile tubes with insertions in the 11bp region (Figure 4a). Interestingly, r_c was always smaller for tubes with insertions in the 10bp region (filled red triangles) than for tubes with insertions in the 11bp region (empty red triangles). The opposite trend was observed by comparing 12- to 4-helix tubes with deletions in the 10bp to the respective tubes with deletions in the 11bp regime (Figure 4b). Here, r_c was always larger for tubes with deletions in the 10bp region (empty blue triangles) than for tubes with deletions in the 11bp region (filled blue triangles). These observations suggest that the amount of bending present in helical tile tubes with base pair insertions or deletions indeed depends on the position of the insertion or deletion and follows the above-proposed mechanism.

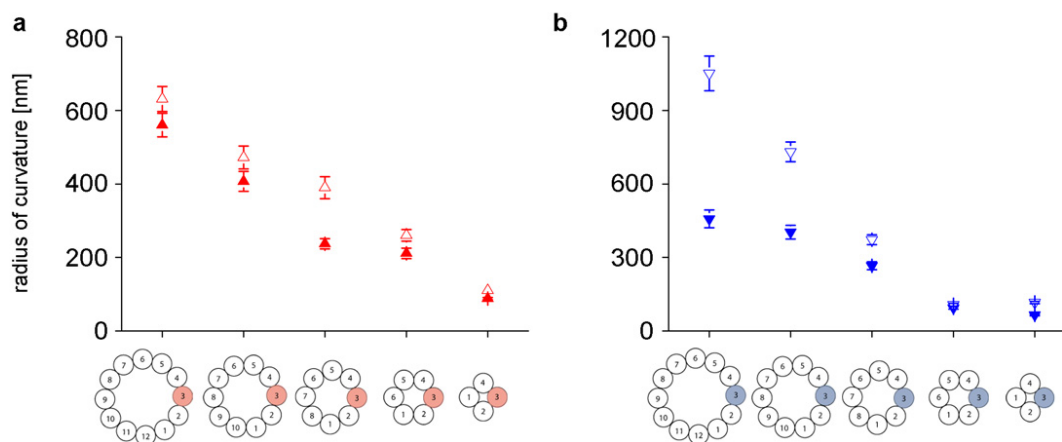


Figure 2.4: Dependence of the position of base pair insertions and deletions on the radius of curvature. We observed that the radius of curvature r_c is (a) continuously smaller for tubes with insertions in the 10bp region (filled red triangles) than for tubes with insertions

in the 11bp region (empty red triangles) and (b) continuously larger for tubes with deletions in the 10bp region (empty blue triangles) than for tubes with deletions in the 11bp region (filled blue triangles). Reprinted by permission from ref. [94]. Copyright (2017) American Chemical Society.

In order to find out whether this position-dependent bending might indeed result from a deformation of the tube's cross section, we compared our measured values to predictions from the DNA toy model assuming an elliptical tube shape instead of a spherical shape. In the supporting information of Publication P1, we presented first indications for 12-helix tile tubes with insertions installed in the 10bp region, which support this assumption. There, energetic predictions of r_c were better in line with the measured data if an elliptical shape of $r^2 = a^2 + b^2$ with $a < b$ was assumed (see Appendix A). Note that a is defined as the minor axis of the ellipse and equals the minimum distance from the tube's bending axis (as illustrated in Figure 2.3a).

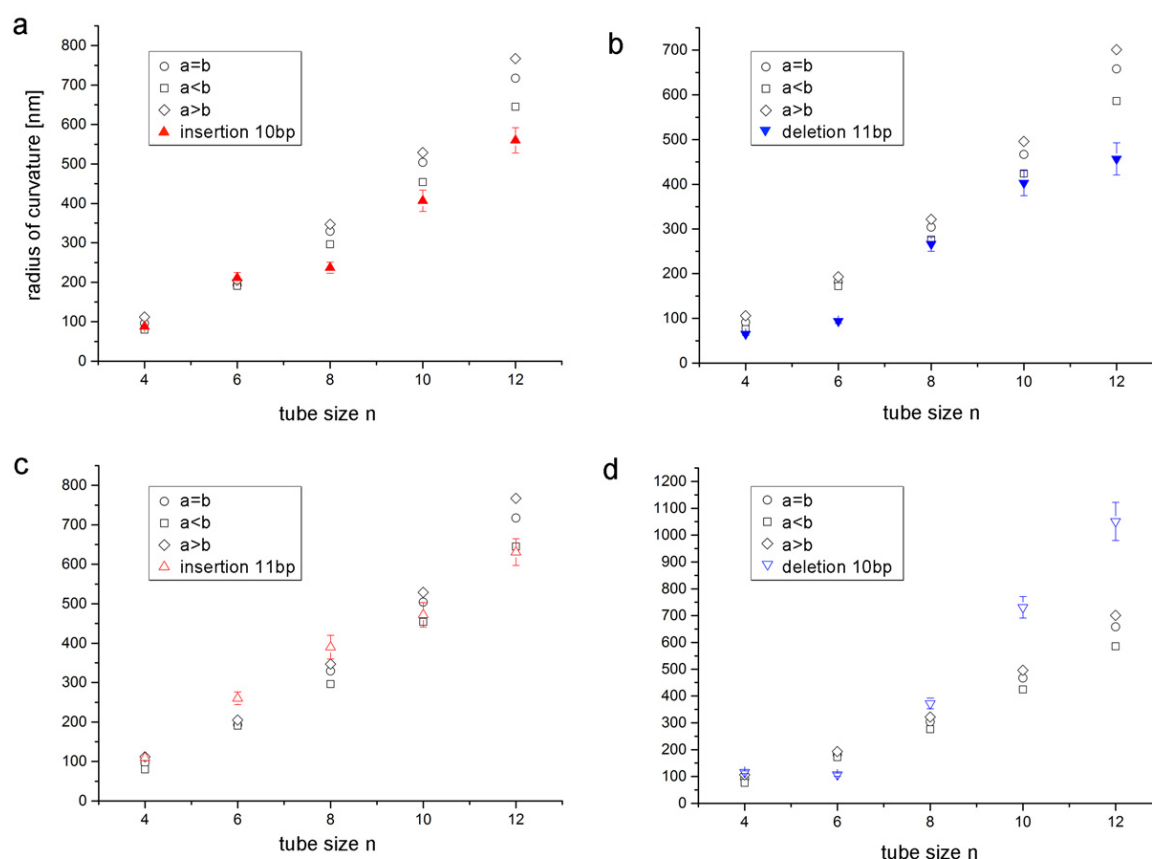


Figure 2.5: Comparison of predicted and measured radius of curvature in tubes with position-dependent base pair insertions or deletions. Energetic predictions (grey symbols) of 12- to 4- helix tile tubes with (a) insertions in the 10 bp region and (b) deletions in the 11bp region are closer to the experiment (filled triangles) if an elliptical shape with $a < b$ (empty grey square) is assumed. (c) For insertions in the 11 bp region, no such clear tendency was found. (d) For deletions in the 10bp region an elliptical shape with $a > b$ (empty grey diamond) is closer to the measured values. Note, however, that especially for larger tubes, the measured data deviated strongly from the predictions.

To substantiate these observations, in Figure 2.5, we applied the energetic model to all four possible combinations of 12- to 4- helix tile tubes with insertions or deletions in the 10bp or the 11bp regime. We expected that tubes with insertions in the 10 bp region or with deletions in the 11bp region favour an elliptical shape with $a < b$ similar to what we observed in Publication P1. Indeed, we observed that for insertions in the 10bp (Figure 2.5a) and for deletions in the 11bp region (Figure 2.5b), predictions with $a < b$ resembled the measured data better than an ellipse with $a > b$ or a circular shape with same circumference ($a = b$). Note that for $a > b$, a is defined as the major axis of the ellipse and equals the maximum distance from the tube's bending axis.

For the case of insertions in the 11bp region and deletions in the 10bp region (Figure 2.5d), we expected a better match for an elliptical shape with $a > b$. Here, however, no clear tendency could be observed. For insertions in the 11bp region (Figure 2.5c), the measured data of the 4-, 6- and 8-helix tube coincided slightly better with predictions for $a > b$, and with $a < b$ for the 10- and 12-helix tube. For the case of deletions in the 10bp region, predictions and measured data were indeed best for $a > b$, however the data deviated strongly especially for larger tube sizes. These observations suggest, that apart from the buffering effect and the elliptical tube deformation other factors also influenced the bending of the DNA tile tubes. In the future, additional studies are required to obtain a more detailed picture of the insertion- and deletion-induced bending in helical DNA tile tubes.

So far we only considered how tube bending, which is directly reflected in the radius of curvature, depends on the position of base pair insertions and deletions. In order to test whether the tube twist is also affected by the position of the insertions or deletions, we constructed four 6-helix tile tubes with equal numbers of insertions and deletions placed at different positions in opposing helices of the tube's cross section (Figure 2.6). From geometrical reasons, we expected that the right-handed twist induced by the insertions cancels out the left-handed twist induced by the deletions. In contrast to the twist, the bending contributions of insertions and deletions on opposing helices, however, add up [66, 95]. Therefore, the tube should ideally only bend and not twist and form a ring structure. We tested the four arrangements of 6HTs with i) insertions and deletions in the 10bp region, ii) insertions and deletions in the 11bp region, iii) insertions in the 11bp and deletions in the 10bp, and iv) insertions in the 10bp and deletions in the 11bp.

Figure 2.6 shows TEM images of all four arrangements. Surprisingly, the 6HT with insertions in the 10bp and deletions in the 11bp region (Figure 6d) preferentially formed helical structures, while the other arrangements (Figure 6a-c) preferentially formed rings. This maintenance of an overall twist in Figure 6d suggests that, similar to the amount of bending, the strength of the twist depends on the position of the installed insertions and/or deletions and may differ substantially for different arrangements.

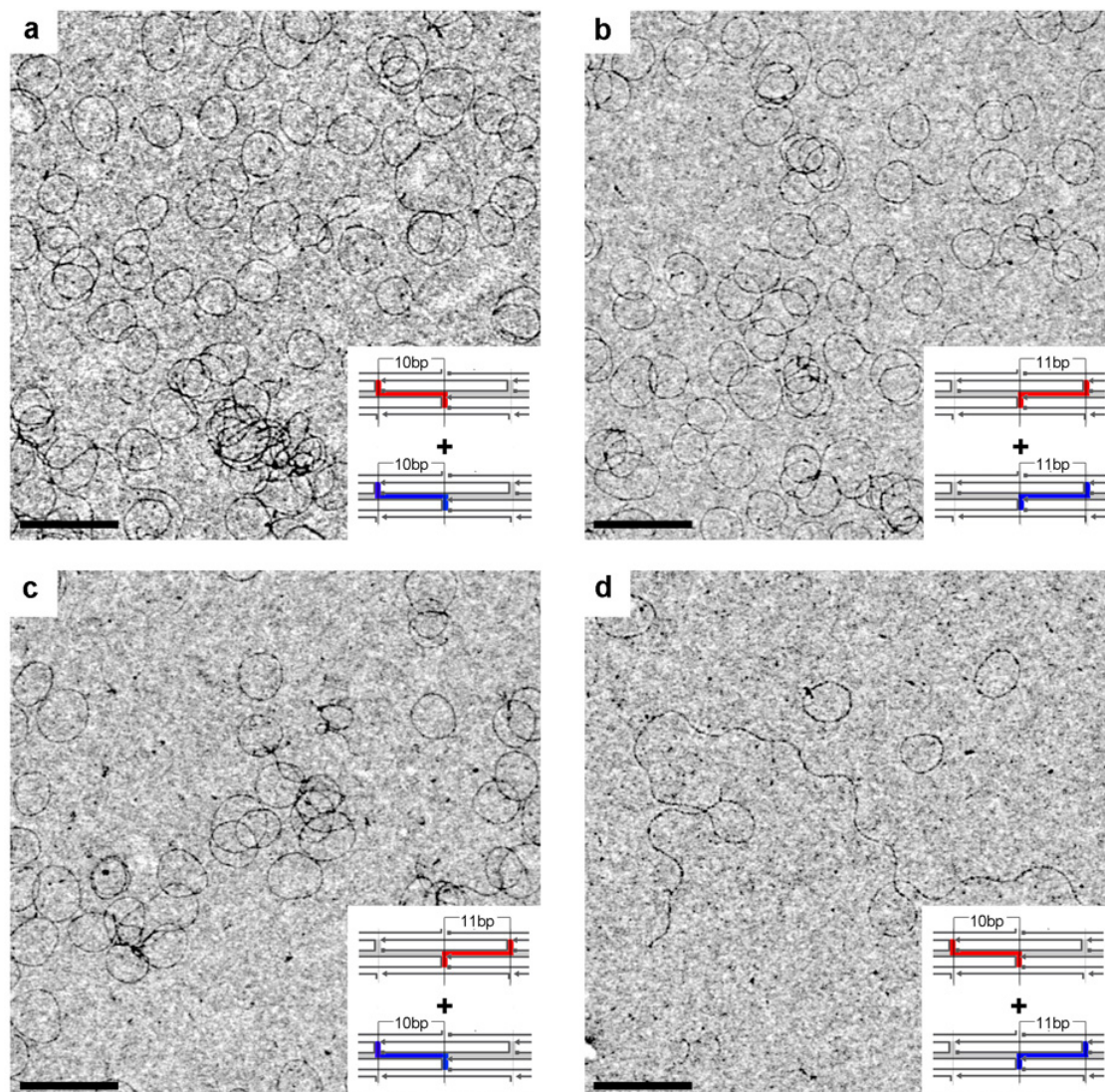


Figure 2.6: 6-helix tile tubes with position-dependent base pair insertions and deletions. 6HT with (a) insertions and deletions in the 10bp region, (b) insertions and deletions in the 11bp region, (c) insertions in the 11bp region and deletions in the 10bp region and (d) insertions in the 10bp region and deletions in the 11bp region. Scale bars: 500nm.

2.3 Controlling the microscale helical shape and chirality of DNA tile tubes through *tile shifting*

In the second part of Publication P1 (see chapter 6.1), we focused on constructing tubes with controlled microscale helical diameter and chirality. This requires smaller amounts of bending and twisting than those arising from single base pair insertions or deletions.

To achieve small quantities of twist, we focused on the reduction of the *supertwist* present in tile tubes with odd number of helices [93]. The *supertwist* results from a discrete offset that an open tube with odd number of helices has to overcome in order to close. Therefore, if the offset is reduced, the *supertwist* of the tube also becomes smaller.

We implemented this reduction of the offset in a process referred to as *tile shifting*, in which single tiles within the tube structure were shifted one nucleotide (nt) position at a time (Figure 2.7).

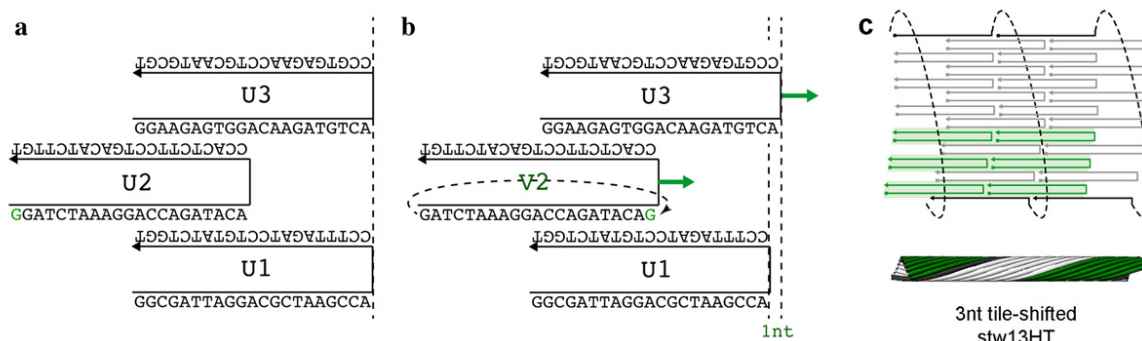


Figure 2.7: Schematic of tile shifting. (a) Three tiles and their respective sequences within the original tile tube design. (b) A 1nt tile shift (shifted nucleotide is highlighted in green) results in a shift of the whole tile and all following tiles (green arrows) by one nucleotide. As a result the offset of closure also changes by 1nt. (c) Schematic of the reduction of supertwist in a 13-helix tile tube by tile-shifting three tiles 1nt at a time (highlighted in green). Reprinted by permission from ref. [94]. Copyright (2017) American Chemical Society.

Figure 2.7a exemplarily demonstrates the nucleotide sequences of three tiles within the original tile tube design. If a tile is shifted by 1 nt (as illustrated in Figure 2.7b), all following tiles also shift by 1 nt, which in turn leads to a 1 nt shift of the offset of closure. Figure 2.7c exemplarily illustrates a 13-helix tile tube with three 1nt tile shifts (highlighted in green). Compared to a 13HT without tile shift, here the offset of closure is reduced by 3 nt. In Publication P1, we presented tile tubes with tile shifts of up to 7 nt (see chapter 6.1). This stepwise reduction of the offset of closure provided us with a fine-control over the amount of twist in the tube structure.

In order to achieve small amounts of bending, we modified tile tubes with Cy3 dyes. Cy3 modifications, which are installed close to a DNA duplex nick, are known to act similar to base pair insertions and introduce a certain amount of bending and twisting to the tube structure [97, 98]. In Publication P1, we observed that Cy3-induced bending and twisting is substantially lower than that exerted by base pair insertions and resulted in microscale tube diameters (see chapter 6.1). Such modifications are therefore promising for the construction of tubes with small and defined quantities of bending.

By combining both techniques, the *supertwist* fine-control and the Cy3-induced bending, we were able to construct helical tile tubes with controllable microscale diameter and chirality. In Figure 2.8, examples of Cy3-modified tile-shifted 11HTs (Figure 2.8a), 13HTs (Figure 2.8b) and 15HTs (Figure 2.8c) with microscale diameters are shown. The chirality of the tube was determined via fluorescence microscopy by taking “tomographic slices” of the structure. This technique also allowed us to reconstruct the 3D shape of the structure as illustrated for 13HTs with 2 nt tile shift in Figure 2.8d.

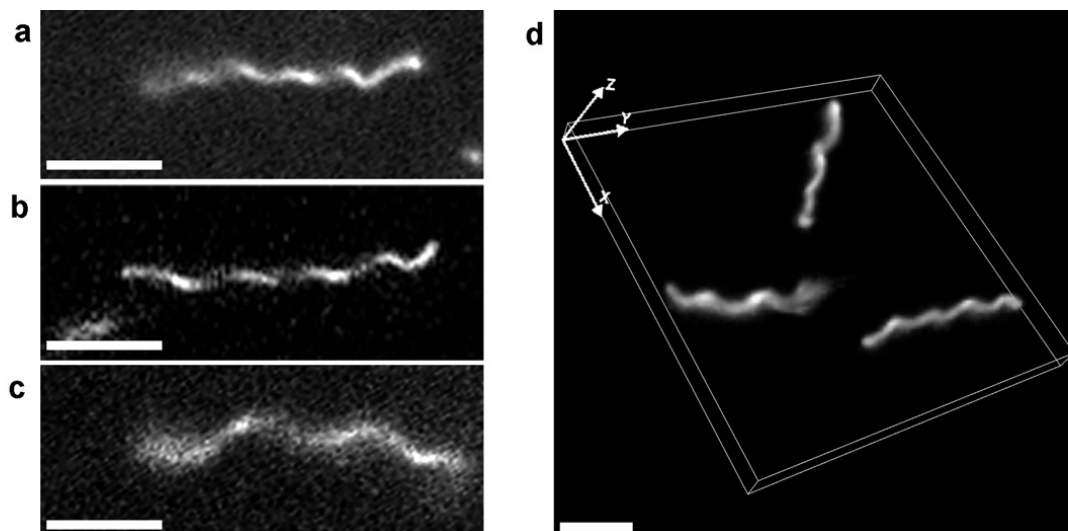


Figure 2.8: DNA tile tubes with microscale helical diameter. Fluorescence microscopy images of (a) an 11-helix tile tube with 3nt tile shift, (b) a 13-helix tile tube with 2nt tile shift and (c) a 15-helix tile tube with 1nt tile shift. (d) 3D reconstruction of 13-helix tile tubes with 2nt tile shift. Scale bars: $5\mu\text{m}$. Reprinted by permission from ref. [94]. Copyright (2017) American Chemical Society.

In Publication P1, *tile shifting* was only applied to selected tiles by 1 nt at a time. In general, however, a shift of up to 21 nt (half the length of the tile sequence) per tile is conceivable before a recurrence in the design occurs. The reason for the self-imposed restriction lied in the relationship between *tile shifting* and the cross sectional geometry of the tile-shifted tube.

Besides the tile's relative position within the tube design, *tile shifting* also affects the position of the DNA cross overs and thereby the interhelical angle between neighbouring helices (Figure 2.9). In the original tile tube design [61], the angles between neighbouring helices alternate between 13° and 47.3° as illustrated for a 12-helix tile tube in Figure 2.9a. This deliberate choice of angles guaranteed that the tubes formed a curved ribbon with a total interhelical angle of $\theta = n_{\text{odd}} \cdot 13^\circ + n_{\text{even}} \cdot 47.3^\circ$, allowing the structure to easily close into a tube. In Publication P1, we only shifted selected tiles by 1 nt , so that the respective interhelical angle between the corresponding helices changed from 47.3° to 13° (Figure 2.9b). Although this 1 nt tile shift slightly altered the total interhelical angle of the tube, it did not change the direction of curvature of the tube before closure. We believe that this kind of *tile shifting* therefore did not influence the successful tube formation. In contrast, however, a tile shift by 2 nt would already result in a negative interhelical angle of -21.3° , a shift by 3 nt in an angle of -55.6° (Figure 2.9c). We expected such tile shifts to hinder a correct tube formation or to strongly deform the circular tube shape and therefore did not consider them for the construction of tile-shifted helical tubes in Publication P1.

It is however worth noting that *tile shifting* with negative interhelical angles can be appropriately used if all interhelical angles within a tube are negative. We exemplarily

constructed a 6-helix and a 7-helix tile tube with alternating interhelical angles of -21.3° and -55.6° as illustrated in Figure 2.9d. The tiles formed well-assembled tubes of several micrometer in length (see Appendix C for oligonucleotide sequences and TEM images of the assembled tube structures). Interestingly, due to the strong *tile shifting*, the 6HT had to overcome a large offset of 10bp and should therefore possess a strong supertwist, while the 7HT should have folded with almost zero offset. Furthermore, due to the opposing direction of tube closure, it is likely that these tubes exhibit a vice versa *supertwist* chirality than tubes, which fold with positive interhelical angles. This feature could make this class of tile tubes an interesting alternative for the constructing of DNA tubes with defined chirality.

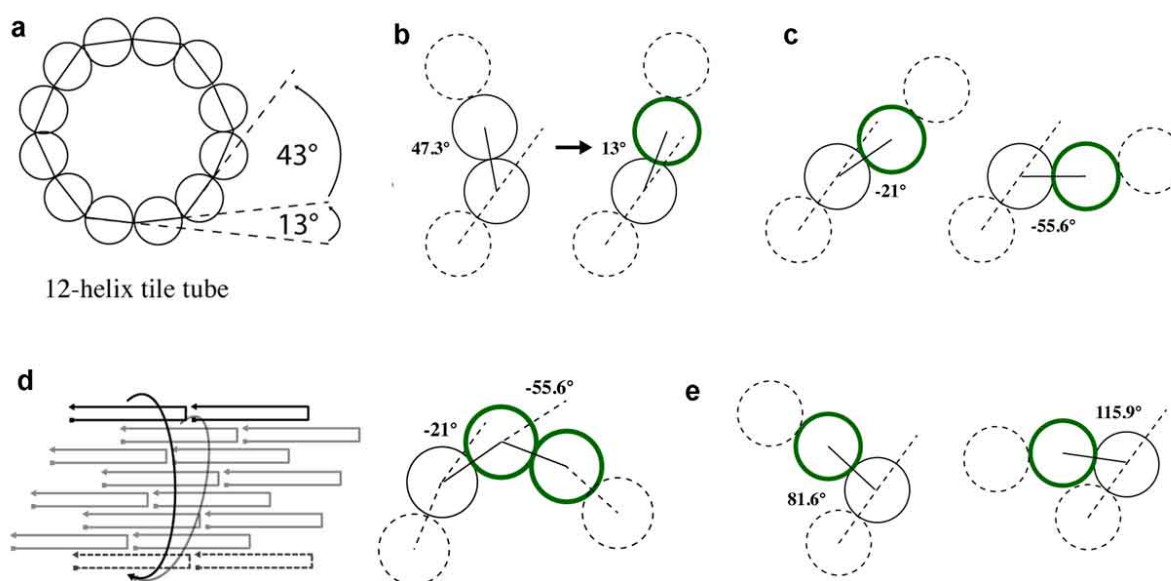


Figure 2.9: Relation between tile-shifting and interhelical angle. (a) In the original tile tube design by Yin et al. [61], angles between neighbouring helices alternate between 43.7° and 13° . (b) A 1 nt tile shift as applied throughout this work changes the angle from 43.7° to 13° , maintaining the direction of curvature. (c) Tile shifting by more than 1 nt within the same tile sequence, however, can result in negative interhelical angles ($2nt = -21^\circ$; $3nt = -55.6^\circ$). (d) Tile scheme for a 6HT and a 7HT constructed with alternating negative interhelical angles of -21° and -55.6° . (e) Tile shifting in the opposite direction along the tube's primary axis results in increased interhelical angles ($-1 nt = 81.6^\circ$; $-2 nt = 115.9^\circ$).

Another conceivable strategy is to shift tiles in the opposite direction along the tube's primary axis. For example, a tile shift by $-1 nt$ would result in an increased angle of 81.6° , by $-2 nt$ in an angle of 115.9° (Figure 9d). Although, these angles keep the overall curvature same, they would drastically increase the total interhelical angle of the tube. For example a 10-helix tile tube with two tile shifts of $-1nt$ already has a total interhelical angle of $\theta = 4 \cdot 13^\circ + 4 \cdot 47.3^\circ + 2 \cdot 81.6^\circ = 404.4^\circ$ before closure, which is larger than that of the closed tube (360°). Such conformations are therefore likely to hinder the correct formation of the tube, which is why we excluded them from our studies. However, for tubes consisting of few helices, which would only exhibit a small total interhelical angle, such *tile shifting* could be applied in a meaningful way.

2.4 Combining base pair insertions/deletions, *tile shifting* and Cy3 modifications in DNA tile tubes

In order to control the helical shape of DNA tile tubes, we so far either installed base pair insertions and/or deletions to straight tile tubes or applied *tile shifting* to Cy3-modified *supertwisted* tile tubes. In what follows, we will demonstrate that these methods can also be combined, thereby giving an even greater freedom of design for the construction of helical tile tubes.

As demonstrated in Publication P1 (see chapter 6.1), a switch of the chirality from left- to right-handedness in tile-shifted Cy3-modified 13HTs occurred at a tile shift of ~ 4 nt. We believe that at this amount of tile shift, the left-handed *supertwist* and the Cy3-induced right-handed twist almost balanced each other. The result was a remaining small overall twist, which led to a large helical diameter of the tube's shape.

In order to figure out, whether such a change in the chirality of *supertwisted* tubes can also be provoked by a base pair insertion, we installed an insertion into the left-handed 13HT with 2nt tile shift. Without insertion, this structure exhibited a left-handed chiral shape with microscale diameter (see chapter 6.1). With insertion, however, the same structure turned out to be right-handed as illustrated by “tomographic” slices taken slightly below and above the center of the tube's primary axis (Figure 2.10a). This demonstrates that base pair insertions and *tile shifting* are compatible and can be used simultaneously to define the helical shape of the DNA tile tube.

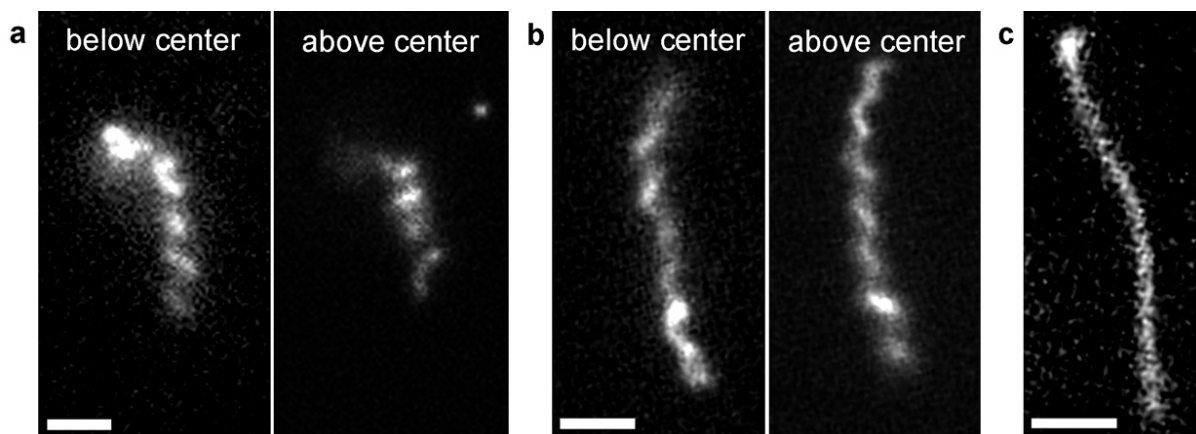


Figure 2.10: Base pair insertion-induced switching of the chirality of tile-shifted tubes. (a) Tomographic slices of a 13HT with 2 nt tile shift and a base pair insertion revealed a right-handed chirality. Note that without base pair insertion, the tube had a left-handed chirality as shown in Figure 7b. (b) A 13HT without tile shift, obtained a visible left-handed chiral shape when an additional base pair was installed. (c) A 13HT with 2nt tile shift lost its visible helical shape when a base pair deletion was installed. Scale bars: $2\mu\text{m}$

Another example of the applicability of combining both techniques is illustrated for a 13HT without tile shift. The helical shape of this structure was too small to be resolved via fluorescence microscopy, which made it impossible to determine its chirality. By installing a base pair insertion, however, we were able to make a microscale left-handed

shape visible (Figure 2.10b). This observation suggests that the chirality of the 13HT was left-handed before base pair insertion and that the right-handed twist of the insertion reduced the overall twist in the structure, thereby increasing its helical diameter. On the other hand, if the 13HT was right-handed prior to the base pair installation, the overall twist should have increased by the additional base pair, resulting in an even smaller helical diameter impossible to visualize by light microscopy.

In order to substantiate this assumption, we installed a base pair deletion into the left-handed 13HT with 2 nt tile shift. Without deletion, this structure exhibited a microscale helical diameter, which was visible via light microscopy (see chapter 6.1). After installing the base pair deletion, however, the diameter became so small that it could no longer be resolved (Figure 2.10c). This observation suggests that the left-handed twist from the deletion increased the already present left-handed twist and led to a decrease in the helical diameter of the tube, vice versa to what we observed for the base pair insertion in the 13HT without tile shift.

Another promising approach for the designed construction of helical tile tubes is to combine the Cy3-induced right-handed twist with the insertion- or deletion-induced twist in straight tile tubes with even number of helices. As described earlier, Cy3-modifications add a small amount of bend and right-handed twist to DNA tile tubes [93]. They can therefore be used to reduce the total twist in tubes with left-handed or vice versa increase the twist in tubes with right-handed chirality. Figure 2.11a shows a Cy3-modified 8-helix tile tube with one base pair deletion. Compared to the unmodified structure, which exhibited a radius of curvature of only $\sim 266\text{ nm}$, the helical diameter increased drastically and became visible via fluorescence microscopy. Surprisingly, the Cy3 modifications even affected the chirality of the structure. The Cy3-modified 8HT with deletion showed a right-handed helical shape, in contrast to a left-handed chirality one would expect for tile tubes with deletion. These observations lead us to believe that the right-handed Cy3-induced twist slightly exceeded the left-handed deletion-induced twist, resulting in a small overall right-handed twist, which led to the large diameter of the helical structure.

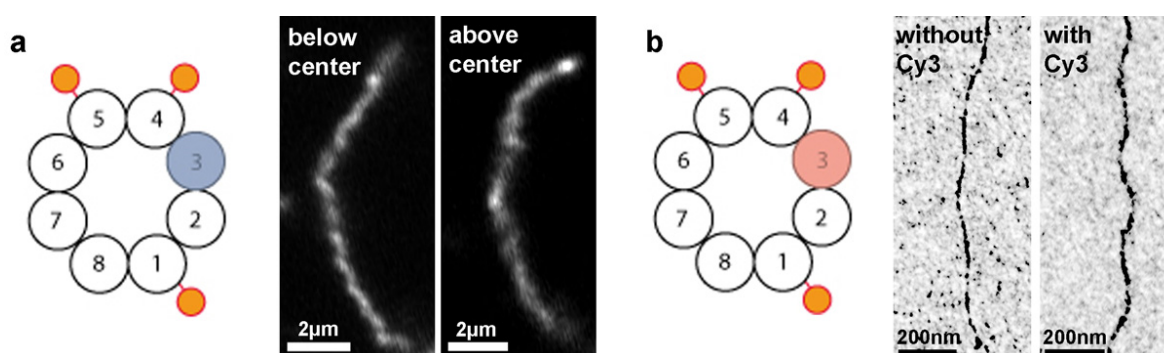


Figure 2.11: Base pair deletion-induced increase of the helical diameter of Cy3-modified tubes. (a) Tomographic slices of a Cy3-modified 8-helix tile tube with one deletion exhibiting a visible right-handed chirality. (b) Comparison of an unmodified and Cy3-modified 8-helix tile tube with one base pair insertion. With Cy3, the radius of curvature is ~ 2 times smaller than without Cy3 modification.

Vice versa, in the case of an 8HT with one insertion, the Cy3-modifications reduced the radius of curvature in comparison to the unmodified structure as observed by TEM (Figure 2.11b). R_c extracted from the Cy3-modified structures was nearly 2 times smaller than for tubes without modifications. These observations suggest that the Cy3-induced twist and the insertion/deletion-induced twist can be applied simultaneously in a controlled manner to shape the tube's helical structure.

2.5 Conclusions and Outlook

One of the major trends in nanotechnology is to produce complex nanostructures with precise control over their size and shape [50]. Especially basic three-dimensional geometries such as spheres, cubes, cylinders, tubes or helices are required building blocks for the construction of advanced materials and their resulting applications. Throughout this chapter, we introduced a variety of novel design rules for the construction of helically shaped DNA tile tubes from a simple motif requiring only a handful of single stranded DNA oligonucleotides.

For the construction of tile tubes with nanoscale helical diameters, we incorporated base pair insertions and deletions into particular DNA double strands of the DNA tile tubes similar to what was previously shown for DNA origami [66]. For the construction of tile tubes with microscale helical diameters and chirality, we combined a novel design technique, the so-called *tile shifting*, with the planned placement of Cy3 dyes on the tubes. We finally demonstrated that base pair insertions/deletions, *tile shifting* and Cy3 modifications can also be applied simultaneously and in a controlled fashion. This gives researchers an even greater freedom in shaping the tile tube's helical structure. In future work, the here-proposed design rules deserve additional attention to fully understand and exploit the underlying mechanisms.

We believe that in upcoming applications our helical DNA nanotubes can serve as nanosprings, providing materials with extraordinary elastic properties [80, 85, 87] and strength [88]. Therefore, additional studies that measure the mechanical characteristics of the helical tubes such as force spectroscopy are required.

Nanotubes with nanoscale helical diameters could further enhance the functionality of devices, which use the assembled structure as a template. For example, plasmonic gold nanoparticles, which are assembled in a chiral conformation on DNA nanostructures are known to alter the polarization of light waves [68]. Our chiral nanotubes could extend the spectrum of such DNA-based plasmonic devices.

Tile tubes with microscale diameters, on the other hand, could be applied in fields that require components of microscale dimensions. For example, artificial microswimmers make use of filaments with microscale helical diameters to achieve propulsion. Such artificial devices are envisioned for biomedical applications where biocompatibility of the components plays a crucial role. Here, our micrometer-sized helical constructs made solely from biocompatible DNA could be advantageous over

non-biocompatible materials. In the following chapter, we will demonstrate how DNA tile tubes can be used to construct artificial DNA-flagellated microswimmers.

3. Magnetic Propulsion of Microswimmer with DNA-based Flagellar Bundles

In comparison to the phoretic propulsion of artificial micro- and nanoswimmers, which exploits electric, chemical, or thermal gradients in the surrounding environment [42-44], magnetic actuation has proven to be especially beneficial due to its highly biocompatible external energy supply and distant remote control.

The first prototype of a magnetic helical low Reynolds number swimmer was proposed by Honda et al. in 1996 [99]. The centimetre tall swimmer was able to swim in a highly viscous fluid and could be actuated from afar by an external rotating magnetic field. In 2005 the same group reduced the size of the swimmer down to a few millimetres, which enabled the controlled swimming in a narrow fluidic channel [100]. In the same year, the first microswimmer with flexible artificial flagellum was demonstrated by Dreyfus et al. [19]. In their work, they induced the self-assembly of magnetic particle chains via DNA strands through an applied external field. By attaching a payload to one end of the chain and applying an oscillating magnetic field, a symmetry breaking in the chains movement led to the actuation of the swimmer. The first magnetic helical microswimmer was presented in 2007 by Bell et al. [25]. It had a length of 30-40 μm and consisted of a magnetic head structure attached to a rigid helical tail fabricated by self-scrolling. In 2009, Ghosh et al. were able to further reduce the size of helical microswimmers to only a few micrometres in length [20]. They constructed a glass propeller that was fabricated by glancing angle deposition (GLAD) and magnetized by the deposition of a cobalt layer and subsequent magnetization along the helical axis. Although their swimmer was only a few micrometers long, it could be manoeuvred in a controlled fashion along a programmed path. In 2012, direct laser writing (DLW) was introduced to fabricate the first functional helical microswimmers with a microholder at one end of the structure that allowed the controlled transportation of microbeads [21]. In 2014, Schamel et al. produced the first nanoscale swimmer, which was able to propel in viscoelastic media [24].

3.1 Magnetic actuation of helical artificial swimmers

The most common mode of propulsion for magnetic micro- and nanoswimmer in highly viscous fluids is by rotating a rigid helical shape, which then performs a corkscrew-like motion as illustrated in Figure 3.1a. This movement is non-reciprocal in time and therefore fulfils the physics of low Reynolds number swimming at small scales [5]. The rotation is usually provided by an external rotating magnetic field, which exerts a torque on the magnetic moment of the swimmer whenever the external field and the internal magnetic moment are not parallel.

$$|\vec{v}| = |\vec{m} \times \vec{B}| = mB \sin \theta \quad (3.1)$$

Here, \vec{m} is the magnetic moment of the particle and \vec{B} the external magnetic field. The rotation around the helical axis is then transformed into a translational movement perpendicular to the rotating field.

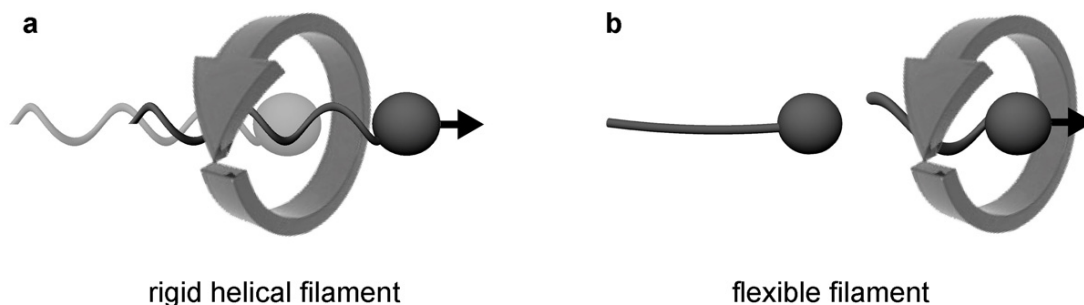


Figure 3.1: Propulsion mechanisms of artificial microswimmers actuated by a rotating magnetic field. Schematics of an actuated microswimmer with (a) a rigid helical filament and with (b) a flexible filament. While the motion of a rigid helical filament already fulfils the requirements of low Reynolds number swimming when rotated, a flexible filament first needs to bend into a helical shape in order to generate propulsion.

Propulsion in a corkscrew-like manner can also be achieved when a flexible filament is deformed into a helical shape (Figure 3.1b). In publication P2 (see chapter 6.2), we presented a new class of microswimmers, which is actuated by such flexible filaments constructed solely from DNA. The artificial DNA filaments were coupled to a magnetic bead of considerable greater mass and exerted to an external rotating magnetic field. The hydrodynamic drag acting on the filament bundle then bent the structures into a helical shape [22, 23].

In contrast to rigid helical filaments, which are usually made out of inorganic materials, our DNA - flagellated microswimmers combine biocompatible materials with the advantages of helical propulsion (such as fast, controlled, and directed steering). The following chapter will give a quick summary of the main results of Publication P2. The full text is provided in chapter 6.2.

3.2 Construction and propulsion of microswimmers with DNA-based flagellar bundles

For the construction of the artificial flagella, we applied the DNA tile tube assembly [61] as described in detail in chapter 2. After the assembly, the artificial flagella were coupled via biotin-functionalized DNA strands to streptavidin-modified $1\mu\text{m}$ magnetic particles

yielding magnetic particle - DNA flagella hybrids (Figure 3.2a). In order to allow visualization of the tubes via fluorescence microscopy, we modified the tubes with Cy3 dyes. Figure 3.2 shows three different types of artificial microswimmers exhibiting straight (Figure 3.2b) and helically shaped filaments of nano- (Figure 3.2c) and microscale (Figure 3.2d) helical diameters constructed by this method.

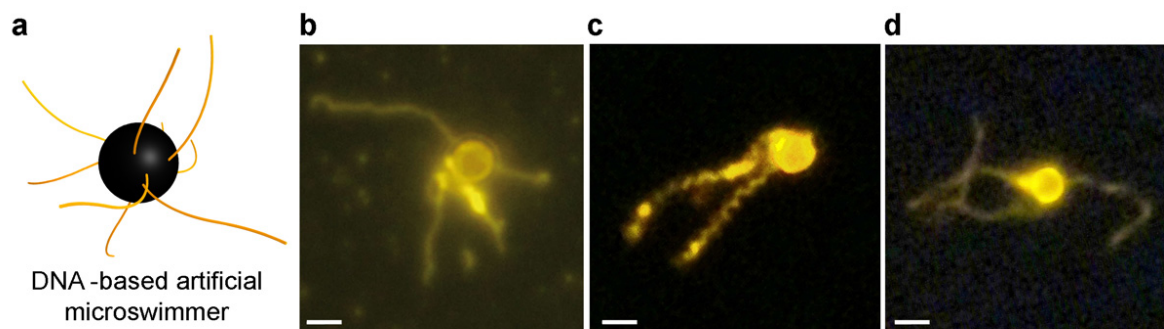


Figure 3.2: Construction of magnetic microswimmers with artificial DNA flagella. (a) Schematic of DNA flagella attached to a $1\ \mu\text{m}$ magnetic particle. Fluorescence microscopy images of artificial microswimmers exhibiting (b) straight flagella, (c) flagella of nanometre-sized helical diameter, and (d) flagella of micrometer-sized helical diameter. Scale bars: $2\ \mu\text{m}$. Reprinted by permission from ref. [27]. Copyright (2016) American Chemical Society.

The hybrid constructs were then actuated by a rotating homogeneous magnetic field. The field was generated by a three axis Helmholtz coil setup, which was incorporated into a fluorescence microscope to allow simultaneous imaging and actuation of the structures. In order to suppress unwanted drift, we sealed the glass chamber that contained the artificial swimmer's solution (see Appendix B for materials and methods).

The rotation of the magnetic bead led to a bundling of the attached straight and nanoscale helical filaments along the rotation axis, similar to what was reported for the propulsion of flagellated bacteria [10], while the filaments of microscale helical diameters from Figure 3.2d refused to bundle properly.

Structures, which successfully formed a bundle on only one side of the bead, started to propel head first with propulsion speeds of up to $0.6\ \mu\text{m}/\text{s}$ as illustrated in Figure 3.3. The dimensionless speed of our artificial microswimmers ($\sim 1/10$ of a body length per turn) corresponds well to that of flagellated *E. coli* bacteria [14]. However, due to the lower persistence length of the applied DNA tile tubes [93] compared to that of bacterial flagella [101], we were not able to propel the swimmers at equal rotational frequencies to those found in bacterial flagellation. Above 3Hz our artificial flagella bundles lost their chiral shape, which resulted in a loss of propulsion efficiency.

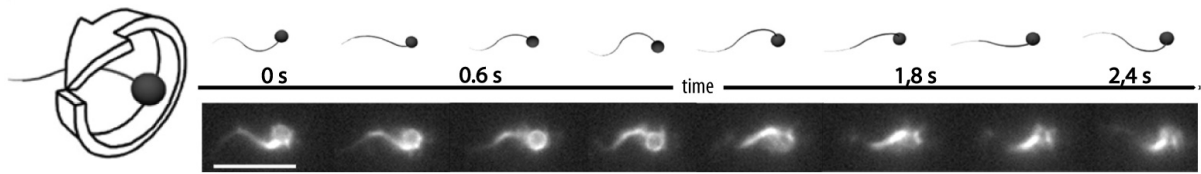


Figure 3.3: Locomotion of a microswimmer driven by a DNA flagellar bundle. Schematic and respective fluorescence microscopy images show a full rotation of the microswimmer with artificial flagella bundle. The rotation is generated by a homogeneous magnetic field, which rotates perpendicular to the propulsion direction. Scale bar: $5\mu\text{m}$.

By changing the rotation axis of the external magnetic field, we were able to control the swimming direction of the artificial microswimmers. We illustrated this controlled steering by making the swimmer perform a U-turn. Similar to the swimming of bacteria near surfaces [102], we observed that our artificial microswimmer slightly drifted perpendicular to the rotation axis due to hydrodynamic interactions with the close-by glass chamber. Run-and-tumble behaviour as found in the flagellation of multiflagellated bacteria [103], however, could not be observed. In this process, the instant change in the rotation of helical filaments results in an opening of the bacteria's flagellar bundle. We tried to mimic this behaviour by spontaneously switching the rotation direction of the external magnetic field. Unlike in bacteria, however, our artificial bundle remained closed and continued propelling the microswimmer along the rotation axis even after the rotation direction was switched (for additional information and images please refer to chapter 6.2).

Examination of the intensity profile of the cross-linked bundles via fluorescence microscopy revealed that our bundles consist of flagella of different lengths, which results in an exponentially decreasing stiffness of the bundle. Because a similar shape was also found within bacterial flagellar bundles, which become thinner towards the bundle ends, we closely examined the relation between the bundle stiffness and the propulsion efficiency of our microswimmer. In collaboration with the group of Prof. Erwin Frey, we therefore modelled the artificial bundle as a rod with length-dependent bending modulus and compared different cases of bundle stiffness. We found that compared to the case of constant stiffness, swimmers driven by a bundle of variable stiffness achieved higher swimming speeds for nearly all parameters tested. This means that our construction technique yields artificial flagella bundle, which are advantageous over single or multiple appendages with constant stiffness. Furthermore, the model allowed us to closely predict the swimming speed of our artificial microswimmers from simple geometric parameters extracted from the movie of the propelled swimmers. This makes the model a helpful tool for future improvements of our DNA – flagellated microswimmers (for additional information and images please refer to chapter 6.2).

3.3 Conclusions and Outlook

We demonstrated that biocompatible artificial flagella with designed shape could be constructed solely from DNA. The artificial DNA filaments had sizes similar to those of small bacteria and exhibited equal helical shapes. Coupling of the filaments to magnetic particles yielded a new class of artificial biocompatible microswimmers, which were actuated by a rotating external magnetic field. The induced rotation of the magnetic particle resulted in bundle formation of the artificial DNA flagella, which drove the particles forward and allowed steering of the swimmers along a complex path. The mechanism behind the propulsion were described by a theoretical model, which revealed that our flagellar bundles with decreasing bending stiffness provide propulsion speeds widely advantageous over appendages with constant stiffness.

We believe that in future studies, insights gained from both model and experiment will allow researchers to gain optimal swimming features for bundle - driven artificial microswimmers, such as improving the speed or mimicking bacteria's run-and-tumble behaviour. Furthermore, our structures may find their way into nanorobotic devices for non-invasive biomedical therapies [38, 48] and into other fields of nanoengineering as envisioned more than half a century ago by Richard Feynman [1].

The here-described swimmers are located in the micrometer scale, where propulsion by reciprocal motion is known for a variety of microorganisms. In the nanoscale regime, however, no natural swimmers exist [104] that can serve as a blueprint for the construction of nanoscale swimmers. In the following chapter, we will enter this size regime and examine construction techniques and the hurdles that have to be overcome to achieve propulsion at such small scales.

4. DNA-based nanoswimmers for enhanced diffusive swimming

At the nanoscale, the effects of thermal fluctuations play an increasingly important role in the dynamics of artificial swimmers [105]. Gosh et al. numerically determined the minimum length of an effectively propelled chiral swimmer to be ~ 900 nm in length [106]. Below this value, the effects of Brownian motion become strong enough to prevent directed motion. These simulations are in agreement with the smallest observed length of actively propelled living organisms (~ 800 nm) [104]. Recently, Schamel et al. realized a 400 nm helical nanoswimmer that could be controllably steered through a biological viscoelastic gel [24]. In aqueous solutions, however, their swimmers were subjected to the strong randomizing forces of Brownian motion and did not actively propel.

As active propulsion is unfeasible at these small scales, diffusion becomes the main mechanism to achieve displacement [107]. Artificial nanoswimmers, which are envisioned to enter cells or provide direct interaction with the cell surface [108], therefore need to exploit the diffusion to achieve propulsion. Lauga et al. recently showed that reciprocally actuated particles have an enhanced diffusion, which can be several orders of magnitude higher than similar objects, which undergo Brownian motion only [109]. Thus actuation can be important for motility even if directed motion fails. Enhanced diffusion has been observed for micron-sized marine bacterial species [109], for nanoparticles in aqueous solution [110] and for biological tissues [111, 112]. Even enzymes have recently been proposed to exhibit enhanced diffusion when they are catalytically active [113]. These examples demonstrate that despite the strong forces associated with Brownian motion, further size reduction of artificial swimmer to the nanoscale is promising and can pave the way for enhanced diffusive nanorobots, which can perform tasks inside or on biological media, such as cells and living microorganisms, faster than non-actuated particles.

4.1 Enhanced diffusion

Without actuation, the motion of nanoswimmers is determined by random collisions with the near-by molecules [114]. In a homogeneous environment, these equilibrium thermal fluctuations result in a purely diffusive behaviour of the particles. A nanoswimmer with hydrodynamic radius R therefore has a translation diffusion coefficient,

$$D_T = \frac{k_B T}{6\pi\eta R} \quad (4.1)$$

Here, k_b is the Boltzmann constant, T is the absolute temperature, and η is the viscosity of the surrounding fluid.

The rotational diffusion coefficient of the particle is given by,

$$D_R = \tau_R^{-1} = \frac{k_B T}{8\pi\eta R^3} \quad (4.2)$$

Here, τ_R is the characteristic time scale in which the particle performs a full rotation.

Because the translational diffusion scales with R^{-1} and the rotational diffusion follows R^{-3} , diffusion strongly increases the smaller the particle gets. For example, a spherical particle with $1\mu\text{m}$ in diameter has a translational and rotational diffusion of $D_T \sim 0.4 \frac{\mu\text{m}}{\text{s}}$ and $D_R \sim 1.3 \text{ Hz}$, while a particle with 100 nm diameter already has $D_T \sim 4 \frac{\mu\text{m}}{\text{s}}$ and $D_R \sim 1300 \text{ Hz}$. A 100 nm nanoswimmer therefore already undergoes a 10 times faster translational diffusion and a 1000 times faster rotational diffusion than its $1\mu\text{m}$ counterpart.

With actuation by an external field, the motion of the particles is an interplay between random diffusion and directed swimming [43] leading to different behaviours at different time scales. At very low time scales, the induced actuation of the swimmer is too slow to lead to propulsion, giving rise to pure Brownian diffusion. At slightly higher time scales, when propulsion contributes, both rotational diffusion and directed motion affect the swimmer, resulting in a directed, superdiffusive behaviour of the particle. At even higher time scales, the randomization through Brownian motion becomes so dominant that a directed motion cannot be maintained anymore. The effective diffusion is then the sum of Brownian motion and a contribution from the random walk the actuated swimmer undergoes. This long-time phenomenon of actuated particles in the diffusive regime is called enhanced diffusion.

An intuitive way of determining whether a nanoswimmer is in one of these states is by looking at its mean square displacement (MSD). It can be easily calculated from the swimmer's trajectory, which for simplicity reasons we considered for two dimensions only.

The MSD for pure diffusion in 2D, which applies for non-actuated particles as well as for actuated swimmers at very small times is given by,

$$MSD(\tau) = 4D_T\tau \quad (4.3)$$

Here, τ is the time between two measurements of the particles position.

The MSD for the superdiffusive regime of actuated swimmers is given by,

$$MSD(\tau) = 4D_T\tau + v^2\tau^2 \quad (4.4)$$

where v is the velocity of the actuated particle.

The MSD for enhanced diffusion at long time scales is given by,

$$MSD(\tau) = (4D_T + v^2\tau_R)\tau \quad (4.5)$$

which corresponds to an enhanced diffusion of $D_{enh} = D_T + \frac{1}{4}v^2\tau_R$.

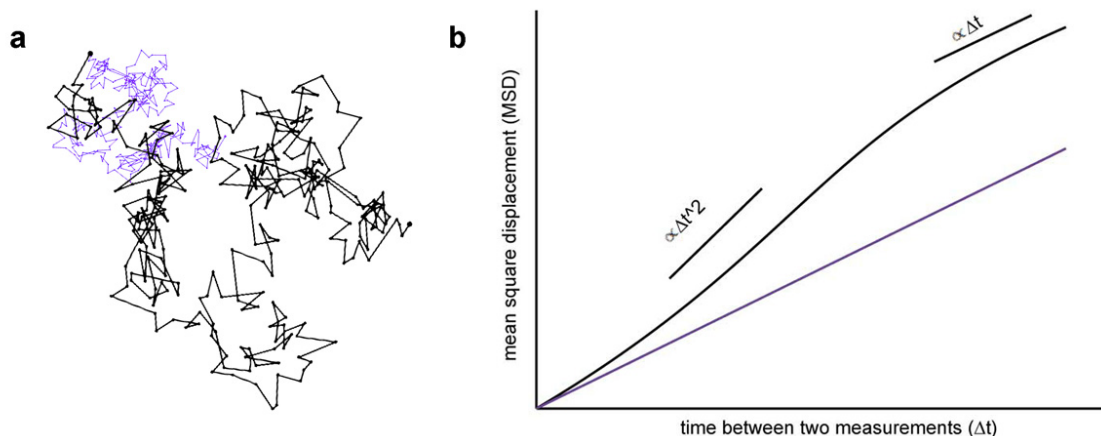


Figure 4.1: Comparison of enhanced and normal diffusion. (a) Schematic trace of a nanoswimmer undergoing normal diffusion (purple) and enhanced diffusion (black). (b) Without propulsion the mean square displacement (MSD) of a nanoswimmer is purely diffusive and grows linearly in time (purple line). With propulsion, the MSD is diffusive ($\propto \Delta t$) for small times, superdiffusive for intermediate times ($\propto \Delta t^2$) and enhanced diffusive ($\propto \Delta t$; with higher offset) for larger times. Note that the different types of diffusion are presented in a log-log plot to enable an easy distinction.

The strength of the enhanced diffusion depends on both the speed v and the rotational diffusion of the swimmer, which scales with R^{-3} and is reflected in τ_R . In order to construct artificial nanoswimmers, which can effectively undergo enhanced diffusion, it is therefore crucial to generate reasonable propulsion speeds and to control the size of the swimmer. In order to deal with these requirements, we applied the DNA origami technique. It allowed us to construct nanoscale artificial flagella with basic propulsion shapes and defined size, which could be specifically functionalized with magnetic materials required for the actuation of the nanoswimmers.

4.2. Construction of DNA-based nanoswimmers

For the construction of nanometer-sized artificial flagella of defined lengths we applied the DNA origami method [64-66]. It relies on the controlled folding of a $\sim 8\text{kb}$ -long single-stranded DNA 'scaffold' strand with the help of hundreds of short DNA 'staple' strands (Figure 4.2a) as described earlier in chapter 1. This bottom-up technique has the

ability to construct nanometer-sized objects from a simple biocompatible building block and with nanometer design precision.

From a wide range of possible designs, we chose three different shapes that are known to propel through highly viscous fluids [5]: i, a straight elastic rod that is designed to bend under hydrodynamic drag when rotated [23], thereby leading to a dynamic chiral shape, which we implemented with a 6-helix-bundle (6HB, 420 nm long). ii, a predefined chiral structure resembling a corkscrew realized with a 14-helix corkscrew bundle (14HC, 150 nm long). iii, a predefined twisted structure resembling a screw formed by a twisted 3-layer sheet (3LS, 58 nm long) (Figure 4.2a) (design details and DNA sequences are given in Appendix D). Multimerization of the monodisperse structures can be applied to generate helical or twisted structures with several turns, as illustrated by the twisted 3LS structure in Figure 4.2b. Single and multimerized structures were designed to have single-stranded overhangs on one side of the structure which allowed us to couple the artificial flagella to magnetic particles of different size and shape via DNA-hybridization of complementary DNA strands (Figure 4.2c). Magnetic particles were functionalized with neutravidin via EDAC/NHS coupling or purchased with streptavidin functionalization and subsequently coupled to biotin-DNA (see Appendix D for Materials and Methods).

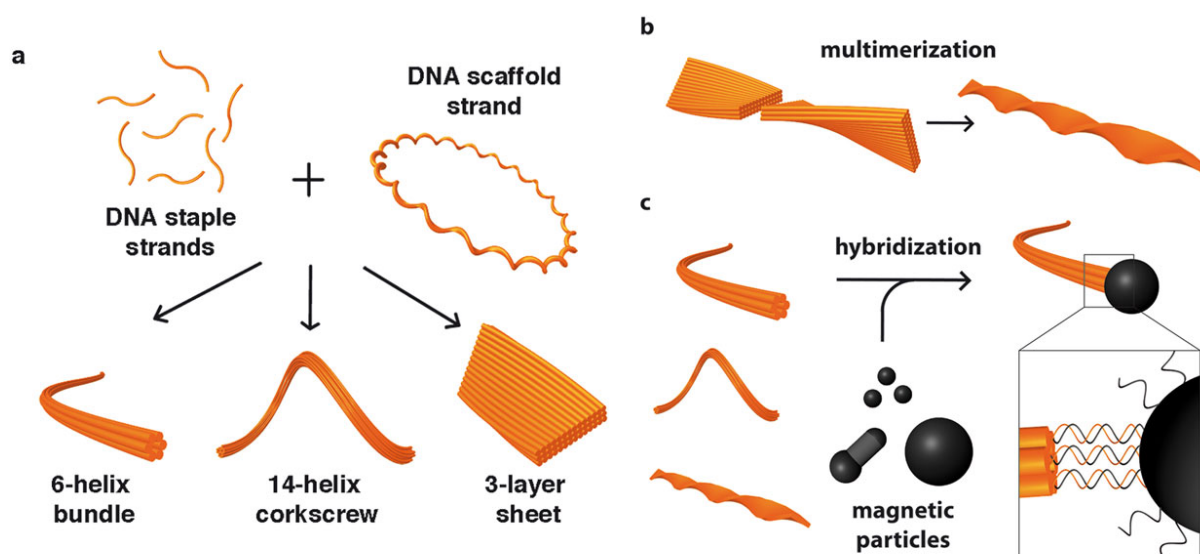


Figure 4.2: Construction scheme for DNA origami - magnetic bead hybrids. (a) Schematic showing the DNA-based self-assembly of a DNA-origami six-helix bundle (6HB), a 14-helix corkscrew (14HC), a twisted 3-layer sheet (3LS) and (b) the multimerization of single twisted 3LS into larger constructs. (c) Coupling of DNA origami to magnetic beads via the hybridization of complementary DNA strands yields DNA origami -magnetic bead hybrids.

Figure 4.3 shows TEM images of the multimerized DNA origami constructs. In all three cases constructs with micrometer length were achieved. The best conditions for the multimerization process were found at 35° reaction temperature (see Appendix D for additional information on multimerization conditions).

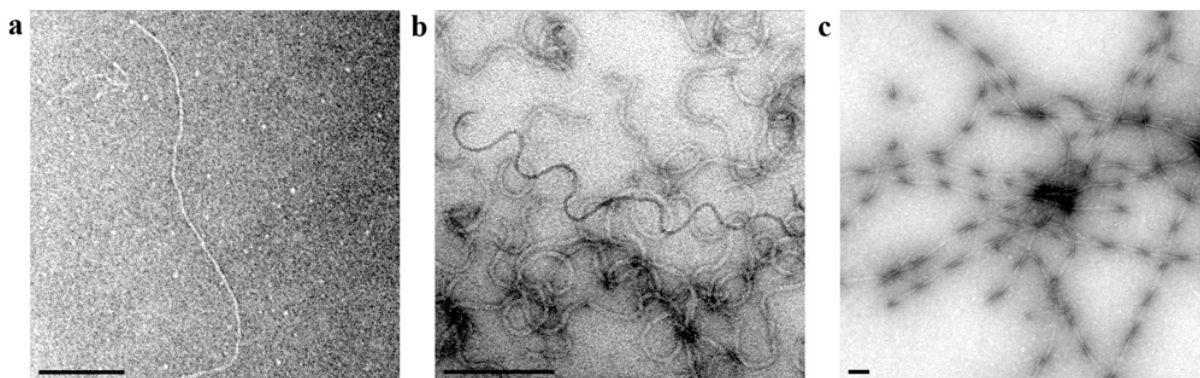


Figure 4.3: Multimerization of DNA Origami monomers. Multimerized (a) 6-helix bundle (6HB), (b) 14-helix corkscrew (14HC), and (c) twisted 3-layer sheet (3LS) as observed by TEM. Scale bars: 200nm

During the functionalization and hybridization steps, we added 0.05 % of the surfactant Tween 20 (Polysorbat 20). This prevented the aggregation of magnetic particles in the divalent salt solution (12 mM $MgCl_2$), which is required for the intactness of the DNA origami constructs. Figure 4.4 exemplarily shows the effect of Tween 20 on 30 nm iron-oxide particles. The nanoparticles remained monodisperse in a 12 mM $MgCl_2$ solution when 0.05 % Tween 20 was added, while sedimentation of the particles occurred without the addition of the surfactant (Figure 4.3a). TEM images confirmed the monodispersity of the nanoparticles in the presence of Tween 20 (Figure 4.3b), while mainly clusters formed without the surfactant (Figure 4.3c).

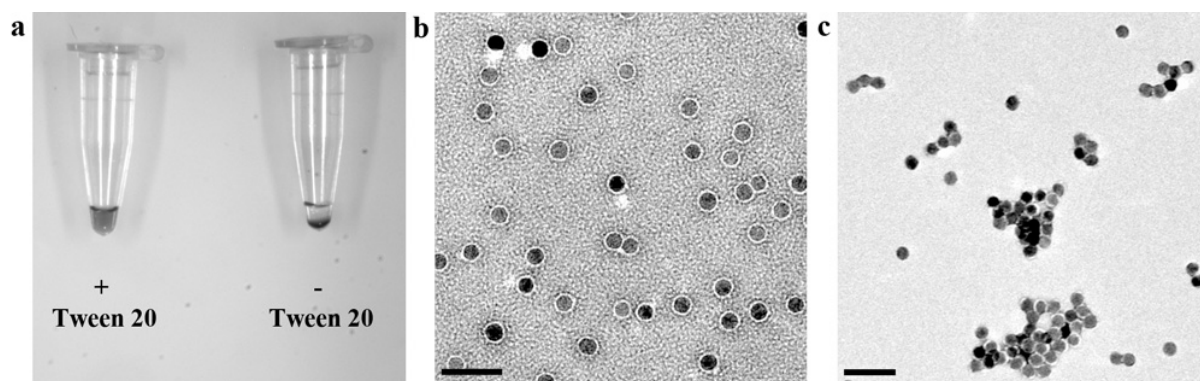


Figure 4.4: Prevention of magnetic nanoparticle aggregation. (a) Aggregation of neutravidin-coated 30 nm magnetic particles in a 0.5xTBE / 11 mM $MgCl_2$ buffer was prevented by adding 0.05 % of the surfactant Tween 20 (Polysorbat 20). Without the surfactant, aggregation of the particles led to a fast sedimentation. Transmission electron microscopy images of both solutions: (b) with and (c) without Tween 20. Scale bars: 90 nm

Figure 4.5 illustrates the diversity of DNA-magnetic particle hybrids that were obtained by the DNA origami technique (for a detailed description of the assembly see Appendix D). A wide variety of DNA magnetic bead hybrids could be constructed for different magnetic particle sizes (30 nm, 280 nm, 560 nm and 1000 nm).

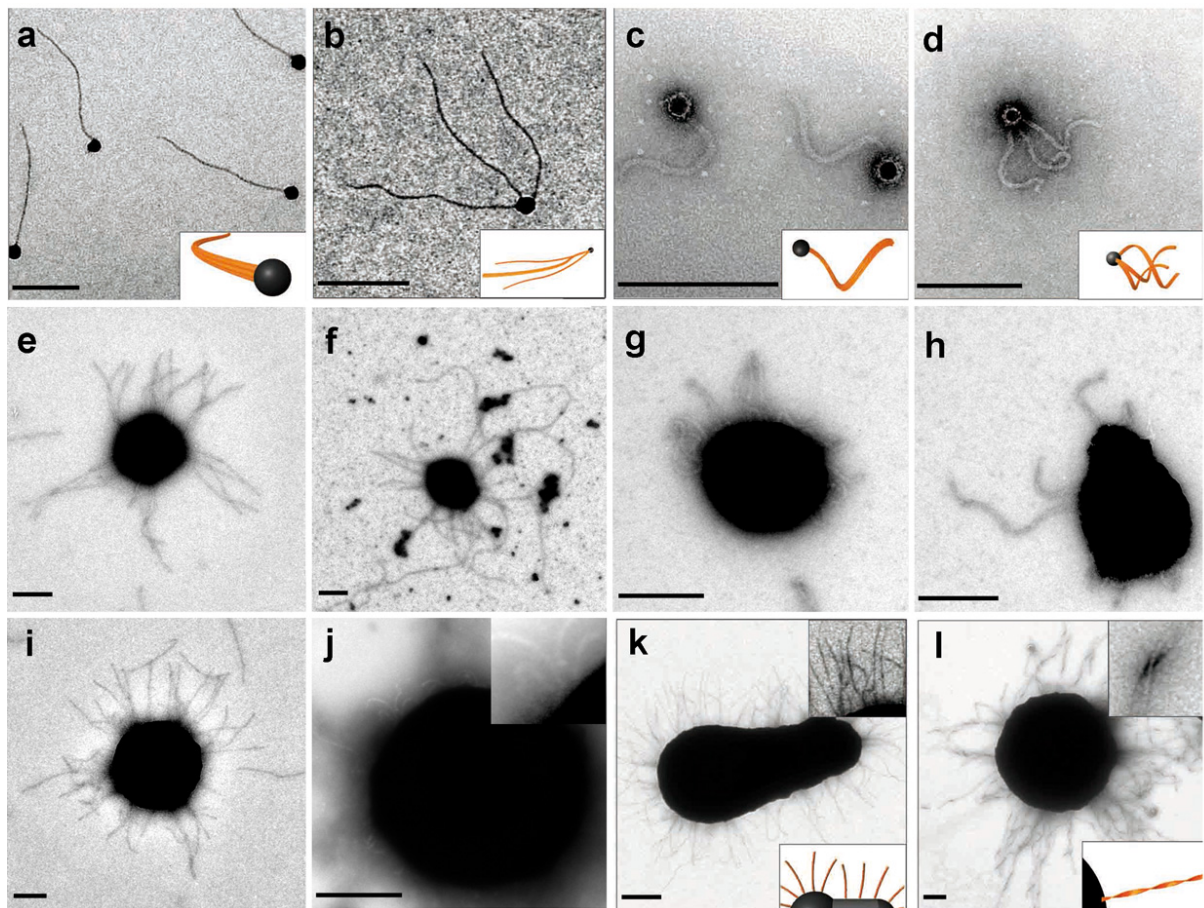


Figure 4.5: Diversity of DNA origami - magnetic bead hybrids. Transmission electron microscopy images of DNA origami - magnetic bead hybrids of (a) single 6HBs attached to 30nm iron oxide particles with and (b) without separation by gel electrophoresis. (c) 14HCs attached to 30 nm iron oxide particles with and (d), without separation by gel electrophoresis. Scale bars 100 nm. (e) Single and (f) multimerized 6HBs and (g) single and (h) multimerized 14HC attached to a 280 nm magnetic particle. (i) 6HBs and (j) 14HCs attached to a 560 nm magnetic particle. (k) 6HBs attached to a 1 μ m glass-titanium composite. (l) Multimerized twisted 3LSs attached to a 1 μ m iron oxide particle. Scale bars: 200 nm.

30 nm bead hybrids were constructed with both, single and many flagella (Figure 4.5a-d) similar to what can be found in motile bacteria. For the construction of multi-flagellated particles, an excess of DNA flagella was added to the magnetic nanoparticles. We observed particles with up to eight DNA flagella attached to a single magnetic nanoparticle (see Appendix D for additional TEM images). For the single-flagellated particles, the artificial flagella were mixed with an excess of nanoparticles. After hybridization a purification step in a 0.5 % agarose gel was performed to separate the well-assembled nanoswimmers from the excess of magnetic particles and from unwanted multi-flagellated particles (Figure 4.6a). Figures 4.6b-c show the high production yield of purified single-flagellated structures.

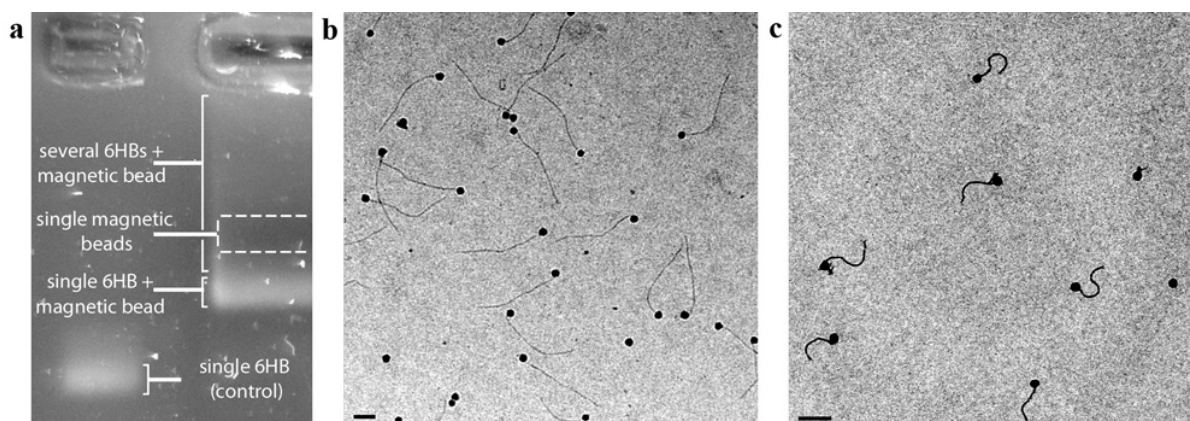


Figure 4.6: Separation of single-tail from multi-tail hybrid structures. (a) Single-head single-tail structures were separated from misfolded or multiple tail formations and unbound magnetic nanoparticles via electrophoresis in a 0.5 % agarose gel. Transmission electron microscopy images show the high yield of b) 6HB and c) 14HC DNA origami – magnetic bead hybrids after gel separation. Scale bars: 100 nm.

For larger nanoparticle sizes (280 nm, 560 nm and 1000 nm), gel purification could not be applied, because the mesh size of the gel was too small for the particles to enter. We therefore constructed only multi-flagellated structures of this kind of nanoswimmers. The successful attachment and multimerization of the DNA flagella on the magnetic particles is shown in Figures 4.6e-l. Unfortunately, we observed that particles with multimerized origami tend to break apart (see Appendix C for TEM images of the destroyed particles). We speculate that their polymeric core shell gets torn open once a certain load of attached material is exceeded. This process seems to be promoted by strong vortexing and during TEM sample preparation, where the attached flagella are exposed to electrostatic forces exerted by the TEM grid.

TEM imaging of the correct attachment of DNA flagella to the magnetic beads was difficult if the attached DNA origami structures were too small compared to the magnetic particles. As illustrated in Figure 4.6j for a 500 nm particle with 14HC flagella, the scattering of the iron-oxide bead strongly overshadowed the origami structure. In such cases, fluorescently labelled DNA origami was used to confirm the successful attachment of the artificial DNA flagella to the magnetic bead via fluorescence microscopy (see Appendix D for details).

Additionally to the iron-oxide particle hybrids, we also constructed a 6HB-covered non-spherical glass-titanium magnetic particle shown in Figure 4.6k, which was provided by the group of Peer Fischer. This demonstrates that our construction method is not solely restricted to spherical geometries or iron oxide as magnetic material.

4.3 Magnetically actuated enhanced diffusion of DNA-based nanoswimmers

In the previous chapter, we demonstrated that by applying the DNA origami technique a variety of swimmer designs could be constructed, which fall within the highly diffusive nanoscale regime. In order to effectively propel, the magnetic nanoswimmers need to fulfil the criteria of low Reynolds number swimming [5]. In other words, their magnetically actuated motion needs to be non-reciprocal in time. However, because diffusion acts increasingly strong and because the magnetic moment of the nanoparticles becomes smaller the smaller the particle gets, an effective propulsion becomes increasingly demanding. In what follows, we will point out three issues that can hinder propulsion of the nanoswimmers:

- i. The magnetic moment of the nanoswimmers needs to follow the rotation of the external magnetic field. Although this demand is trivial for macroscopic magnetic materials with strong magnetic moments, it turns out to be difficult to maintain for nanometre-sized particles. When a ferromagnetic material surpasses a certain size (~ 100 nm for iron-oxide nanoparticles [115]), it undergoes a transition from a multi to a single magnetic domain state. Near room temperature, this transition is accompanied by a change of the magnetic property from ferromagnetism to superparamagnetism. In contrast to the ferromagnetic bulk material, which can exhibit a permanent magnetic moment, superparamagnetic nanoparticles exhibit only two remaining antiparallel orientations of the magnetic moment. These two states rapidly switch with an average time given by the Neel-Arrhenius equation. If the Neel relaxation time t_n is faster than the period of the actuation, a torque on the particle is difficult to realize, because the particle will not be able to follow the rotation. For 20-35 nm superparamagnetic iron oxide particles t_n has typical values of 50 ms – 2 s [116] and therefore requires actuation frequencies of at least 0.5 – 200 Hz.

Larger iron-oxide superparamagnetic nanoparticles (>100 nm) consist of a cluster of smaller nanoparticles embedded in a polymer matrix and therefore exhibit a bigger magnetic moment and higher t_n than that of single nanoparticles. For example, the 1 μm beads used to construct microswimmers in Publication P2 consisted of clustered iron-oxide nanoparticles and already followed the rotation of an externally applied magnetic field with a field frequency of 1 Hz. [27].

- ii. Another factor that has to be taken into account is the rotational diffusion that acts on the nanoswimmers. A helical swimmer needs to be aligned with the rotation axis of the external magnetic field in order to propel. To guarantee this alignment, the rotation speed exerted by the external magnetic fields needs to be faster than the rotational diffusion acting on the swimmer [24, 106]. In our setup, the maximum rotation speed was limited to a maximum angular frequency of ~ 500 Hz at 15 Gauss. This frequency corresponds to a rotational diffusion of a spherical particle with hydrodynamic diameter of ~ 150 nm. In other word, the maximum frequency of the used setup determines a minimal size for the

nanoswimmers the setup can effectively propel. Even more, this limit assumes that the swimmer can rotate at the same speed as the external magnetic field. In general the swimmer will, however, only rotate in sync with the external field up to the so-called “step-out” frequency [117]. Therefore, a realistic lower limit for the propulsion of nanoswimmers at 500 Hz is likely to be higher than 150 nm. Schamel et al. recently calculated that the minimal length their helical swimmers can have before rotational diffusion dominates is ~ 200 nm for an actuation frequency of 100 Hz. This type of swimmer, however, contained a non-biocompatible magnetic material with comparatively strong magnetic moment and therefore exhibits a higher step-out frequency than that of iron oxide – based particles.

- iii. Finally, the relative size between the artificial flagella and the magnetic bead has to be considered. The optimal ratio for rigid chiral structures, which exhibit a spherical cargo on one end, was recently proposed by Keveney et al. [118]. Flexible filaments, on the other hand, need to be flexible on a similar length scale as the bead in order to bend into a chiral shape during propulsion [119].

In applying iii) to our nanoswimmers from Figure 4.5, we conclude that for magnetic particles larger than 560 nm, single origami structures are too small in comparison to the bead size. Unfortunately, the attachment of multimerized origami structures led to the destruction of the magnetic particle similarly to what we reported in the preceding subchapter for 1 μm magnetic particles (see also Appendix D).

On the other end of the size regime, 30 nm particle hybrids are likely to violate i) and ii), since their magnetic moment is very small and their Neel relaxation time is very high. Such swimmers require a very high rotation frequency, while their step out frequency is comparatively low due to their small magnetic moment [117]. Realizing high magnetic fields with high frequencies, however, is technically very demanding.

We tested the ability of the DNA-flagellated magnetic nanoparticle hybrids to propel at low Reynolds number by externally applying a rotating homogeneous magnetic field. The samples were placed in the center of a 3-axis Helmholtz coil system that was integrated into an inverted fluorescence microscope (see Appendix D for detailed information on the setup). The hybrids were exposed to rotating homogeneous magnetic fields of up to 100 Gauss, and their motion captured on video.

No enhanced diffusion was found for the flagellated 30 nm and 280 nm particles from Figure 4.5 even at full field strength (up to 100 Gauss < 100 Hz) and excitation frequencies of up to 500 Hz (with 15 Gauss). We believe, that at these length scales the rotational diffusion was too strong and the magnetic moment too weak to permit propulsion of such small swimmers [106]. Furthermore, due to the small sizes it was not possible to observe the rotation of the particles via microscopy techniques, which is important to confirm the rotational coupling between the external field and the particle’s magnetic moment. We therefore focused our study on the 560 nm hybrids,

which showed a rotation in sync with the external magnetic field already at 2 HZ and 100 Gauss.

Without applied external field the particles were purely diffusive. We determined the translational diffusion constant of the nanoswimmers by tracking the trajectory of the diffusing particles via ImageJ's manual tracking software as illustrated in Figure 4.7a. Therefore, we confined the diffusive motion of the particle to two dimensions by putting the sample between two tightly pressed glass slides. This enabled us to continuously follow the movement of the structures. In order to prevent sticking of the particles to the glass surface, we passivated the surface with BSA overnight prior to the experiment. For a clearer visualization of the hybrid structures via fluorescence microscopy, we further attached Cy3 dyes to the origami structures via hybridization of complementary DNA strands (see Appendix D for a detailed description of the applied methods and materials).

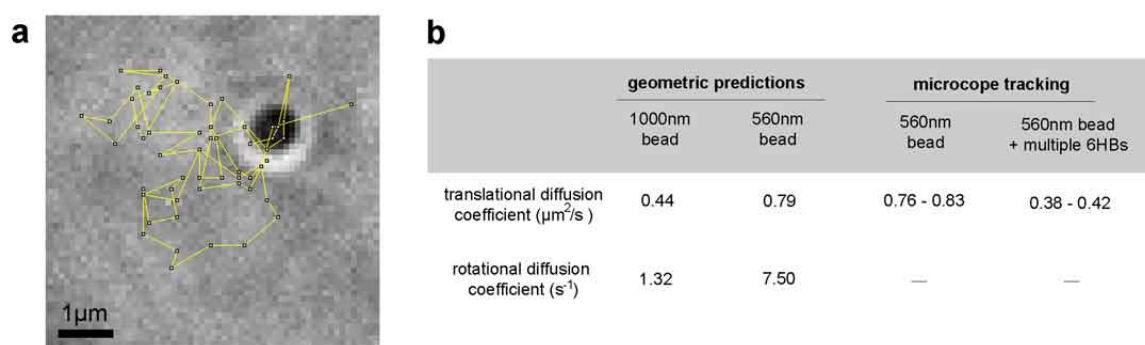


Figure 4.7: Determination of the diffusion coefficient of nanoparticles via 2D tracking. (a) 2D tracking of the diffusive motion via ImageJ's manual tracking software, exemplarily shown for a 560 nm magnetic particle. (b). Translational and rotational diffusion coefficient calculated for a sphere with 1000 nm and 500 nm diameter compared to the measured translational diffusion coefficients for a 560 nm magnetic bead w/o attached 6HBs.

From the recorded data of the 2D diffusive motion of the particles, we extracted the mean square displacement (MSD) at different time steps τ , from which we then received the diffusion constant via

$$D_T = \frac{MSD(\tau)}{4\tau} \quad (4.6)$$

In Figure 4.7b, the measured translational diffusion coefficient of 6HB - magnetic bead hybrids, and single 560 nm magnetic particles are compared to the Stokes-Einstein diffusion coefficient of a sphere:

$$D_{T_{sphere}} = \frac{k_B T}{6\pi\eta R} \quad (4.7)$$

The 560 nm beads with multiple 6HB flagella showed a similar translational diffusion to that of a sphere with 1000 nm in diameter. This value is reasonable assuming that the DNA flagella protruding from the bead's surface are flexible structures and therefore did not attribute with their full length to the hydrodynamic radius of the hybrid. The calculated value for a 560 nm bead also coincided remarkably well with the measured value.

The good accordance of measured and theoretical values suggested that the applied particle tracking technique is a promising method for determining the translational diffusion coefficient of the magnetically actuated particles. However, in order to fully understand the diffusive behaviour of our nanoswimmers, it is also important to know the rotational diffusion constant. Unfortunately, our setup did not allow determining this value experimentally. We therefore representatively calculated the rotational diffusion for the 1000 nm sphere with similar translational diffusion coefficient as the nanoswimmers (Figure 4.7b) via

$$D_{R_{sphere}} = \frac{k_B T}{8\pi\eta R^3} \quad (4.8)$$

Because the 560nm - 6HB flagella nanoswimmers are uniformly decorated with the artificial flagella, this estimation seems reasonable. From the above equation, we get $D_{R_{1000nm}} = 1.32 \text{ Hz}$ for the 1000nm bead. Because the applied actuation frequency of 2Hz was higher than $D_{R_{1000nm}}$, we expect the nanoswimmer to couple to the rotation of the external magnetic field.

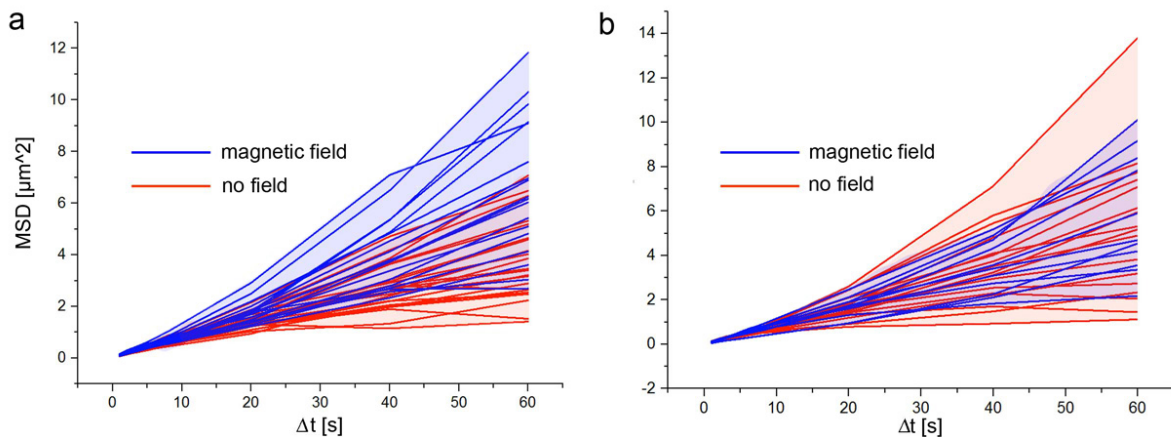


Figure 4.8: Diffusion of hybrid particles w/o magnetic actuation. Mean square displacement (MSD) of (a) 14HC - 560 nm and (b) 6HB - 560 nm hybrid particles at increasing times between two measurements Δt . Blue colouring signifies that the external magnetic field was activated, while red colouring belongs to hybrid particles where no field was applied. Note that the MSD data of each particle is connected by a solid line to facilitate identification.

Figure 4.8 shows the mean square displacement at increasing times between two measurements for 14HC - and 6HB - 560 nm hybrids actuated at 2 HZ and 100 Gauss. Each trace represents one tracking event.

We observed a tendency towards an enhancement in the diffusivity of the 14HC hybrids (blue area in Figure 4.8a), while the 6HB hybrids showed no apparent change. We assumed that the 6HB hybrid's persistence length is too large to allow bending into a chiral shape, which is required for active propulsion. The 14HC, on the other hand, already exhibits a helical shape by design, which allows for an active propulsion of the swimmer and an associated increase in the diffusion.

In order to examine whether this enhancement in the MSD is indeed from an active propulsion, we averaged the MSD for all tracked particles (Figure 4.9a) and independently analysed the diffusion in the in-plane axes x and y (Figure 4.9b). The magnetic field rotated perpendicular to the x -axis and should therefore only effectively propel the particle along this particular axis. We therefore expected a purely diffusive behaviour along the y -axis and an enhanced diffusion for long time scales on the x -axes.

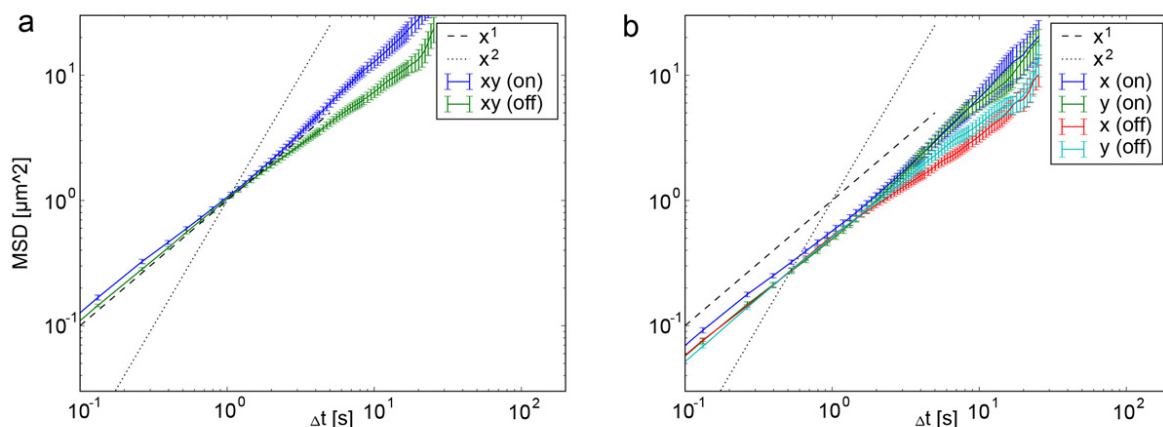


Figure 4.9: Diffusion of hybrid particles along and perpendicular to the rotation axis of the external magnetic field. (a) Log-log plot of the MSD (averaged value of the 14HC-500 nm hybrids from Figure 4.8) at increasing times between two measurements Δt . At larger time scales, an enhanced diffusion was observed for particles where the external magnetic field was applied (blue data points) compared to particles where no field was applied (green data points). (b) The MSDs calculated independently for the x -axis (perpendicular to the applied rotating field) and y -axis (in plane with the rotating field) showed no significant difference regarding the diffusion along the x and y -axis.

Surprisingly, we observed an enhancement in the diffusion at higher time scales along both the x and the y -axis. This contradicts with the assumption that the enhancement is caused by an active propulsion along the x -axis. Additionally, we found an oscillatory behaviour around the actuation frequency of 2 HZ. A similar behaviour was previously reported for reciprocal swimmers by Lauga et al. [105, 109]. This suggests that our swimmers are actuated in a reciprocal instead of a non-reciprocal way. This would also explain why we did not observe a different diffusive behaviour along the x and y -axis.

We speculate that the reciprocal motion might be caused by an incomplete coupling between the external magnetic field and the magnetic moment, which resulted in a wobbling of the swimmer instead of a full rotation.

4.4 Conclusions and Outlook

Throughout this chapter, we demonstrated that the DNA origami technique is a promising approach for the assembly of biocompatible artificial swimmers at the nanoscale. The DNA origami toolbox allowed us to construct a broad variety of artificial flagella with pre-determined shapes that are known to propel at low Reynolds number [5]. Furthermore, DNA origami provides a conjugation method for the attachment of magnetic nanoparticles, which allowed us to realize magnetic bead – DNA flagella hybrids in a multi- or single-tail like fashion with sizes as small as 150 nm.

In our initial study on the magnetic actuation of the nanoswimmers, we exerted the particles to an external magnetic field and analysed their diffusive behaviour. We observed a slight enhancement in the diffusion accompanied by an oscillatory behaviour, which occurred around the actuation frequency. We believe that this effect comes from a reciprocal motion of the swimmer, as previously reported by Lauga et al. [105, 109].

In future studies, it will be interesting to explore why our magnetically actuated nanoswimmers underwent a reciprocal as opposed to a nonreciprocal motion. One possibility is that the coupling between the external magnetic field and the magnetic moment of the particle was too weak, which led to a reciprocal wobbling rather than a complete rotation of the swimmers. Nevertheless, if the remaining hurdles can be overcome, nanoswimmers could provide great advantages over their macroscopic counterparts, for example in penetrating tissues and membranes, which are inherently too dense for macroscopic structures to enter.

5. ATPase-functionalized DNA nanostructures for the propulsion of autonomous microswimmers

In recent years, biomolecular motors have received increasing research attention due to their ability to provide actuation at the nano- and microscale. By converting biochemical energy, these structures drive fundamental biomechanical tasks, such as translocation along microtubule filaments, transport of cellular cargo, muscle contraction and bacterial flagellation. Famous and well-studied representatives are kinesin [120], myosin [121], the bacterial flagellar motor [13] and the ATP-hydrolysing motor adenosine triphosphate synthase (ATPase) [122].

In nanotechnology, these biomolecular motors are hoped for providing mechanical motion and work in future micro- and nanodevices [4, 31]. Exploration of the efficient energy conversion and of the incorporation into larger biological materials, similar to what is found in muscle sarcomeres and bacterial flagella filaments, are envisioned. Achieving such hybrid constructs, however, requires an interface between the biological motor and the artificial micro- or nanodevice, which is difficult to realize. Preliminary solutions to this problem have been presented by immobilizing kinesin and myosin on microscopy cover slips [123, 124] or in narrow channels [125].

For the construction of hybrid microswimmers, which can propel by rotating helical filaments similar to motile bacteria, the rotary motor complex ATPase is of special interest.

5.1. The F1Fo-ATPase rotary motor complex

The F1Fo-ATPase is a rotary molecular motor belonging to the F-Typ ATPase family, which uses a gradient of positively charged hydrogen ions to produce ATP from ADP. It is composed of the catalytic F1 and the membrane-embedded Fo part, as illustrated in Figure 5.1.

The energy for the ATP synthase is provided by an ion flux through Fo. This flux drives a conformational change in F1, which rotates the structure and produces ATP from ADP. This process, however, can also work in reverse [126]. Consumption of ATP leads to a rotation of the motor and pumps the ions against their electrochemical gradient. The resulting rotation has been visualized in different microorganisms such as bacillus PS3 [122], *E. coli* [127], spinach chloroplasts [128] and human mitochondria [129].

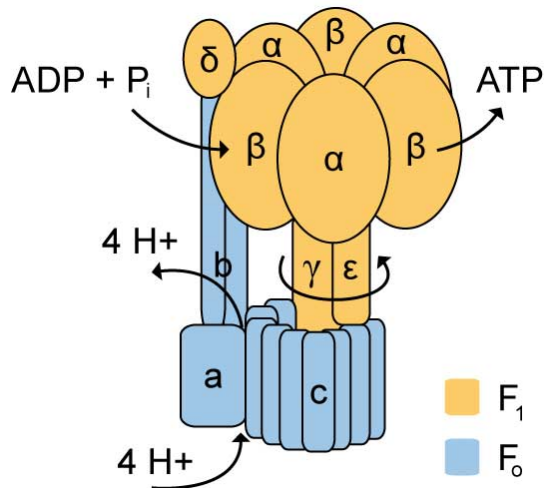


Figure 5.1: Schematic of the F₁F₀-ATPase rotary motor protein. The structure is subdivided into the membrane-embedded F₀ part and the catalytic F₁ part. The F₀ part anchors the motor in the cell wall and provides an ion flux from the inside to the outside of the cell. The F₁ part uses this ion flux to provoke a rotation, which produces ATP from ADP.

For applications in micro- and nanodevices, the rotary part F₁ is usually isolated from the stator F₀. First examples of F₁-ATPase driven nanostructures were demonstrated by rotating nickel nanopropellers [130], polystyrene beads [131], gold nanocolloids and rods [131, 132] and magnetic beads [133] through the addition of ATP. These devices are generally constructed by coupling the F₁-ATPase to a surface via a histidine tag on the beta subunits of the ATPase and by attaching the nanostructure via biotin-streptavidin to the gamma or epsilon part of the biomolecule.

5.2. DNA filament – F₁-ATPase motor protein hybrids

For the construction of ATPase-driven microswimmers, in a first attempt, we focused on mimicking the bacterial flagella complex. It consists of the bacterial flagellar motor attached to a bacterial filament. In order to mimic the bacterial filament, we applied the DNA origami technique. As described in chapter 1 and 4, this method allows the realization of arbitrary nanostructures with nanometre design precision and is therefore a sophisticated choice for mimicking the bacterial flagella shape. Furthermore, DNA origami constructs can be functionalized on predefined sites of the structure, which enables the specific attachment of the motor protein. This is a crucial requirement for the construction of a motor protein-based microswimmer, as each filament needs to be connected to exactly one motor protein. This quality is not self-evident for all DNA self-assembly techniques. For example, DNA tile assembled artificial flagella presented in chapter 1 and 2 would exhibit repetitive binding sites due to their repetitive tube segments. Such structures would bind several motors with the same filament, which would block the rotation mechanism of the motor proteins.

For the actuation of our artificial flagella, we chose the F1-ATPase as rotary motor in analogy to the bacterial flagellar motor in real bacteria. It was provided by the group of Peer Fischer, who extracted the protein from *E. coli* bacteria [134]. *E. coli* bacteria serve as an especially reliable source of rotary molecular motors as they are the most widely studied prokaryotic model organism and can be easily modified and reproduced under favourable conditions and in short times. For the attachment of the motor to the DNA filaments, two biotin molecules were coupled to genetically modified cysteine sites on the gamma and epsilon part of the ATPase via biotin-maleimide chemistry [134].

Because cluster formation hinders the correct formation of hybrid flagella, we tested the F1-ATPase towards its stability against aggregation under DNA origami-friendly salt concentrations (Figure 5.2). No significant enhancement in cluster formation was observed even under relatively high salt conditions (12 mM MgCl₂ and 500 mM NaCl).

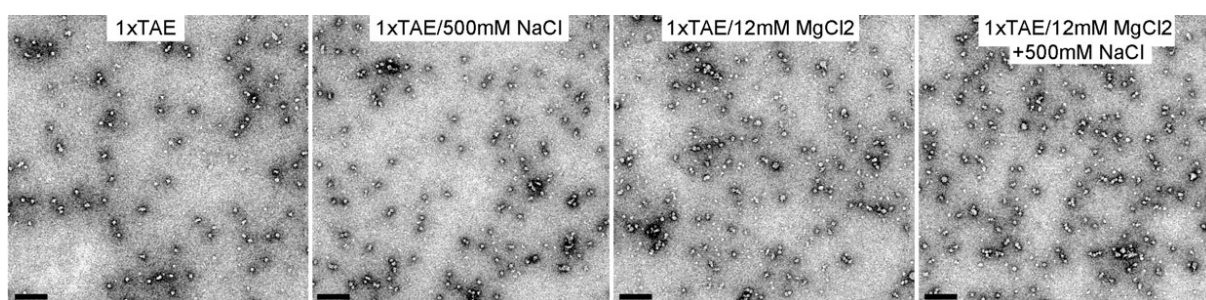


Figure 5.2: ATPase at varying salt concentrations. Even at high salt concentrations of 12 mM MgCl₂ and 500 mM NaCl, the ATPase remained mostly monodisperse in a 1xTAE buffer. Scale bars: 100 nm.

We chose four different DNA origami shapes for the construction of DNA filaments illustrated in Figure 5.3a. As mentioned in chapter 3, the 6HB, 14HC and 3LS have shapes that are known to propel at low Reynolds number and are therefore promising candidates as flagella mimics. We extended this set of artificial filaments by constructing a 24-helix corkscrew (24HC), which is designed to constitute a helical shape of microscale diameter when multimerized (TEM images of the single and multimerized structure are provided in Appendix E). Compared to the 14-helix corkscrew, the 24HC has a higher stiffness [71] and larger helical diameter, which more closely resembles the dimensions of bacterial flagella.

The DNA origami constructs were further designed to exhibit several biotin molecules protruding from one end of the structure as exemplarily illustrated for the 6HB in Figure 5.3b. These modifications enable coupling to the F1-ATPase motor protein via a two-step reaction (Figure 5.3c). In the first step, DNA origami structures were mixed with an excess of neutravidin, so that each biotin position was occupied and then purified from the excess neutravidin. In a second, the neutravidin-modified origami structures were coupled to the biotin-modified F1-ATPase to yield hybrid flagella. Note that the purification of excess neutravidin is essential, as remaining unbound neutravidin could block the biotin sites on the ATPase and hinder the attachment of the origami filament.

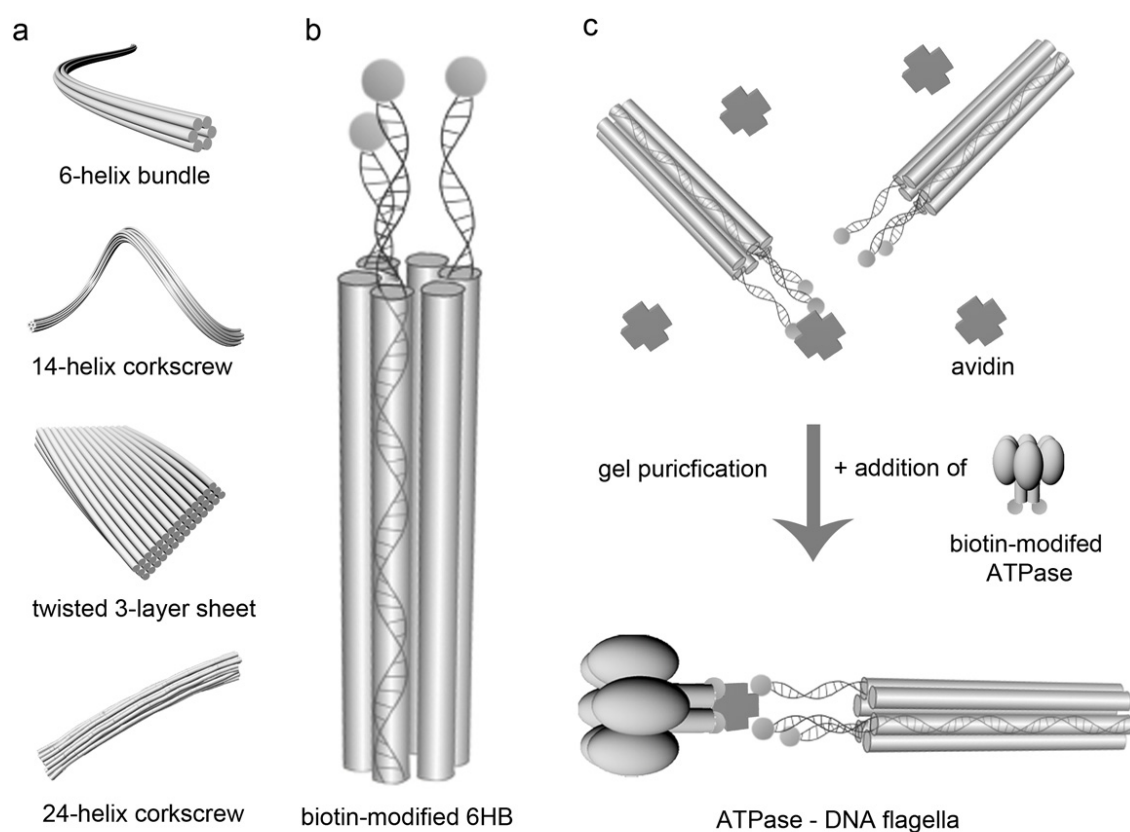


Figure 5.3: Design scheme of DNA filament – F1-ATPase motor protein hybrids. (a) Four different DNA origami structures were designed for the construction of artificial DNA filaments. From top to bottom: 6-helix bundle (6HB), 14-helix corkscrew (14HC), 3-layer sheet (3LS) and 24-helix corkscrew (24HC). (b) Artificial filaments were first modified with biotin at one end of the structure. (c) After the addition of an excess of neutravidin and subsequent purification, the neutravidin-functionalized particles were coupled to the biotin-modified sites on the F1-ATPase motor protein resulting in DNA filament – F1-ATPase motor protein hybrids.

Figure 5.4a shows a 0.7 % agarose gel containing the origami structures after neutravidin attachment. For each sample, a characteristic band corresponding to the respective monodisperse structure could be identified via ethidium bromide staining. After extraction from the gel, the structures were imaged by TEM (Figure 5.4b). The extracted particles exhibited white spots at one side of their structure, which speaks for the correct attachment of the neutravidin molecules. The spots coincided well with the designed positions of the biotin modifications on the DNA origamis and also corresponded well to the size of single neutravidin proteins (~ 5 nm in diameter; see TEM picture of the 24HC). Besides well-attached neutravidin, we also observed bigger spots (see TEM picture of the twisted 3LS) that exceeded the size of single neutravidin. We speculate that neutravidin clusters formed due to electrostatic forces between the molecules induced by the divalent Mg^{2+} ions present in the solution.

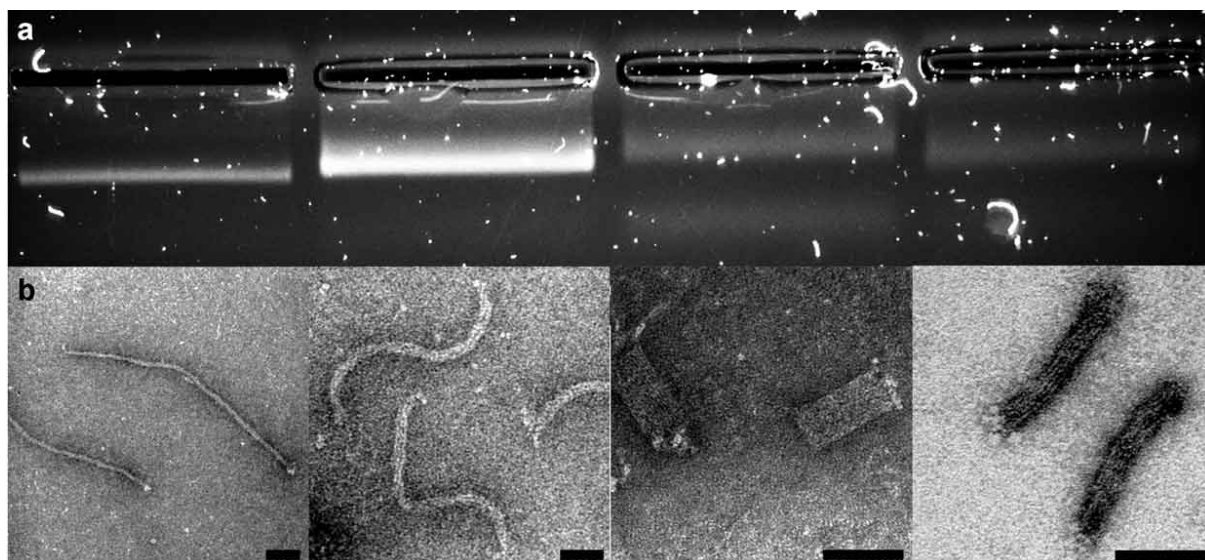


Figure 5.4: Purification of neutravidin-modified DNA origami constructs. (a) Purification of neutravidin-modified 6HB, 14HC, twisted 3LS, and 24HC in a 0.7 % agarose gel. All four samples showed a single band, which corresponded to the designed monodisperse structure. (b) TEM images of the extracted structures showed the successful attachment of neutravidin to one side of the particles. Scale bars: 50 nm.

In Figure 5.5, neutravidin-modified origami structures are shown after the addition of an excess of biotin-modified F1-ATPase and overnight incubation. We distinguished the attached ATPase from neutravidin molecules by its larger size (~ 10 nm) and by its coarse structure, which often exhibited a hole in the middle when imaged from the top (see inlets of Figure 5.5a and c). In some cases, however, a clear distinction was not possible as neutravidin proteins formed clusters with similar sizes to that of the ATPase. Considering this source of error in the identification of the ATPase, we found that only < 5 % of the origami structures had ATPase attached at the correct position of the structure.

From the low yield of well-assembled structures, we conclude that the observed coupling was either unspecific or that the majority of biotin sites on the ATPases were already blocked before they could attach to the neutravidin-functionalized origami. This blockage could be caused by free neutravidin, which remained in the purified origami solution. Indeed, we found unbound neutravidin in the vicinity of the origami structures by TEM even after gel purification (see Appendix D). We believe that the neutravidin bound unspecifically to single stranded DNA overhangs on the origami during the electrophoresis and therefore was not removed during purification. To clean the sample of the excess neutravidin, we also tested purifying the sample via gel electrophoresis in a monovalent salt buffer (500 mM NaCl) and by PEG purification. Unfortunately, sodium chloride increased cluster formation of the neutravidin, while PEG purification resulted in an even higher amount of unbound neutravidin (see Appendix D for TEM images).

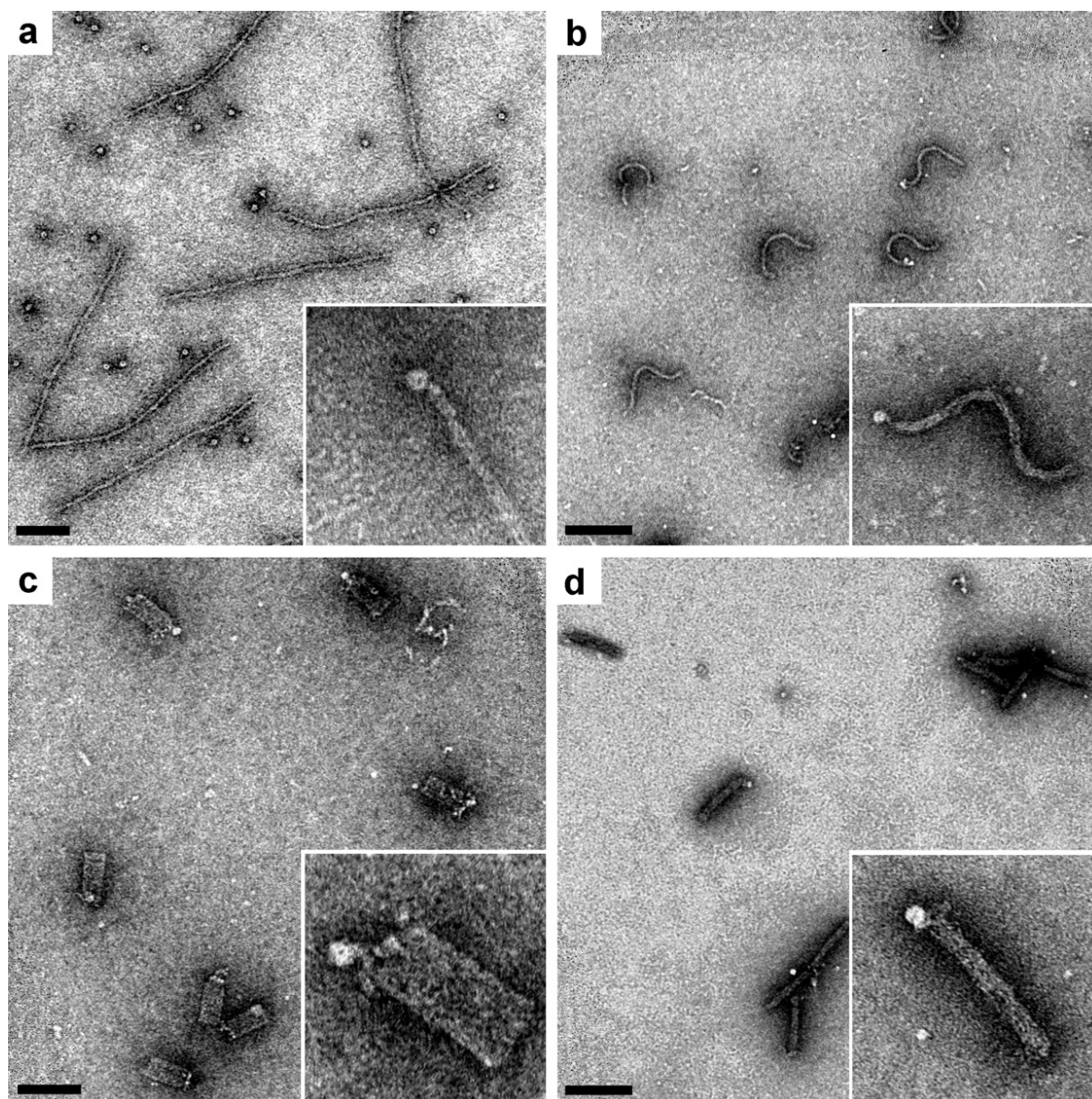


Figure 5.5: Attachment of ATPase to neutravidin-modified DNA constructs. TEM images of single ATPases attached to neutravidin-modified (a) 6HB, (b) 14HC, (c) twisted 3LS and (d) 24HC. Only few particles with an attached ATPase (inlets) were found. Scale bars: 100 nm.

In order to test whether the low attachment yield is due to free neutravidin in the solution, we mixed neutravidin-modified origami structures with biotin-modified origami structures in a control experiment. If free neutravidin indeed blocked all the biotin sites, we would expect to see a low coupling yield of the different origami structures. We chose the neutravidin-modified 6HB and the biotin-modified 14HC for this test, as both structures are easily distinguishable by their different shapes and have a similar structural cross section, which allows them to attach one by one.

We found $\sim 50\%$ of well-assembled 6HB-14HC dimers (Figure 5.6a and 5.6b), $\sim 30\%$ of uncoupled structures (Figure 5.6a), $\sim 10\%$ of 14HC-14HC dimers (Figure 5.6c) and $\sim 10\%$ of 6HB-6HB dimers (Figure 5.6d). Next to the many unbound

structures, especially the 14HC-14HC dimers attracted our attention as these structures could only have formed if free neutravidin was in the solution and cross-linked the biotin-modified origami.

From these observations, we conclude that free neutravidin might indeed affect the yield of ATPase binding to neutravidin-modified origami structures. However, as the yield of ATPase binding differed by an order of magnitude from that observed in the control experiment, other factors like inaccessible or missing biotin molecules on the ATPase might have played an equally if not stronger role. For the construction of hybrid microswimmers, we changed our strategy and assembled the artificial hybrid flagella on the surface of a magnetic bead, as we will describe in the following chapter.

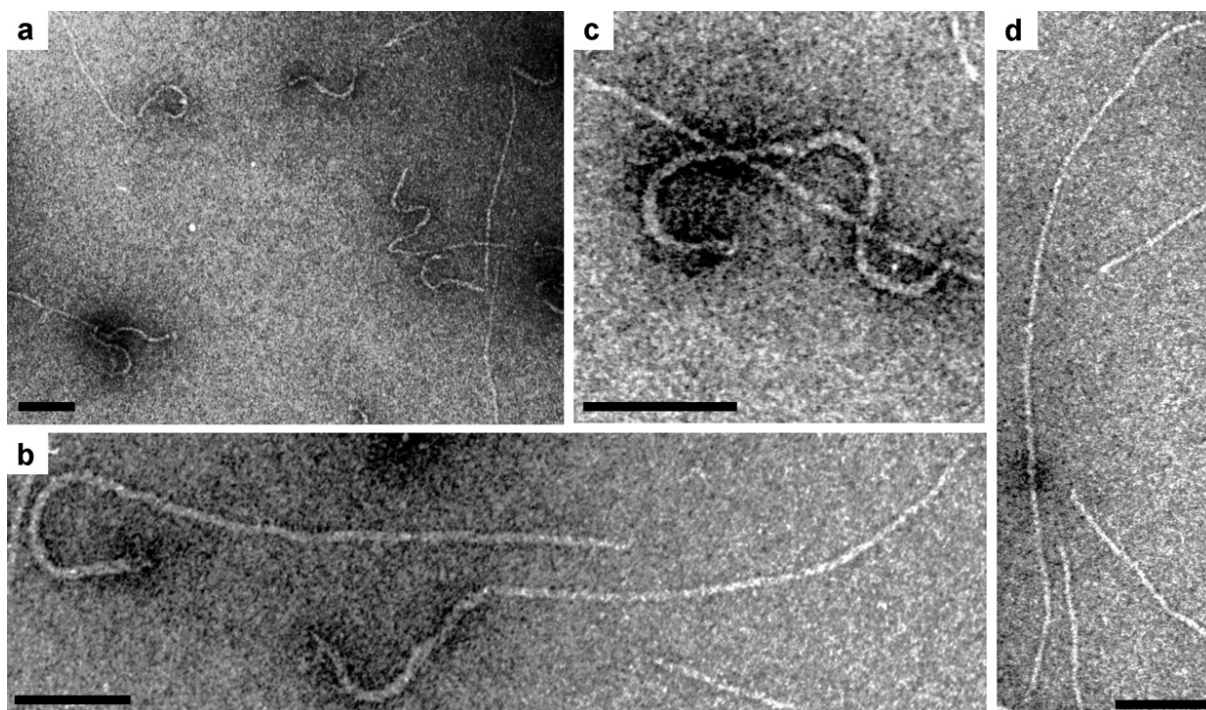


Figure 5.6: Coupling efficiency between neutravidin-modified and biotin-modified DNA origami constructs. (a) Approximately 50 % of well-assembled dimers formed. (b) The biotin-neutravidin connection was visible as a “white spot” between the connected structures. Besides the well-assembled structures, also unwanted (c) 14HC-14HC and (d) 6HB-6HB dimers formed. Scale bars: 100 nm.

5.3 F1-ATPase – DNA Filament Hybrids Coupled to a Microparticle: A prototype for autonomous microswimmers

For the construction of artificial ATPase-driven microswimmers, the F1-ATPase - DNA filament hybrids have to be anchored in a body of considerably greater mass, similar to the connection between a bacterial flagella and its cell body. The mass difference between our artificial flagella and body guarantees that the flagella can rotate at high frequencies, while the body remains nearly static.

We chose a 1 μm magnetic particle for our microswimmer's body, as it brings the required high mass and allows a gentle and easy purification through magnetic pull-down compared to non-magnetic material. This is especially useful considering that a complete purification of excess neutravidin could not be achieved during the constructing of ATPase – DNA filament hybrids via agarose gel purification as described in the previous chapter. Performing the assembly of the artificial hybrid swimmers on the surface of magnetic beads, which can be easily purified, could bypass this problem.

Figure 5.7 demonstrates the construction scheme for artificial hybrid microswimmers. First, F1-ATPases were coupled to the 1 μm magnetic beads via His₁₀-tags (Figure 5.7a). F1-ATPase possesses ten histidine tags at the *N* termini of each β subunit, which can couple to a cobalt-based chemistry on the bead surface in the presence of a tetradentate metal chelator. The ATPase-functionalized magnetic particles were then purified by magnetic pull-down and coupled to neutravidin molecules via the two biotin modification on the γ and ϵ part of the ATPases (Figure 5.7b and Figure 5.1). After a second purification step, biotin-modified DNA-origamis were added to obtain the hybrid swimmers (Figure 5.7c).

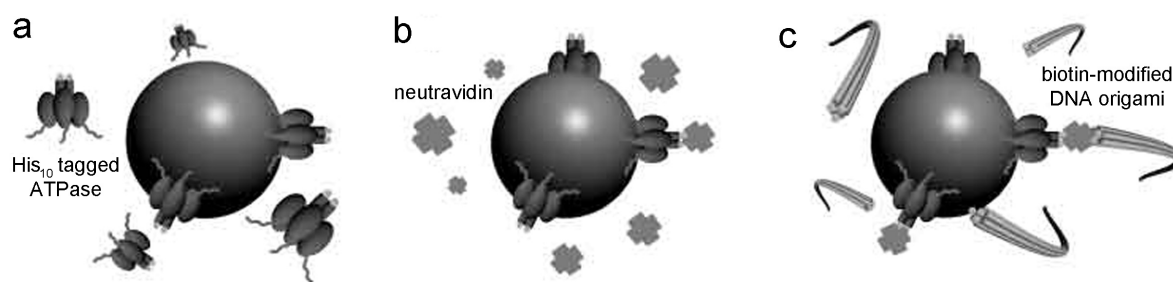


Figure 5.7: Construction scheme for autonomous microswimmers. (a) ATPases are coupled to the surface of 1 μm magnetic particles via His₁₀ tags. (b) Neutravidin is attached to biotin modifications on the His tag - opposing side of the ATPase. (c) Biotin-modified DNA origamis are coupled to the neutravidin-modified ATPases.

Figure 5.8a shows TEM images of hybrid microswimmers constructed by the above-described method. We chose the 6HB as representative for all four origami structures as its long shape (~ 428 nm) facilitated the visualization of the correct attachment on the magnetic bead's surface by TEM. We observed a great number of 6HB origami radially attached to the magnetic bead and only few unattached structures in the vicinity of the bead.

In order to rule out that the observed attachment resulted from unspecific binding between components which were not supposed to couple, we examined control samples where one or more sub steps in the assembly and the corresponding components were intentionally left out, such as neutravidin (Figure 5.8b), ATPase (Figure 5.8c) or both (Figure 8d). In all three samples, no or only little binding was observed.

We further assembled the hybrid structures in an EDTA-rich buffer. EDTA is known to chelate metal ions and thereby destroys the his-tag connection. Figure 5.8e shows magnetic beads, which have undergone the same assembly steps as the particles shown

in Figure 5.8a, with the exception that the buffer contained EDTA. We observed hardly any attached artificial flagella, which confirmed that the formation of the his-tag bond was indeed impeded by EDTA. This suggests that the his-tag bond has formed correctly in the well-assembled hybrid structures from Figure 5.8a.

Taken together, these observations suggest a great specificity for the coupling between the different components in the presented construction method. Nevertheless, we could not finally exclude that unspecific binding might have occurred within one or more of the coupling steps.

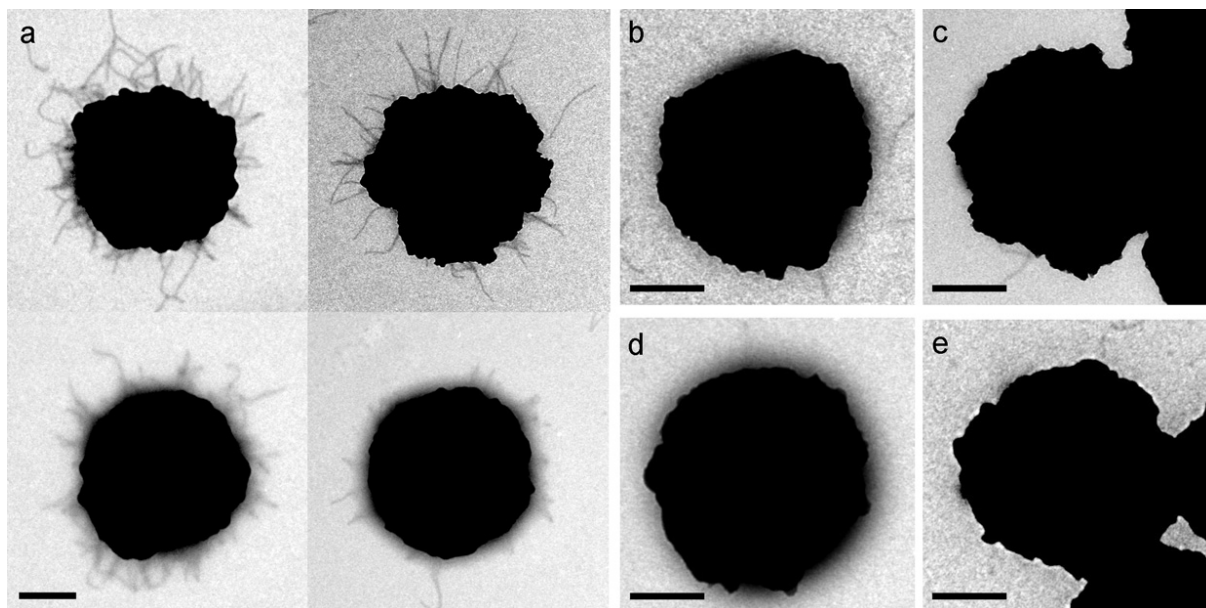


Figure 5.8: Magnetic microparticle - ATPase - DNA origami hybrids. (a) TEM images of well-formed hybrid structures assembled from a $1\mu\text{m}$ magnetic particle, ATPases and 6HB origamis. (b-d) TEM images of control samples, where the following components of the construction sequence were intentionally left out: (b) neutravidin, (c) ATPase, (d) neutravidin and ATPase. Hardly any attachment of 6HBs to the magnetic bead surface was observed. (e) No coupling occurred further when the construction was performed in an EDTA-rich buffer. Scale bars: 300 nm.

In order to test whether the incorporated ATPases are still active and can propel the hybrid constructs, we added the coenzyme adenosine triphosphate (ATP) to the microswimmer solution and imaged the structures via fluorescence microscopy. For a better visualization, the DNA origami filaments were functionalized with Cy3 dyes prior to the experiment. ATP is known to induce a rotation of the F1-ATPase motor [126] and we expected that the motor rotation will translate to the DNA filaments, which then drive the swimmer.

Unfortunately, we did not observe an ATP-induced motion of the hybrid particles. Instead, the origami structures seemed to detach from the beads immediately after the addition of the ATP. We deduced this detachment from a reduction of the fluorescence intensity on the beads and from a simultaneous increase of fluorescent spots on the surface surrounding the beads. We speculate that the ATP-induced rotation of the motor

protein exerted such strong forces that it destroyed the connection between bead and artificial flagella. In order to find the weak spot in the assembly, we imaged the swimmers after ATP addition via TEM as illustrated in Figure 5.9.

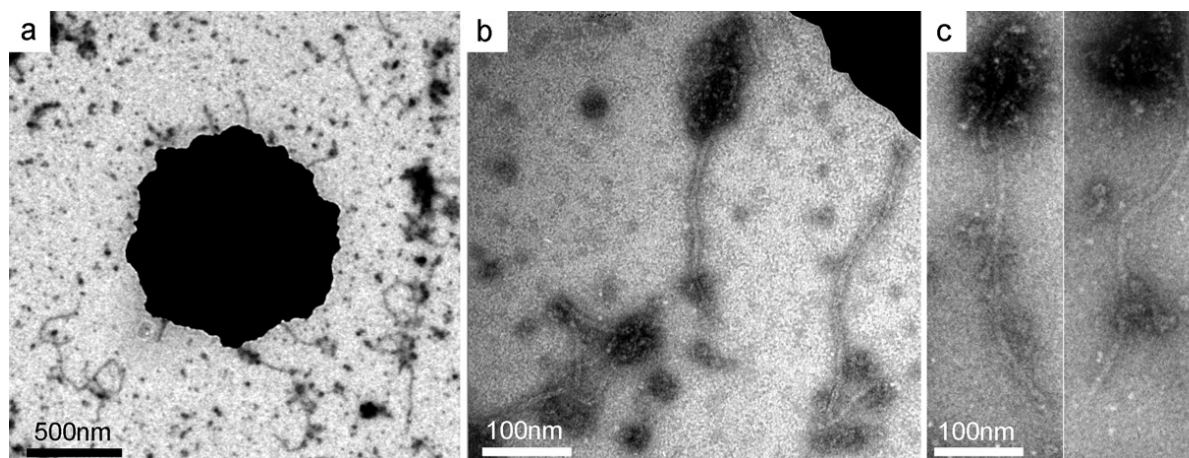


Figure 5.9: Detachment of hybrid flagella from magnetic particles upon addition of ATP. (a) Few 6HB hybrid flagella remained attached to the magnetic particles after the addition of ATP. (b) Many partly destroyed 6HBs were found in the vicinity of the bead, which (c) exhibited unidentifiable constructs at one end of the origami structure.

TEM imaging revealed that after the addition of ATP, only few flagella remained attached to the magnetic beads (Figure 5.9a) compared to the well-assembled structures before actuation shown in Figure 5.8a. Many unattached and partly destroyed origami structures were found in the bead's vicinity (Figure 5.9b). These structures often exhibited dark spots at one of their ends (Figure 5.9c). These constructs resembled pieces of destroyed magnetic particles similar to what we observed in chapter 4 after the attachment of multimerized DNA origami to magnetic particles. We believe that the force exerted by the rotating artificial flagella ripped the flagella and the connected part of the particle's polymer shell from the bead, which resulted in the detachment of the flagella.

5.4. Conclusion and Outlook

The incorporation of a molecular motor such as the FoF1-ATPase into an artificial microswimmer is of great interest in the field of nanorobotics [4, 31]. It can lead to a new class of artificial devices that move autonomously similar to the motion of motile bacteria. Throughout this chapter, we provided a concept for the construction of such ATPase-driven microswimmers by placing the molecular motor ATPase between a DNA-based filament and a magnetic microparticle.

To realize this goal, in a first attempt, we constructed DNA origami filaments, which we functionalized with the molecular motor F1-ATPase through biotin/streptavidin coupling. Although we were able to achieve some well-assembled structures, the

construction yield was too low to continue the construction of microswimmers from these artificial flagella.

We therefore, in a second approach, initiated the assembly on the surface of magnetic microparticles by attaching the ATPase via a His-tag to the bead surface and successively attaching the DNA filaments via biotin/neutralavidin coupling to the ATPases. We indeed observed the correct attachment of many DNA filaments per bead suggesting a successful assembly. Unfortunately, upon addition of ATP, the DNA filaments detached from the microparticle's surface. We believe that the ATP-induced rotation of the molecular motor ripped part of the polymer shell and the attached filaments from the bead.

In future experiments, the choice of the microparticle's surface should be reconsidered. For example, commercially available SiO₂ microparticles constitute a more rigid surface compared to polystyrene-coated beads and might therefore withstand the force exerted by the molecular motor.

If the described construction hurdles can be overcome, it will be important to find ways of asymmetrically decorating the particle surface with the artificial flagella. Such an asymmetric decoration is required in order to move in a directed way. In the case of a symmetric decoration, opposing flagella would work against each other resulting in no net displacement.

6. Associated Publications

6.1. Associated Publication P1

Self-Assembled DNA Tubes Forming Helices of Controlled
Diameter and Chirality

By

Alexander Mario Maier, Wooli Bae, Daniel Schiffels, Johannes
Friedrich Emmerig, Maximilian Schiff, and Tim Liedl

published in

ACS Nano 2017

Reprinted with permission from Ref [94]. Copyright 2017
American Chemical Society.

Self-Assembled DNA Tubes Forming Helices of Controlled Diameter and Chirality

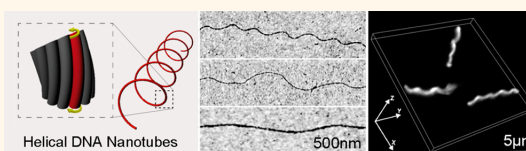
Alexander Mario Maier, Wooli Bae, Daniel Schiffels,^{||} Johannes Friedrich Emmerig, Maximilian Schiff, and Tim Liedl*^{||}

Faculty of Physics and Center for NanoScience, Ludwig-Maximilians-Universität (LMU), Geschwister-Scholl-Platz 1, 80539 München, Germany

S Supporting Information

ABSTRACT: Multihelical DNA bundles could enhance the functionality of nanomaterials and serve as model architectures to mimic protein filaments on the molecular and cellular level. We report the self-assembly of micrometer-sized helical DNA nanotubes with widely controllable helical diameters ranging from tens of nanometers to a few micrometers. Nanoscale helical shapes of DNA tile tubes (4-, 6-, 8-, 10-, and 12-helix tile tubes) are achieved by introducing discrete amounts of bending and twist through base pair insertions and/or deletions. Microscale helical diameters, which require smaller amounts of twist and bending, are achieved by controlling the intrinsic “supertwist” present in tile tubes with uneven number of helices (11-, 13-, and 15-helix tile tubes). Supertwist fine-tuning also allows us to produce helical nanotubes of defined chirality.

KEYWORDS: DNA nanotechnology, DNA self-assembly, helical nanotubes, chirality, protein filament mimics



Helical motifs can be found throughout biological micro- and nanostructures. Famous examples are the double helix of DNA,¹ cellulose fibrils of tendrils² or the shell of holoplanktonic mollusks³ to name just a few. At the macroscopic world, screws and springs, both helical structures, serve essential mechanical functions in classical engineering such as conversion of rotational into linear motion or storing and releasing mechanical energy by using a combination of rigidity and elasticity. Miniaturizing these concepts to the micro- and nanoscale would not only allow the construction of materials, which can function as mechanical nanotools, but also provide an adjustable helical building block to mimic hierarchically assembled structures such as protein filaments. Top-down fabrication methods have so far produced micro- and nanohelices by strain-induced self-scrolling,^{4–6} glancing angle deposition^{7–10} of evaporated or sputtered materials, and 3D direct laser writing^{11,12} in photoresists. Micro- and nanoscrews fabricated by these methods were recently used for the propulsion of artificial micro- and nanoswimmers,^{5,8,13–16} which are foreseen to achieve future biomedical tasks such as *in vivo* drug delivery or blood clot removal.^{17–19} Micro- and nanosprings were found to possess extraordinary properties, such as superelasticity^{6,20,21} and high mechanical strength,²² making them promising candidates for the construction of shape memory materials^{6,20} and composites with improved mechanical integrity.²³ However, large-scale production of three-dimensional structures at the nanometer scale is challenging for conventional techniques, and many of the employed materials are not biocompatible, which hampers their potential for biomedical applications. Bottom-up DNA self-assembly, on the other hand, offers the above-mentioned features

while enabling the design of structures with nanometer precision.^{24–28} For example, DNA origami allows the construction of rigid nanostructures with designed amount of bending and twist.²⁹ We recently showed that several micrometer-long helical DNA nanotubes are assembled in a simple one-pot reaction from only eight different oligonucleotides.¹⁴ By systematically testing the various parameters of DNA tile design, such as the number and relative positions of inserted or deleted base pairs and the relative position of tiles, we now establish a set of rules for the rational design of custom-shaped DNA tube helices of defined chirality and helical diameters.

RESULTS AND DISCUSSION

In DNA tile tube assembly, single-stranded DNA oligonucleotides (tiles) assemble into repetitive segments of n -helix tubes that can polymerize into tubes of micrometer length.²⁴ If the number of DNA double helices n of a given tube design is even, the sheet of parallel double helices can roll up into a tube (see Figure S1) with zero offset along its two long edges, as exemplarily illustrated for a 12-helix tile tube (12HT) in Figure 1a. This design results in straight and unstressed tubular structures.^{14,24} When a base pair is inserted into or deleted from a selected double helix (Figure 1b), local stress and strain is generated and distributed over the whole tube structure as was previously demonstrated for similar DNA constructs.^{14,29,30} For

Received: August 19, 2016

Accepted: January 26, 2017

Published: January 26, 2017

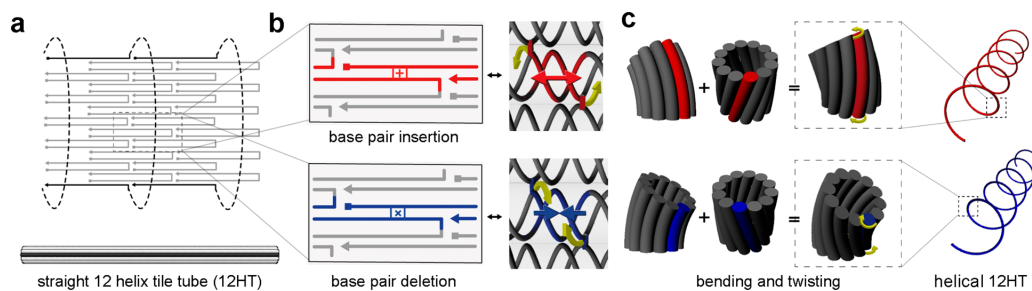


Figure 1. Design principles for the construction of helical DNA tile tubes. (a) DNA tile tubes with an even number of double helices (here a 12-helix tile tube design is shown) close with zero offset of the edges, resulting in a straight overall shape. (b) Insertion of an additional base pair into a double helix generates expansion (red double arrow) and a right-handed torque. Deletion of a base pair leads to compression (blue double arrow) and a left-handed torque. (c) Expansion or compression leads to bending, while torque results in twisting of the overall tube structure. The combination of both effects forces the tube into a helical shape.

example, in the case of a base pair insertion, the particular double helix gets longer than the other double helices, so that the entire tube bends (Figure 1b, c red parts). At the same time the cross over points with the two neighboring helices are pushed toward opposite directions at different positions, inducing a twist along the tubes primary axis. The combination of bending and twist then results in a helical tube structure (Figure 1c).

Following these design principles, we expect that for tubes with larger number of helices n the effect of insertions and deletions will be distributed over more double helices and thus become smaller. Within a tube of a given number of double helices, we expect to get a stronger effect for more insertions and deletions. To test these hypothesis, we changed the number of insertions or deletions $N_{\text{ins,del}}$ for a variety of tube sizes n (for design details and tile sequences see Note S1 and Figure S2).

Figure 2a shows transmission electron microscopy images of tile tubes for decreasing tube size n (from 12HT to 4HT) and constant number of insertions ($N_{\text{ins}} = 1$). All tubes revealed an undulatory shape of nanometer dimensions that became more pronounced for smaller tube sizes. Exact quantification of the helix parameters, such as helical diameter, pitch, and chirality, was not possible as TEM sample preparation resulted in a 2-D confinement of the original helical shape of the tubes. However, Nam *et al.* recently proposed that such squeezed conformations, so-called *squeelices*, have almost the same curvature ω as their unconfined 3D predecessors.³¹ In place of the helical diameter and pitch, we therefore extracted the radius of curvature $r_c = \frac{1}{\omega}$ from the 2D confined helical shape (see inset of Figure 2a) and compared it for the different tube types (detailed information on the statistical analysis is provided in Figure S3 and Table S1). Note that r_c is related to the helical diameter (D) and pitch (P) by $r_c = \frac{D}{2} + \frac{P^2}{2\pi^2 D}$, so that $r_c \geq \frac{D}{2}$. We found that r_c steadily decreased with decreasing tube size n for both tubes with insertions (Figure 2b) and deletions (Figure 2c) from 560 to 88 nm and from 457 to 65 nm, respectively (TEM images of tubes with deletions are shown in Figure S4).

Figure 2d shows images of tile tubes with increasing amount of insertions N (from 1 to 6) and constant tube size $n = 12$. We chose the 12-helix tile tube (12HT) for these experiments as its total interhelical angle is $\sim 360^\circ$ by the geometry of DNA so that it is least stressed when forming a tube (illustrated in Figure S5).²⁴ Insertions and deletions in the 12HT were placed in such a way that they successively increase the total amount of bending. We found that r_c steadily decreased for increasing amounts of

insertions (Figure 2e) or deletions (Figure 2f) from 554 to 155 nm and from 556 to 110 nm, respectively (TEM images of 12HT tubes with deletions are shown in Figure S6). To achieve even stronger bending, we constructed tubes with the same number of insertions and deletions located on opposite double helices (Figure 2g). Indeed, r_c decreased drastically for all five tube types. The minimum radius that we achieved with this approach was 77 nm (Figure 2h). At higher numbers of insertions and deletions proper folding of the tubes was inhibited. In previous studies on 6- and 4-helix bundles, such arrangements led to the formation of rings,³⁰ however, we observed that preferentially helical structures formed. This discrepancy can be explained by the greater persistence length of the 12HT^{32–34} which reduces the probability of fluctuation-induced ring closure during tube growth. An asymmetric design with N insertions and $N-1$ deletions is shown in Figure 2i (TEM images are shown in Figure S7). Its radii were consistently smaller than those for tubes with only insertions or deletions and larger than for tubes with both insertions and deletions.

In order to determine whether this technique is generally applicable for the controlled construction of nanoscale helical structures, we compared our results to radii predicted from energetic considerations using a DNA toy model recently presented by Dietz *et al.*²⁹ It expresses the energy stored within the DNA tile tube as a sum of stretch (S) and bend energy (B) (for detailed information, see Note S2). Remarkably, the energetic predictions (presented as black symbols in the graphs of Figure 2, respectively) show good agreement and only slightly overestimate the experimental data in all of the tubes examined. A similar overestimation also occurred for large r_c in the original DNA toy model study.²⁹ We can only speculate that the comparatively strong deviations for the first values in all graphs are the result of a buffering effect in DNA nanostructures. In contrast to perfect double-stranded DNA, which is assumed in the model, our structures have nicks and cross overs. The additional flexibility that these features give to the structures could absorb some of the insertion- or deletion-induced bending. As this effect needs to be overcome only once, it would affect tubes with few insertions or deletions more than those with many insertions or deletions. For small r_c , the deviations can be attributed to a structural change in the cross section of the modified tile tubes from a perfect circle (see Figure S8 for detailed information). In conclusion, we were able to generate DNA tile tubes with radii of curvature ranging from 65 to 560 nm using the insertion and deletion method.

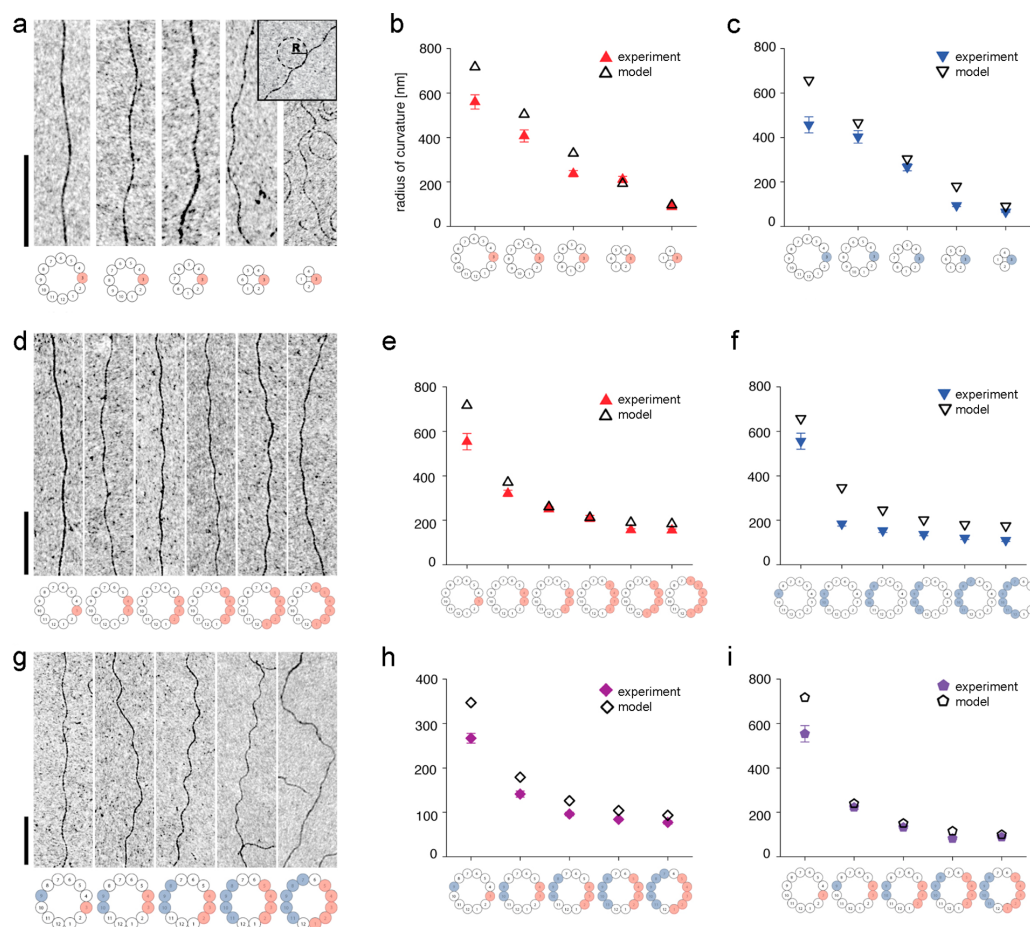


Figure 2. Construction of helical DNA tile tubes with controlled nanometer-sized radius of curvature. (a) DNA tile tubes with decreasing size n (from 12HT to 4HT) and constant number of insertions $N = 1$ as observed by TEM. Inset: Radius of curvature r_c extracted from the 2D-confined undulatory shape. (b) Relationship between r_c and tubes of different size with insertions (red triangles) and with (c) deletions (blue triangles). (d) Tubes with constant size ($n = 12$) and increasing amounts of insertions N (from 1 to 6) as observed by TEM. Relationship between r_c and the amount of (e) insertions (red triangles) and (f) deletions (blue triangles) in tubes of constant size. (g) Tubes with increasing amounts of both insertions and deletions N (from 1 to 5) as observed by TEM. Relationship between r_c and tubes of (h) symmetric (violet rhombi) and (i) asymmetric (violet pentagons) arrangements of insertions and deletions. Error bars are the standard error of the mean calculated for each tube type respectively (see Table S1). Theoretical predictions of r_c from an energetic model are shown in black symbols for each tube type. Scale bars: 500 nm.

In certain applications such as microswimmers, filaments with microscale helical diameters are desirable as they provide stronger propulsion forces.¹⁴ This requires even smaller amounts of twist and bending than those arising from single base pair insertions or deletions. We therefore introduced a technique referred to as *tile shifting*, which relies on the stepwise reduction of the intrinsic *supertwist* of DNA tile tubes to generate tubes with smallest quantities of twist along the tube's primary axis. Due to the alternating tile alignment, DNA tile tubes with an odd number of double helices close with a discrete offset resulting in a supertwisted helix bundle (Figure 3a). This supertwist can be attenuated in small steps by reducing the offset of closure through shifting of single tiles one nucleotide (nt) position at a time within the structure (Figure 3b). This also allows the predefinition of the chirality of the supertwist. In the depicted case of a tile-shifted 13-helix tube (stw13HTs) it is left-handed

for geometrical reasons (for design details and tile sequences see Note S3 and Figures S9 and S10).

Smaller quantities of bending were achieved by modifying the tube structures with defined arrangements of Cy3 dyes (see Figure S2 for Cy3-modified tile sequences). This also enabled us to visualize the tubes in solution *via* fluorescence microscopy. In our previous work, we noticed that a Cy3-modified 6-helix tile tube exerted quantities of bending so small that it resulted in a helical microscale diameter of the overall tube structure.³² A Cy3 dye in the vicinity of a DNA duplex nick can thus induce a stretch and a right-handed twist deformation of the DNA helix (Figure 4a) similar to that of a base pair insertion.^{35,36} In accordance with this observation, we found that the amount of bending in a 6HT strongly depends on the arrangement of the Cy3 dyes on the tube. Figure 4b demonstrates that Cy3-modifications on one side of the tube give stronger bending, and an associated smaller

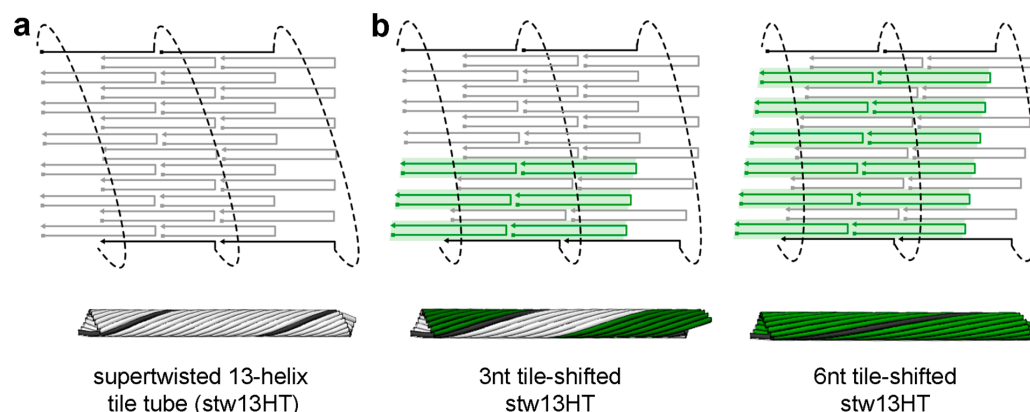


Figure 3. Design principles for controlling the supertwist of DNA tile tubes: (a) Tile tubes with an odd number of tubes close with a discrete offset resulting in a supertwisted shape of the structure. (b) By shifting single tiles in the design, the offset can be reduced stepwise as illustrated for the case of a 3 nt (left) and 6 nt tile shift (right) in a supertwisted 13-helix tile tube (stw13HT). Here, the tile-shifting gradually reduces the amount of supertwist in the structure.

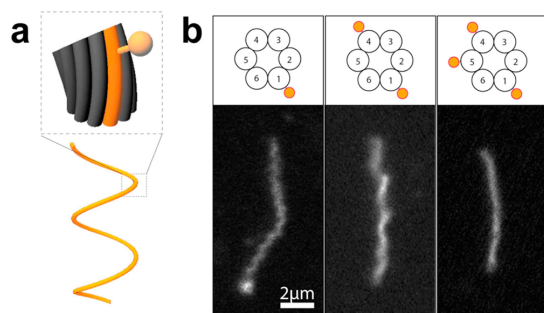


Figure 4. Cy3-induced bending and twisting of DNA tile tubes: (a) A Cy3-modification on a DNA tile tube can act similar to a base pair insertion and lead to a helical shape of the structure. (b) 6-helix tile tubes (6HTs) with three different arrangements of Cy3 dyes showed different bending and twisting as observed by fluorescence microscopy. Note that opposing Cy3 modifications reduced the total amount of bending whereas the induced twisting added up, resulting in a helical shape with increased diameter and pitch. Scale bar: 2 μm .

helical diameter of the tube, than modifications on opposing sides of the tube. Such opposing arrangements are therefore promising to construct tubes with small quantities of bending.

By combining the bending through Cy3 modifications with the fine-controlled supertwisting *via* tile shifting, we were able to stepwise control the microscale helical diameter of DNA tile tubes (Figure 5a). Fluorescence microscopy images of Cy3-modified supertwisted 13HTs (stw13HTs) with increasing amount of tile shift (from 0 to 6 nt) are shown in Figure 5b. Without tile shift (0 nt), the 13HT had a small helical diameter, which was barely resolvable with light microscopy (see Figure S11 for TEM images of this structure). A stepwise tile shift (from 0 to 4 nt), however, resulted in a stepwise increase of the helical diameter to a maximum of $\sim 2 \mu\text{m}$ at 4 nt. Further tile shifting (5 nt and 6 nt) decreased the helical diameter again.

To understand this behavior we considered the total amount of bending and twist present in the 13HTs. While keeping the amount of Cy3-induced bending constant in all tubes, the overall twist, a superposition of supertwist and Cy3-induced twist, was changed in small steps through tile shifting (from 0 to 6 nt). For small shifts (< 4 nt), the left-handed supertwist dominated over the right-handed Cy3-induced twist. As more tile shift was

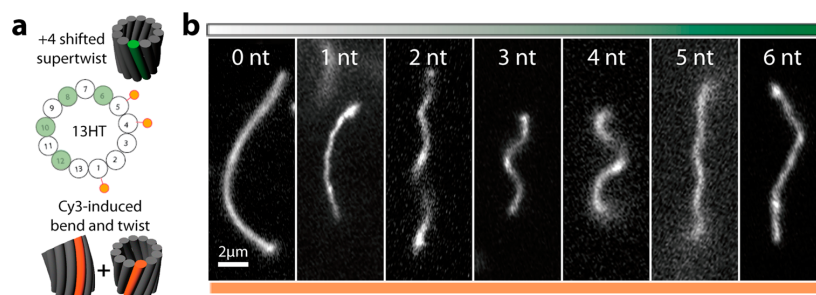


Figure 5. Construction of helical DNA tile tubes with controlled micrometer-sized diameter: (a) Scheme of a DNA tile tube, which combines tile shifting and Cy3 modifications for a controlled bending and twisting of the structure. (b) Fluorescence microscopy images of stw13HTs with increasing amount of tile shifting (from 0 to 6 nt). The tubes were constructed from three Cy3-modified and 10 unmodified tiles. Helical diameters of up to $\sim 2 \mu\text{m}$ were observed for a 4 nt tile shift. The decrease of the helical diameter after reaching this maximum already suggests a change in the chirality of the tube shape. Helical diameters for 1, 2, 3, and 5 nt shift are ~ 0.4 , ~ 1 , ~ 1.5 , and $\sim 0.6 \mu\text{m}$, respectively. Scale bar: 2 μm .

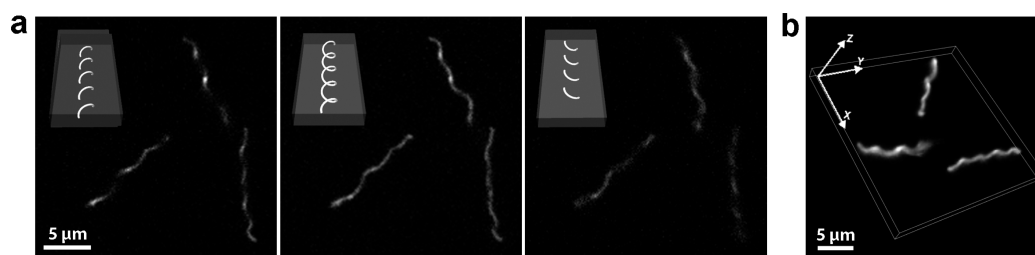


Figure 6. Determination of the chirality of DNA tile tubes: (a) Fluorescence microscopy “tomographic” slices of tile-shifted stw13HTs at three different z -positions of the focal plane (left to right: slightly below, centered, and slightly above the center of the helix). The distinct patterns from the images were used to determine the chirality of the tube. In the depicted case of stw13HTs with a 2 nt tile shift, the chirality was determined to be left-handed. (b) A 3D reconstruction was generated from the entire set of images. Scale bars: 5 μm .

introduced (from 0 to 4 nt), the supertwist decreased which resulted in a reduced overall twist and therefore larger helical diameters. A helical maximum diameter of $\sim 2 \mu\text{m}$ was reached at a 4 nt shift, which suggests that the total twist is minimal. By further reducing the supertwist (>5 nt), the Cy3-induced right-handed twist became dominant over the supertwist and again reduced the tube’s helical diameter.

We tested this hypothesis by determining the chirality of the tubes by taking “tomographic” slices of their 3D shapes *via* fluorescence microscopy. For each sample, a set of images was taken while the focal plane was moved through the sample volume. Figure 6a exemplarily shows fluorescence images of stw13HTs with a 2 nt tile shift in three distinct positions of the focal plane: slightly beneath (left), centered (middle) and slightly above (right) the center of the helical tile tube. The contours of each plane yielded a distinct pattern, which allowed us to determine the tubes chirality. Furthermore, a 3D reconstruction of the structures could be generated from the set of images (Figure 6b). In the depicted sample the chirality was determined to be left-handed. We successively applied this technique to the tile-shifted stw13HTs from Figure 5 and additionally to tile-shifted stw11HTs and stw15HTs (see Figure S12). In all three cases, a change of chirality from left- to right-handed was observed for increasing amounts of tile shift (see Figure S13).

CONCLUSIONS

Our DNA-based self-assembly scheme allows large-scale production of biocompatible helical nanotubes with precise control over their micro- and nanoscale helical diameter and chirality. Incorporation of base pair insertions and deletions enables us to adjust the radius of curvature within the nanometer regime in accordance with an energetic model. Microscale helical diameters of defined chirality are achieved through fine controlling the intrinsic supertwist *via* tile shifting in Cy3-modified tubes. Design rules derived from this work and the good correspondence of our experimental results with a simple theoretical model can be utilized to design and construct predefined helical shapes for future applications. For example, micrometer-sized helical constructs can be applied to optimize the swimming behavior of artificial microswimmers, which allows researchers to gain further insights into the swimming strategies of microorganisms. For our helical tubes to serve as nanosprings, force spectroscopic analysis and cryo-electron microscopy could be applied to determine their mechanical properties such as their spring constants and to obtain additional information over their helical diameter and pitch. Our design techniques demonstrate the flexibility and simplicity of DNA self-assembly for the

construction of fully biocompatible nanoscrews and -springs, which may find their way into nanorobots for noninvasive biomedical therapies and in other fields of nanoengineering.

MATERIALS AND METHODS

Folding of DNA Tile Tubes. Tile tubes were assembled in a one-pot reaction with 1 μM of each oligonucleotide in a 1X TAE/12 mM MgCl_2 buffer by exposing the folding mixture to a thermal annealing ramp. Annealing started with a heating step to 80 $^\circ\text{C}$ for 10 min followed by a stepwise cooling from 65 to 45 $^\circ\text{C}$ at a cooling rate of 0.5 $^\circ\text{C}/5$ min. After the assembly, the particles were stored at room temperature. Cy3-modified tubes were kept away from light in a dark place to prevent possible photobleaching. In order to reduce the amount of entangled tube structures, which formed over time, we gently resuspended the sample before each measurement.

Transmission Electron Microscopy. Carbon-coated TEM grids (Ted Pella) were plasma cleaned for 1 min at 240 V. Two μL of a tile tube sample was put onto the grid and incubated for 2 min. The solution was removed from the grid, which was then washed with 5 μL of 1% aqueous uranyl acetate solution. A second 5 μL drop was then added and incubated for 10 s. After the second drop was removed, the grid was allowed to dry for at least 30 min before imaging *via* a JEM/1011 transmission electron microscope.

Fluorescence Microscopy. Fluorescence microscopy images were taken by a Zeiss Observer Z1 microscope connected to an Andor Solis camera with a pixel resolution of 6,4 pixels/ μm . Before imaging, tile tubes were 100 times diluted into a 12 mM MgCl_2 , 1X TE buffer with 0.05% Tween 20. The surfactant prevented the particles from adhering to the glass surface, allowing them to freely float in the solution. “Tomographic” image series were taken by rapidly turning the focus plane through the fluorescent particle. All experiments were carried out at room temperature.

ASSOCIATED CONTENT

Supporting Information

The Supporting Information is available free of charge on the ACS Publications website at DOI: 10.1021/acsnano.6b05602.

Additional data and protocols (PDF)

AUTHOR INFORMATION

Corresponding Author

*E-mail: tim.liedl@physik.lmu.de.

ORCID

Tim Liedl: 0000-0002-0040-0173

Present Address

^{||}(D.S.) National Institute of Standards and Technology, Gaithersburg, Maryland 20899, United States and University of Maryland, Maryland and Nanocenter, College Park, Maryland 20740, United States.

Author Contributions

A.M.M. and T.L. conceived the experiments. A.M.M., W.B., D.S., J.F.E., and M.S. produced the structures and performed and analyzed the measurements. A.M.M. and T.L. interpreted the results and wrote the manuscript.

Notes

The authors declare no competing financial interest.

ACKNOWLEDGMENTS

We thank Susanne Kempter for experimental support. This project was supported by the Deutsche Forschungsgemeinschaft via Project A06 within the SFB 1032 “Nanoagents for Spatiotemporal Control of Molecular and Cellular Reactions”, the NanoSystems Initiative Munich (NIM), the Center for Nanoscience (CeNS), and the ERC grant agreement no. 336440 for ORCA.

REFERENCES

- (1) Watson, J. D.; Crick, F. H. The Structure of DNA. In *Cold Spring Harbor Symposia on Quantitative Biology*; Cold Spring Harbor Laboratory Press, 1953; pp 123–131.
- (2) Wang, J.-S.; Wang, G.; Feng, X.-Q.; Kitamura, T.; Kang, Y.-L.; Yu, S.-W.; Qin, Q.-H. Hierarchical Chirality Transfer in the Growth of Towel Gourd Tendrils. *Sci. Rep.* **2013**, DOI: 10.1038/srep03102.
- (3) Li, L.; Weaver, J. C.; Ortiz, C. Hierarchical Structural Design for Fracture Resistance in the Shell of the Pteropod *Clio* Pyramidata. *Nat. Commun.* **2015**, *6*, 6216.
- (4) Schmidt, O. G.; Eberl, K. Nanotechnology: Thin Solid Films Roll up into Nanotubes. *Nature* **2001**, *410*, 168–168.
- (5) Zhang, L.; Abbott, J. J.; Dong, L. X.; Kratochvil, B. E.; Bell, D.; Nelson, B. J. Artificial Bacterial Flagella: Fabrication and Magnetic Control. *Appl. Phys. Lett.* **2009**, *94*, 064107.
- (6) Li, W.; Huang, G.; Wang, J.; Yu, Y.; Wu, X.; Cui, X.; Mei, Y. Superelastic Metal Microsprings as Fluidic Sensors and Actuators. *Lab Chip* **2012**, *12*, 2322–2328.
- (7) Robbie, K.; Broer, D.; Brett, M. Chiral Nematic Order in Liquid Crystals Imposed by an Engineered Inorganic Nanostructure. *Nature* **1999**, *399*, 764–766.
- (8) Ghosh, A.; Fischer, P. Controlled Propulsion of Artificial Magnetic Nanostructured Propellers. *Nano Lett.* **2009**, *9*, 2243–2245.
- (9) Mark, A. G.; Gibbs, J. G.; Lee, T. C.; Fischer, P. Hybrid Nanocolloids with Programmed Three-Dimensional Shape and Material Composition. *Nat. Mater.* **2013**, *12*, 802–807.
- (10) Singh, J.; Liu, D.-L.; Ye, D.-X.; Picu, R.; Lu, T.-M.; Wang, G.-C. Metal-Coated Si Springs: Nanoelectromechanical Actuators. *Appl. Phys. Lett.* **2004**, *84*, 3657–3659.
- (11) Gansel, J. K.; Thiel, M.; Rill, M. S.; Decker, M.; Bade, K.; Saile, V.; von Freymann, G.; Linden, S.; Wegener, M. Gold Helix Photonic Metamaterial as Broadband Circular Polarizer. *Science* **2009**, *325*, 1513–1515.
- (12) Tottori, S.; Zhang, L.; Qiu, F.; Krawczyk, K. K.; Franco-Obregon, A.; Nelson, B. J. Magnetic Helical Micromachines: Fabrication, Controlled Swimming, and Cargo Transport. *Adv. Mater.* **2012**, *24*, 811–816.
- (13) Schamel, D.; Mark, A. G.; Gibbs, J. G.; Miksch, C.; Morozov, K. I.; Leshansky, A. M.; Fischer, P. Nano-Propellers and their Actuation in Complex Viscoelastic Media. *ACS Nano* **2014**, *8*, 8794–8801.
- (14) Maier, A. M.; Weig, C.; Oswald, P.; Frey, E.; Fischer, P.; Liedl, T. Magnetic Propulsion of Microswimmers with DNA-Based Flagellar Bundles. *Nano Lett.* **2016**, *16*, 906–910.
- (15) Gao, W.; Kagan, D.; Pak, O. S.; Clawson, C.; Campuzano, S.; Chuluun-Erdene, E.; Shipton, E.; Fullerton, E. E.; Zhang, L.; Lauga, E.; Wang, J. Cargo-Towing Fuel-Free Magnetic Nanoswimmers for Targeted Drug Delivery. *Small* **2012**, *8*, 460–467.
- (16) Wang, J.; Gao, W. Nano/Microscale Motors: Biomedical Opportunities and Challenges. *ACS Nano* **2012**, *6*, 5745–5751.
- (17) Wang, J. *Nanomachines: Fundamentals and Applications*; John Wiley & Sons: 2013.
- (18) Wang, J. Can Man-Made Nanomachines Compete with Nature Biomotors? *ACS Nano* **2009**, *3*, 4–9.
- (19) Fischer, P.; Ghosh, A. Magnetically Actuated Propulsion at Low Reynolds Numbers: Towards Nanoscale Control. *Nanoscale* **2011**, *3*, 557–563.
- (20) Gao, P. X.; Mai, W.; Wang, Z. L. Superelasticity and Nanofracture Mechanics of ZnO Nanohelices. *Nano Lett.* **2006**, *6*, 2536–2543.
- (21) Motojima, S.; Chen, X.; Yang, S.; Hasegawa, M. Properties and Potential Applications of Carbon Microcoils/Nanocoils. *Diamond Relat. Mater.* **2004**, *13*, 1989–1992.
- (22) Hayashida, T.; Pan, L.; Nakayama, Y. Mechanical and Electrical Properties of Carbon Tubule Nanocoils. *Phys. B* **2002**, *323*, 352–353.
- (23) Liu, J.; Lu, Y. L.; Tian, M.; Li, F.; Shen, J.; Gao, Y.; Zhang, L. The Interesting Influence of Nanosprings on the Viscoelasticity of Elastomeric Polymer Materials: Simulation and Experiment. *Adv. Funct. Mater.* **2013**, *23*, 1156–1163.
- (24) Yin, P.; Hariadi, R. F.; Sahu, S.; Choi, H. M.; Park, S. H.; Labean, T. H.; Reif, J. H. Programming DNA Tube Circumferences. *Science* **2008**, *321*, 824–826.
- (25) Rothemund, P. W. Folding DNA to Create Nanoscale Shapes and Patterns. *Nature* **2006**, *440*, 297–302.
- (26) Seeman, N. C. Nanomaterials Based on DNA. *Annu. Rev. Biochem.* **2010**, *79*, 65.
- (27) Rothemund, P. W.; Ekani-Nkodo, A.; Papadakis, N.; Kumar, A.; Fyngson, D. K.; Winfree, E. Design and Characterization of Programmable DNA Nanotubes. *J. Am. Chem. Soc.* **2004**, *126*, 16344–16352.
- (28) Kuzuya, A.; Wang, R.; Sha, R.; Seeman, N. C. Six-Helix and Eight-Helix DNA Nanotubes Assembled from Half-Tubes. *Nano Lett.* **2007**, *7*, 1757–1763.
- (29) Dietz, H.; Douglas, S. M.; Shih, W. M. Folding DNA into Twisted and Curved Nanoscale Shapes. *Science* **2009**, *325*, 725–730.
- (30) Yang, Y.; Zhao, Z.; Zhang, F.; Nangreave, J.; Liu, Y.; Yan, H. Self-Assembly of DNA Rings from Scaffold-Free DNA Tiles. *Nano Lett.* **2013**, *13*, 1862–1866.
- (31) Nam, G.-M.; Lee, N.-K.; Mohrbach, H.; Johnner, A.; Kulić, I. M. Helices at Interfaces. *Europhys. Lett.* **2012**, *100*, 28001.
- (32) Schiffels, D.; Liedl, T.; Fyngson, D. K. Nanoscale Structure and Microscale Stiffness of DNA Nanotubes. *ACS Nano* **2013**, *7*, 6700–6710.
- (33) Wang, T.; Schiffels, D.; Martinez Cuesta, S.; Kuchnir Fyngson, D.; Seeman, N. C. Design and Characterization of 1D Nanotubes and 2D Periodic Arrays Self-Assembled from DNA Multi-Helix Bundles. *J. Am. Chem. Soc.* **2012**, *134*, 1606–1616.
- (34) Kauert, D. J.; Kurth, T.; Liedl, T.; Seidel, R. Direct Mechanical Measurements Reveal The Material Properties of Three-Dimensional DNA Origami. *Nano Lett.* **2011**, *11*, 5558–5563.
- (35) Iqbal, A.; Arslan, S.; Okumus, B.; Wilson, T. J.; Giraud, G.; Norman, D. G.; Ha, T.; Lilley, D. M. Orientation Dependence in Fluorescent Energy Transfer Between Cy3 and Cy5 Terminally Attached to Double-Stranded Nucleic Acids. *Proc. Natl. Acad. Sci. U. S. A.* **2008**, *105*, 11176–11181.
- (36) Norman, D. G.; Grainger, R. J.; Uhrin, D.; Lilley, D. M. Location of Cyanine-3 on Double-Stranded DNA: Importance for Fluorescence Resonance Energy Transfer Studies. *Biochemistry* **2000**, *39*, 6317–6324.

6.2 Associated Publication P2

Magnetic Propulsion of Microswimmers with DNA-Based Flagellar Bundles

By

Alexander M. Maier[†], Cornelius Weig[‡], Peter Oswald[§], Erwin
Frey^{*‡}, Peer Fischer^{*§||}, and Tim Liedl^{*†}

published in

Nanoletters 2016, 16, 906-910

Reprinted with permission from Ref [27] under a Creative
Commons Attribution (CC-BY) License.



Magnetic Propulsion of Microswimmers with DNA-Based Flagellar Bundles

Alexander M. Maier,[†] Cornelius Weig,[‡] Peter Oswald,[§] Erwin Frey,^{*,‡} Peer Fischer,^{*,§,||} and Tim Liedl^{*,†}

[†]Faculty of Physics and Center for NanoScience, Ludwig-Maximilians-Universität, Geschwister-Scholl-Platz 1, 80539 München, Germany

[‡]Arnold Sommerfeld Center for Theoretical Physics and Center for NanoScience, Department of Physics, Ludwig-Maximilians-Universität München, Theresienstraße 37, 80333 Munich, Germany

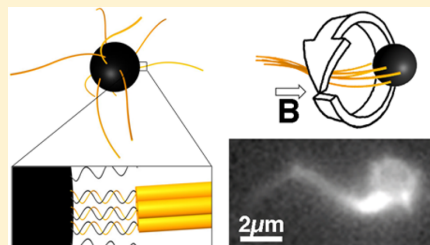
[§]Max Planck Institute for Intelligent Systems, Heisenbergstrasse 3, 70569 Stuttgart, Germany

^{||}Institut für Physikalische Chemie, Universität Stuttgart, Pfaffenwaldring 55, 70569 Stuttgart, Germany

Supporting Information

ABSTRACT: We show that DNA-based self-assembly can serve as a general and flexible tool to construct artificial flagella of several micrometers in length and only tens of nanometers in diameter. By attaching the DNA flagella to biocompatible magnetic microparticles, we provide a proof of concept demonstration of hybrid structures that, when rotated in an external magnetic field, propel by means of a flagellar bundle, similar to self-propelling peritrichous bacteria. Our theoretical analysis predicts that flagellar bundles that possess a length-dependent bending stiffness should exhibit a superior swimming speed compared to swimmers with a single appendage. The DNA self-assembly method permits the realization of these improved flagellar bundles in good agreement with our quantitative model. DNA flagella with well-controlled shape could fundamentally increase the functionality of fully biocompatible nanorobots and extend the scope and complexity of active materials.

KEYWORDS: Propulsion, low-Reynolds-number, slender-body theory, nanorobots, DNA self-assembly, flagella



Many motile micro-organisms possess flagella to propel¹ or swim² through viscous fluids.³ Mimicking these highly evolved microstructures with nanoscale features is challenging but would enable the realization of functional microswimmers.^{4,5} Artificial flagella have been constructed from various materials, such as alloys and glass, with sizes ranging from a few millimeters down to several hundreds of nanometers using top-down fabrication methods.^{6–10} A prominent example of a self-assembled swimmer was demonstrated by linking magnetic particles while an applied magnetic field induces the formation of particle chains.¹¹ For the actuation of such artificial flagella, externally applied magnetic fields have proven to be advantageous as they are fully biocompatible and can be applied in aqueous environments from afar, avoiding the need for potentially toxic chemical reactions commonly used to propel phoretic swimmers.¹² Within these approaches, miniaturization to the nanoscale,⁹ complex maneuvering,⁶ functionalization for targeted drug delivery,^{10,13} large scale production,^{6,8,9} and a certain degree of biocompatibility⁸ were shown. However, for future applications it is desirable to develop more versatile and naturally biocompatible means of realizing artificial flagella with the potential to mimic the complex hierarchically assembled protein structure of real flagella while ideally combining all of the above-mentioned features in one single system. DNA-based self-assembly^{14–16}

can meet these requirements as it allows for systematic design at the nanoscale, large-scale production and straightforward functionalization, while being fully biocompatible. We show that even isotropically covered spherical particles of 1 μm in diameter can be propelled by virtue of hydrodynamically formed DNA flagellar bundles. Interestingly, compared to swimmers with a single appendage,¹⁷ our bundles exhibit a stiffness profile that is shown to underlie favorable swimming shapes that can also be found in flagellar bundles of bacteria.

To realize artificial flagella, we employed DNA tile-tube assembly^{14,18} schematically depicted in Figure 1. In this technique, short single-stranded DNA fragments assemble into n -helix tubes (n HT) (Figure 1a), where each tube consists of repeating structural units of n adjacent DNA duplexes, which can polymerize along the axis of the tube. From a large variety of possible tube types (Supporting Information Figure S1), three designs with varying degree of twist and stiffness are shown in Figure 1b: straight 8-helix-tubes (st8HT), twisted^{18,19} 8-helix tubes (tw8HT), and supertwisted²⁰ 13-helix tubes (stw13HT). The tubes were attached to 1 μm iron oxide particles via the hybridization of complementary DNA strands

Received: September 15, 2015

Revised: January 25, 2016

Published: January 28, 2016

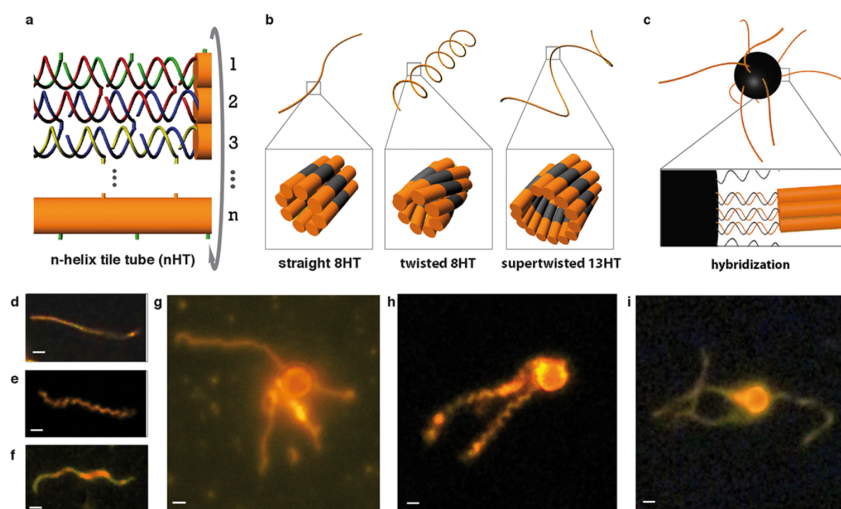


Figure 1. DNA tile-tube–magnetic bead hybrids. (a) Schematic showing the self-assembly of single DNA strands into DNA tile-tube structures consisting of n double helices and (b) the design of straight 8-helix (st8HT), twisted 8-helix (tw8HT), and supertwisted 13-helix (stw13HT) tile-tubes. (c) Attachment of tile-tubes to DNA-modified magnetic beads via biotin–streptavidin coupling yields DNA tile-tube–magnetic bead hybrids. (d–i) Fluorescence microscopy images showing (d) st8HT, (e) tw8HT, and (f) stw13HT, and $1\ \mu\text{m}$ magnetic beads decorated with (g) st8HT, (h) tw8HT, and (i) stw13HT. The demonstrated hybrid structures have only a few artificial flagella attached to facilitate a simultaneous visualization of the magnetic bead and the tile-tubes. Tw8HTs in (e) and (h) were imaged in 75% glycerol to slow down thermal fluctuations, which here also increased the twist diameter. Swimming motions were examined in glycerol-free solutions. Also, note that due to their brightness the magnetic beads appear larger than their actual size of $1\ \mu\text{m}$. Scale bars: $1\ \mu\text{m}$.

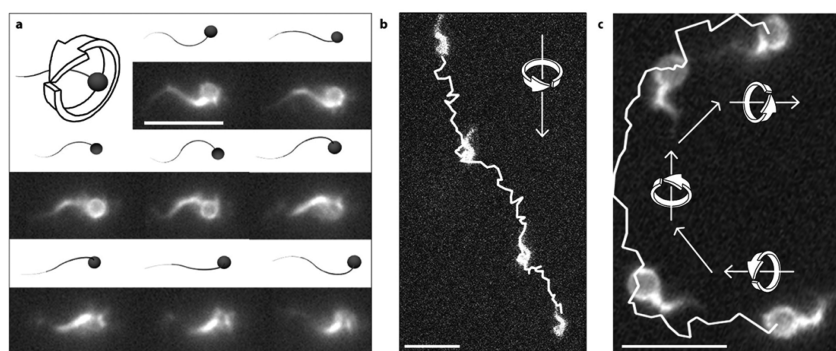


Figure 2. Directed motion of DNA-flagellated magnetic bead hybrids. (a) Schematic and respective fluorescence microscopy images of a tw8HT hybrid structure driven by a homogeneous magnetic field, which rotates perpendicular to the swimming direction. (b,c) Superimposed images of the tracking of DNA-flagellated magnetic bead hybrids (b) in directed motion and (c) following a curved path. Scale bars: $10\ \mu\text{m}$.

(Figure 1c) (for design details see Supporting Information Note S1). For imaging and tracking, a subset of the DNA strands forming the tubes were modified with Cy3 dyes on their 5' ends. All three types of the tubes (Figure 1d–f) and their respective hybrid structures (Figure 1g–i) were imaged in a liquid cell of a few micrometers in height. Remarkably, the hybrids visually resembled flagellated bacteria, were similar in size, and possessed equal amounts of twist as natural flagella. For example, the stw13HT (Figure 1f,i) had a pitch of $2.51 \pm 0.51\ \mu\text{m}$ and a diameter of $0.57 \pm 0.19\ \mu\text{m}$, which compares well to an *E. coli* filament in its normal form, whereas the tw8HT (Figure 1e,h) had a pitch of $0.98 \pm 0.22\ \mu\text{m}$ and a diameter of $0.30 \pm 0.17\ \mu\text{m}$, which resembles the curly state of the *E. coli*.²¹

To test the ability of the DNA-flagellated magnetic particle hybrids to propel at low Reynolds number, we externally

applied a rotating homogeneous magnetic field. Magnetic beads can also be pulled by a magnetic gradient field, however, it is generally not viable to achieve significant gradients at a distance, and so homogeneous (nongradient) fields are much more practical for potential applications. The samples were placed in the center of a three-axis Helmholtz coil system that was integrated into an inverted fluorescence microscope (Supporting Information Note S2). The hybrids were exposed to rotating homogeneous magnetic fields of up to 100 G, and their motion was captured on video. Video samples containing hybrid structures (displayed in Figure 1g–i) revealed that all the particles rotated in phase and approximately 10% of the st8HTs and tw8HTs decorated structures formed a bundle of DNA flagella on only one side of the bead (see Figure 2a and Supporting Information Video 1 for a well-assembled structure and Supporting Information Figure S7 for non-functional side

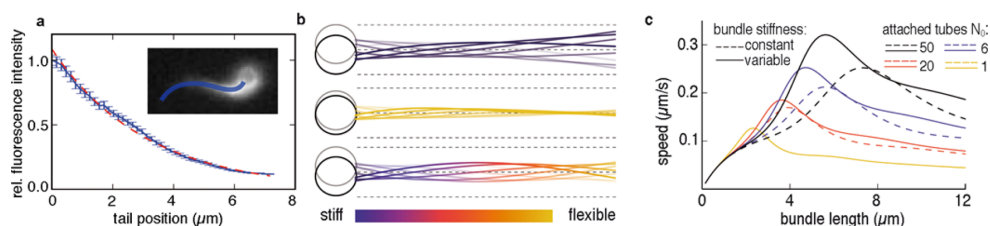


Figure 3. Analysis of a DNA tile-tube bundle. (a) The fluorescence intensity of an artificial flagellar bundle (inset) drops exponentially (red dashed line) when moving away from the bead due to a decreasing number of tubes in the bundle. Data was gained by averaging over several movie frames to rule out errors emerging from a change in the fluorescence distribution along the particle during rotation (see Supporting Information Figure S7 for additional bundle analysis). The fluorescence decay length of the demonstrated swimmer is $3 \mu\text{m}$. (b) Numerical solutions of the shape of one stiff (top) and floppy (middle) bundle with constant bending stiffness in comparison to a bundle with decreasing stiffness (bottom) at eight positions during one full rotation. (c) Within the theoretical model, swimmers with decreasing stiffness of the bundle (solid lines) achieve a higher speed than swimmers with constant stiffness of the bundle (dashed lines) for a broad range of bundle lengths and stiffnesses.

products). Because we did not observe a qualitative difference in the bundle structure of st8HTs, tw8HTs, and stw13HT-bundles (see Supporting Information Figure S8 and S9), and since stw13HT formed with a yield of only $\sim 1\%$, we limited our study to the tw8HT-bundle swimmers. Figure 2a shows eight snapshots of a tw8HTs decorated $1 \mu\text{m}$ magnetic particle during one full rotation. Similar to real bacterial flagella, upon rotation the DNA flagella formed a hydrodynamically assembled corkscrew-like bundle with a length of several micrometers. The rotated tube bundle propelled the DNA-magnetic bead hybrids (see Figure 2b and Supporting Information Video 2) head first along the rotation axis. The propulsion speed of up to $1/10$ of a body length per turn (along the rotation axis) is in good agreement with the dimensionless speed (body lengths per turn) of flagellated bacteria, although bacteria swim at higher frequencies and therefore effectively propel much faster. The fastest artificial swimmer observed was driven at 3 Hz and propelled with a speed of $\sim 0.6 \mu\text{m/s}$ (see Supporting Information Figure S6). At higher frequencies, the DNA flagellar bundles lost their corkscrew-like form, which led to a decreased speed (see Supporting Information Video 3). This divergent behavior from bacterial flagellation can be explained by the smaller persistence length of the DNA tube-based flagellum ($\sim 8 \mu\text{m}$ for 8HT²⁰) in comparison to that of bacteria ($\sim 0.7 \text{ mm}$ for *E. coli*²²). For higher-frequency swimmers, one would therefore have to employ a more rigid DNA flagella design. Higher flagella rigidity could also allow for observing differences in swimming speeds of (super)twisted and straight flagella. An additional movement perpendicular to the rotation axis has been observed in most swimmers and can be attributed to hydrodynamic interactions of the swimmer with the surface of the fluid-cell. This is analogous to the motion of bacteria in the vicinity of glass surfaces, where the same effect has been reported.²³ By gradually changing the rotation axis of the external magnetic field, the DNA-magnetic bead hybrids could also be steered to follow a curved path (Figure 2c and Supporting Information Video 4). In contrast to a bacterial flagellar bundle, the artificial bundle did not reopen when switching the rotation from clockwise to counterclockwise or vice versa, which would permit the observation of run-and-tumble behavior. Instead, the artificial swimmers retained their overall swimming direction, while the movement perpendicular to the rotation axis reversed every time the field was switched (Supporting Information Video 5). The continuous forward propulsion is direct evidence for a change of the bundle's helicity, as in a static helix a reversal

of the direction of rotation would lead to reversal of the swimming direction. From these two observations, no reopening and switch of helicity of the DNA-tube bundles upon reversal of rotation direction, we conclude that the individual tubes cross-link weakly during bundle formation (tight cross-linking would lead to static helicity and no cross-linking would allow bundles to reopen). Cross-linking could be a result of possible domain exchanges between adjacent tubes within the bundle. We further observed an exponential drop of the fluorescence intensity along the tube bundle (Figure 3a and Supporting Information Figure S7), which we can attribute to an exponential decay in the length distribution of the bundled DNA tubes.¹⁴ Interestingly, also naturally occurring bundles of flagella often exhibit thinning toward the bundles' end. This raises the question whether the varying lengths of flagella within our artificial bundle has an effect on the swimming speed.

To address this question, we modeled the bundle of tubes as a single appendage with a length-dependent bending modulus. This approach is reasonable, as the DNA tubes in the bundle are only weakly cross-linked, such that the effective stiffness is to a good approximation proportional to the number of tubes present at the respective bundle position.^{24–26} If a polymerization process with sufficient supply of monomer units is assumed during the growth phase of the DNA filaments, the expected length distribution of free filaments falls exponentially.²⁷ Accordingly, the fluorescence intensity of the bundles in our experiments decreases exponentially toward their tails [see Figure 3 and Supporting Information Figure S10]. We thus infer an exponentially decreasing number of filaments in the bundles and an analogous decrease in their bending stiffness from head to tail. In general, the equation of motion of a bundle in a viscous medium at low Reynolds number is given by the force balance of the anisotropic friction on the tube bundle^{28,29} Γ with the elastic forces due to the bending of the bundle,

$$\Gamma \vec{u} = -\partial_s^2 (A \partial_s^2 \vec{r}) + \partial_s (\sigma \partial_s \vec{r})$$

Here, \vec{u} is the local velocity of the bundle, A is the local bending stiffness, \vec{r} is the bundle position and σ a Lagrange multiplier ensuring inextensibility. All variables depend on the arc length position s along the bundle. We solved this equation by generalizing previous work on actuated swimmers¹⁷ using boundary conditions taking into account that the bundle is attached to a rotating bead (Supporting Information Note S3). The crucial difference to earlier works,¹⁷ however, is that in our case the bending stiffness $A(s)$ changes along the bundle, which extends the scope of our model to bundles of variable stiffness.

At low Reynolds numbers, swimming requires a swimming stroke that is not time-reversible.³ Therefore, a rotating straight passive bundle needs to bend into a chiral shape to generate propulsion. The propulsion efficiency then depends on the curvature and the beat amplitude of this induced shape. In order to ascertain how well our bundle of variable stiffness meets these requirements, we compared it to the cases of constant high and low bending stiffness. Figure 3b shows that constant high stiffness (top) achieves high amplitudes but lacks bending especially toward the end of the bundle. In contrast, a constant low stiffness (middle) permits bending but lacks beat amplitude. A bundle with variable stiffness (bottom), however, can achieve both large amplitudes and bending along the entire length of the bundle (see also Supporting Information Video 6). Figure 3c shows a comparison of the swimming speed as a function of bundle length for bundles of decreasing stiffness (solid), and bundles of constant stiffness (dashed) comprising 1, 6, 20, and 50 tubes. Remarkably, the swimming speed of the variable stiffness swimmer is faster for nearly all parameters. In other words, a bead with a bundle of multiple tubes of different lengths surpasses one with the same number of equal-length tubes, which is a feature that arises naturally in our method of construction.

Finally, we tested our theoretical model by comparing the predicted and the observed swimming speeds of 10 individual tw8HT-bundle swimmers (Figure 4). The solutions from the

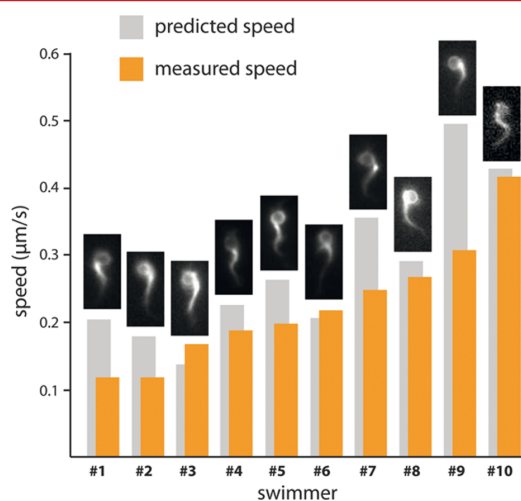


Figure 4. Comparison of simulated and measured swimming speeds. Measured speeds (orange) of 10 different DNA - magnetic bead hybrid swimmers (inlets) in comparison to the simulated values (gray) that were obtained for the respective swimmer. All swimmers were rotated with a frequency of 1 Hz. The swimmers were selected for their constant swimming behavior throughout the measurement from a pool of 40 swimmers depicted in Supporting Information Figure S6.

model allowed us to predict the swimming speed of a swimmer from its geometric parameters, which we determined for each swimmer from the experimental data. The so predicted swimming speeds differed by less than 40% from the observed speed. Differences between the model and the observations are attributed to errors in determining some of the parameters that enter the model (see Supporting Information Note S3) as well as to neglecting the additional drag, which arises in the vicinity of the glass surface. Despite these differences, our observations

agree remarkably well with the quantitative predictions from the model.

Our general and flexible self-assembly scheme allows constructing biocompatible artificial flagella of comparable size to small bacteria and in large numbers. Coupling of DNA-tubes to magnetic beads results in hybrid structures that swim by means of a flagellar bundle when actuated by an external magnetic field, which also allows for complex maneuvering. Our quantitative model reveals that our artificial and bacterial flagellar bundles whose stiffness decreases toward their ends achieve an improved speed compared to bundles with homogeneous rigidity. Design rules derived from the theoretical model can be applied in future experiments to optimize the swimmers to reach even higher speeds. To better understand and improve the assembly process of our artificial flagella, real-time bundle formation dynamics could be studied using magnetic tweezers, which can trap and rotate the swimmers in solution with no interfering glass surface nearby. If unfolding of the bundle can be achieved, further insights into run-and-tumble³⁰ and swimming strategies used by microorganisms can be gained. Our method demonstrates the feasibility and advantages of DNA self-assembly techniques for the construction of new microswimmer and nanorobot^{31,32} designs, including hierarchically assembled fully biocompatible soft materials that are difficult to realize with other fabrication methods.

■ ASSOCIATED CONTENT

Supporting Information

The Supporting Information is available free of charge on the ACS Publications website at DOI: 10.1021/acs.nanolett.5b03716.

Methods and materials, DNA sequences, additional fluorescence microscopy and TEM images, gels, statistical analysis, and model for swimmers with length-dependent bending modulus. (PDF)

Rotation of swimmer from Figure 2a. (AVI)

Directed motion of swimmer from Figure 2b. (AVI)

Structural change of the artificial bundle upon changing the rotation frequency. (AVI)

Swimmer from Figure 2c steered to follow a curved path. (AVI)

Swimmer exposed to a rotating magnetic field that repeatedly switches from clock- to counterclockwise. (AVI)

Analytic solution for the shape of a swimmer with decreasing tail stiffness. (AVI)

■ AUTHOR INFORMATION

Corresponding Authors

*E-mail: tim.liedl@physik.lmu.de.

*E-mail: fischer@is.mpg.de.

*E-mail: frey@lmu.de.

Author Contributions

A.M.M. and C.W. contributed equally to this work. A.M.M., C.W., E.F., and T.L. conceived the experiments. A.M.M. produced the structures. A.M.M., P.O., and P.F. performed and analyzed the swimming measurements. C.W. provided the analytic and numeric calculations. A.M.M., C.W., E.F., P.F., and T.L. interpreted the results and wrote the manuscript.

Notes

The authors declare no competing financial interest.

■ ACKNOWLEDGMENTS

We thank Susanne Kempter, Robert Schreiber, Johannes Emmerig, and Anastasiya Puchkova for experimental support and Dr. Christoph Weber for helpful discussions. This project was supported by the Deutsche Forschungsgemeinschaft via projects A06 and B02 within the SFB 1032 “Nanoagents for Spatiotemporal Control of Molecular and Cellular Reactions”, the NanoSystems Initiative Munich (NIM), the Center for Nanoscience (CeNS), and in part by the European Research Council under the ERC Grant Agreement Chiral MicroBots 278213 (P.O. and P.F.).

■ REFERENCES

- (1) Berg, H. C.; Anderson, R. A. *Nature* **1973**, *245* (5425), 380–382.
- (2) Gibbons, I. R. *J. Cell Biol.* **1981**, *91* (3 Pt 2), 107s–124s.
- (3) Purcell, E. M. *Am. J. Phys.* **1977**, *45* (1), 3–11.
- (4) Wang, J. *ACS Nano* **2009**, *3* (1), 4–9.
- (5) Lauga, E.; Powers, T. R. *Rep. Prog. Phys.* **2009**, *72* (9), 096601.
- (6) Ghosh, A.; Fischer, P. *Nano Lett.* **2009**, *9* (6), 2243–5.
- (7) Zhang, L.; Abbott, J. J.; Dong, L.; Peyer, K. E.; Kratochvil, B. E.; Zhang, H.; Bergeles, C.; Nelson, B. J. *Nano Lett.* **2009**, *9* (10), 3663–7.
- (8) Gao, W.; Feng, X.; Pei, A.; Kane, C. R.; Tam, R.; Hennessy, C.; Wang, J. *Nano Lett.* **2014**, *14* (1), 305–10.
- (9) Schamel, D.; Mark, A. G.; Gibbs, J. G.; Miksch, C.; Morozov, K. L.; Leshansky, A. M.; Fischer, P. *ACS Nano* **2014**, *8* (9), 8794–8801.
- (10) Gao, W.; Kagan, D.; Pak, O. S.; Clawson, C.; Campuzano, S.; Chuluun-Erdene, E.; Shipton, E.; Fullerton, E. E.; Zhang, L.; Lauga, E.; Wang, J. *Small* **2012**, *8* (3), 460–7.
- (11) Dreyfus, R.; Baudry, J.; Roper, M. L.; Fermigier, M.; Stone, H. A.; Bibette, J. *Nature* **2005**, *437* (7060), 862–5.
- (12) Fischer, P.; Ghosh, A. *Nanoscale* **2011**, *3* (2), 557–563.
- (13) Mhanna, R.; Qiu, F.; Zhang, L.; Ding, Y.; Sugihara, K.; Zenobi-Wong, M.; Nelson, B. J. *Small* **2014**, *10* (10), 1953–7.
- (14) Yin, P.; Hariadi, R. F.; Sahu, S.; Choi, H. M.; Park, S. H.; Labean, T. H.; Reif, J. H. *Science* **2008**, *321* (5890), 824–6.
- (15) Rothemund, P. W. *Nature* **2006**, *440* (7082), 297–302.
- (16) Seeman, N. C. *Annu. Rev. Biochem.* **2010**, *79*, 65.
- (17) Lauga, E. *Phys. Rev. E Stat. Nonlin. Soft Matter Phys.* **2007**, *75* (4), 041916.
- (18) Yang, Y.; Zhao, Z.; Zhang, F.; Nangreave, J.; Liu, Y.; Yan, H. *Nano Lett.* **2013**, *13* (4), 1862–1866.
- (19) Dietz, H.; Douglas, S. M.; Shih, W. M. *Science* **2009**, *325* (5941), 725–730.
- (20) Schiffels, D.; Liedl, T.; Fyngenson, D. K. *ACS Nano* **2013**, *7* (8), 6700–10.
- (21) Turner, L.; Ryu, W. S.; Berg, H. C. *J. Bacteriol.* **2000**, *182* (10), 2793–2801.
- (22) Darnton, N. C.; Turner, L.; Rojevsky, S.; Berg, H. C. *J. Bacteriol.* **2007**, *189* (5), 1756–1764.
- (23) Lauga, E.; DiLuzio, W. R.; Whitesides, G. M.; Stone, H. A. *Biophys. J.* **2006**, *90* (2), 400–12.
- (24) Heussinger, C.; Bathe, M.; Frey, E. *Phys. Rev. Lett.* **2007**, *99* (4), 048101.
- (25) Bathe, M.; Heussinger, C.; Claessens, M. M. A. E.; Bausch, A. R.; Frey, E. *Biophys. J.* **2008**, *94* (8), 2955–2964.
- (26) Claessens, M. M. A. E.; Bathe, M.; Frey, E.; Bausch, A. R. *Nat. Mater.* **2006**, *5* (9), 748–753.
- (27) Flory, P. J. *J. Am. Chem. Soc.* **1936**, *58*, 1877–1885.
- (28) Keller, J. B.; Rubinow, S. I. *J. Fluid Mech.* **1976**, *75* (Jun25), 705–714.
- (29) Batchelor, G. K. *J. Fluid Mech.* **1970**, *44* (03), 419.
- (30) Vogel, R.; Stark, H. *Phys. Rev. Lett.* **2013**, *110* (15), 158104.
- (31) Nelson, B. J.; Kaliakatsos, I. K.; Abbott, J. J. *Annu. Rev. Biomed. Eng.* **2010**, *12*, 55–85.
- (32) Wang, J. *Nanomachines: Fundamentals and Applications*; John Wiley & Sons: New York, 2013.

Appendix A: Supporting Information for Associated Publication P1

Supplementary Information

Self-Assembled DNA Tubes Forming Helices of Controlled Diameter and Chirality

Alexander Mario Maier, Wooli Bae, Daniel Schiffels, Johannes Friedrich Emmerig, Maximilian Schiff, and Tim Liedl

Supplementary Note S1: Design and construction of helical DNA tile-tubes through base pair insertions or deletions

Design of DNA tile tube structures with nanoscale helical diameters. An unmodified DNA tile strand has a standard length of 42 nucleotides. During assembly, it participates in forming two double helices with its two neighbouring tile strands¹. Thereby half of its sequence (21bp) hybridizes with the complementary sequence of one neighbouring tile and the other 21bp hybridize with the other neighbouring tile. Introduction of a base pair insertion or deletion in a specific helix, therefore requires adding or deleting a complementary nucleotide pair in the respective 21bp sections of each of the two tiles. If a tile participates in the formation of two neighbouring helices which both have an insertion and/or a deletion, then the sequence of the tile has to be changed in both 21bp section once. Depending on the arrangement of helices with insertion or deletion in the tube design, the length of the respective oligonucleotides can therefore vary between 40 (two deletions), 41 (one deletion), 42 (no insertion and no deletion or one deletion and one insertion), 43 (one insertion), and 44bp (two insertions) nucleotides (see oligonucleotides sequences in Figure S2).

We maintained the nomenclature used in previous work on DNA tile tubes. Formation of a straight n -helix tile tube requires $n-1$ U-tiles and one T-tile to form¹. For example, a 12-helix tile tube forms from the strands U1-U11 and T12. Helically shaped 12- to 4-helix tile tubes with one insertion or deletion from Figure 2a-c form when U2 and U3 are exchanged with U2+1 and U3+1 or U2-1 and U3-1, respectively (+1 and -1 indicating the insertion or deletion of a nucleotide in the tile sequence). 12-helix tile tubes with N insertions or deletions from Figure 2d-i, require exchanging $N+1$ tiles. For example, in a 12HT with 3 insertions or 3 deletions, four tiles (U1, U2, U3 and U4) have to be exchanged by U1+1, U2+2, U3+2 and U4+1, or U7-1, U8-2, U9-2 and U10-1, respectively. Note that in such designs, tiles that contribute to the formation of two helices with insertions or deletions (e.g. U2+2, U3+2, U8-2 and U9-2) require insertion or deletion of two nucleotides in their sequence (indicated by +2 and -2).

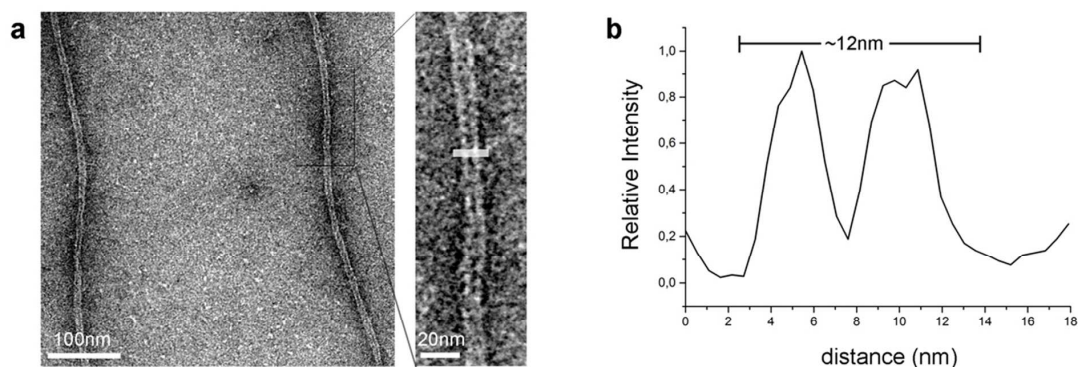


Figure S1: a) TEM images of 12 helix tile tubes with one base pair insertion revealed a darker region in the middle (cavity of hollow tube) flanked by two brighter regions (the DNA). This "wall contrast" occurs as uranyl staining can fill only the space around the DNA. b) An intensity profile along the tube's cross section confirmed the existence of the cavity and gave an estimation of the tube diameter of ~ 12 nm, which coincides well with the geometrical value for a tube like conformation of 12 DNA double helices.

```

unmodified oligonucleotides
U1      GGC GAT TAG GAC GCT AAG CCA CCT TTA GAT CCT GTA TCT GGT
U2      GGA TCT AAA GGA CCA GAT ACA CCA CTC TTC CTG ACA TCT TGT
U3      GGA AGA GTG GAC AAG ATG TCA CCG TGA GAA CTT GCA ATG CGT
U4      GGT TCT CAC GGA CGC ATT GCA CCG CAC GAC CTG TTC GAC AGT
U5      GGT CGT GCG GAC TGT CGA ACA CCA ACG ATG CCT GAT AGA AGT
U6      GGC ATC GTT GGA CTT CTA TCA ATG CAC CTC CAG CTT TGA ATG
U7      GGA GGT GCA TCA TTC AAA GCT AAC GGT AAC TAT GAC TTG GGA
U8      TAG TTA CCG TTT CCC AAG TCA AAC ACT AGA CAC ATG CTC CTA
U9      GTC TAG TGT TTA GGA GCA TGT CGA GAC TAC ACC CTT GCC ACC
U10     GTG TAG TCT CGG GTG GCA AGG TAC TAC CGC TCC ATT AAG AAT
U11     AGC GGT AGT AAT TCT TAA TGG ATC CGT CTA TCT ACA CTA TCA
U12     GAT AGA CGG ATT GAT AGT GTA AGA CGA AAT CAG CAG AAC TAA
U13     GAT TTC GTC TTT AGT TCT GCT CTG CGA AGT AAT CAG CCG AGC
U14     TTA CTT CGC AGG CTC GGC TGA GAA CTC GCT CCA GAA TCG ACG
T4      GGT TCT CAC GGA CGC ATT GCA CCT AAT CGC CTG GCT TAG CGT
T6      GGC ATC GTT GGA CTT CTA TCA CCT AAT CGC CTG GCT TAG CGT
T8      TAG TTA CCG TTT CCC AAG TCA CCT AAT CGC CTG GCT TAG CGT
T10     GTG TAG TCT CGG GTG GCA AGG CCT AAT CGC CTG GCT TAG CGT
T11     AGC GGT AGT AAT TCT TAA TGG CCT AAT CGC CTG GCT TAG CGT
T12     GAT AGA CGG ATT GAT AGT GTA CCT AAT CGC CTG GCT TAG CGT
T13     GAT TTC GTC TTT AGT TCT GCT CCT AAT CGC CTG GCT TAG CGT
T14     TTA CTT CGC AGG CTC GGC TGA CCT AAT CGC CTG GCT TAG CGT
T15     GAG CGA GTT CCG TGG ATT CTG CCT AAT CGC CTG GCT TAG CGT

Cy3-modified oligonucleotides
U1-Cy3  /5Cy3/TTG GCG ATT AGG ACG CTA AGC CAC CTT TAG ATC CTG TAT CTG GT
U4-Cy3  /5Cy3/TTG GTT CTC ACG GAC GCA TTG CAC CGC ACG ACC TGT TCG ACA GT
U5-Cy3  /5Cy3/TTG GTC GTG CCG ACT GTC GAA CAC CAA CGA TGC CTG ATA GAA GT

oligonucleotides for constant n=12 and varying N (insertions)
T12+1  GAT AGA CGG ATT GAT AGT GTA CCT AAT CGC CTG GCT TAG CGT
U1+1   GGC GAT TAG GAC GCT AAG CCA CCT TTA GAT CCT GTAT TCT GGT
U2+1   GGA TCT AAA GGA CCA GAT ACA CCA CTC TTC CTG ACA TTC TTG T
U3+1   GGA AGA GTG GAC AAG AAT GTC ACC GTG AGA ACC TGC AAT GCG T
U4+1   GGT TCT CAC GGA CGC AATT GCA CCG CAC GAC CTG TTC GAC AGT
U5+1   GGT CGT GCG GAC TGT CAGA ACA CCA ACG ATG CCT GAT AGA AGT
U1+2   GGC GAT TAG GAC GCT AAAG CCA CCT TTA GAT CCT GTAT TCT GGT
U2+2   GGA TCT AAA GGA CCA GAAT ACA CCA CTC TTC CTG ACAT TCT TGT
U3+2   GGA AGA GTG GAC AAG AATG TCA CCG TGA GAA CCT GCAA ITG CGT
U4+2   GGT TCT CAC GGA CGC AATT GCA CCG CAC GAC CTG TTCT GAC AGT
U5+2   GGT CGT GCG GAC TGT CAGA ACA CCA ACG ATG CCT GATT AGA AGT

oligonucleotides for constant n=12 and varying N (deletions)
U6-1   GGC ATC GTT GGA CTT CTA TCA ATG CA CTC CAG CTT TGA ATG
U7-1   GGA GGT GCA TCA TTC AAA GCT AAC GG AAC TAT GAC TTG GGA
U8-1   TAG TTA CCG TTT CCC AAG TCA AAC AC AGA CAC ATG CTC CTA
U9-1   GTC TA TGT TTA GGA GCA TGT CGA GAC TAC ACC CTT GCC ACC
U10-1  GTG TA TCT CGG GTG GCA AGG TAC TAC CGC TCC ATT AAG AAT
U11-1  AGC GG AGT AAT TCT TAA TGG ATC CGT CTA TCT ACA CTA TCA
U12-1  GAT AG CGG ATT GAT AGT GTA CCT AAT CGC CTG GCT TAG CGT
U7-2   GGA GG GCA TCA TTC AAA GCT AAC GG AAC TAT GAC TTG GGA
U8-2   TAG TT CCG TTT CCC AAG TCA AAC AC AGA CAC ATG CTC CTA
U9-2   GTC TA TGT TTA GGA GCA TGT CGA GA TAC ACC CTT GCC ACC
U10-2  GTG TA TCT CGG GTG GCA AGG TAC TA CGC TCC ATT AAG AAT
U11-2  AGC GG AGT AAT TCT TAA TGG ATC CG CTA TCT ACA CTA TCA
U6+1-1 GGC ATC GTT GGA CTT CATA TCA ATG CA CTC CAG CTT TGA ATG

```

Figure S2: Oligonucleotide sequences used for the construction of helical DNA tile tubes with nanometre-sized radius of curvature. Nucleotides contributing to a base pair insertion are highlighted in red, while two green nucleotides indicate the position of a deleted nucleotide contributing to a base pair deletion. Cy3-modifications including a TT-spacer are highlighted in orange.

Statistical analysis of DNA tile tubes. The analysis of helical DNA tile tubes from TEM images (Figure S3a) relies on work by Nam *et al.*, who recently proposed a model for such 2D confined filaments based on 2D confined Helical Worm-Like Chains (cHWLC).¹ In their study they found

that the filaments radius of curvature r_c can be determined between two curvature inversion points along the 2D confined contour, where it is almost constant. Figure S6a illustrates that the radius of curvature r_c can be determined from

$$r_c = \frac{a^2 + b^2}{2b}$$

once the coordinates of three points along its contour are measured – for example by two curvature inversion points and one middle point (blue and red dots) from the arc. We therefore extracted the coordinates of the minima and maxima (red dots) along the contour of the undulatory shape via ImageJ (Public Software, National Institute of Health), from which we then calculated the inversion points (blue dots) assuming that they lie in the centre of two middle points (Figure S3b). An example of the distribution of measured r_c is shown in Figure S3c for a 8-helix tube with one insertion. Data sets for all other tubes from Figure 2 are shown in Table S1.

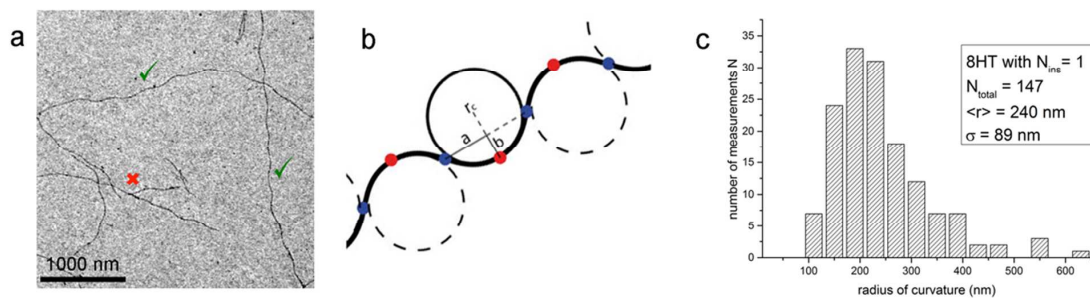


Figure S3: **a)** TEM image showing 8HTs with $N_{ins} = 1$ from Figure 2, which were chosen for the statistical analysis (green check marks). Structures were ignored if they were obviously aggregated, entangled or overlapping. Also short tubes of length less than a full “wavelength” were not included (red cross). **b)** Schematic showing how r_c was extracted from the contour of a 2D confined helical DNA tile tube **c)** Exemplary histogram of 8HTs with $N_{ins} = 1$. Error bars gained by this method are the standard error of the mean from all measurements.

tube type	$\langle r \rangle$ (nm)	σ (nm)	N (nm)	σ/\sqrt{N} (nm)	tube type	$\langle r \rangle$ (nm)	σ (nm)	N (nm)	σ/\sqrt{N} (nm)
12+1	561	207	41	32	12-1	556	184	31	36
10+1	407	180	49	26	12-2	184	68	42	10
8+1	240	89	147	7	12-3	153	58	50	8
6+1	211	93	44	14	12-4	137	46	47	7
4+1	88	19	38	3	12-5	120	37	44	6
					12-6	110	38	48	5
12-1	457	231	42	36	12+1-1	267	66	39	11
10-1	403	186	44	28	12+2-2	141	47	48	7
8-1	266	102	42	16	12+3-3	96	28	43	4
6-1	94	22	16	5	12+5-5	77	18	18	4
4-1	65	11	16	3	12+4-4	84	17	41	3
12+1	554	221	43	34	12+1-0	554	221	43	34
12+2	321	99	48	14	12+2-1	222	61	42	9
12+3	250	67	49	10	12+3-2	132	30	45	4
12+4	208	80	31	14	12+4-3	82	31	48	4
12+5	157	41	45	6	12+5-4	88	22	29	4
12+6	155	39	36	6					

Table S1: Statistical analysis of r_c for the helical tubes from Figure 2.

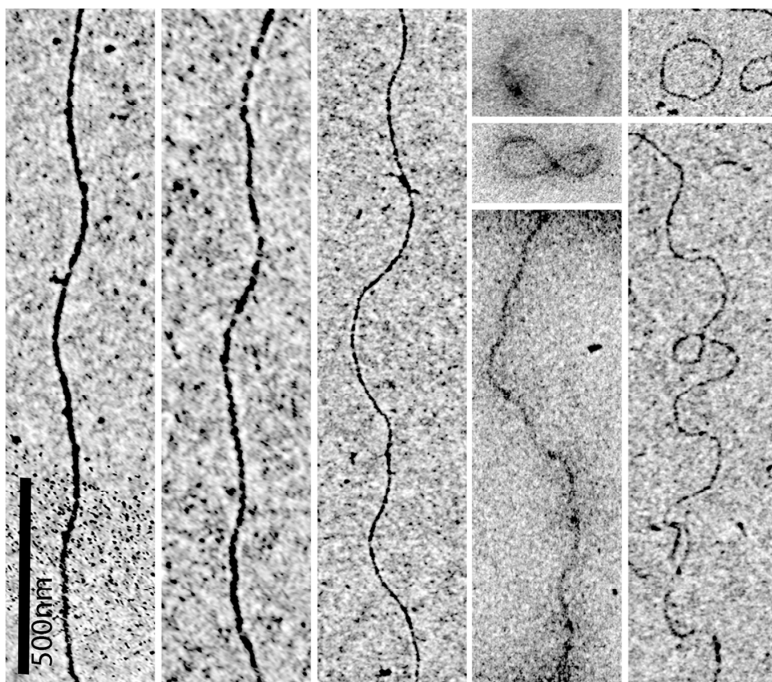


Figure S4: Transmission electron microscopy images of tile tubes for decreasing tube size n (from left to right: 12-, 10-, 8-, 6-, and 4HT) and constant number of deletions $N_{del} = 1$. The radius of the tube curvature r_c steadily decreased for smaller tube sizes from 457 nm to 65 nm as shown in Figure 2c in the main text. For the smaller tube sizes, the formation of rings and other closed structures with similar r_c was observed (insets). Scale bar: 500 nm

Interhelical angle of DNA tile tubes before closure. Before closing into a tube, the interhelical angle of a DNA tile tube is usually quite different from that of a closed circle of 360° as illustrated in Figure S3. By design, angles between neighbouring helices alternate between 13° and 47.3° , as was described in detail in the previous work by Yin et al.². Therefore, the central angle of an open 12-helix tile tube is $6 \cdot 13^\circ + 6 \cdot 47.3^\circ = 361.8^\circ$ and requires hardly any deformation to form a closed tube structure compared to the 10-, 8-, 6- and 4-helix tile tube.

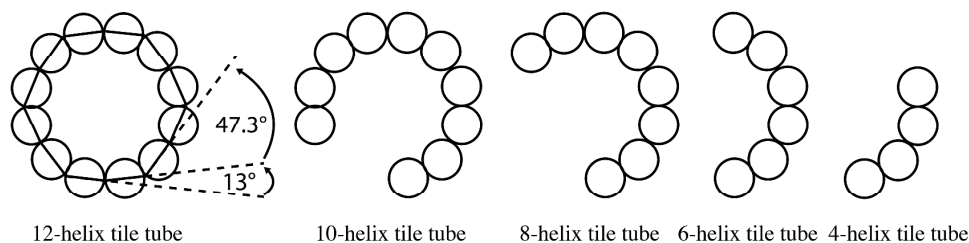


Figure S5: Schematic showing the cross sectional geometry of DNA tile tubes before closing into a tube. Except for the 12-helix tile tube, which has a natural central angle of $\sim 360^\circ$, tile tubes require additional bending in order to close into a tube structure.

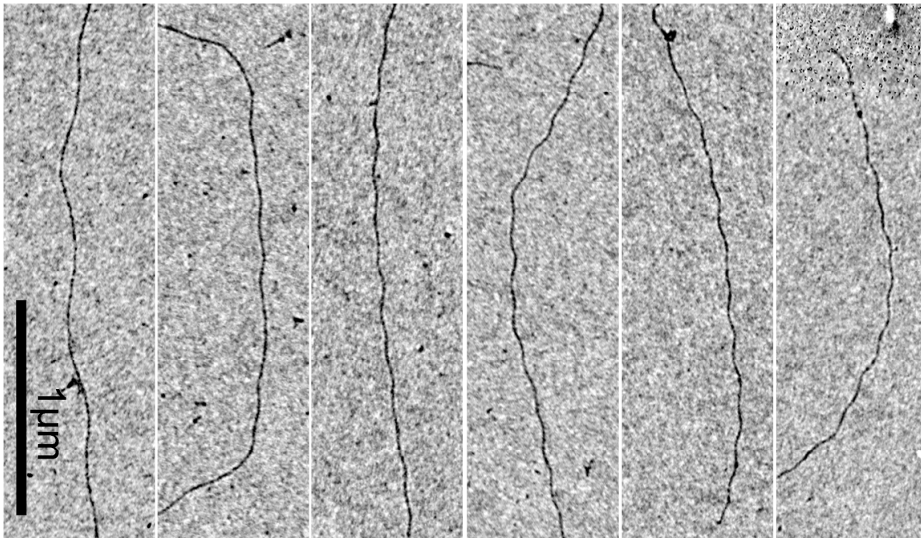


Figure S6: Transmission electron microscopy images of tile tubes with increasing amount of deletions N_{del} (left to right: from 1 to 6) and constant tube size $n = 12$. R_c steadily decreased for increasing amounts of deletions from 556 nm to 110 nm as shown in Figure 2f of the main text. Scale bar: 1 μm

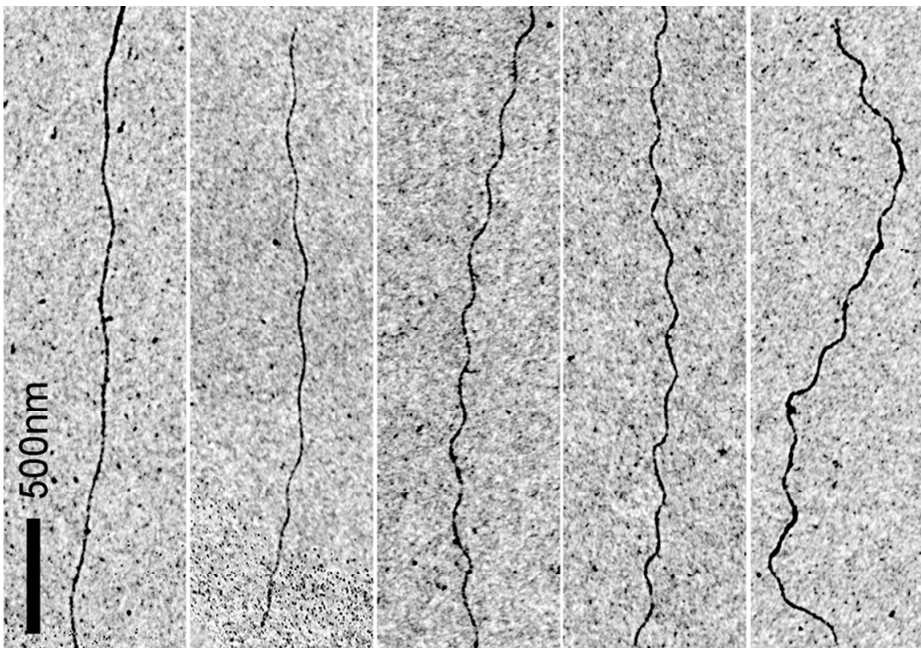


Figure S7: Transmission electron microscopy images of tile tubes with N insertions and $N-1$ deletions (left to right: from $N=1$ to 6) and constant tube size $n = 12$. R_c steadily decreased for increasing amounts of insertions and deletions from 554 nm to 88 nm as shown in Figure 2f of the main text. Scale bar: 500 nm.

Supplementary Note S2: Energetic predictions for the radius of curvature of helical DNA tile tubes

The radius of curvature r_c of helical tile tubes was predicted from a computer program published by Dietz *et al.*³ It calculates the total energy of a helical bundle with given geometry for different amounts of bending angle. From the angle, which corresponds to the minimal energy, R_c can be calculated.

The program was originally written for DNA origami constructs and assumed a stretch modulus of $S = 660$ and a bend modulus $B = 230$. For DNA tile tubes, we adjusted the bending modulus to $B = 156$ and assumed a circular cross section with radius $R = \frac{s}{2 \cdot \sin(\pi/n)}$ with $s = 2.8$ nm (spacing between neighbouring helices) in accordance with recent studies on the stiffness of DNA tile tubes⁴. An example of a python program for a 4-helix tile tube with $N_{ins}=1$ is given below:

Python script for a 4-helix tile tube with $N_{ins}=1$:

```
deq = 0.335
S = 660
B = 156
nref = 1680
dref = deq

# n is the number of basepairs installed in a region with a default 1680 bp

n = [0 for i in range(4)]
n
n[0] = 1760
n[1] = 1680
n[2] = 1680
n[3] = 1680

total_n = 0
for i in range(4):
    total_n += n[i]
average_n = float(total_n)/4
print "average n is", average_n, "\n"

# delta is the distance in nm from the center of mass midline bending axis
# invert sign for bending in other direction from mass midline bending axis

delta = [0 for i in range(4)]
delta[0] = 1.9796
delta[1] = 0
delta[2] = -1.9796
delta[3] = 0

for i in range(4):
    delta[i] *= +1

for angle_in_degrees in range(1, 500):
    angle_in_radians = angle_in_degrees/180.0*3.14159
    rref = deq*nref/angle_in_radians
    helix_stretch_energy = 0
    helix_bending_energy = 0
    for i in range(4):
        d = (float(nref)/n[i])*float(dref)*(delta[i]/rref + 1)
        helix_stretch_energy += 0.5*S*n[i]*((d-deq)**2)/deq
        helix_bending_energy += 0.5*B*n[i]*deq/((rref + delta[i])**2)

    total_energy = helix_stretch_energy + helix_bending_energy
    print "degree", angle_in_degrees, " stretch-compression energy", helix_stretch_energy, "\tbending energy",
    helix_bending_energy, "\ttotal energy", total_energy
```

Energetic predictions for tile tubes of elliptical shape: One major parameter that affects the energetic predictions is the distance of the DNA duplexes from the bending axis of the tube Δ_i . Shorter distances should result in stronger bending from insertions or deletions and therefore give smaller r_c . These considerations lead us to speculate that the overestimation of the radius for tubes with several insertions ($N_{\text{ins}} = 5$ and 6) as shown in Figure 2 can be attributed to a structural change in the tube's cross section from a spherical to an elliptical shape. We believe that this structural change results from stress exerted by insertions and/or deletions on its neighbouring helices. As illustrated in a simplified form for one insertion (Figure S8a), the stress exerted by an insertion pushes its adjacent helices *via* the cross over points towards bigger interhelical angles. This pushing generates a deformation of the overall tube cross section into an elliptical shape. To test this hypothesis, we assumed an elliptical shape $r^2 = a^2 + b^2$ with equal circumference to that of a spherical cross-section and recalculated r_c for different values of a and b for the case of 12HTs with $N_{\text{ins}}=1$ to 6 from Figure 2. For small r_c , we found the best accordance between model and experiment for $a = 4.25$ and $b = 6.56$, which led to an improvement of the fitting by $\sim 20\%$ for both 12HT with $N_{\text{ins}} = 5$ and 6 (Figure S8b). In contrast, tubes with $N_{\text{ins}} = 3$ and 4 insertions are best described by a spherical cross section. These observations suggest that elliptical deformations occur only in tubes with many insertions or deletions.

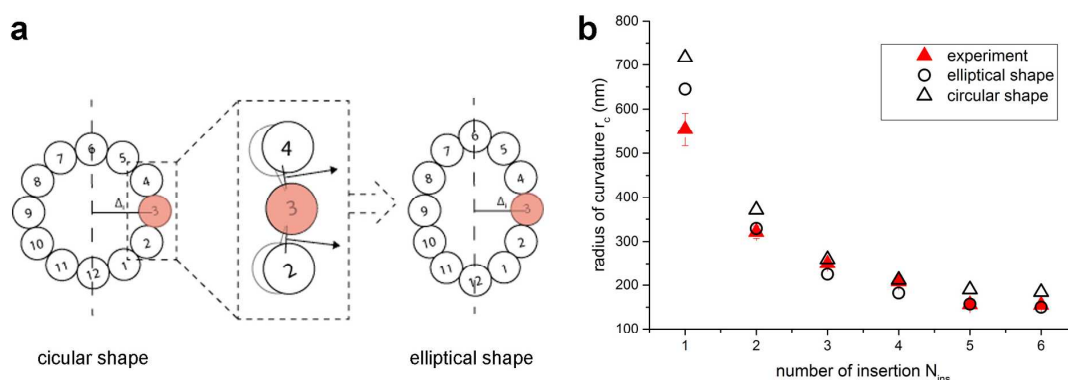


Figure S8: **a)** Possible structural change in the cross section geometry of DNA tile tubes through a base pair insertion. **b)** Comparison of the measured radius of curvature r_c (black) to predictions assuming an elliptical (green) or a spherical (red) cross sectional shape.

Supplementary Note S3: Design and construction of helical DNA tile tubes through *tile shifting*

Design of helical DNA tile tube structures with microscale diameters. DNA tile tubes with odd number of helices possess an intrinsic "supertwist"² and can assemble large helical diameters through a combination of *tile shifting* and Cy3- induced bending as illustrated in Figure 4 in the maintext. Figure S9 demonstrates an exemplary tile shift for a subset of three adjacent oligonucleotides. Each tile consists of two partial sequences, with each sequence being complementary to one neighbouring partial sequence (Figure S9a). Shifting of a partial sequence by 1 nt results in a displacement of the position of the neighbouring and all subsequent tiles by 1 nt. N shifts are achieved by shifting n tiles by 1 nt each.

Tile shifting also affects the position of cross over points to neighbouring helices and thereby the interhelical angle between them as illustrated in Figure S9c. In order to keep the cross sectional geometry of tile-shifted tubes as circular as possible we only exchanged tiles with even number, which corresponds to a change of the respective interhelical angle from 47.3° to 13° . For example, a 13-helix tile tube with 2nt shift is constructed by exchanging U10 and U12 by V10 and V12 (a list of the shifted oligonucleotide sequences is shown in Figure S10).

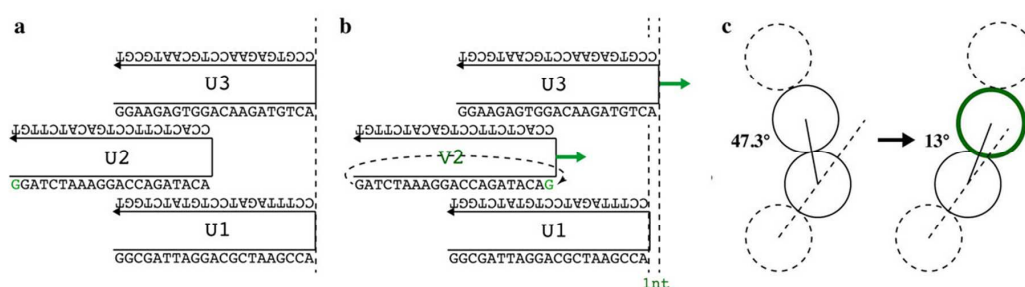


Figure S9: a) Schematic showing a tile shift by 1nt and b) the corresponding change in the interhelical angle between the neighbouring helices.

	oligonucleotides for base pair shifting
V2	GAT CTA AAG GAC CAG ATA CAG CCA CTC TTC CTG ACA TCT TGT
V4	GTT CTC ACG GAC GCA TTG CAG CCG CAC GAC CTG TTC GAC AGT
V6	GCA TCG TTG GAC TTC TAT CAG ATG CAC CTC CAG CTT TGA ATG
V8	AGT TAC CGT TTC CCA AGT CAT AAC ACT AGA CAC ATG CTC CTA
V10	TGT AGT CTC GGG TGG CAA GGG TAC TAC CGC TCC ATT AAG AAT
V12	ATA GAC GGA TTG ATA GTG TAG AGA CGA AAT CAG CAG AAC TAA
V14	TAC TTC GCA GGC TCG GCT GAT GAA CTC GCT CCA GAA TCG ACG

Figure S10: Oligonucleotide sequences used for the construction of DNA tile tubes with microscale helical diameters. In n -helix tile tubes, a tile shift of m nucleotides requires exchanging m out of n U staples from Figure S1 by m V-staples.

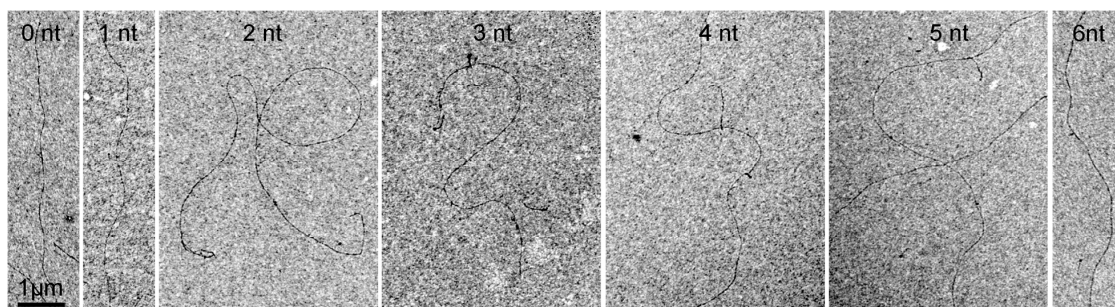


Figure S11: Transmission electron microscopy of 13-helix tile tubes with 0 to 6 nt tile shift. Tile tubes with 0, 1 and 6 nt shift showed an undulatory shape similar to that observed for the tubes from Figure 2. The increase in radius of curvature from 0 and 1 nt (~ 0.5 to $0.7 \mu\text{m}$) and the anew decrease for 6 nt ($\sim 0.6 \mu\text{m}$) coincides with the observations from Figure 4. Tubes with 2 to 5 nt tile shift exhibited a more random contour from which it was not possible to determine the radius of curvature. Scale bar: $1 \mu\text{m}$

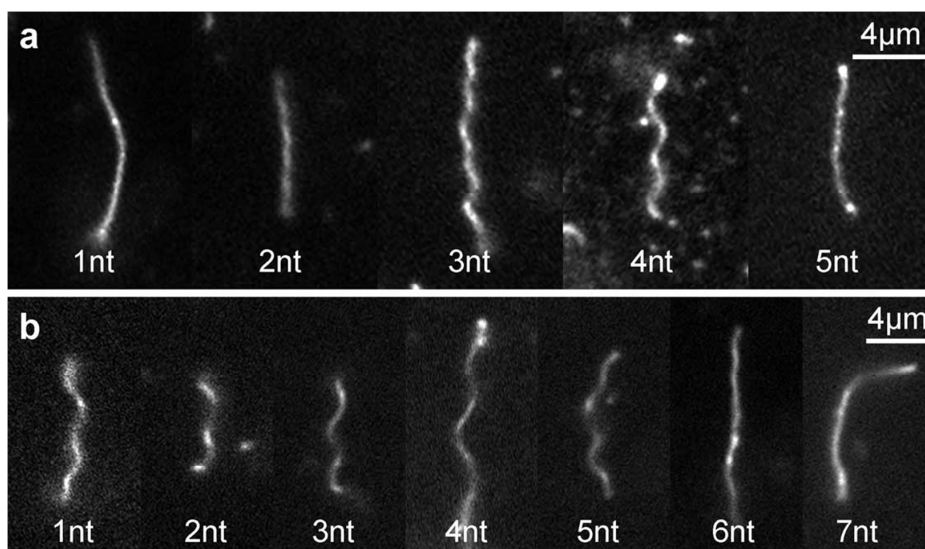


Figure S12: Fluorescence microscopy images of **a)** 11HT with 1 to 5 nt tile shift. Similarly to the tile shifting in the 13HT shown in Figure 3, the 11HT diameter first increased, reached its maximum at 4 nt and then decreased again. **b)** The same behaviour was observed for the 15HT for 1 to 7 nt tile shift, however here helical structures were already observed for a 1 nt tile shift. Maximum diameters of $\sim 1 \mu\text{m}$ and $\sim 2 \mu\text{m}$ were observed for the 11HT and 15HT at 4nt tile shift, respectively. In all three tube types (11HT, 13HT and 15HT) the effect of the Cy3 modifications on the overall twist of the helical tube seems to be stronger for higher numbers of tile shift (= less supertwist), which leads to a more rapid change of the overall twist. We believe this phenomenon is related to interactions of the Cy3 dyes with the supertwisted tube geometry. For example, different amounts of supertwist can lead to a change in the distance between neighboring Cy3 dyes, the geometry of the attachment site and the supertwisted DNA structure itself, which might affect the probability of the Cy3 dyes to stack with the DNA double helix and therefore alter the strength of the Cy3-induced right-handed twist. Scale bars: $4 \mu\text{m}$

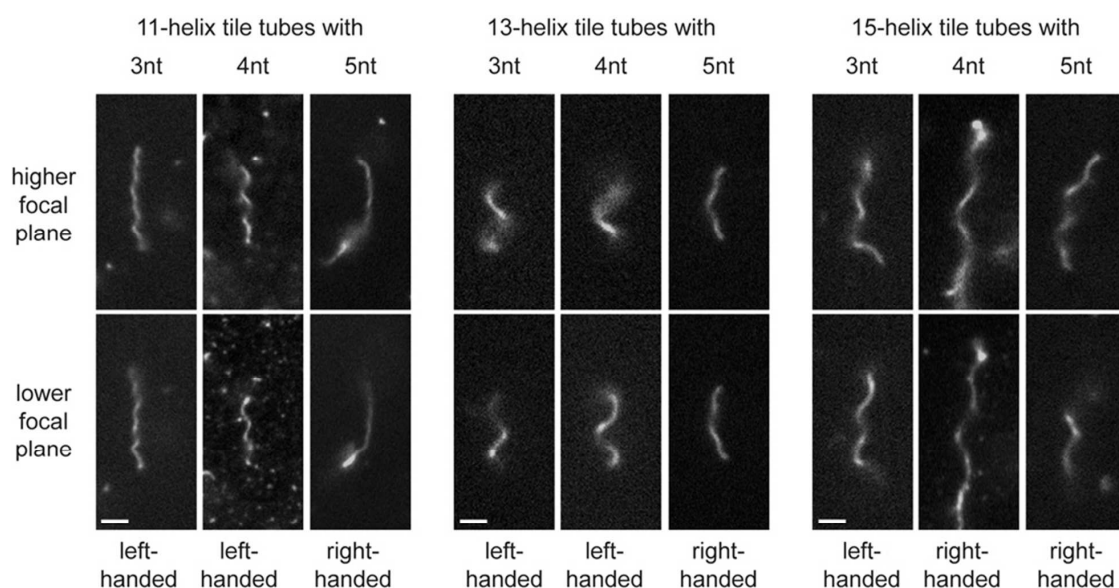


Figure S13: Fluorescence microscopy images of 3 to 5nt tile shifted 11HT (left), 13HT (middle) and 15HT (right) imaged in their higher and lower focal plane. A change in chirality from left- to right-handedness was observed for all three tube types. While the right-handed helical shape of the 5nt-shifted 11HT is difficult to image due to its small helical diameter, it is pronounced for the 5nt-shifted 13HT and the 4nt- and 5nt-shifted 15HT. Note that the transition to right-handedness already occurred at 4nt for the 15HT, as same amounts of tile-shifting give less left-handed twist in bigger tubes. Scale bars: 2 μm

References:

1. Nam, G.-M.; Lee, N.-K.; Mohrbach, H.; Johner, A.; Kulić, I. M., Helices at Interfaces. *Europhys. Lett.* **2012**, *100*, 28001.
2. Yin, P.; Hariadi, R. F.; Sahu, S.; Choi, H. M.; Park, S. H.; Labean, T. H.; Reif, J. H., Programming DNA Tube Circumferences. *Science* **2008**, *321*, 824-826.
3. Dietz, H.; Douglas, S. M.; Shih, W. M., Folding DNA into Twisted and Curved Nanoscale Shapes. *Science* **2009**, *325*, 725-730.
4. Schiffels, D.; Liedl, T.; Fygenon, D. K., Nanoscale Structure and Microscale Stiffness of DNA Nanotubes. *ACS Nano* **2013**, *7*, 6700-6710.

Appendix B: Supporting Information for Associated Publication P2

Supplementary Information

Magnetic propulsion of microswimmers with DNA-based flagellar bundles

Alexander M. Maier, Cornelius Weig, Peter Oswald, Erwin Frey, Peer Fischer & Tim Liedl

Supplementary Videos:

Supplementary Video 1. The video shows a close-up of the rotation of the swimmer demonstrated in Figure 2a. The video frame co-moves with the swimmer, so that the artificial tile-tube bundle swimmer stays in the center. The swimmer was actuated at 1Hz.

Supplementary Video 2. The video shows the directed motion of the swimmer from Figure 2b. The driving frequency was 1Hz and the rotation was along the horizontal axis. In addition to the forward swimming, a movement perpendicular to the rotation axis due to hydrodynamic drag with the close-by surface can be observed. The video is threefold accelerated.

Supplementary Video 3. The video shows the structural change of the artificial bundle upon changing the rotation frequency. By switching from 3Hz to 1Hz, the initially straight bundle changes to a chiral shape, which then propels the swimmer. The video is threefold accelerated.

Supplementary Video 4. The video shows the swimming along a curved path of the swimmer from Figure 2c. By gradually changing the rotation axis of the external magnetic field the swimming path can be controlled. The swimmer was driven at 1Hz. The video is eightfold accelerated.

Supplementary Video 5. The video shows a swimmer exposed to a rotating magnetic field along the horizontal axis that repeatedly switches from clock- to counterclockwise. The swimmer retains its forward motion while moving up and down due to a reversed interaction with the surface. The swimmer was driven at 1Hz. The video is threefold accelerated.

Supplementary Video 6. The video shows the analytic solution for the shape of a swimmer with decreasing tail stiffness. The colour code and the width of the tail indicate the local stiffness. In the front and rear view it becomes apparent that the tail has a static chiral structure.

Supplementary Note S1: Design and construction of DNA tile-tube - magnetic bead hybrids

Design of DNA tile tube structures. DNA tile tubes were constructed according to Yin et al.¹. The shape and the stiffness of the DNA tile-tubes were controlled by adjusting the number of DNA strands, where n strands form a n -helix tube, and by changing their respective lengths. Depending on the design, the DNA strands had a length of 42 or 43 base pairs where each oligonucleotide was partially complementary to two adjacent strands. An even number n of strands leads to straight tubes with a stiffness that increases with the 4th power of the tube radius². The st8HT from Figure 1d, for example, has a diameter of ~ 8 nm, a persistence length of ~ 8.2 μm , and readily polymerizes to a length of several micrometers. Elongating one of the n strands by inserting an additional base pair gives the assembled tubes a controlled pre-defined twist and curvature³. For example, the insertion of one base pair per structural unit in any double strand of an 8HT results in an overall helical shape (see Figure S1). The resulting helical structures (tw8HT) shown in Figure 1e exhibit a pitch and a diameter of sub-micrometer size. Larger diameter helices assemble when an odd number of DNA duplexes are used in the DNA tile tubes introducing a so-called "supertwist"². Here the repeating structural unit assembles into a bundle with its neighboring units introducing a small relative twist to the DNA duplexes that causes the overall supertwist (as illustrated in Figure 1b). For example, the st13HT, shown in Figure 1f with a tube diameter of ~ 11 nm, shows a helical diameter of about 1 μm .

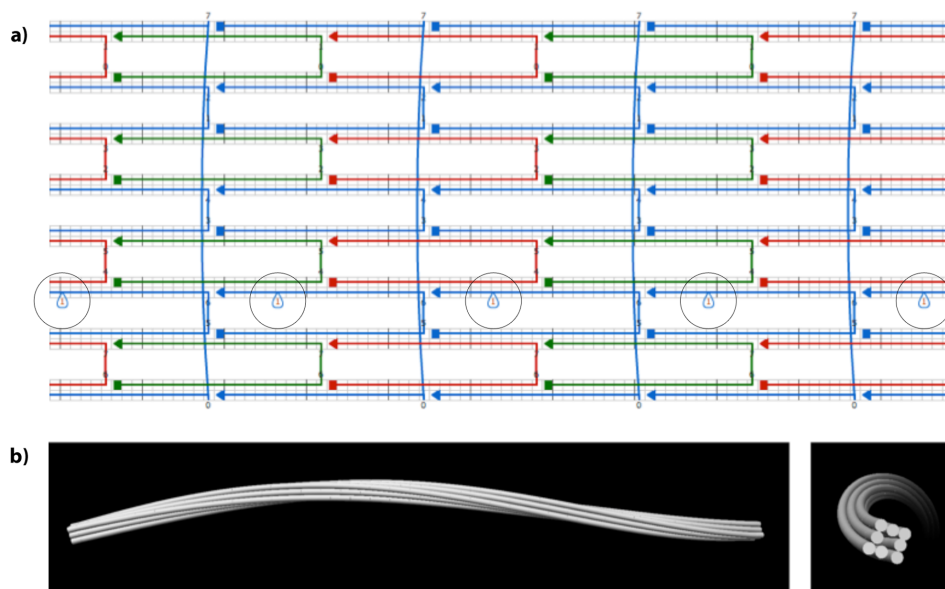


Figure S1: Design and simulation of twisted 8-helix tile tube. **a)** For a defined twist in the 8-helix tube (8HT), one extra base pair was added into every repeating segment of one double helix (illustrated by the blue loop). **b)** A cando⁴ simulation shows the overall twist in the structure.

Folding and purification of DNA-tile tube structures. Assembly of the tile tube structures was carried out in a one-pot reaction with 1 μM of each oligonucleotide in 1x TAE buffer and 12 mM MgCl_2 . The folding mixture was then exposed to a thermal annealing ramp, starting with a heating step to 80°C for 10 min, followed by a stepwise cooling from 65°C to 45°C at a cooling rate of 0.5°C / 5 min. (folded tile tube structures are shown in Figure S2-S4). After folding, larger tile tube structures were separated from smaller constructs via agarose gel electrophoresis (Fig. S3).

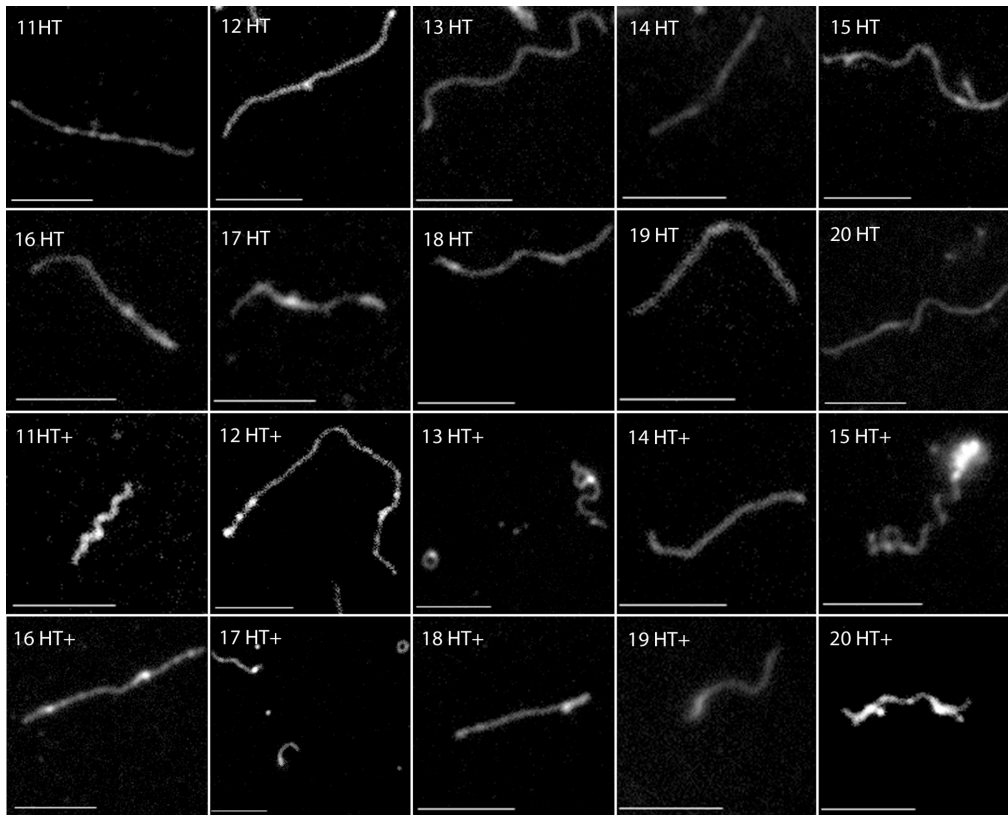


Figure S2: DNA tile tubes. Beside the structures presented in the main text (Fig. 1), DNA tile tubes were constructed that consisted of 11 to 20 double helices (11HT-20HT). In addition, we introduced an intrinsic twist (11HT+-20HT+) as is shown for the 8HT+ in Figure 1. This shows the great versatility in constructing helical shapes and bending stiffnesses easily accomplished by this method. All scale bars: $3 \mu\text{m}$

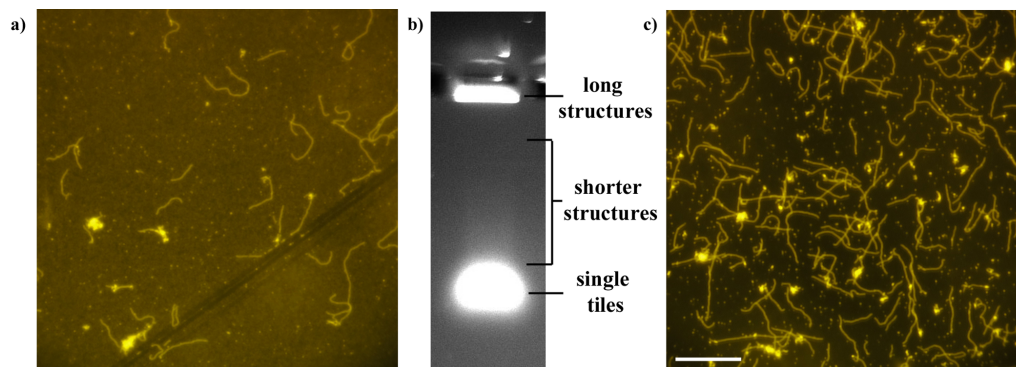


Figure S3: Purification of large tile tubes from smaller constructs. **a)** Fluorescence microscopy image of unpurified tile tubes taken directly after folding. The image shows a high background that can be attributed to light emitted by nanometer-sized tile tubes and unfolded oligonucleotides. **b)** In a 0.5% agarose gel, long tile-tube structures remain in the gel pocket and can be purified from smaller constructs and excess of single tiles. **c)** After purification of the sample, the background signal is drastically reduced. This separation of larger tile tubes is achieved by letting smaller constructs run into the gel, while larger structures remain in the pocket and can be pipetted out. Scale bars: $10 \mu\text{m}$

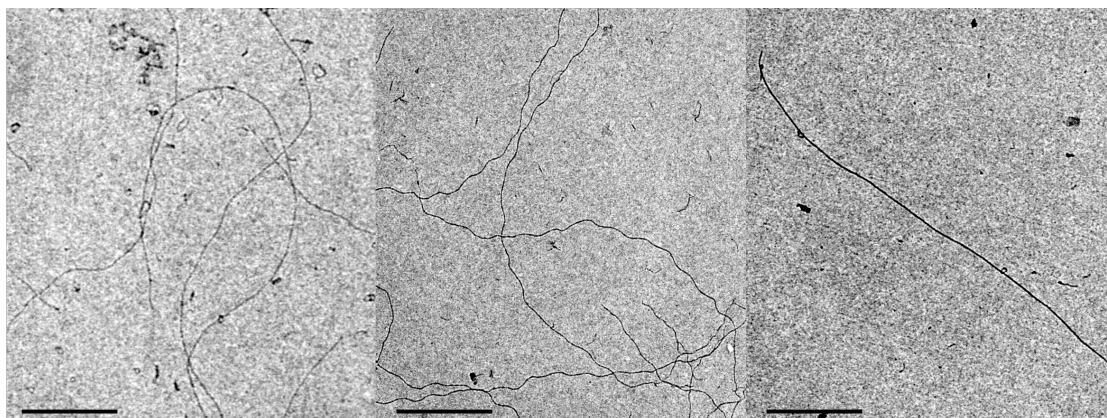


Figure S4: Structural characterization of purified tile-tubes. Correct folding of a) 8HT, b) tw8HT and c) 13HT as revealed by transmission electron microscopy. Scale bars: 1 μm

Magnetic particle - DNA conjugation: 1 μm streptavidin-coated magnetic particles (Sigma Aldrich, Germany) were functionalized with biotin-modified DNA strands (MWG Eurofins, Germany) (Table S1) by mixing a high excess of DNA (10 μM) with the 1 μm (3 pM) particles in a 0.5x TBE buffer. After incubation for 30 min at room temperature, biotin-DNA-modified particles were purified from the excess of biotin-DNA by centrifugating the sample for 5 min at 15,871 rcf followed by three additional washing steps at same rotation speed. In each step, the supernatant liquid was carefully removed, while keeping the pallet of the magnetic nanoparticles at the bottom of the centrifugation tube by a strong permanent magnet.

biotin-ACCAGATACACCACTCTCC biotin-ACGCATTGCACCGCAGACC	biotin-ACTTCTATCAATGCACCTCC biotin-TCCCAAGTCACCTAATCGCC	coupling of magnetic particles to tile-tubes
--	--	---

Table S1: Staple sequences used for coupling DNA tile-tubes to magnetic particles. Biotin-modified sequences of oligonucleotides that were used to couple magnetic particles to tile-tube structures via the hybridization of complementary DNA strands. Sequences are written from 5' to 3'.

Coupling of DNA tile-tube structures to magnetic beads. For the construction of DNA tile-tube magnetic bead hybrids from Figure 1g-i, 1 μl of biotin-DNA 1 μm particles (~ 32 pM) were hybridized to 3 μl of 8HTs, 8HT+s (~ 26 ng/ μl) and 13HTs (~ 42 ng/ μl), respectively, in a total volume of 100 μl 0.5x TBE buffer with 11 mM MgCl_2 and 0.05% Tween 20. The conjugation step took place at room temperature for 30 min. To avoid sedimentation of the assembled structures, the samples were put on a rotator at moderate speed.

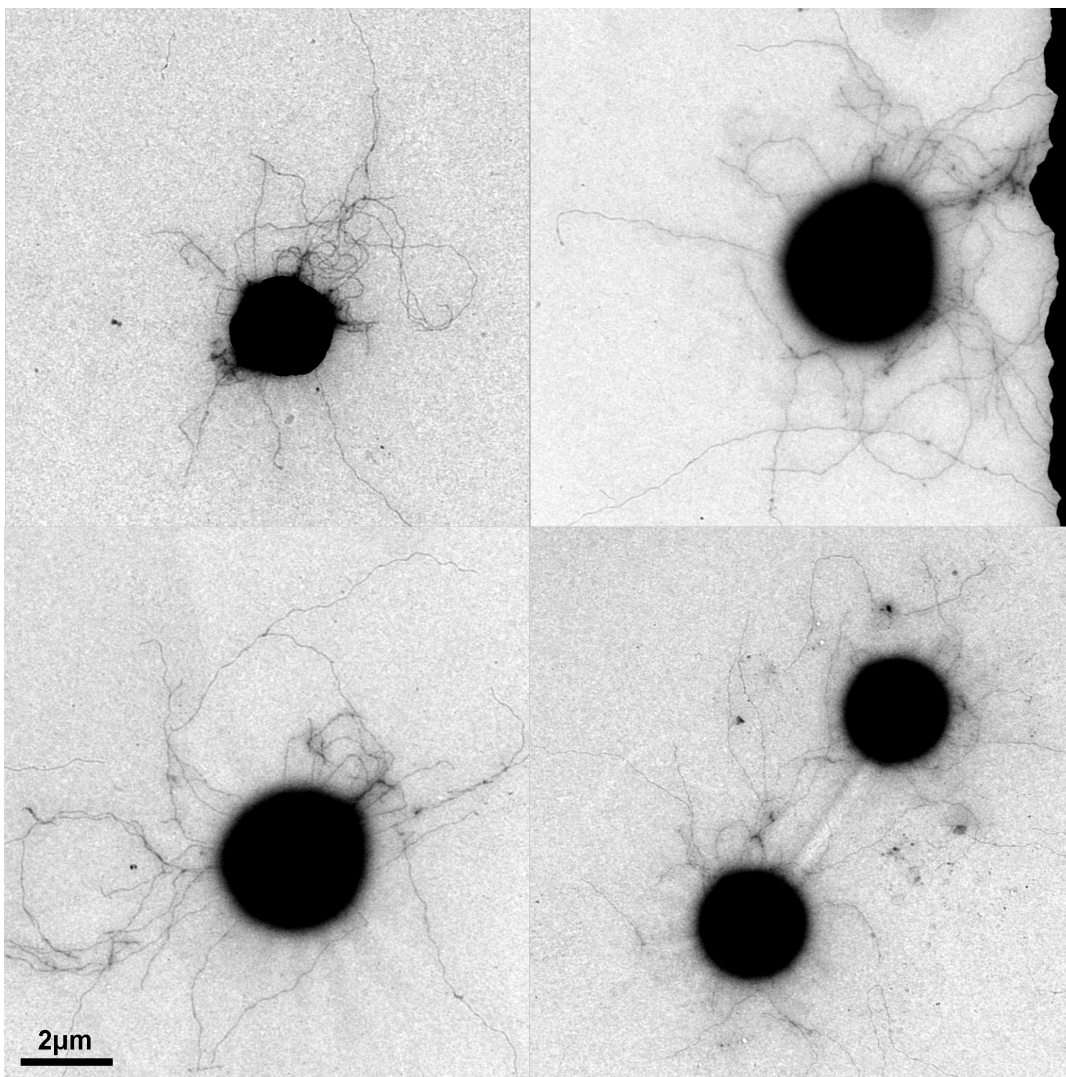


Figure S5: Structural characterization of DNA tile-tube magnetic bead hybrids. Transmission electron microscopy images of purified tw8HTs attached to $1\mu\text{m}$ magnetic beads. Scale bars: $1\mu\text{m}$

Supplementary Note S2: Fluorescence microscopy and magnetic actuation

To visualize tile tubes via fluorescence microscopy, three out of n tiles of an n -helix tube were modified with Cy3 dyes on their 5' ends as described in Schiffels *et al.*² We used a Zeiss Observer Z1 in fluorescence mode with a 100x objective, mercury lamp illumination, a Cy3 filter set and an Andor Solis camera (pixel resolution: 6.4 pixels/ μm). All experiments were carried out at room temperature.

DNA - magnetic bead hybrids were actuated by a water-cooled three-axis Helmholtz coil that was incorporated into the microscopy setup. The coil generates a spatially homogeneous time-varying magnetic field, which exerts a torque on the magnetic bead. The magnetic actuation was initiated before the sample was placed into the setup to allow for an instantaneous bundle formation of the hybrid particles in the absence of a close-by surface. However, observation of the hybrid structures was not possible until the structures sank into the focus volume close to the glass surface. Initiation of the magnetic actuation after the particles reached the focus, however, did not lead to bundle formation due to the close proximity with the (sticky) glass surface (we therefore could not observe the dynamics of bundle formation). Similarly, switching the magnetic field off while the swimmers were near the surface led to swimmers attaching to the surface, even though the glass surface was previously functionalized with BSA.

After actuation 10% of the tw8HT and st8HT and 1% of the stw13HT hybrid structures formed a bundle on one side of the bead. Next to these well-assembled bundles, a variety of unwanted side products formed (*e.g.* bundles protruding from two sides of a magnetic particle, clusters of magnetic beads, appendages with (multiple) bifurcations, particles adhering to the surface) as demonstrated for the tw8HT in Figure S6. Hybrids that formed a corkscrew-like bundled tail on one side of the bead started to propel along the rotation axis, whereas particles with bundles on two sides did not. Figure S7 shows the speed distribution of tw8HT swimmers driven by an externally applied magnetic field with frequencies of 1, 2 and 3 Hz.

We further compared the bundle structure of tw8HTs and st8HTs after bundle formation. As demonstrated in Figure S7, both swimmer types show very similar bundle structures resulting in swimmers of similar speeds. The difference in the model parameters - gained from fluorescence intensity measurements - between a tw8HT and a st8HT can be smaller than that between two tw8HT swimmers (see Table S2), which is why we cannot determine a qualitative difference in the bundle structure of the two swimmer types.

The speed of stw13HT hybrid structures varied between 0 and 0.56 $\mu\text{m/s}$, which is similar to the speed of tw8HT swimmers. However, our fluorescence data indicates that well-assembled corkscrew-like stw13HT bundles consist of fewer tubes (see Figure S9). We speculate that the combination of higher stiffness of the stw13HT (~ 2.64 times²) and fewer tubes in the bundle result in a comparable overall bundle stiffness of tw8HT and stw13HT swimmers, which in turn leads to similar swimming speeds.

Because stw13HT did form with a far lower yield and because we did not observe a difference between tw8HT and st8HT bundles, we focused our study on the tw8HT swimmers, which provided us with a sufficiently broad variety of bundles of different stiffness for testing our theoretical model.

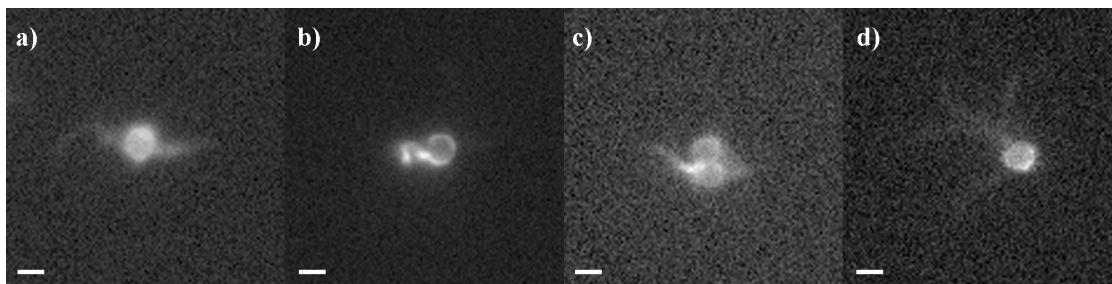


Figure S6: Unwanted tw8HT shapes that formed during bundle formation. Besides properly formed flagellar bundles shown in Figure 2 of the main text, hybrid structures can a) form bundles on two sides of a particle, b) have deformed bundles, c) cluster due to magnetic interaction between to or more particles or d) attach to the glass surface before bundle formation can occur. All scale bars: 2 μm .

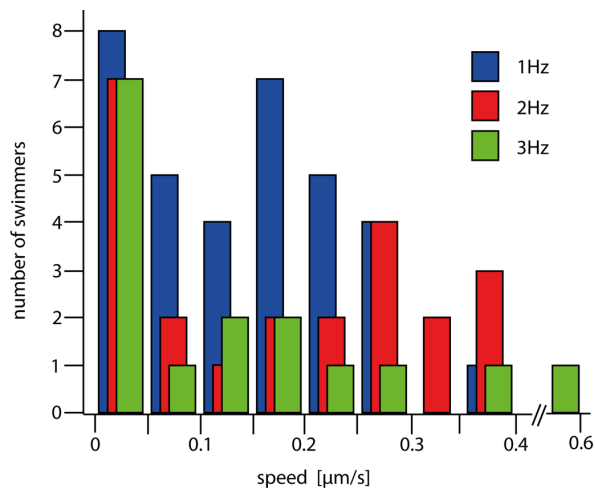


Figure S7: Speed of tw8HT DNA-magnetic bead hybrid swimmers. Histogram shows the speed distribution of artificial swimmers driven by an externally applied magnetic field with frequencies of 1 Hz (blue), 2 Hz (red) and 3 Hz (green), respectively.

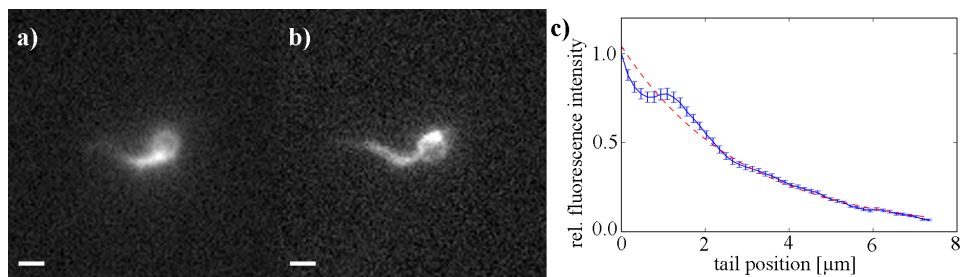


Figure S8: Comparison of the tw8HT and st8HT bundle structure. Snapshots of a) a st8HT swimmer and of b) the tw8HT swimmer #9 from Figure 4. Both swimmers have comparable speeds (0.28 and 0.31 $\mu\text{m/s}$, respectively) and form similar helical shapes. c) A fluorescence intensity analysis of the bundle from a) shows that the amount of tubes decreases exponentially as in tw8HT bundles. All model parameters and the predicted swimming speed (shown in the inset) agree well with those found for tw8HT swimmers in Table S2. All scale bars: 2 μm .

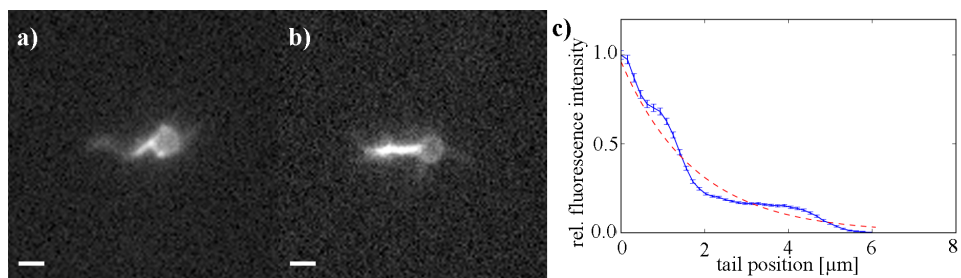


Figure S9: Bundle formation of stw13HT. Among the stw13HT hybrids with a single bundle on one side of the bead, we observed a heterogeneous population of a) proper corkscrew-like and b) arbitrarily shaped structures. c) An analysis of the fluorescence intensity along the bundle of the stw13HT swimmer from a) indicates that its bundle consists of only approximately five tubes. All scale bars: 2 μm .

Supplementary Note S3:

Model for swimmers with length-dependent bending modulus

Solving the equations of motion in a hydrodynamic setting is notoriously difficult, rendering adroit simplifications inevitable for an analytic treatment. As a first step, we neglect hydrodynamic fluctuations so that the model becomes deterministic. Without noise, we lose any notion of diffusion, but since we are mainly interested in active swimming here, this is acceptable. The swimmer basically consists of a spherical head with several thin appendages. The main text showed that the attached tubes become entangled through the driven rotation and thus form a tight bundle. Consequently, in the following calculations we treat the whole bundle as a *single* thin appendage. This filament is flexible and accordingly has many degrees of freedom, so the main task is to determine its shape. The structure of this supplement is roughly as follows: First, we present a general treatment of flexible filaments with variable stiffness in a small-slope approximation. The shape equation of this filament is then solved with the boundary condition for a spherical bead at one end. From this filament shape, we then determine the swimming speed. Finally, we apply this model to the experimentally realized swimmers from the main text.

Equations of motion for the tail

Actuated swimmers have been discussed in-depth by Lauga,⁵ however only for tails with constant stiffness. In the following, we generalize this work to tails with variable stiffness. Because the following line of argument closely resembles the steps in Lauga's work, we try to be brief and focus on the differences. As argued in the main text, we model the bundle of attached tubes as a *single* inextensible elastic filament with a bending stiffness $\alpha(s)$ that changes along the contour of the filament. The elastic energy of the filament with length-dependent bending modulus is given by

$$\mathcal{E} = \int_0^L \left((\alpha(s) \partial_s^2 \mathbf{r})^2 + (\sigma(s) \partial_s \mathbf{r})^2 \right) ds , \quad (1)$$

where $\sigma(s)$ is a Lagrange multiplier ensuring inextensibility of the filament. We stress that both $\alpha(s)$ and $\sigma(s)$ depend on the position s along the filament. From the energy Eq. 1 the force density due to bending and constraint forces are obtained via variation of the contour path. In the low-Reynolds number regime where inertia plays no role, this force needs to balance with the anisotropic friction forces on the filament from the fluid as given by standard slender body theory,^{6,7}

$$(\xi_{\parallel} \mathbf{t} \otimes \mathbf{t} + \xi_{\perp} (1 - \mathbf{t} \otimes \mathbf{t})) \mathbf{u} = -\partial_s^2 (\alpha(s) \partial_s^2 \mathbf{r}) + \partial_s (\sigma(s) \partial_s \mathbf{r}) . \quad (2)$$

Here $\mathbf{t}(s) = \partial_s \mathbf{r}(s)$ is the local tangent to the filament and $\mathbf{u}(s) = \dot{\mathbf{r}}(s)$ is the local speed of the filament with respect to the surrounding fluid. Note the difference on the RHS to the original work of Lauga, where the term $\partial_s^2 (\alpha(s) \partial_s^2 \mathbf{r})$ is replaced by $\alpha \partial_s^4 \mathbf{r}$. An equation for the Lagrange multiplier which ensures the constraint $|\mathbf{t}^2| = 1$ is given in an implicit form by

$$\mathbf{t} \cdot \partial_s \mathbf{u} = 0 . \quad (3)$$

These two equations have the boundary conditions

$$\mathbf{F}_{\text{ext}} = \partial_s(\alpha \partial_s^2 \mathbf{r}) - \sigma \partial_s \mathbf{r}, \quad \mathbf{T}_{\text{ext}} = -\mathbf{t} \times \alpha \partial_s^2 \mathbf{r} \quad \text{at } s = 0, \quad (4a)$$

$$\mathbf{F}_{\text{ext}} = -\partial_s(\alpha \partial_s^2 \mathbf{r}) + \sigma \partial_s \mathbf{r}, \quad \mathbf{T}_{\text{ext}} = +\mathbf{t} \times \alpha \partial_s^2 \mathbf{r} \quad \text{at } s = L, \quad (4b)$$

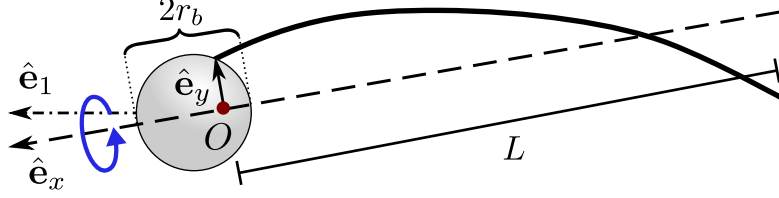
where \mathbf{F}_{ext} and \mathbf{T}_{ext} are externally applied forces and torques on the filament, respectively. We remark, that a drag force from the bead is also called “external” in this nomenclature.

Small-slope approximation

The compound head-tail object is torqued into a steady rotation by the externally applied rotating homogeneous magnetic field. The rotation of the head creates a rotating fluid flow around the head that falls off with $1/r$. This is true for both externally and internally actuated swimmers, though the head of externally actuated swimmers co-rotates with the tail whereas for internally actuated swimmers it counter-rotates. In both cases however, this rotational fluid flow is small over the major part of the bundle, so it will be neglected in what follows.

After the swimmer has reached a stationary shape, the magnetic field rotates the head about the axis in which it propels himself and the attachment point of the bundle follows a circular path on the bead surface. We choose this rotation axis as the $\hat{\mathbf{e}}_x$ direction and the orthogonal vectors $\hat{\mathbf{e}}_y$ and $\hat{\mathbf{e}}_z$ as the local coordinate system that co-rotates with the head (Fig. S1). As long as the rotations about the y and z axes are small, it is straight-forward to find this coordinate system. The origin of this coordinate system is placed at the projection of the attachment point on the rotation axis of the swimmer. Consequently, the origin does not coincide with the center of the head, but is offset by some distance in the range $[0, r_b]$ where r_b is the bead radius.

The actuation of the bundle is about the x -axis in this coordinate system. In the following



Scheme S1: Coordinate system of the swimmer. The local coordinate system of the swimmer is indicated by $\hat{\mathbf{e}}_x$ and $\hat{\mathbf{e}}_y$. The origin of this coordinate system is at the projection of the attachment point on the x -axis, indicated by O (red dot). The swimmer rotates around the $\hat{\mathbf{e}}_x$ axis (blue arrow). The effective swimming direction $\hat{\mathbf{e}}_1$ is slightly off the $\hat{\mathbf{e}}_x$ axis, because the $\hat{\mathbf{e}}_x$ axis precesses with a small opening angle around the $\hat{\mathbf{e}}_1$ axis. The arrows indicate the direction of the coordinate directions.

we assume small actuations of the bundle about the x -axis, such that $s \approx x$ and

$$\mathbf{r} \approx x \hat{\mathbf{e}}_x + y(x, t) \hat{\mathbf{e}}_y + z(x, t) \hat{\mathbf{e}}_z, \quad (5)$$

where $y(s, t)$ and $z(s, t)$ are the small amplitudes along the contour. Equations Eq. 2 and Eq. 3 written in this coordinate frame become with the definitions $\gamma = \xi_{\perp}/\xi_{\parallel}$ and $\mathbf{r}_{\perp}(x, t) = y(x, t) \hat{\mathbf{e}}_y + z(x, t) \hat{\mathbf{e}}_z$,

$$\xi_{\parallel} u_x + (\xi_{\parallel} - \xi_{\perp})(u_y y' + u_z z') = \sigma' \quad (6a)$$

$$u_y (\xi_{\perp} - (\xi_{\parallel} - \xi_{\perp})z'^2) + (\xi_{\parallel} - \xi_{\perp})(u_x + u_z z') y' = -\partial_x^2(\alpha y'') + \partial_x(\sigma y') \quad (6b)$$

$$u_z (\xi_{\perp} + (\xi_{\parallel} - \xi_{\perp})z'^2) + (\xi_{\parallel} - \xi_{\perp})(u_x + u_y y') z' = -\partial_x^2(\alpha z'') + \partial_x(\sigma z') \quad (6c)$$

$$\alpha \cdot \left(\left(\frac{1}{\gamma} - 1 \right) \mathbf{r}_{\perp}'' \mathbf{r}_{\perp}^{(4)} - \mathbf{r}_{\perp}' \mathbf{r}_{\perp}^{(5)} \right) - \left(\frac{2}{3\gamma} + \frac{7}{3} \right) \mathbf{r}_{\perp}' \mathbf{r}_{\perp}^{(4)} \alpha' - \left(\frac{1}{\gamma} + 2 \right) \mathbf{r}_{\perp}' \mathbf{r}_{\perp}^{(3)} \alpha'' + \frac{1}{\gamma} \mathbf{r}_{\perp}' \mathbf{r}_{\perp}^{(3)} \sigma + \sigma'' = 0. \quad (6d)$$

Here and in the following a prime denotes a derivative with respect to x . Note the appearance of terms with α' and α'' in the equation for σ .

This set of equations is greatly simplified by an order of magnitude analysis. If \mathbf{r}_{\perp} is of order ε , σ must be of order ε^2 by Eq. 6d. Likewise by (6a-6c) u_x is of order ε^2 and u_{\perp} of

order ε . Keeping only terms of leading order, Eq. 6 simplify to

$$\xi_{\parallel} u_x + (\xi_{\parallel} - \xi_{\perp})(u_y y' + u_z z') = \sigma' \quad (7a)$$

$$\xi_{\perp} u_y + \partial_x^2(\alpha y'') = 0 \quad (7b)$$

$$\xi_{\perp} u_z + \partial_x^2(\alpha z'') = 0. \quad (7c)$$

The corresponding small-amplitude approximation of the boundary conditions Eq. 4 for a bundle of length L are

$$\mathbf{F}_{\text{ext}} = \partial_x(\alpha \partial_x^2 \mathbf{r}_{\perp}) - \sigma \hat{\mathbf{e}}_x, \quad T_{\text{ext},y} = -\alpha \partial_x^2 z \quad T_{\text{ext},z} = \alpha \partial_x^2 y \quad \text{at } s = 0 \quad (8a)$$

$$\mathbf{F}_{\text{ext}} = -\partial_x(\alpha \partial_x^2 \mathbf{r}_{\perp}) + \sigma \hat{\mathbf{e}}_x, \quad T_{\text{ext},y} = \alpha \partial_x^2 z \quad T_{\text{ext},z} = -\alpha \partial_x^2 y \quad \text{at } s = L. \quad (8b)$$

Natural units

It is convenient to use intrinsic units such that all pre-factors are numbers. The externally applied magnetic field revolves in the yz -plane with an angular speed ω and periodically actuates the swimmer, hence time is best measured in multiples of ω^{-1} . Only a single tube can extend towards the far end of the bundle, therefore $\alpha(L)$ must be the stiffness of a single tube. It is a natural unit to stiffness in units of the stiffness of a single tube, so that $A(x) \equiv \alpha(x)/\alpha(L)$ becomes the number of tubes making up the bundle at position x . For elasto-hydrodynamic equations the intrinsic bending length $\ell_{\omega} = (\alpha(L)/\omega \xi_{\perp})^{1/4}$ is a natural unit for the length.⁸ Forces and torques are measured by $\xi_{\perp} \ell_{\omega}$ and $\xi_{\perp} \ell_{\omega}^3$, respectively. In the following we will only refer to the dimensionless quantities but use the same symbols as before.

Free swimmer with head

In the preceding sections we developed the equations of motion of the tail in the small amplitude approximation. The next step is to employ this equation of motion when the tail

is attached to a freely movable bead. The motion of the bead shall be given by the velocity $\mathbf{U}(t)$ and rotation speed $\boldsymbol{\Omega}(t)$. Given the current speed of the bead, the total speed with respect to the fluid \mathbf{u} of any point on the bundle is then a superposition of the velocity and rotation of the bead coordinate system and the local bundle velocity in the reference frame of the bead:

$$u_x = U_x + z\Omega_y - y\Omega_z \quad u_y = U_y + x\Omega_z - z\Omega_x + \dot{y} \quad u_z = U_z + y\Omega_x - x\Omega_y + \dot{z} \quad (9)$$

Because the local coordinate system co-rotates with the head, the tail shape becomes static in these coordinates and $\dot{y} = \dot{z} = 0$. In the low-Reynolds number regime drag through motion and rotation must balance with external force and torque,

$$\tilde{\mathbf{F}}_{\text{ext}} = - \begin{pmatrix} \mathcal{R}_{\parallel}^{FU} & 0 & 0 \\ 0 & \mathcal{R}_{\perp}^{FU} & 0 \\ 0 & 0 & \mathcal{R}_{\perp}^{FU} \end{pmatrix} \tilde{\mathbf{U}} \quad \tilde{\mathbf{T}}_{\text{ext}} = - \begin{pmatrix} \mathcal{R}_{\parallel}^{L\Omega} & 0 & 0 \\ 0 & \mathcal{R}_{\perp}^{L\Omega} & 0 \\ 0 & 0 & \mathcal{R}_{\perp}^{L\Omega} \end{pmatrix} \tilde{\boldsymbol{\Omega}},$$

when taken with respect to the center of mass of the bead. When expressed in the shifted local coordinate system these equations become

$$\mathbf{F}_{\text{ext}} = - \begin{pmatrix} \mathcal{R}_{\parallel}^{FU} & 0 & 0 \\ 0 & \mathcal{R}_{\perp}^{FU} & 0 \\ 0 & 0 & \mathcal{R}_{\perp}^{FU} \end{pmatrix} \cdot \mathbf{U} + \begin{pmatrix} 0 & 0 & 0 \\ 0 & 0 & a\mathcal{R}_{\perp}^{FU} \\ 0 & -a\mathcal{R}_{\perp}^{FU} & 0 \end{pmatrix} \cdot \boldsymbol{\Omega} \quad (10a)$$

$$\mathbf{T}_{\text{ext}} = \begin{pmatrix} 0 & 0 & 0 \\ 0 & 0 & -a\mathcal{R}_{\perp}^{FU} \\ 0 & a\mathcal{R}_{\perp}^{FU} & 0 \end{pmatrix} \cdot \mathbf{U} - \begin{pmatrix} \mathcal{R}_{\parallel}^{L\Omega} & 0 & 0 \\ 0 & \mathcal{R}_{\perp}^{L\Omega} + a^2\mathcal{R}_{\perp}^{FU} & 0 \\ 0 & 0 & \mathcal{R}_{\perp}^{L\Omega} + a^2\mathcal{R}_{\perp}^{FU} \end{pmatrix} \cdot \boldsymbol{\Omega}, \quad (10b)$$

where a is the offset of the origin from the center of the head (see Fig. S1). Because the external magnetic field is strong enough to ensure a phase-locked rotation of the head, we take $\Omega_x = -1$ as given. However, for the remaining components, the forces need to balance

out. Therefore with Eq. 8 we find for the attached end of the tail

$$\mathcal{R}_{\parallel}^{FU} U_x = \sigma(0) \quad (11a)$$

$$\mathcal{R}_{\perp}^{FU} U_y - a\mathcal{R}_{\perp}^{FU} \Omega_z = -\partial_x(A(x)y''(x,t))|_{x=0} \quad (11b)$$

$$\mathcal{R}_{\perp}^{FU} U_z + a\mathcal{R}_{\perp}^{FU} \Omega_y = -\partial_x(A(x)z''(x,t))|_{x=0} \quad (11c)$$

$$a\mathcal{R}_{\perp}^{FU} U_z + (\mathcal{R}_{\perp}^{L\Omega} + a^2\mathcal{R}_{\perp}^{FU})\Omega_y = -A(0)z''(0) \quad (11d)$$

$$-a\mathcal{R}_{\perp}^{FU} U_y + (\mathcal{R}_{\perp}^{L\Omega} + a^2\mathcal{R}_{\perp}^{FU})\Omega_z = A(0)y''(0) \quad (11e)$$

and for the free end at $x = L$ where no external force applies

$$y''(L) = z''(L) = y^{(3)}(L) = z^{(3)}(L) = \sigma(L) = 0. \quad (12)$$

With the driving of the bundle

$$y(0) = \Re[\varepsilon_1] \quad y'(0) = \Re[\varepsilon_2] \quad (13a)$$

$$z(0) = \Im[\varepsilon_1] \quad z'(0) = \Im[\varepsilon_2] \quad (13b)$$

there are eight boundary conditions (13, 12) for the two fourth order equations for y and z and two boundary conditions 11a, 12 for the second order equation for σ . For each of the unknowns $y, z, \sigma, U_x, U_y, U_z, \Omega_y, \Omega_z$ there is a determining function 6, 11b-11e. As long as the rotation about the y and z axes remains small, we can safely assume that the swimmer revolves mainly about the x -axis with an angular speed ω . We will argue below that this condition is well met in our experiment.

Rewriting Eq. 7b, 7c in natural units and using Eq. 9 yields

$$U_y + x\Omega_z + z + \partial_x^2(Ay'') = 0 \quad (14a)$$

$$U_z - x\Omega_y - y + \partial_x^2(Az'') = 0 \quad (14b)$$

where we have used $\Omega_x = -1$. With the definitions $\zeta = y + \imath z$, $U = U_y + \imath U_z$ and $\Omega = \Omega_y + \imath \Omega_z$ these two equations can be combined into one complex equation

$$U + \imath x \Omega - \imath \zeta + \partial_x^2 (A \zeta'') = 0 \quad (15)$$

with boundary conditions corresponding to (12, 13)

$$\zeta(0) = \varepsilon_1 \quad \zeta'(0) = \varepsilon_2 \quad \zeta''(L) = 0 \quad \zeta^{(3)}(L) = 0 . \quad (16)$$

Inversion of the equation system 11b and 11e determines U and Ω in terms of x and y :

$$U_y = -\frac{\mathcal{R}_\perp^{L\Omega} + a^2 \mathcal{R}_\perp^{FU}}{\mathcal{R}_\perp^{L\Omega} \mathcal{R}_\perp^{FU}} \partial_x (A(x) y''(x, t)) \Big|_{x=0} + \frac{aA(0)}{\mathcal{R}_\perp^{L\Omega}} y''(0) \quad (17a)$$

$$U_z = -\frac{\mathcal{R}_\perp^{L\Omega} + a^2 \mathcal{R}_\perp^{FU}}{\mathcal{R}_\perp^{L\Omega} \mathcal{R}_\perp^{FU}} \partial_x (A(x) z''(x, t)) \Big|_{x=0} + \frac{aA(0)}{\mathcal{R}_\perp^{L\Omega}} z''(0) \quad (17b)$$

$$\Omega_y = \frac{a}{\mathcal{R}_\perp^{L\Omega}} \partial_x (A(x) z''(x, t)) \Big|_{x=0} - \frac{A(0)}{\mathcal{R}_\perp^{L\Omega}} z''(0) \quad (17c)$$

$$\Omega_z = \frac{-a}{\mathcal{R}_\perp^{L\Omega}} \partial_x (A(x) y''(x, t)) \Big|_{x=0} + \frac{A(0)}{\mathcal{R}_\perp^{L\Omega}} y''(0) \quad (17d)$$

With the abbreviations

$$\begin{aligned} \beta &= A(0) \frac{\mathcal{R}_\perp^{L\Omega} + a^2 \mathcal{R}_\perp^{FU}}{\mathcal{R}_\perp^{L\Omega} \mathcal{R}_\perp^{FU}} & \sigma &= A(0) \frac{a}{\mathcal{R}_\perp^{L\Omega}} \\ \lambda &= -A(0) \frac{a}{\mathcal{R}_\perp^{L\Omega}} + A'(0) \frac{\mathcal{R}_\perp^{L\Omega} + a^2 \mathcal{R}_\perp^{FU}}{\mathcal{R}_\perp^{L\Omega} \mathcal{R}_\perp^{FU}} & \mu &= -A(0) \frac{1}{\mathcal{R}_\perp^{L\Omega}} + A'(0) \frac{a}{\mathcal{R}_\perp^{L\Omega}} \end{aligned}$$

these relations can be written in a more compact form

$$U = -(\beta \zeta^{(3)}(0) + \lambda \zeta''(0)) \quad \Omega = -\imath (\sigma \zeta^{(3)}(0) + \mu \zeta''(0)) . \quad (18)$$

Using this result in Eq. 15 yields the final form

$$-i\zeta + \partial_x^2(A\zeta'') = (\beta + \sigma x)\zeta^{(3)}(0) + (\lambda + \mu x)\zeta''(0). \quad (19)$$

The major challenge is to find a solution ζ for variable $A(x)$. Lauga has presented an analytic solution for constant A . For a variable $A(x)$ however, we could only find numerical solutions to this equation.

Determining the swimming speed

From the bundle shape the swimming speed will be determined in the following. For this Eqs. 7b, 7c are substituted into Eq. 7a which reads in natural units

$$u_x - (1 - \gamma)(y'\partial_x^2(Ay'') + z'\partial_x^2(Az'')) = \gamma\sigma'. \quad (20)$$

Here $\gamma = \xi_\perp/\xi_\parallel$ is the ratio of the drag coefficient perpendicular and parallel to the bundle. Using Eq. 11a and Eq. 9, integration along the contour of the bundle yields

$$\begin{aligned} (\gamma\mathcal{R}_\parallel^{FU} + L)U_x = \Omega_z \int_0^L y \, dx - \Omega_y \int_0^L z \, dx + (1 - \gamma) \\ \left(A(0)|\mathbf{r}'_\perp(0)|^2 - \mathbf{r}'_\perp(0) \cdot \left(A(0)\mathbf{r}'_\perp(0) + A'(0)\mathbf{r}'_\perp(0) \right) + \int_0^L A(x) \mathbf{r}''_\perp(x) \cdot \mathbf{r}'_\perp(x) dx \right). \end{aligned} \quad (21)$$

Note that with our choice of coordinates, this relation is time-independent. It is straightforward to express this equation in terms of the complex quantities

$$\begin{aligned} (\gamma\mathcal{R}_\parallel^{FU} + L)U_x = \Im \left[\Omega^* \int_0^L \zeta \, dx \right] + (1 - \gamma) \\ \Re \left[A(0)|\zeta''(0)|^2 - \zeta'(0)^* \left(A(0)\zeta^{(3)}(0) + A'(0)\zeta''(0) \right) + \int_0^L A(x) \zeta''(x)\zeta^{(3)}(x)^* dx \right]. \end{aligned} \quad (22)$$

Integration along the bundle of Eq. 15 with the boundary conditions (11b, 11c) yields the relation

$$\int_0^L \zeta \, dx = \iota(\mathcal{R}_\perp^{FU} + L)U + \left(a\mathcal{R}_\perp^{FU} - \frac{L^2}{2}\right)\Omega, \quad (23)$$

therefore $\Im[\Omega^* \int_0^L \zeta \, dx] = (\mathcal{R}_\perp^{FU} + L) \Re[\Omega^* U]$. With the expressions for Ω and U from Eq. 18 one finds

$$\Re[\Omega^* U] = \frac{A(0)^2}{\mathcal{R}_\perp^{FU} \mathcal{R}_\perp^{L\Omega}} \Im[\zeta''(0)\zeta^{(3)}(0)^*]. \quad (24)$$

Collecting the previous results, the final expression for the swimming speed in the local frame of reference becomes

$$\begin{aligned} (\gamma\mathcal{R}_\parallel^{FU} + L)U_x = & A(0)^2 \frac{\mathcal{R}_\perp^{FU} + L}{\mathcal{R}_\perp^{FU} \mathcal{R}_\perp^{L\Omega}} \Im[\zeta''(0)\zeta^{(3)}(0)^*] + \\ & (1 - \gamma) \Re \left[A(0)|\zeta''(0)|^2 - \zeta'(0)^* \left(A(0)\zeta^{(3)}(0) + A'(0)\zeta''(0) \right) + \int_0^L A(x) \zeta''(x)\zeta^{(3)}(x)^* dx \right]. \end{aligned} \quad (25)$$

Transformation into the lab system

The swimming speed in Eq. 25 refers to a local coordinate system that co-rotates with the swimmer's head. Therefore, it must be transformed into the laboratory system. We define the lab frame along the orthogonal vectors $\hat{\mathbf{e}}_1, \hat{\mathbf{e}}_2, \hat{\mathbf{e}}_3$, where $\hat{\mathbf{e}}_1$ points along the average swimming direction. The swimmer revolves at constant angular velocity $\{\Omega_x = -1, \Omega_y, \Omega_z\}$ about its local axes. Hence, in the lab system the local coordinate vectors change according to

$$\frac{d}{dt} \mathbf{e}_{xyz} = \begin{pmatrix} 0 & -\Omega_z & \Omega_y \\ \Omega_z & 0 & -1 \\ -\Omega_y & 1 & 0 \end{pmatrix} \cdot \mathbf{e}_{xyz}. \quad (26)$$

The analytical solution of this rotation is given through the matrix exponential $\Re[\exp(Mt)] \cdot \mathbf{e}_{xyz}$ where M is the above rotation matrix. Dropping all terms of second order in Ω one

finds

$$\hat{\mathbf{e}}_x = \hat{\mathbf{e}}_1 - \Re[\Omega(1 - e^{it})] \hat{\mathbf{e}}_2 - \Im[\Omega(1 - e^{it})] \hat{\mathbf{e}}_3 \quad (27a)$$

$$\hat{\mathbf{e}}_y = -\Re[\Omega(1 - e^{-it})] \hat{\mathbf{e}}_1 + \cos t \hat{\mathbf{e}}_2 + \sin t \hat{\mathbf{e}}_3 \quad (27b)$$

$$\hat{\mathbf{e}}_z = -\Im[\Omega(1 - e^{-it})] \hat{\mathbf{e}}_1 - \sin t \hat{\mathbf{e}}_2 + \cos t \hat{\mathbf{e}}_3 \quad (27c)$$

which is exact up to order $|\Omega|^2$. The total swimming velocity of the head is given by $\mathbf{U} = U_x \hat{\mathbf{e}}_x + U_y \hat{\mathbf{e}}_y + U_z \hat{\mathbf{e}}_z$ of which we are only interested in the $\hat{\mathbf{e}}_1$ component. Hence,

$$U_1 = U_x - \Re[\Omega(1 - e^{-it})]U_y - \Im[\Omega(1 - e^{-it})]U_z . \quad (28)$$

In contrast to the velocity in co-rotating coordinates, this expression depends on time due to the oscillating motion of the bead. However, the time-dependent terms average out over one period, such that

$$\langle U_1 \rangle = U_x - \Re[\Omega^* U] . \quad (29)$$

With the previous results from (24,25) this yields the swimming speed in the lab system

$$\begin{aligned} \langle U_1 \rangle = \frac{1}{\gamma \mathcal{R}_{\parallel}^{FU} + L} & \left(A(0)^2 \frac{\mathcal{R}_{\perp}^{FU} - \gamma \mathcal{R}_{\parallel}^{FU}}{\mathcal{R}_{\perp}^{FU} \mathcal{R}_{\perp}^{L\Omega}} \Im[\zeta''(0)\zeta^{(3)}(0)^*] + \right. \\ & \left. (1 - \gamma) \Re \left[A(0)|\zeta''(0)|^2 - \zeta'(0)^* \left(A(0)\zeta^{(3)}(0) + A'(0)\zeta''(0) \right) + \int_0^L A(x) \zeta''(x)\zeta^{(3)}(x)^* dx \right] \right) . \end{aligned} \quad (30)$$

Because the experimentally implemented swimmer has a spherical head for which $\mathcal{R}_{\perp}^{FU} = \mathcal{R}_{\parallel}^{FU}$ and $\mathcal{R}_{\perp}^{L\Omega} = \mathcal{R}_{\parallel}^{L\Omega}$, this expression simplifies further to

$$\begin{aligned} \langle U_1 \rangle = \frac{1 - \gamma}{\gamma \mathcal{R}^{FU} + L} & \left(\frac{A(0)^2}{\mathcal{R}^{L\Omega}} \Im[\zeta''(0)\zeta^{(3)}(0)^*] + \right. \\ & \left. \Re \left[A(0)|\zeta''(0)|^2 - \zeta'(0)^* \left(A(0)\zeta^{(3)}(0) + A'(0)\zeta''(0) \right) + \int_0^L A(x) \zeta''(x)\zeta^{(3)}(x)^* dx \right] \right) . \end{aligned} \quad (31)$$

For $A = \text{const}$ this result is consistent with the one from the work of Lauga. The conversion of this result into physical coordinates is accomplished by multiplying the result with $\ell_\omega \cdot 2\pi f$ where f is the rotation frequency of the external magnetic field. The extra factor of 2π is necessary because the natural unit of time is given by *angular* frequency ω^{-1} and not frequency f^{-1} .

The applicability of this result depends on the solvability of Eq. 19. When fixed to a solid wall where the RHS of Eq. 19 becomes zero, an analytic solution for ζ can be found. For a free swimmer however, the inhomogeneous equation has to be solved which we could only achieve numerically. We did this with Mathematica where in a first step the equation was solved numerically with $\zeta''(0)$ and $\zeta^{(3)}(0)$ on the RHS as parameters. In a second step we matched these intermediate parameters to the actual derivative of the numerical solution through a root-finding algorithm. The integrated residual of the so-obtained solution was of the order 10^{-6} per unit length and therefore negligibly small.

Stiffness model and parameter estimation

Our model depends on several parameters which we group in global and individual ones. The global parameters are well controlled and need no discussion. These are the fluid viscosity ($\eta \approx 1 \text{ mPa s}$ at 20°C), the persistence length of one fibre ($8.2 \mu\text{m}$,²), the frequency at which the magnetic field was rotated ($f = 1\text{--}3 \text{ Hz}$) and the head diameter ($1 \mu\text{m}$). We note that the head appears visually enlarged on the video material by its high brightness, but this is misleading. Electron-microscopy of the same batch of beads revealed that their diameter was well within specification.

The individual parameters varied for different swimmers, so they had to be determined for each swimmer instance. These are the bundle length, the number of tubes in the bundle, the amplitude parameters ε_1 and ε_2 and their respective phase. The bundle length could be determined from snapshots of the swimmer by integrating the contour length of the bundle. Typical values of the bundle length range from $4.8\text{--}8.0 \mu\text{m}$ (Tab. S2), which is consistent

with TEM measurements.

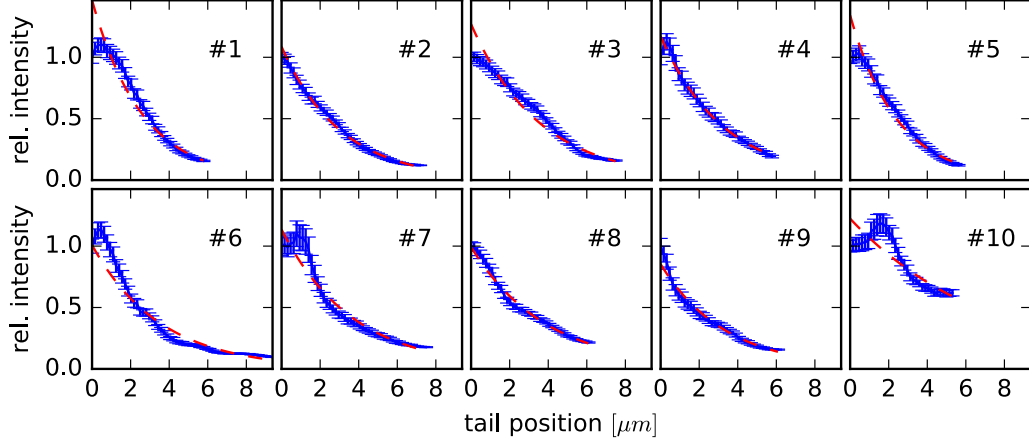


Figure S10: Fluorescence intensity of DNA tile-tube bundles. The data show the fluorescence intensity profiles of the bundles of ten different swimmers from Figure 4 (blue, with standard error). Data was gained by averaging over several movie frames to rule out possible errors due to a change in the fluorescence distribution along the particle during a rotation. These data were fit with an exponential (dashed red) in order to determine the decay length χ of the attached tails (for numerical values see Table S2).

Beside length, a stiffness model $A(x)$ has to be chosen. Because each tube of the tail results from a linear polymerization process, we expect an exponential distribution of tube lengths.⁹ Yin¹ found an exponential length distribution in the length of unbound DNA tubes. To verify this length distribution, we measured the fluorescence intensity along the contour of the bundle which we expect to be proportional to the number of tubes. Figure 3a shows the expected exponential drop in fluorescence intensity, therefore we assumed that the number of tubes in the bundle scales as $N_0 e^{-s/\chi}$. Without cross-links the stiffness scales linearly with the number of tubes in the tail,¹⁰⁻¹² therefore we take $A(x) = N_0 e^{-x/\chi}$ as the stiffness model. The parameters N_0 and χ could be estimated by an exponential fit of the fluorescence intensity, if we assume that one single tube extends to the far end (see Fig. fig:decay-lengths). Typical numbers of attached tubes N_0 range from 7 to 25, which is consistent with TEM pictures of the hybrids. We note, that the increased swimming speed is a generic feature of decreasing tail stiffness and is also found for other stiffness decay

functions. In particular, our model also applies if the stiffness scales differently with the number of filaments, e.g. $\alpha(x) \propto n^a$, because this only amounts to a change of the decay length $\alpha(x) \propto e^{x/(\chi/a)}$. Additional cross-links among the filaments increase a ,^{10–12} so that the effects from a thinning bundle become even stronger.

The amplitude parameters ε_1 and ε_2 have a major impact on the swimming speed. This can be seen in the formula for the swimming speed Eq. 30, where ζ enters quadratically in each term. Because the tail amplitude ζ depends as a rule of thumb linearly on both ε_1 and ε_2 , the swimming speed reacts quadratically on their values. Consequently, these parameters must be determined carefully, which is challenging due to the small size of the swimmers. For that, we took snapshots of the video sequence where the tail was maximally deflected. This allowed to measure the amplitude of the attachment point, ε_1 , in fractions of the bead radius and we found values ranging from 0.1–1.0. Likewise, the opening angle θ between tail and swimming direction was measured for which we found values ranging from 20–40 degrees. This opening angle θ determines ε_2 via $\varepsilon_2 = \tan \theta$. The relative phase of ε_1 and ε_2 corresponds to the torsion of the tail close to the head. Without loss of generality we take ε_2 as real. From our data it was not possible to reliably determine the phase difference, therefore it had to be estimated. Because the tail is pulled through the fluid, it feels a drag directed against its current direction of movement and bends accordingly. This induced bending corresponds to a phase shift of $-\pi/2$ which we take as an estimate for the phase shift. We note that the phase shift has only a minor impact on the swimming speed of about 5%.

Finally the friction coefficients of tail and bead need to be estimated. For the tail, the friction coefficient can be calculated via slender-body theory,^{6,7} where we assumed an aspect ratio of 200 for the tail bundle resulting in $\gamma \approx 1.6$. The Stokes friction coefficients of a solid sphere are given by

$$\mathcal{R}_{\perp}^{FU} = \mathcal{R}_{\parallel}^{FU} = 6\pi\eta r_b \qquad \mathcal{R}_{\perp}^{L\Omega} = \mathcal{R}_{\parallel}^{L\Omega} = 8\pi\eta r_b^3, \qquad (32)$$

where η is the fluid viscosity and r_b the head radius. In the experiment, translational motion is free, so that \mathcal{R}^{FU} is a reasonable value for the translational friction. On the other hand, the bead rotation is *not* free, because the external magnetic field aligns the magnetic moment of the bead with its direction. As a consequence, a torque on the bead works against the magnetic field and therefore has a much smaller effect. To emulate this suppressed rotation, we scaled the rotational friction coefficient by a large factor (500). Because the resulting values of the swimming speed differ by only 20% in the range $[200, \infty]$, the error inflicted by this arbitrariness is small.

Table S2: Model parameters and swimming speeds for the swimmers from Figure 4

swimmer	#1	#2	#3	#4	#5	#6	#7	#8	#9	#10
length [μm]	6.2	7.8	6.8	6.5	6.3	8.0	6.5	6.0	4.8	7.0
χ [μm]	2.60	3.08	3.54	3.28	2.43	3.55	3.67	3.88	3.36	7.27
frequency [Hz]	1	1	1	2	1	1	1	2	2	1
$\varepsilon_1/e^{-i\pi/2}$ [r_b]	0.9	1.	0.9	0.25	0.5	0.1	0.9	0.5	0.9	0.8
$\arctan(\varepsilon_2)$ [deg]	21	20	20	26	26	30	28	23	30	42
measured speed [$\mu m/s$]	0.12	0.12	0.17	0.19	0.20	0.22	0.25	0.27	0.31	0.42
predicted speed [$\mu m/s$]	0.16	0.14	0.12	0.18	0.20	0.15	0.19	0.16	0.36	0.29

Table S2 shows the model parameters and predicted swimming speeds for ten swimmers from the experiment corresponding to Figure 4. Typically, we measured swimming speeds around $0.2 \mu m/s$, and our predicted swimming speeds were off by less than 40%. This agreement is completely satisfactory, considering that some parameters could only be estimated and that this calculation was done in the approximation of small amplitudes.

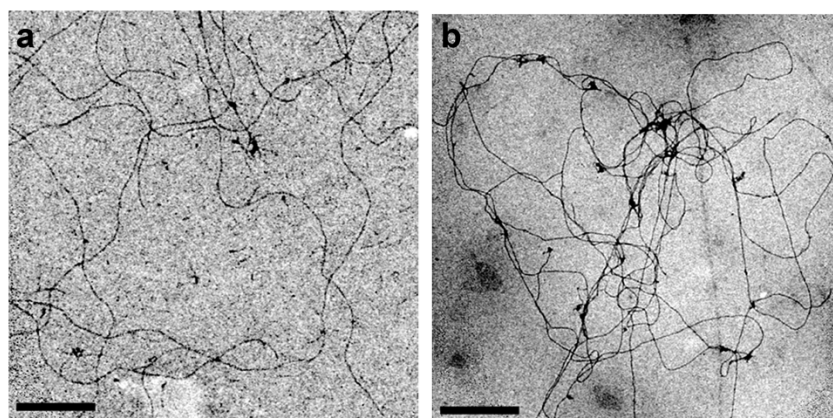
A great advantage of the theoretical model is that different stiffness profiles can be easily compared. In particular, the swimming speed of constant stiffness versus variable stiffness can be compared as shown in Figure 3c. It is remarkable, that the swimming speed for variable stiffness outperforms a bundle of equal length tubes for all parameters shown. This behaviour is valid over the entire parameter range we looked at and is no coincidence of a particular parameter choice but a general feature of thinning bundles of passive flagella.

References

- (1) Yin, P.; Hariadi, R. F.; Sahu, S.; Choi, H. M.; Park, S. H.; Labean, T. H.; Reif, J. H. *Science* **2008**, *321*, 824–826.
- (2) Schiffels, D.; Liedl, T.; Fyngenson, D. K. *ACS Nano* **2013**, *7*, 6700–6710.
- (3) Dietz, H.; Douglas, S. M.; Shih, W. M. *Science* **2009**, *325*, 725–730.
- (4) Castro, C. E.; Kilchherr, F.; Kim, D. N.; Shiao, E. L.; Wauer, T.; Wortmann, P.; Bathe, M.; Dietz, H. *Nat. Methods* **2011**, *8*, 221–229.
- (5) Lauga, E. *Phys. Rev. E* **2007**, *75*, 041916.
- (6) Keller, J. B.; Rubinow, S. I. *Journal of Fluid Mechanics* **1976**, *75*, 705–714.
- (7) Batchelor, G. K. *Journal of Fluid Mechanics* **1970**, *44*, 419–440.
- (8) Wiggins, C. H.; Rivelino, D.; Ott, A.; Goldstein, R. E. *Biophys. J.* **1998**, *74*, 1043–1060.
- (9) Flory, P. J. *J. Am. Chem. Soc.* **1936**, *58*, 1877–1885.
- (10) Claessens, M. M. A. E.; Bathe, M.; Frey, E.; Bausch, A. R. *Nature Materials* **2006**, *5*, 748–753.
- (11) Heussinger, C.; Bathe, M.; Frey, E. *Physical Review Letters* **2007**, *99*, 048101.
- (12) Bathe, M.; Heussinger, C.; Claessens, M. M. A. E.; Bausch, A. R.; Frey, E. *Biophys. J.* **2008**, *94*, 2955–2964.

This material is available free of charge via the Internet at <http://pubs.acs.org/>.

Appendix C: Materials and Methods for Chapter 2



C

U1-Cy3	/5Cy3/TTG GCG ATT AGG ACG CTA AGC CAC CTT TAG ATC CTG TAT CTG GT
X2	A TCT AAA GGA CCA GAT ACAGG CCA CTC TTC CTG ACA TCT TGT
X3	A AGA GTG GAC AAG ATG TCAGG CCG TGA GAA CCT GCA ATG CGT
X4	T TCT CAC GGA CGC ATT GCAGG CCG CAC GAC CTG TTC GAC AGT
X5	T CGT GCG GAC TGT CGA ACAGG CCA ACG ATG CCT GAT AGA AGT
X6	C ATC GTT GGA CTT CTA TCAGG ATG CAC CTC CAG CTT TGA ATG
XT6	C ATC GTT GGA CTT CTA TCAGG T AAT CGC CTG GCT TAG CGTCC
XT7	A GGT GCA TCA TTC AAA GCTGG T AAT CGC CTG GCT TAG CGTCC

Figure C1: Transmission electron microscopy images of (a) 6-helix and (b) 7-helix tile tubes constructed with negative angles between neighbouring helices in the tube design (see schematic in figure 2.9e of chapter 2). (c) Tile sequences used for the formation of the negative angle 6-helix (U1-Cy3, X2, X3, X4, X5 and XT6) and 7-helix (U1-Cy3, X2, X3, X4, X5, X6 and XT7) tile tube. Scale bars: 500 nm

Appendix D: Materials and Methods for Chapter 4

Design and construction of DNA origami - magnetic bead hybrids

Design of DNA origami structures. All three DNA origami structures from Figure 1 (6HB, 14HC and 3LS) were designed using caDNAno [67] software. DNA staples were ordered from MWG (Eurofins, Germany). The scaffolds are based on the M13mp18 plasmid and were produced in the lab. The original DNA origami designs were modified to allow coupling to magnetic particles and multimerization of the single structures via hybridization of complementary DNA strands. Therefore, we changed the staples of the left and right outer end of each structure with a new set of "sticky end" staples, respectively (design details and DNA sequences are given in Figure S1-S3 and Table S1). Best results for the multimerization process were found at 35 °C in a 1xTBE buffer with 12 mM MgCl₂ /500 mM NaCl and a 10 time excess of sticky end staples over DNA origami structures (30 nM). Saturation in the growth of the multimers occurred after ~ 5 hrs.

Folding and purification of DNA origami structures. Assembly of the DNA origami structures was carried out in 1xTE buffer and 14 mM (for 6-helix bundle), or 16 mM MgCl₂ (for 14-helix corkscrew and 3-layer sheet). A 10-fold excess of staple strands (100 nM) was mixed with scaffold p7560 (for 6-helix bundle), p8064 (for 3-layer sheet), or p8364 (for 14-helix corkscrew) (10 nM), respectively. The folding mixture was then exposed to a thermal annealing ramp, starting with a heating step to 65 °C for 15 min, followed by a stepwise cooling to 59 °C at a cooling rate of 1 °C/5 min, to 36 °C at a cooling rate of 1 °C/30 min, and to 25 °C at a cooling rate of 1 °C/5 min. The folded DNA origami structures were purified from excess staples by 0.7 % agarose gel electrophoresis in a buffer of 0.5x TBE and 11mM MgCl₂. After approximately 2 hours at 70V and ethidium bromide staining, the favoured bands containing the origami structures were cut out under UV-light and extracted via Freeze `N Squeeze spin columns (BioRad, Germany).

Magnetic nanoparticle - DNA conjugation. 1 µm streptavidin-coated magnetic particles (Sigma Aldrich, Germany) and 30 nm SPP nanoparticles (Ocean Nanotech, USA) were functionalized with biotin-modified 15T-DNA strands (MWG Eurofins, Germany). The 30 nm SPP particles with carboxyl surface (COOH) were first covered with neutravidin (Thermo Fischer Scientific, USA) by standard EDC/NHS crosslinking (ICK conjugation kit from ocean nanotech). The neutravidin-coated SPP particles as well as the 1 µm streptavidin-coated particles were then conjugated to single-stranded biotin-modified DNA by mixing a high excess of DNA (10 µM) with the 30 nm (30 nM) and 1 µm (3 pM) particles in a 0.5x TBE buffer, separately. After incubation for 30min at room temperature, biotin-DNA-modified particles were purified from the excess of neutravidin and biotin-DNA by centrifugation of the sample for 5 min at 13,000 rpm followed by another three times washing steps at same speed. For each step, the supernatant liquid was carefully removed, while keeping the pallet of the magnetic nanoparticles at the bottom of the centrifugation tube by a strong permanent magnet.

Coupling of DNA origami structures to magnetic beads. For the construction of nanometer-sized DNA origami magnetic bead hybrids from Figure 1d-g, the biotin-DNA modified SPP particles were hybridized to 6HBs and 14HCs. The conjugation step took place at room temperature overnight in a 0.5x TBE buffer with 11 mM MgCl₂ and 0.05 % Tween. Micrometer-sized hybrids from Figure 1h-i were constructed by hybridizing biotin-DNA modified 1 μ m particles to an excess of multimerized 3LSs.

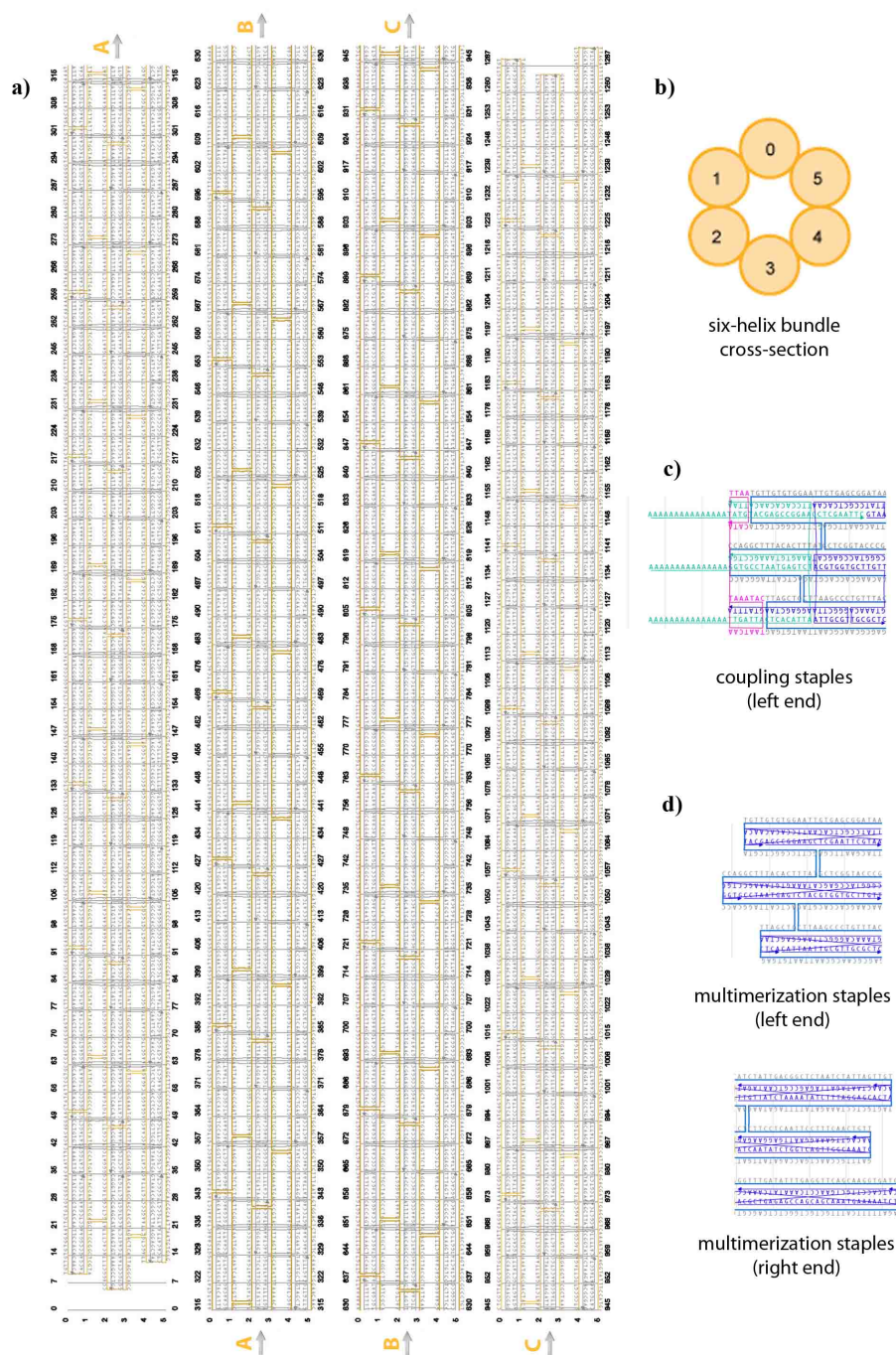


Figure D1: CaDNAno image of the 6-helix bundle. (a) The schematic picture shows the scaffold path (orange) and the staple oligonucleotides (grey) of the unmodified 6HB. (b) Cross-section of the 6HB. Modified versions of the 6HB outer left and right end (c) for coupling to magnetic particles (green) and (d) for multimerization (blue).

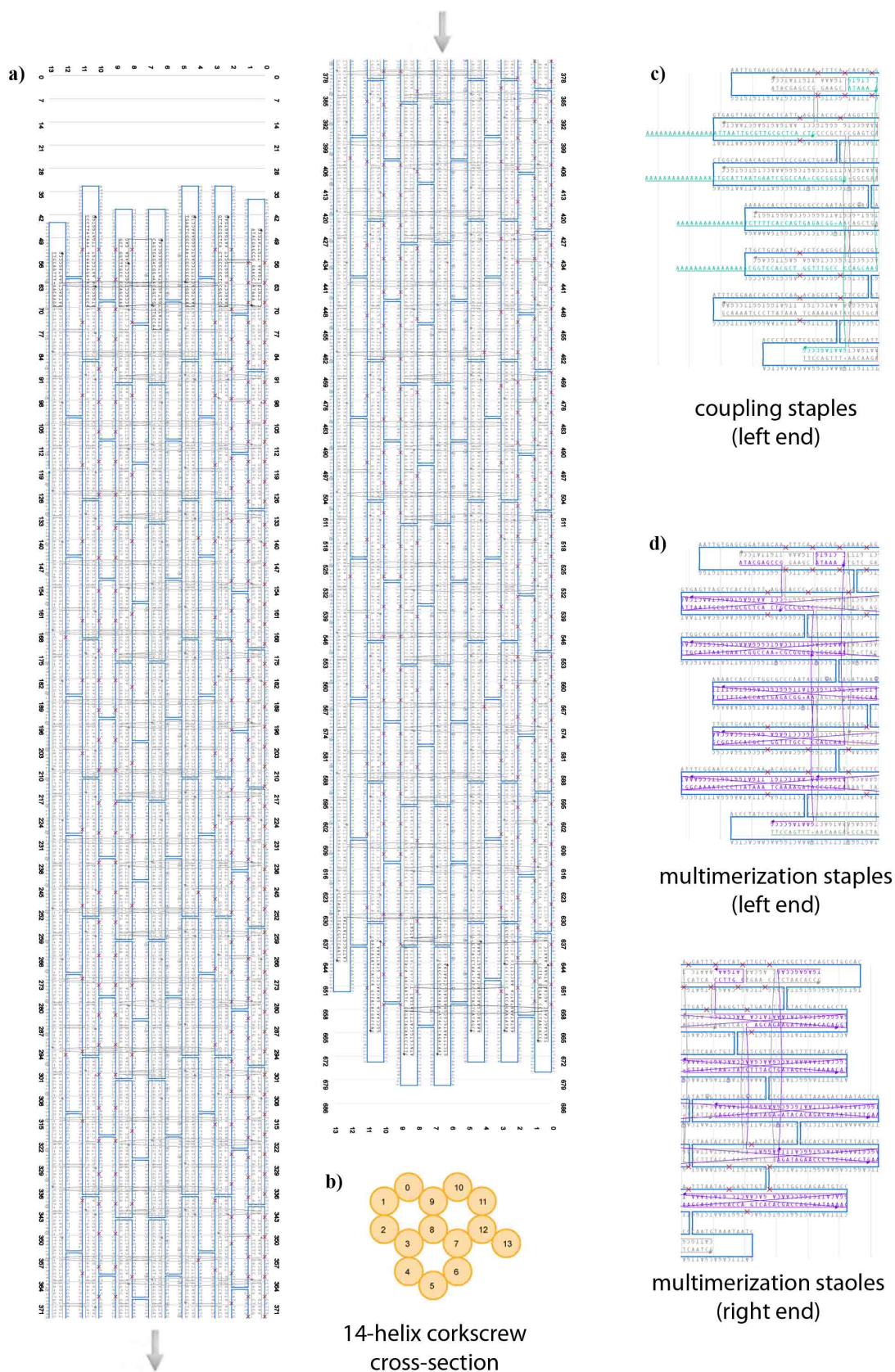


Figure D2: CaDNAo image of the 14-helix corkscrew. (a) The schematic picture shows the scaffold path (blue) and the staple oligonucleotides (grey) of the unmodified 14HC. (b) Cross-section of the 14HC. Modified versions of the 14HC outer left and right end (c) for coupling to magnetic particles (green) (d) and for multimerization (violet).

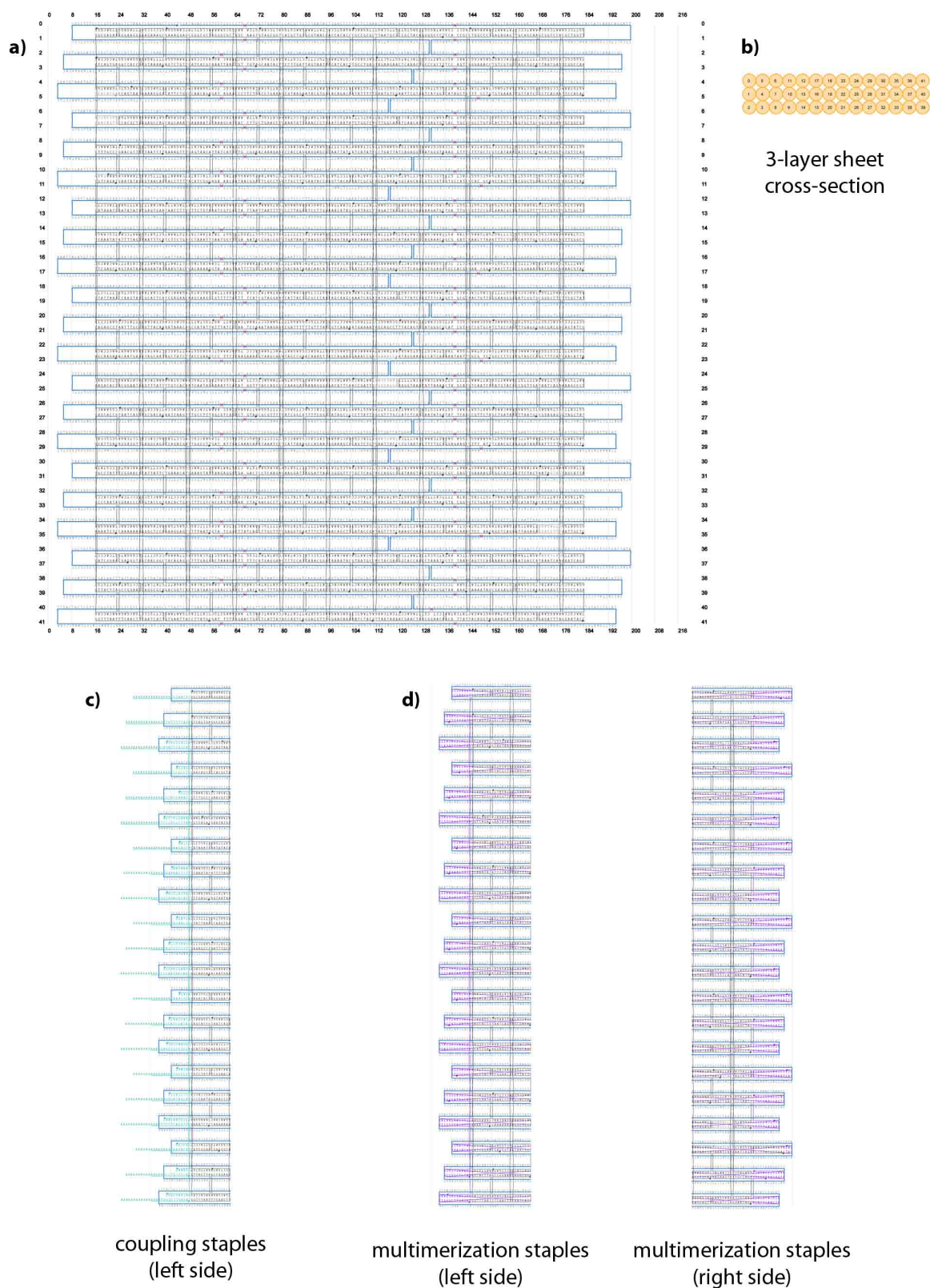


Figure D3: CaDNAno image of the twisted 3LS. (a) The schematic picture shows the scaffold path (blue) and the staple oligonucleotides (grey) of the unmodified 3LS. (b) Cross-section of the 3LS. Modified versions of the 3LS outer left and right end (c) for coupling to magnetic particles (green) and (d) for multimerization (violet).

a)

<p>GTAATTATCCGCTCACAAATTGCGTGGGCTTAAGGAGCTAAGTATTTA AAAAAAAAAAAAAAAAAATTGACTCACATTATCCACACAACATTA AAAAAAAAAAAAAAAAAATGTACGAGCCGGAAGCTCGAATTC AAAAAAAAAAAAAAAAAAGTGCCTAATGAGCTAAAGGTAAAGCCTGG</p> <p>6HB coupling</p>	<p>TTATCCGCTCACAAATCCACACAACAA AGCCGGAAGCTCGAATTCGTAA CGGGTACCGAGCATAAAGTGTAAAGCCTGGAACA CCTAATGAGTCTACGTGGTCTGT GTAAACAGGGCTTAAGGAGCTAAAGCA CATTAAATGCGTTCGCTC</p> <p>6HB left multimerization</p>	<p>CTAATAGATTAGCCGCTCAATAGAT TTGTATCTAAAATCTTTAGGAGCATACTACG GTTGAAGGAATTGAGGAAGAG ATCAATATCTGGTCACTGGCAAATCGGTG TCACCTGTGAACCTCAAATATCAAACC ACGCTGAGAGCCAGCAGCAATGAAAAATCTAACTCA</p> <p>6HB right multimerization</p>
---	--	---

b)

<p>AAAAAAAAAAAAAAAAAATAATTGCGTTGCGCTCACTG AAAAAAAAAAAAAAAAAACTGATTAATGAATCGGCCAACGCGGGGA AAAAAAAAAAAAAAAAAATCTTTCCAGTGTGAGACGGGCAAGAATAGCCCG AAAAAAAAAAAAAAAAAAGCGTCCACGCTGTTGCCAGCAACCCTGTGATAAAG</p> <p>14HC coupling</p>	<p>TGAGAGCCAGAGATAGAACCCTCTGACCTG GTATTAATTGCGTTGCGCTCACTG AGGTTATCTAAAATCTTTACTGATAGCCCTAAAAC ATCTGCATTAATGAATCGGCCAACGCGGGGA GAGCCGCTCAATAGATAATACACAGACAATATTTTG AATCTTTCCAGTGTGAGACGGGCAAGAATAGCCCG AGGATTCAGCAGAAGATAAAAACAGAG AAGCGGTCCACGCTGTTTGGCCAGCAACCCTGTGATAAAG AAGCAGATTCCAGTGTGAGACGCAAGTAAATAA AGCGGCAAAATCCCTTATAAATCAAAGATACCGTCAATGGCGA</p> <p>14HC left multimerization</p>	<p>ATACGAGCCGCTAATGAGTGTGAGTCACT ACGAGGCGGTGAGTATAAATATCAAACCCTCCCTGATGAA CCCGCTCGCCCTGAGAGAGTTGACG AGCGCATTAAAAATACCGAACGAACCAACAGTTGAAAG GAGGCGAAAAATGCACCTTTCCAGTGGGAAACCTGTGCGTGC TTTGGCTATTAGTCTTAATGCGGGAAGGAGCACTAACAA TTGCCAAATTTTATCGTGTTCGCTATTGGGCGCAGGGTGGTT AAAGCGTAAGAATACGTGGCATTGG ATGGACATTCTGGCCAACAGCAACTCGTATTAAT AAATCCTGTTGATGGTGGTCCGAA</p> <p>14HC right multimerization</p>
--	--	---

c)

<p>AAAAAAAAAAAAAAAAAGCGAACGTATTATTACATTG AAAAAAAAAAAAAAAAAAGTGTTTTTATAATCGACAAC AAAAAAAAAAAAAAAAAAGCAGATTCCAGGTATTAAAC AAAAAAAAAAAAAAAAAACCGCTGGAAATTCGCTAGA AAAAAAAAAAAAAAAAAACGTATTAATCAAAGAACGCG AAAAAAAAAAAAAAAAAATTTTCAGGTTAATTTAATGG AAAAAAAAAAAAAAAAAACAGTACAACATGTAATTT AAAAAAAAAAAAAAAAAAGAAACTTTTCCACGCTAAC AAAAAAAAAAAAAAAAAAGGAGGAGGCAATATCATTCC AAAAAAAAAAAAAAAAAAGAACGGAGAAATGAGTTAA AAAAAAAAAAAAAAAAAAGAGCGCTTTCTCCACCAATGAA AAAAAAAAAAAAAAAAAAGCCCAATAAAGATATAAAA AAAAAAAAAAAAAAAAAAGAACGCAGAACCAACC AAAAAAAAAAAAAAAAAACCATCGATAGCCCTCATTTTC AAAAAAAAAAAAAAAAAAGAGCCCGCCAAACAGTTA AAAAAAAAAAAAAAAAAATGCCCCCTTGCGAATAATA AAAAAAAAAAAAAAAAAAGGATAGCAACGAAATCCGCG AAAAAAAAAAAAAAAAAATTTTTCAGTTGAGCAGCG AAAAAAAAAAAAAAAAAAGACAGACGAGTAGTAAA</p> <p>3LS coupling</p>	<p>GAAAGCCGAATCCTGTTGATGGTGCACGAGG GCGCTTTCAAATCGTTAACGCGT CATCCTCATAAGGCGAGCCTCCGGCCAGAAAA CAGTACAACATGTAATTTTACCAGTCCCGTTGTACATCGAGA GGGATGTGCTGCATACGCGAGTGGCGAAAAAG ACAACCCGCGCTCAGGAAGATGAG AAGCAAATTTTAAAAACAGGAAGATTGGAA CAATGCTTTTGTGAGAGATCTACC GGCAAGGCAAGAACAATCAAATAATCATATG TCAATTTTCTGCGAACGAGTAAGG AGTCAGAAGCAAATCTTTACCCCTGAC AAGCATAACGCGCGGGGAGAGGTG AAAATGCAGATACAGGGGGT GGGGTTTCTGCGCCTTTTCCAGGTAACCG</p> <p>3LS left multimerization</p>	<p>CGAAGCGAACGTATTATTACATTGCGG CGGGTCAATGTTTTCAGGTTAATTTAATGGGCA AACGGAGAATTGAGTTAAGTA AGCGCCATGTTAGGACAGGCAATATCATTCCAGG AATGTGAGCGAGCCCAATAAAGATATAAATAAT ACGCAGAACCAACCATG ATATATTTTAAAGGCCCGCCAAACAGTTAACA CCCCTTGCGAATAATAAAGG CTTTGTAAAGTTTTTTCAGGTTGAGCAGCGTAT TATAAAGACAGAACGAGTAGT AATAGTAACCTGCTCCAT AACATACGAGCGCAGATTCCAGGATTAATACTACC CCTGGAAATTCGCTAGACAG AAACTTTTCAACGCTAACCGCACTCCAGCCA CGCTTTTCCACCAATGAAACAAAGGCTATCA AATCCTGAGAAGCGGTTTGCCTAT ATCGATAGCCCTCATTTTCGATTTAGTTGAC TTTTATAATTCGACAACGATCAGATGCGG GATAGCAACGAAATCCGCGAAATGTTTAGACT ACATTCAACTATTGGGCTGAGAT ATTAATCCAAAGAACGGACATAAAAAATC</p> <p>3LS right multimerization</p>
---	--	--

Table D1: Staple sequences for coupling and multimerization. Sequences of the oligonucleotides used for coupling to magnetic particles and for multimerization of the (a) 6HB, (b) 14HC, and (c) 3LS.

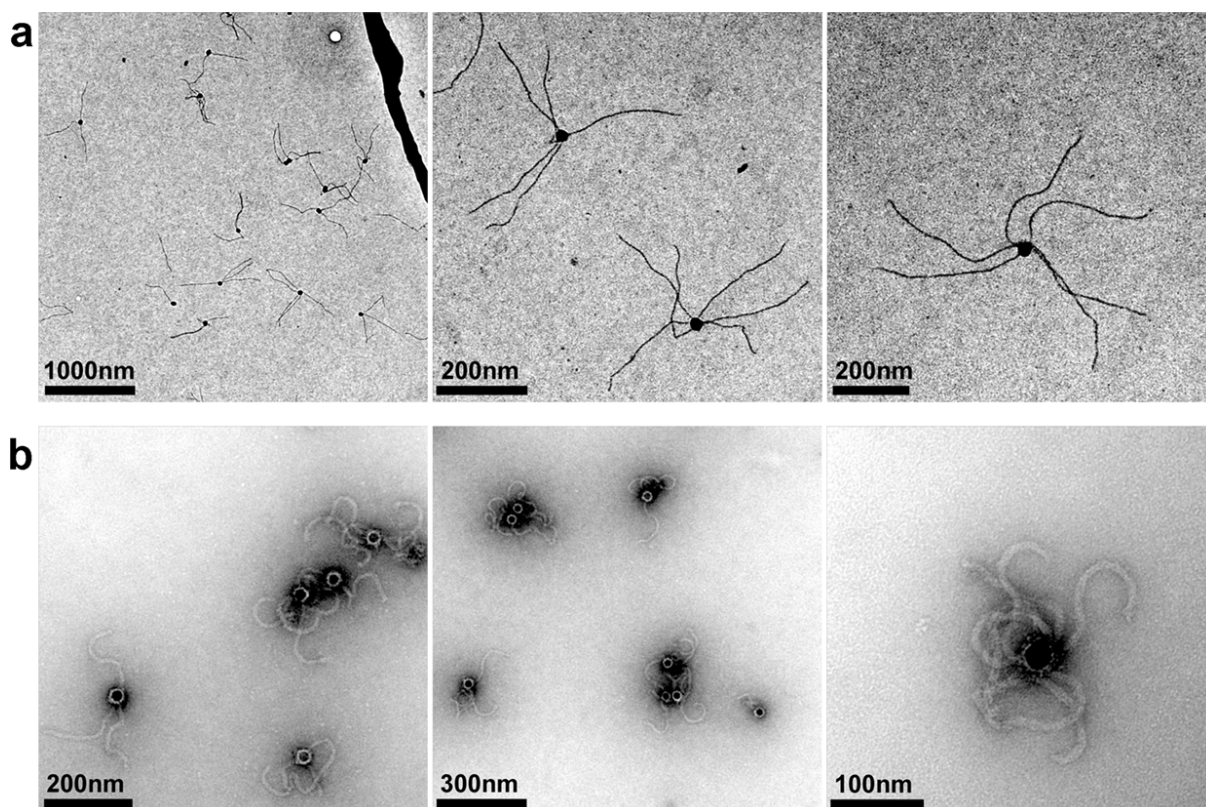


Figure D4: Additional TEM images of 30 nm magnetic nanoparticles functionalized with multiple **a)** 6-helix bundles (6HB) and **b)** 14-helix corkscrews (14HC). We observed as much as six 6HBs and eight 14HCs attached to a single nanoparticle.

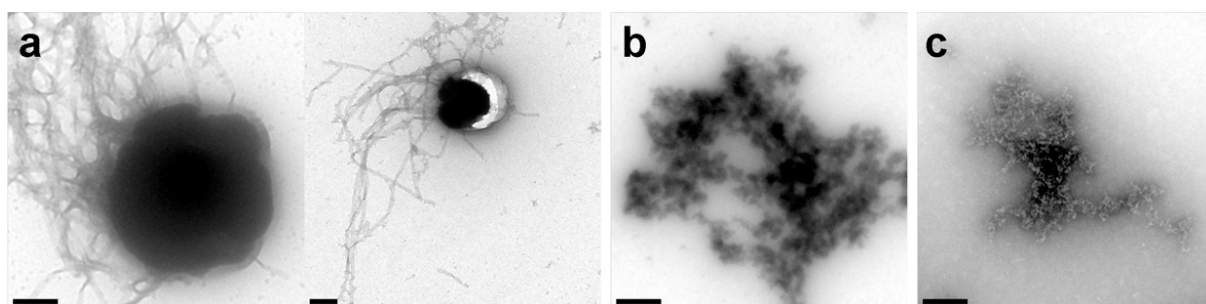


Figure D5: (a) Images of multimerized three-layer sheets (3LS) attached to fragments of 1 μm magnetic particles as observed on TEM grids containing the hybrid structures. We believe that the attached artificial filaments exert sufficient force on the magnetic particle's polymer shell to rip the particle into smaller pieces. (b) Destroyed structures found all over the TEM grid closely resemble (c) the structures found in a control sample, where we intentionally destroyed the magnetic particles by freezing them to $-20\text{ }^{\circ}\text{C}$. Scale bars: 200 nm

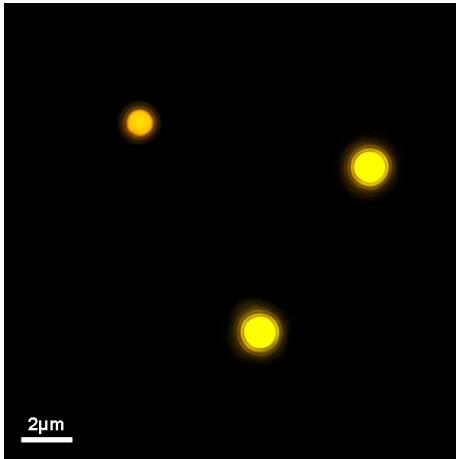
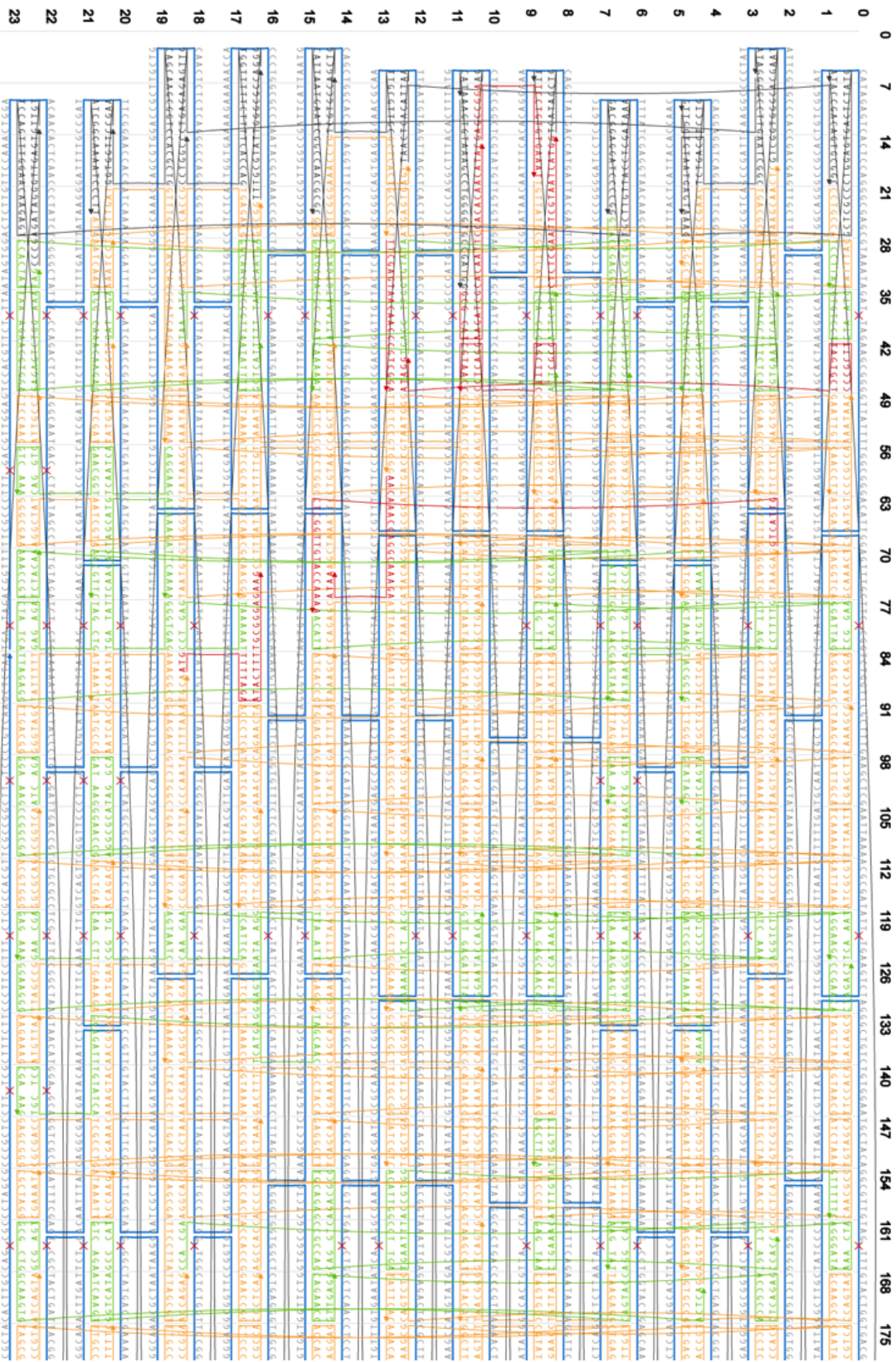


Figure D6: Fluorescence microscopy image showing a mixture of 1 μm magnetic particles functionalized with (brighter particles) and without (dimmer particle) single Cy3-modified DNA origami. The functionalized particles had an increased fluorescence intensity and an increased size compared to the non-functionalized particles.

Fluorescence microscopy and magnetic actuation. Before imaging, the hybrid structures were diluted into a 12 mM MgCl_2 1x TE buffer with 0.05 % of the surfactant Tween 20 to prevent the particles from adhering to the glass surface. A second glass slide was put on top of the sample and the glass slides sealed with glue in order to reduce evaporation and an associated drift in the liquid. Images of the hybrid structures were taken by a Zeiss Observer Z1 microscope in fluorescence mode with a 100x objective, mercury lamp illumination and a Cy3 filter set. The microscope was connected to an Andor Solis camera with pixel resolution of 6,4 pixels/ μm . For the actuation of the hybrid structures we incorporated a water-cooled three-axis Helmholtz coil into the microscopy setup, which generated a spatially homogeneous time-varying magnetic field. All experiments were carried out at room temperature.

Appendix E: Materials and Methods for Chapter 5



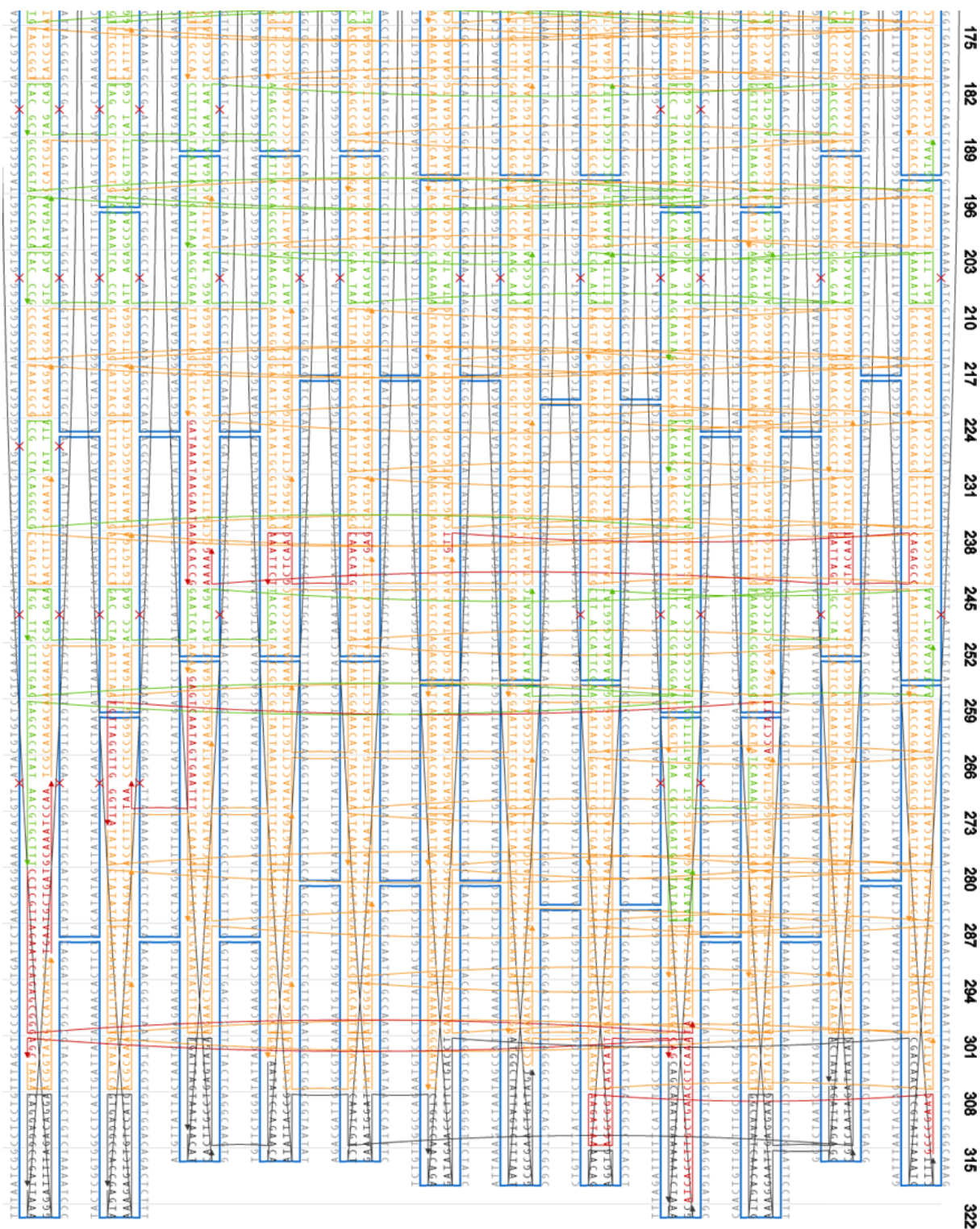


Figure E1: CaDNAno image of the twisted 24HB. The schematic picture shows the scaffold path (blue) and the staple oligonucleotides of the twisted 24-helix bundle. Staples coloured in grey are designed to connect 24HBs with each other, which leads to a multimerization process of the structures.

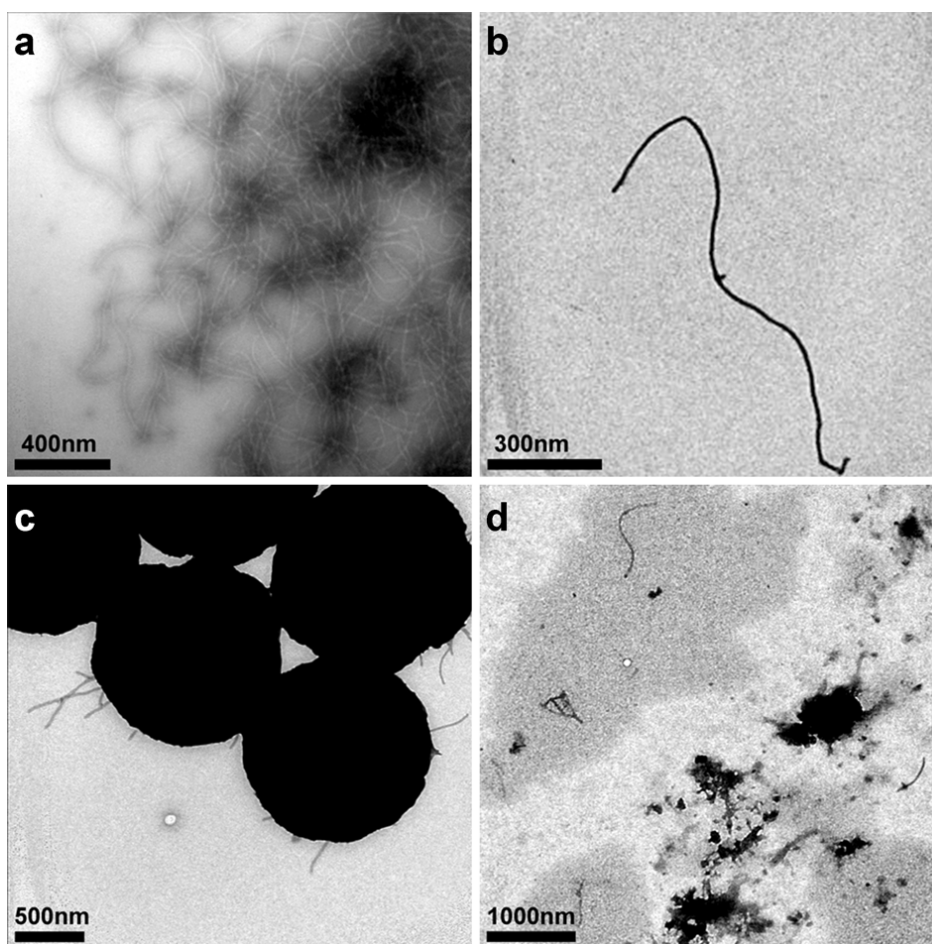


Figure E2: Coupling of the twisted 24HB to $1\mu\text{m}$ magnetic particles. TEM images of (a) clusters and (b) single multimers build up from several twisted 24HBs. The artificial filaments showed the designed curvature, but also exhibited many unwanted nicks. (c) Only few $1\mu\text{m}$ particles with attached multimers could be found, while (d) many destroyed structures and free multimers were found.

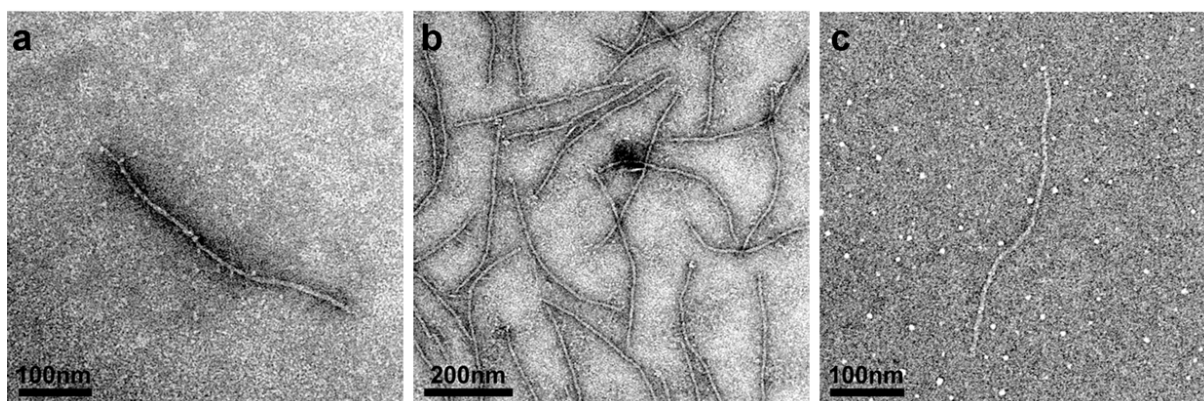


Figure E3: Purification of the 6HB from excess neutravidin. (a) TEM image of a 6HB (with 29 DNA overhangs throughout the structure) after agarose gel purification. Free neutravidin was visible as “white spots” in the vicinity of the structure. We believe that the neutravidin unspecifically bound to the single stranded DNA overhangs on the origami during gel electrophoresis and therefore could not be separated. (b) Addition of 500 mM NaCl during gel electrophoresis reduced the amount of unbound neutravidin but resulted

in an increased cluster formation of the neutravidin at the binding site of the origami. (c) PEG purification as an alternative for agarose gel purification led to an even higher amount of unbound and clustered neutravidin in the sample.

Bibliography:

1. Feynman, R.P., *There's plenty of room at the bottom*. Engineering and science, 1960. **23**(5): p. 22-36.
2. Wang, J., *Can Man-Made Nanomachines Compete with Nature Biomotors?* ACS nano, 2009. **3**: p. 4-9.
3. Mavroidis, C. and A. Ferreira, *Nanorobotics: current approaches and techniques*. 2013: Springer Science & Business Media.
4. Wang, H. and M. Pumera, *Fabrication of micro/nanoscale motors*. Chemical reviews, 2015. **115**(16): p. 8704-8735.
5. Purcell, E.M., *Life at low Reynolds number*. Am. J. Phys, 1977. **45**(1): p. 3-11.
6. Vincent, J.F., et al., *Biomimetics: its practice and theory*. Journal of the Royal Society Interface, 2006. **3**(9): p. 471-482.
7. Elgeti, J., R.G. Winkler, and G. Gompper, *Physics of microswimmers—single particle motion and collective behavior: a review*. Reports on progress in physics, 2015. **78**(5): p. 056601.
8. Jahn, T.L. and E.C. Bovee, *Movement and locomotion of microorganisms*. Annual Reviews in Microbiology, 1965. **19**(1): p. 21-58.
9. Lasa, I., P. Dehoux, and P. Cossart, *Actin polymerization and bacterial movement*. Biochimica et Biophysica Acta (BBA)-Molecular Cell Research, 1998. **1402**(3): p. 217-228.
10. Berg, H.C. and R.A. Anderson, *Bacteria swim by rotating their flagellar filaments*. 1973.
11. Gibbons, I., *Cilia and flagella of eukaryotes*. The Journal of cell biology, 1981. **91**(3): p. 107s-124s.
12. Macnab, R.M., *How bacteria assemble flagella*. Annual Reviews in Microbiology, 2003. **57**(1): p. 77-100.
13. Berg, H.C., *The rotary motor of bacterial flagella*. Biochemistry, 2003. **72**(1): p. 19.
14. Magariyama, Y., S. Sugiyama, and S. Kudo, *Bacterial swimming speed and rotation rate of bundled flagella*. FEMS microbiology letters, 2001. **199**(1): p. 125-129.
15. Kudo, S., Y. Magariyama, and S.-I. Aizawa, *Abrupt changes in flagellar rotation observed by laser dark-field microscopy*. 1990.
16. Inaba, K., *Sperm flagella: comparative and phylogenetic perspectives of protein components*. Molecular human reproduction, 2011. **17**(8): p. 524-538.
17. Konno, A., et al., *Branchial cilia and sperm flagella recruit distinct axonemal components*. PloS one, 2015. **10**(5): p. e0126005.
18. Lauga, E. and T.R. Powers, *The hydrodynamics of swimming microorganisms*. Reports on Progress in Physics, 2009. **72**(9): p. 096601.
19. Dreyfus, R., et al., *Microscopic artificial swimmers*. Nature, 2005. **437**(7060): p. 862-865.
20. Ghosh, A. and P. Fischer, *Controlled propulsion of artificial magnetic nanostructured propellers*. Nano letters, 2009. **9**(6): p. 2243-2245.
21. Tottori, S., et al., *Magnetic Helical Micromachines: Fabrication, Controlled Swimming, and Cargo Transport*. Adv. Mater., 2012. **24**: p. 811-6.
22. Manghi, M., X. Schlagberger, and R.R. Netz, *Propulsion with a rotating elastic nanorod*. Physical review letters, 2006. **96**(6): p. 068101.
23. Qian, B., T.R. Powers, and K.S. Breuer, *Shape transition and propulsive force of an elastic rod rotating in a viscous fluid*. Physical review letters, 2008. **100**(7): p. 078101.

24. Schamel, D., et al., *Nano-Propellers and their Actuation in Complex Viscoelastic Media*. ACS nano, 2014. **8**: p. 8794-8801.
25. Bell, D.J., et al. *Flagella-like Propulsion for Microrobots Using a Nanocoil and a Rotating Electromagnetic Field*. in ICRA. 2007.
26. Gao, W., et al., *Bioinspired helical microswimmers based on vascular plants*. Nano Lett., 2014. **14**(1): p. 305-10.
27. Maier, A.M., et al., *Magnetic Propulsion of Microswimmers with DNA-Based Flagellar Bundles*. Nano Lett., 2016. **16**: p. 906-910.
28. Sundararajan, S., et al., *Catalytic motors for transport of colloidal cargo*. Nano letters, 2008. **8**(5): p. 1271-1276.
29. Burdick, J., et al., *Synthetic nanomotors in microchannel networks: Directional microchip motion and controlled manipulation of cargo*. Journal of the American Chemical Society, 2008. **130**(26): p. 8164-8165.
30. Wang, J., *Cargo-towing synthetic nanomachines: towards active transport in microchip devices*. Lab on a Chip, 2012. **12**(11): p. 1944-1950.
31. Guix, M., C.C. Mayorga-Martinez, and A. Merkoçi, *Nano/micromotors in (bio) chemical science applications*. Chemical reviews, 2014. **114**(12): p. 6285-6322.
32. Fan, D., et al., *Subcellular-resolution delivery of a cytokine through precisely manipulated nanowires*. Nature nanotechnology, 2010. **5**(7): p. 545-551.
33. Gao, W., et al., *Cargo - Towing Fuel - Free Magnetic Nanoswimmers for Targeted Drug Delivery*. small, 2012. **8**(3): p. 460-467.
34. Campuzano, S., et al., *Motion-driven sensing and biosensing using electrochemically propelled nanomotors*. Analyst, 2011. **136**(22): p. 4621-4630.
35. Xu, X., et al., *Near - field enhanced plasmonic - magnetic bifunctional nanotubes for single cell bioanalysis*. Advanced Functional Materials, 2013. **23**(35): p. 4332-4338.
36. Hanay, M., et al., *Single-protein nanomechanical mass spectrometry in real time*. Nature nanotechnology, 2012. **7**(9): p. 602-608.
37. Zhang, L., K.E. Peyer, and B.J. Nelson, *Artificial bacterial flagella for micromanipulation*. Lab on a Chip, 2010. **10**(17): p. 2203-2215.
38. Nelson, B.J., I.K. Kaliakatsos, and J.J. Abbott, *Microrobots for minimally invasive medicine*. Annual review of biomedical engineering, 2010. **12**: p. 55-85.
39. Gultepe, E., et al., *Biopsy with Thermally - Responsive Untethered Microtools*. Advanced materials, 2013. **25**(4): p. 514-519.
40. Paxton, W.F., et al., *Catalytic nanomotors: autonomous movement of striped nanorods*. Journal of the American Chemical Society, 2004. **126**(41): p. 13424-13431.
41. Fournier-Bidoz, S., et al., *Synthetic self-propelled nanorotors*. Chemical Communications, 2005(4): p. 441-443.
42. Loget, G. and A. Kuhn, *Electric field-induced chemical locomotion of conducting objects*. Nature communications, 2011. **2**: p. 535.
43. Ebbens, S.J. and J.R. Howse, *Direct observation of the direction of motion for spherical catalytic swimmers*. Langmuir, 2011. **27**(20): p. 12293-12296.
44. Jiang, H.-R., N. Yoshinaga, and M. Sano, *Active motion of a Janus particle by self-thermophoresis in a defocused laser beam*. Physical review letters, 2010. **105**(26): p. 268302.
45. Mair, L.O., et al., *Highly controllable near-surface swimming of magnetic Janus nanorods: application to payload capture and manipulation*. Journal of Physics D: Applied Physics, 2011. **44**(12): p. 125001.

46. Liu, M., et al., *Light-driven nanoscale plasmonic motors*. Nature nanotechnology, 2010. **5**(8): p. 570-573.
47. Rao, K.J., et al., *A force to be reckoned with: a review of synthetic microswimmers powered by ultrasound*. Small, 2015. **11**(24): p. 2836-2846.
48. Wang, J., *Nanomachines: Fundamentals and Applications*. 2013: John Wiley & Sons.
49. Schaller, V., et al., *Polar patterns of driven filaments*. Nature, 2010. **467**(7311): p. 73-77.
50. Castro, C.E., et al., *A primer to scaffolded DNA origami*. Nature Methods, 2011. **8**(3): p. 221-229.
51. Carlson, R., *The changing economics of DNA synthesis*. Nature biotechnology, 2009. **27**(12): p. 1091.
52. Watson, J.D. and F.H. Crick. *The Structure of DNA*. in *Cold Spring Harbor symposia on quantitative biology*. 1953. Cold Spring Harbor Laboratory Press.
53. Seeman, N.C., *Nucleic acid junctions and lattices*. Journal of theoretical biology, 1982. **99**(2): p. 237-247.
54. Li, X., et al., *Antiparallel DNA double crossover molecules as components for nanoconstruction*. Journal of the American Chemical Society, 1996. **118**(26): p. 6131-6140.
55. Seeman, N.C., *Nanomaterials based on DNA*. Annual review of biochemistry, 2010. **79**: p. 65.
56. Winfree, E., et al., *Design and self-assembly of two-dimensional DNA crystals*. Nature, 1998. **394**(6693): p. 539-544.
57. Li, H., et al., *DNA-templated self-assembly of protein and nanoparticle linear arrays*. Journal of the American Chemical Society, 2004. **126**(2): p. 418-419.
58. Le, J.D., et al., *DNA-templated self-assembly of metallic nanocomponent arrays on a surface*. Nano Letters, 2004. **4**(12): p. 2343-2347.
59. Rothmund, P.W., et al., *Design and characterization of programmable DNA nanotubes*. Journal of the American Chemical Society, 2004. **126**(50): p. 16344-16352.
60. Mohammed, A.M. and R. Schulman, *Directing self-assembly of DNA nanotubes using programmable seeds*. Nano letters, 2013. **13**(9): p. 4006-4013.
61. Yin, P., et al., *Programming DNA Tube Circumferences*. Science, 2008. **321**: p. 824-6.
62. Ke, Y., et al., *Three-dimensional structures self-assembled from DNA bricks*. science, 2012. **338**(6111): p. 1177-1183.
63. Seeman, N.C., *DNA in a material world*. Nature, 2003. **421**(6921): p. 427-431.
64. Rothmund, P.W., *Folding DNA to create nanoscale shapes and patterns*. Nature, 2006. **440**(7082): p. 297-302.
65. Douglas, S.M., et al., *Self-assembly of DNA into nanoscale three-dimensional shapes*. Nature, 2009. **459**(7245): p. 414-418
66. Dietz, H., S.M. Douglas, and W.M. Shih, *Folding DNA into Twisted and Curved Nanoscale Shapes*. Science, 2009. **325**: p. 725-730.
67. Douglas, S.M., et al., *Rapid prototyping of 3D DNA-origami shapes with caDNAno*. Nucleic Acids Res., 2009. **37**(15): p. 5001-6.
68. Kuzyk, A., et al., *DNA-based self-assembly of chiral plasmonic nanostructures with tailored optical response*. Nature, 2012. **483**(7389): p. 311-314.
69. Saccà, B., et al., *Orthogonal protein decoration of DNA origami*. Angewandte Chemie International Edition, 2010. **49**(49): p. 9378-9383.
70. Roller, E.-M., et al., *DNA-assembled nanoparticle rings exhibit electric and magnetic resonances at visible frequencies*. Nano letters, 2015. **15**(2): p. 1368-1373.

71. Kauert, D.J., et al., *Direct mechanical measurements reveal the material properties of three-dimensional DNA origami*. Nano letters, 2011. **11**(12): p. 5558-5563.
72. Wang, J.-S., et al., *Hierarchical chirality transfer in the growth of Towel Gourd tendrils*. Scientific reports, 2013. **3**.
73. Li, L., J.C. Weaver, and C. Ortiz, *Hierarchical structural design for fracture resistance in the shell of the pteropod *Clio pyramidata**. Nature communications, 2015. **6**.
74. Grason, G.M., *Braided bundles and compact coils: The structure and thermodynamics of hexagonally packed chiral filament assemblies*. Physical Review E, 2009. **79**(4): p. 041919.
75. Dogic, Z. and S. Fraden, *Ordered phases of filamentous viruses*. Current Opinion in Colloid & Interface Science, 2006. **11**(1): p. 47-55.
76. Wang, Y., et al., *Emerging chirality in nanoscience*. Chemical Society Reviews, 2013. **42**(7): p. 2930-2962.
77. Sanchez, C., H. Arribart, and M.M.G. Guille, *Biomimetism and bioinspiration as tools for the design of innovative materials and systems*. Nature materials, 2005. **4**(4): p. 277-288.
78. Schmidt, O.G. and K. Eberl, *Nanotechnology: Thin solid films roll up into nanotubes*. Nature, 2001. **410**(6825): p. 168-168.
79. Chen, X., et al., *Mechanics of a carbon nanocoil*. Nano Letters, 2003. **3**(9): p. 1299-1304.
80. Li, W., et al., *Superelastic metal microsprings as fluidic sensors and actuators*. Lab on a Chip, 2012. **12**(13): p. 2322-2328.
81. Robbie, K., D. Broer, and M. Brett, *Chiral Nematic Order in Liquid Crystals Imposed by an Engineered Inorganic Nanostructure*. Nature, 1999. **399**: p. 764-766.
82. Mark, A.G., et al., *Hybrid nanocolloids with programmed three-dimensional shape and material composition*. Nature materials, 2013. **12**(9): p. 802-807.
83. Singh, J., et al., *Metal-coated Si springs: Nanoelectromechanical actuators*. Applied physics letters, 2004. **84**(18): p. 3657-3659.
84. Gansel, J.K., et al., *Gold helix photonic metamaterial as broadband circular polarizer*. Science, 2009. **325**(5947): p. 1513-1515.
85. Motojima, S., et al., *Properties and potential applications of carbon microcoils/nanocoils*. Diamond and Related materials, 2004. **13**(11): p. 1989-1992.
86. Kuzuya, A., et al., *Six-helix and eight-helix DNA nanotubes assembled from half-tubes*. Nano letters, 2007. **7**(6): p. 1757-1763.
87. Gao, P.X., W. Mai, and Z.L. Wang, *Superelasticity and nanofracture mechanics of ZnO nanohelices*. Nano letters, 2006. **6**(11): p. 2536-2543.
88. Hayashida, T., L. Pan, and Y. Nakayama, *Mechanical and electrical properties of carbon tubule nanocoils*. Physica B: Condensed Matter, 2002. **323**(1): p. 352-353.
89. Liu, J., et al., *The Interesting Influence of Nanosprings on the Viscoelasticity of Elastomeric Polymer Materials: Simulation and Experiment*. Adv. Funct. Mater., 2013. **23**: p. 1156-1163.
90. Chen, X., et al., *The design and performance of tactile/proximity sensors made of carbon microcoils*, in *Smart Sensors and Sensing Technology*. 2008, Springer. p. 251-261.
91. Zhang, L., et al., *Artificial bacterial flagella: Fabrication and magnetic control*. Applied Physics Letters, 2009. **94**(6): p. 064107.
92. Fischer, P. and A. Ghosh, *Magnetically actuated propulsion at low Reynolds numbers: towards nanoscale control*. Nanoscale, 2011. **3**(2): p. 557-563.

93. Schiffels, D., T. Liedl, and D.K. Fygenson, *Nanoscale structure and microscale stiffness of DNA nanotubes*. ACS nano, 2013. **7**(8): p. 6700-6710.
94. Maier, A.M., et al., *Self-Assembled DNA Tubes Forming Helices of Controlled Diameter and Chirality*. ACS nano, 2017.
95. Yang, Y., et al., *Self-Assembly of DNA Rings from Scaffold-Free DNA Tiles*. Nano Lett., 2013. **13**: p. 1862-6.
96. Nam, G.-M., et al., *Helices at interfaces*. EPL (Europhysics Letters), 2012. **100**(2): p. 28001.
97. Iqbal, A., et al., *Orientation dependence in fluorescent energy transfer between Cy3 and Cy5 terminally attached to double-stranded nucleic acids*. Proceedings of the National Academy of Sciences, 2008. **105**(32): p. 11176-11181.
98. Norman, D.G., et al., *Location of cyanine-3 on double-stranded DNA: importance for fluorescence resonance energy transfer studies*. Biochemistry, 2000. **39**(21): p. 6317-6324.
99. Honda, T., K. Arai, and K. Ishiyama, *Micro swimming mechanisms propelled by external magnetic fields*. Magnetism, IEEE Transactions on, 1996. **32**(5): p. 5085-5087.
100. Tomie, M., et al., *Turning performance of fish-type microrobot driven by external magnetic field*. IEEE Transactions on Magnetism, 2005. **41**(10): p. 4015-4017.
101. Darnton, N.C., et al., *On torque and tumbling in swimming Escherichia coli*. Journal of bacteriology, 2007. **189**(5): p. 1756-1764.
102. Lauga, E., et al., *Swimming in circles: motion of bacteria near solid boundaries*. Biophysical journal, 2006. **90**(2): p. 400-412.
103. Vogel, R. and H. Stark, *Rotation-induced polymorphic transitions in bacterial flagella*. Physical review letters, 2013. **110**(15): p. 158104.
104. Dusenbery, D.B., *Minimum size limit for useful locomotion by free-swimming microbes*. Proceedings of the National Academy of Sciences, 1997. **94**(20): p. 10949-10954.
105. Mandal, P. and A. Ghosh, *Observation of enhanced diffusivity in magnetically powered reciprocal swimmers*. Physical review letters, 2013. **111**(24): p. 248101.
106. Ghosh, A., et al., *Velocity fluctuations in helical propulsion: how small can a propeller be*. The journal of physical chemistry letters, 2013. **5**(1): p. 62-68.
107. Bechinger, C., et al., *Active particles in complex and crowded environments*. Reviews of Modern Physics, 2016. **88**(4): p. 045006.
108. Douglas, S.M., I. Bachelet, and G.M. Church, *A logic-gated nanorobot for targeted transport of molecular payloads*. Science, 2012. **335**(6070): p. 831-834.
109. Lauga, E., *Enhanced diffusion by reciprocal swimming*. Physical review letters, 2011. **106**(17): p. 178101.
110. Lee, T.-C., et al., *Self-propelling nanomotors in the presence of strong Brownian forces*. Nano letters, 2014. **14**(5): p. 2407-2412.
111. Xu, Q., et al., *Nanoparticle diffusion in, and microrheology of, the bovine vitreous ex vivo*. Journal of Controlled Release, 2013. **167**(1): p. 76-84.
112. Nance, E.A., et al., *A dense poly (ethylene glycol) coating improves penetration of large polymeric nanoparticles within brain tissue*. Science translational medicine, 2012. **4**(149): p. 149ra119-149ra119.
113. Sengupta, S., et al., *Enzyme molecules as nanomotors*. Journal of the American Chemical Society, 2013. **135**(4): p. 1406-1414.
114. Babič, D., C. Schmitt, and C. Bechinger, *Colloids as model systems for problems in statistical physics*. Chaos: An Interdisciplinary Journal of Nonlinear Science, 2005. **15**(2): p. 026114.

115. Issa, B., et al., *Magnetic nanoparticles: surface effects and properties related to biomedicine applications*. International journal of molecular sciences, 2013. **14**(11): p. 21266-21305.
116. Adolphi, N.L., et al., *Characterization of single-core magnetite nanoparticles for magnetic imaging by SQUID relaxometry*. Physics in medicine and biology, 2010. **55**(19): p. 5985.
117. Ishiyama, K., et al., *Swimming micro-machine driven by magnetic torque*. Sensors and Actuators A: Physical, 2001. **91**(1): p. 141-144.
118. Keaveny, E.E., S.W. Walker, and M.J. Shelley, *Optimization of chiral structures for microscale propulsion*. Nano letters, 2013. **13**(2): p. 531-537.
119. Lauga, E., *Floppy swimming: Viscous locomotion of actuated elastica*. Physical Review E, 2007. **75**(4): p. 041916.
120. Schnitzer, M.J. and S.M. Block, *Kinesin hydrolyses one ATP per 8-nm step*. Nature, 1997. **388**(6640): p. 386-390.
121. Kitamura, K., et al., *A single myosin head moves along an actin filament with regular steps of 5.3 nanometres*. Nature, 1999. **397**(6715): p. 129-134.
122. Noji, H., et al., *Direct observation of the rotation of F1-ATPase*. Nature, 1997. **386**(6622): p. 299-302.
123. Vale, R.D., T.S. Reese, and M.P. Sheetz, *Identification of a novel force-generating protein, kinesin, involved in microtubule-based motility*. Cell, 1985. **42**(1): p. 39-50.
124. Kron, S.J. and J.A. Spudich, *Fluorescent actin filaments move on myosin fixed to a glass surface*. Proceedings of the National Academy of Sciences, 1986. **83**(17): p. 6272-6276.
125. Hiratsuka, Y., et al., *Controlling the direction of kinesin-driven microtubule movements along microlithographic tracks*. Biophysical Journal, 2001. **81**(3): p. 1555-1561.
126. Van den Heuvel, M.G. and C. Dekker, *Motor proteins at work for nanotechnology*. Science, 2007. **317**(5836): p. 333-336.
127. Noji, H., et al., *Rotation of Escherichia coli F1-ATPase*. Biochemical and biophysical research communications, 1999. **260**(3): p. 597-599.
128. Hisabori, T., A. Kondoh, and M. Yoshida, *The γ subunit in chloroplast F1 - ATPase can rotate in a unidirectional and counter - clockwise manner*. FEBS letters, 1999. **463**(1-2): p. 35-38.
129. Suzuki, T., et al., *Chemomechanical coupling of human mitochondrial F1-ATPase motor*. Nature chemical biology, 2014. **10**(11): p. 930-936.
130. Soong, R.K., et al., *Powering an inorganic nanodevice with a biomolecular motor*. Science, 2000. **290**(5496): p. 1555-1558.
131. Yasuda, R., et al., *Resolution of distinct rotational substeps by submillisecond kinetic analysis of F1-ATPase*. Nature, 2001. **410**(6831): p. 898-904.
132. Enoki, S., et al., *High-speed angle-resolved imaging of a single gold nanorod with microsecond temporal resolution and one-degree angle precision*. Analytical chemistry, 2015. **87**(4): p. 2079-2086.
133. Rondelez, Y., et al., *Highly coupled ATP synthesis by F1-ATPase single molecules*. Nature, 2005. **433**(7027): p. 773-777.
134. Oswald, P., *H+-ATPsynthasen: Immobilisierung an Grenzflächen und Einbau in Lipidmembranen und deren Untersuchung mittels Einzelmolekül-Fluoreszenz-Spektroskopie*. 2011: Albert-Ludwigs-Universität Freiburg im Breisgau.

Vielen Dank ...

- **Prof. Tim Liedl** für die hervorragende Betreuung und für das in mich gesetzte Vertrauen eigenständig an einem neuen und einzigartigen Arbeitsgebiet forschen zu dürfen. Und für die Möglichkeit Teil einer außergewöhnlich freundschaftlichen und kollegialen Arbeitsgruppe in einem jungen und spannenden Arbeitsgebiet sein zu können.
- **Prof. Joachim Rädler** für die idealen Forschungsbedingungen und die gute Atmosphäre an seinem Lehrstuhl.
- **Prof. Peer Fischer und Prof Erwin Frey** für die reibungslose und immer freundliche Zusammenarbeit.
- **Den ehemaligen und aktuellen Mitgliedern der Arbeitsgruppe** für die Allzeit verfügbare Hilfe und die immer gute Zeit im und außerhalb des Labors: Philipp, Tao, Eva, Wooli, Timon, Susi, Luisa, Mauricio, Caro, Francesca, Kevin, Amelie, Linh, Robert, Samet, David, Daniel, Ian, Yongzheng, Verena, Stephe.
- **Meinen Bachelorstudenten** für ihre Beiträge und die Begeisterung die sie mitgebracht haben: Sophia, Johannes, Christoph, Max
- **Susanne Kempter und Gerlinde Schwake** für die jederzeitige Unterstützung im und ausserhalb des Labor.
- **Daniel Schiffels** für die wichtige wissenschaftliche Vorarbeit.
- **Cornelius Weig** für die freundschaftliche Zusammenarbeit und gegenseitige Unterstützung auf dem Weg zur gemeinsamen Veröffentlichung.
- **Meiner Familie** für die seelische Unterstützung .
- **Lisa** für dich!
- **Pepe** für die Zukunft!

Danke.